Magnetic properties of two geometrically frustrated compounds: $SrHo_2O_4$ and $SrGd_2O_4$

by

Olga Young

Thesis

Submitted to the University of Warwick

for the degree of

Doctor of Philosophy

Department of Physics

October 2013

THE UNIVERSITY OF

WARWICK

In memory of my father, Игорь,

(15th December 1960 - 30th October 2012)

I hope you found peace.

Contents

List of Tables

List of Figures

Acknowledgments

Declarations

This thesis is submitted to the University of Warwick in support of my application for the degree of Doctor of Philosophy. The experimental work presented (including the data generated and the data analysis) was carried out by myself (except where explicitly stated) between October 2009 and March 2013 at the University of Warwick Physics Department, the ISIS facility at the Rutherford Appleton Laboratory (RAL) in Oxford, and the Institut Laue Langevin (ILL) in Grenoble. All of the polycrystalline samples of the SrLn_2O$_4$ materials and the SrGd$_2$O$_4$ single crystals were prepared by myself under the guidance of Prof. Geetha Balakrishnan, who also grew the single crystal of SrHo$_2$O$_4$ prior to the start of my Ph.D. All of the Rietveld refinements of the powder X-ray data were done by me after training in the use of the diffractometers and the TopasRuns software by Dr. Dean Keeble. The magnetic and physical properties measurements were carried out by myself at Warwick after initial training by Dr. Martin Lees and Dr. Oleg Petrenko. The specific heat measurements on single crystals of non-magnetic analogues of the SrLn_2O$_4$ systems, SrY$_2$O$_4$ and SrLu$_2$O$_4$, taken in zero field, were performed by Dr. Oleg Petrenko prior to the start of my Ph.D. The experiments at the neutron scattering facilities were performed with the help of local contacts, and I was either the sole experimentalist or a leading member of the experimental team. The Rietveld refinement of the neutron powder diffraction data from SrHo$_2$O$_4$ presented in Section 5.1.3 was performed under the guidance of Dr. Laurent Chapon. All other neutron scattering data presented in the thesis was analysed by myself with advice from instrument scientists and Dr. Oleg Petrenko.

     This thesis has been composed by myself and no part has been submitted for examination at any other institute. Parts of the work described herein have been published as

follows:

- Highly frustrated magnetism in $SrHo_2O_4$: Coexistence of two types of short-range order

  O. Young, A. R. Wildes, P. Manuel, B. Ouladdiaf, D. D. Khalyavin, G. Balakrishnan and O. A. Petrenko

  Phys. Rev. B **88**, 024411 (2013).

- Low temperature magnetic structure of geometrically frustrated $SrHo_2O_4$

  O. Young, L. C. Chapon and O. A. Petrenko

  J. Phys.: Conf. Ser. **391**, 012081 (2012).

- Magnetisation studies of geometrically frustrated antiferromagnets $SrLn_2O_4$, with $Ln = $ Er, Dy, and Ho

  T. J. Hayes, O. Young, G. Balakrishnan and O. A. Petrenko

  J. Phys. Soc. Jpn. **81**, 024708 (2012).

- Magnetisation studies of geometrically frustrated $SrGd_2O_4$

  O. Young, G. Balakrishnan and O. A. Petrenko

  (In preparation)

- Nature of the field induced behaviour of the highly frustrated antiferromagnet $SrHo_2O_4$

  O. Young, A. R. Wildes, P. Manuel, D. D. Khalyavin, G. Balakrishnan and O. A. Petrenko

  J. A. M. Paddison and A. L. Goodwin

  (In preparation)

  I have presented the $SrHo_2O_4$ work described in this thesis at the following meetings:

- Talk at the Theoretical and Experimental Magnetism Meeting, 4-5th July 2013, Abingdon, UK

- Contributed talk at the International Conference on Magnetism, 8-13th July 2012, Busan, S. Korea

- Poster at the Highly Frustrated Magnetism Conference, 4-8th June 2012, Hamilton, Canada

- Poster at the Condensed Matter and Materials Physics Conference, 13-15th December 2011, Manchester, UK

- Poster presentation at the Strongly Correlated Electron Systems Conference, 29th September-3rd October 2011, Cambridge, UK

Abstract

Frustrated magnetism is the study of competing interactions, and when these are incompatible with the geometry of the lattice, systems can find it hard to establish a unique ground state. Recently, a new family of frustrated rare earth compounds, with the formula $SrLn_2O_4$, have started to be investigated. The crystal structure of the $SrLn_2O_4$ systems allows for two crystallographically inequivalent sites of the rare-earth ions in a unit cell. These magnetic ions form zigzag chains that run along the c axis. The triangular ladders can be frustrated, and are magnetically equivalent to one-dimensional chains with first- and second-nearest-neighbour interactions. The chains of Ln^{3+} ions interconnect by forming a distorted honeycomb structure, a bipartite lattice made up of edge-sharing hexagons, in the *a-b* plane.

An investigation into two members of the $SrLn_2O_4$ family of geometrically frustrated magnets, $SrHo_2O_4$ and $SrGd_2O_4$, is presented in this thesis. Even though both compounds share the same structure, very different magnetic behaviour is expected. In the ground state Gd has $L = 0$, and it is found to be a good realisation of a classical Heisenberg antiferromagnet. Conversely, $SrHo_2O_4$, shows pronounced Ising anisotropy at low temperatures, and more unusually, the spins on the two magnetic sites point along orthogonal crystallographic axes. Both powders and single crystals have been used to study the magnetic behaviour of $SrHo_2O_4$ and $SrGd_2O_4$, and the single crystals of $SrGd_2O_4$ have been grown for the first time. Bulk property measurements of magnetisation, susceptibility and specific heat have been performed to map out the complex magnetic phase diagram of $SrGd_2O_4$, and to investigate the highly anisotropic behaviour of $SrHo_2O_4$. Powder neutron diffraction has been used to determine the unusual coexistence of two magnetic phases in $SrHo_2O_4$, and to solve the magnetic structure. Further single crystal neutron diffraction data shows that all of the scattering from $SrHo_2O_4$ is short-range in nature, and one of the magnetic Ho^{3+} sites orders in a one-dimensional structure. The changes to the diffraction patterns upon the application of a magnetic field were also investigated. These measurements point to an new up-up-down spin phase being stabilised for certain values of the applied field along the b axis. Inelastic scattering experiments on powder samples have also been used to try and understand the origin of the highly anisotropic nature of this compound by studying the crystalline electric field. However, these have lead to new mysteries and the need for further analysis and investigation.

Overall, both $SrHo_2O_4$ and $SrGd_2O_4$ exhibit a variety of magnetic phenomena, and their magnetic properties contribute to the understanding of the physics of the $SrLn_2O_4$ compounds.

Chapter 1

Introduction

It has been known since antiquity that lodestone (magnetite, Fe_3O_4) and iron attract each other. For example, Plato uses the analogy of magnets being able to draw iron rings (to suggest that even a great poet such as Homer has no knowledge of his own writing and that instead he is divinely possessed!) in the dialogue *Ion* [1], which indicates at least some familiarity with the existence of magnets, if not, perhaps, any technical understanding. Originally, the word "magnet" was almost an abbreviation for a "stone from Magnesia", a region in the Asia Minor, but it is likely that permanent magnets like these stones had found their first technological use as compasses in the 11th century in China [2]. For a long time a scientific understanding of the properties of magnets was still lacking, but an important breakthrough came in 1820 when Oersted proved that there is a connection between electricity and magnetism by observing the deflection of a compass needle around a current-carrying wire. Many great early scientists worked on the phenomenon, including Ampère, who put Oersted's work on a mathematic basis, Sturgeon who made the first electromagnet, and Faraday who built the first electric motor and discovered electromagnetic induction. The early experiments and theoretical efforts established the idea that magnetism is due to permanent motion of the electrons (which is equivalent to an electric current) and the mathematical relationships between electric currents and magnetic induction, with Maxwell eventually formalising the complete classical theory of electromagnetism.

At the beginning of the 20th century, Einstein's theory of relativity fundamentally changed the way we think about magnetism—magnetic fields are, in fact, a (small) rela-

tivistic correction which can only be detected when electrical charges move relative to an observer. However, in order to give a proper description of how these fields are produced by materials, it is necessary to consider magnets from the point of view of another 20th century paradigm shift—the revolution of quantum physics. During the 1920s and 1930s, the ideas of quantum magnetism were developed, including the experimental and theoretical identifications of 'spin', such that the theory for diamagnets and paramagnets, the ordered magnetic arrangement found in lodestone and the (then) newly proposed antiferromagnetic (Néel) state of materials were all phenomena that could be explained using the ideas of exchange symmetry and electrostatic repulsion.

Nowadays, magnetism is a diverse research area studied in geophysics, solar physics, life sciences and condensed matter physics, to name a few. In the latter discipline, it is the science of cooperative effects of orbital and spin magnetic moments in matter and fits under the umbrella of correlated electrons and collective phenomena. There is a huge variety of magnetic behaviour, from the longest known and most straightforward case of ferromagnetism to exotic phenomena such as spin glasses, liquids and ices. A vast range of materials are studied, with just a few examples being metals, insulators and molecular magnets. Studying cooperative phenomena can help to inform and improve the understanding of interacting many-body systems, and in magnetic research there are usually strong links between experiments and theory. Materials can be found (and engineered) to have the presence of certain conditions, such as the promotion of competing interactions and anisotropy on lattices of different dimensionality, which then allow for the realisation of exotic magnetic states, that can be studied in extreme conditions such as low-temperatures and high magnetic fields. Overall, these new systems provide the opportunity to investigate many novel phenomena, and research on magnets can enhance the current understanding of strongly correlated electron systems.

Lastly, it is important to stress that many notable advances in technology are based on the properties of magnetic materials, including hard discs, early televisions, motors, MRI scanners, to name but a few, and, in general, magnets are ubiquitous in much of modern technology. Their use in the electronics industry, recording media and data storage is continuously expanding, and potential applications of magnetic materials in the future

are vast. Overall, magnets have continued to inspire research, investigation and technology throughout the ages, and a delightful narrative about their origins and history to the present day can be found in [2].

In this thesis, an investigation into the magnetic properties of two rare-earth anti-ferromagnets, $SrHo_2O_4$ and $SrGd_2O_4$, will be presented. In order to fully appreciate the physics of these compounds, the thesis is broadly arranged into two parts: initially, a brief theoretical introduction is given in Chapters 2 and 3, and then all of the experimental techniques employed and results derived are presented in Chapters 4 to 7. The first theoretical chapter is concerned with a discussion of some of the basic features of magnetism; including the origin of magnetic moments, free ion, crystalline electric field and magnetic exchange interactions, which promote different types of magnetic order and give rise to collective excitations. In order to facilitate the discussion of the research presented later in the thesis, some features of geometric frustration, as well as the known properties of the $SrLn_2O_4$ compounds, are also outlined in Chapter 2. The fundamental concepts of crystal and magnetic structures, diffraction and the theoretical basics of neutron scattering theory, which forms the foundation of multiple experiments conducted on the $SrLn_2O_4$ compounds, are presented in Chapter 3.

The majority of the thesis is concerned with the magnetic properties of $SrHo_2O_4$ and $SrGd_2O_4$. The methodology of sample preparation, compositional analysis, single crystal growth, methods and the equipment used for bulk property measurements (such as magnetisation, susceptibility, and specific heat), including those performed at the large scale neutron scattering facilities (for diffraction and spectroscopy measurements), are described in the experimental techniques Chapter 4. This information is presented separately in order not to disrupt the flow of Chapters 5 and 6 which present the results of these experiments. The $SrHo_2O_4$ and $SrGd_2O_4$ compounds share the same space group and almost identical positions of their magnetic ions in the unit cell, but have very different properties. Chapter 5 explains the magnetic characterisation of the frustrated antiferromagnet $SrHo_2O_4$ using both powder and single crystal bulk property measurements, as well as neutron diffraction and spectroscopy, and concludes with an assessment of how this new information correlates with what is known about the other $SrLn_2O_4$ compounds. The magnetic properties

of $SrGd_2O_4$, found from magnetisation, susceptibility and specific heat measurements, are discussed in Chapter 6. These two magnets show very different behaviour, where $SrHo_2O_4$ is a highly anisotropic system that does not appear to show any transitions to long-range order down to the lowest experimental temperatures, and $SrGd_2O_4$, in contrast, shows quite a few low-temperature phase transitions, and has a complex magnetic phase diagram indicating the proximity of many low energy states. Finally, the main results of the investigations into both $SrHo_2O_4$ and $SrGd_2O_4$ are reviewed in Chapter 7, along with the explanations of current collaborations and suggestions for possible future experimental and theoretical work on these compounds. The work presented in this thesis is only a small part of the larger investigation into the SrLn_2O_4 family of compounds, which are in themselves a new family looked at from the point of view of geometric frustration which often gives rise to a rich variety of magnetic behaviour.

Chapter 2

Magnetism, frustration and the SrLn_2O$_4$ compounds

In this chapter a brief theoretical introduction to some of the topics most pertinent to the study of magnetic materials is presented. The first section is devoted to an exposition of some of the basic physical concepts of magnetism that are required to explain the behaviour of the SrLn_2O$_4$ compounds. Where possible, emphasis is placed on elucidating the properties of rare earth ions. A general discussion of frustrated magnetism in condensed matter systems follows this introduction, and the final section is reserved for a summary some of the important structural and magnetic properties of the SrLn_2O$_4$ compounds that have been established prior to the investigations presented in this thesis.

2.1   Magnetism

A summary of some basic concepts in magnetism is presented in this section. The material is not an exhaustive overview of the subject, comprehensive treatments of which can instead be found in [3–5]. This short introduction aims to highlight a few particulars of magnetic theory that may be necessary to understand the context of the work presented in subsequent chapters. First, from elementary considerations of both classical and quantum physics, the magnetic properties of atoms are described as if there were no interactions between different atoms and their environment. This means that these ions can be treated as isolated

magnetic moments, and their interaction with the magnetic field will be discussed in relation to diamagnetism and paramagnetism. Since in condensed matter the magnetic ions are not free, later sections discuss the effect of the immediate environment of a magnetic moment on its behaviour, the common exchange interactions between magnetic moments and the different long-range ordered structures that such interactions may establish. This review concludes with a brief summary of the collective excitations that can arise in condensed matter systems.

2.1.1 Magnetic moments and atomic ground states

In general, magnetism is a property of unfilled electronic shells, and as such would concern almost all of the atoms. In condensed matter, however, atoms are chemically bonded together and this often leads to no net magnetic moments except for compounds containing transition metal ions or rare-earth elements. Magnetism is a collective quantum phenomenon, but phenomenological classical models can be used to describe magnetism in terms of circulating electric currents, namely electrons moving around the nuclei of atoms. Here, the orbital motion of electrons can be approximated as a current, I, around an oriented elementary loop of area $|\mathbf{dS}|$ (an object equivalent to a magnetic dipole) and this can be used to define a fundamental property of magnetic materials called the magnetic moment, $\boldsymbol{\mu}$:

$$\boldsymbol{\mu} = I \int \mathbf{dS}. \tag{2.1}$$

The simplest case of a single electron performing a circular orbit around a hydrogen nucleus defines a rather useful quantity in magnetic research known as the Bohr magneton, μ_{B}:

$$\mu_{\mathrm{B}} = \frac{e\hbar}{2m_{\mathrm{e}}} = 9.274 \times 10^{-24} \ \mathrm{Am^2}. \tag{2.2}$$

Since the electric current comes from the motion of the electron around a loop, the mass of the electron implies that the magnetic moment is related to angular momentum, $\mathbf{L}$, via

$$\boldsymbol{\mu} = \frac{e}{2m}\mathbf{L} = \gamma\mathbf{L} \tag{2.3}$$

where γ is the gyromagnetic ratio. Due to the charge of the electron, its magnetic moment is antiparallel to its orbital angular momentum.

In real atoms, the electronic states occupied by electrons are defined in terms of quantum numbers l and m_l (where $l = 0, 1, 2, ...$; and $m_l = -l, -l + 1, ..., l - 1, l$) and quantised in units of the Plank's constant $\hbar = h/2\pi = 1.0546 \times 10^{-34}$ Js. The electronic orbitals are eigenstates of the momentum operator $\hat{\mathbf{L}}^2$, the values of which are $l(l + 1)\hbar^2$. The projection onto the z axis is given by the operator $\hat{L}_z$, and the component of the orbital angular momentum along this direction is $m_l\hbar$. Due to the charge of an electron, the angular momentum would have a magnetic moment associated with it, giving the total dipole moment of $l(l + 1)\mu_B^2$ and the magnitude of the projected value along the z of $-m_l\mu_B$.

Electrons also possess an intrinsic angular momentum, called spin, which has no classical analogue. The quantum mechanical origin of spin has been discussed at length in the literature, for example see [6]. Spin can be characterised by another angular momentum quantum number, s, which for a single electron has the value $\frac{1}{2}$, and hence $m_s = \pm\frac{1}{2}$. The eigenstate of the operator $\hat{\mathbf{S}}^2$ for the electron is $s(s+1)\hbar^2 = \frac{3}{4}\hbar$. The component of the spin along the z axis is given by the operator $\hat{S}_z$, is $m_s\hbar$ and thus only two states are possible: the 'up' $\hbar/2$ and 'down' $-\hbar/2$ states. The corresponding magnitude of the spin magnetic moment is $s(s + 1)g\mu_B^2 = \frac{3}{4}g\mu_B$, and the component along the z axis is $-g\mu_B m_s \approx \mp\mu_B$. (The g-factor in the equations is a constant that for electrons is ≈ 2.)

In magnetic atoms that contain many electrons, the individual electronic contributions are combined (by filling the electronic shells in order to minimise the electrostatic potential energy between electrons and taking into account the Pauli exclusion principle) to give the total orbital, $\mathbf{L}$, and total spin, $\mathbf{S}$, angular momenta. The spin and orbital angular momenta can couple via the dipole spin-orbit interaction, and hence the total angular momentum, $\mathbf{J}$, associated with a magnetic moment for a magnetic atom is the sum of the orbital and spin components:

$$\mathbf{J} = \mathbf{L} + \mathbf{S}. \tag{2.4}$$

Thus, it is the total angular momentum which is conserved, and states with S and L are split into a number of levels with different J, which is known as fine structure. $\mathbf{J}$ can take any value from $|L - S|$ to $|L + S|$; the degeneracy of each J level is $2J + 1$, and the

component of J along the z axis is $m_J \hbar$. (Also, for different atoms, the g-factor would take different values depending upon the relative contribution of the orbital and spin angular momenta, and is defined later in Eq 2.20.) For light atoms the spin-orbit interaction is a weak perturbation to the energy scheme established from the Coulomb interactions that govern the atomic values of S and L, which means that the energy differences between the fine structure levels are much smaller. For the rare earth ions, even though the electrostatic interaction is much larger than the spin-orbit coupling, the ground state is nevertheless well defined by **J** because the unfilled 4f electron orbitals lie inside the outer 5s and 5p shells and are thus closer to the nucleus so the higher effective nuclear charge tends to enhance the spin-orbit interaction, as well as reducing the interaction with other external charges that compete with the spin-orbit coupling as the leading perturbation.

A lot of different combinations of L, S and J are possible, so in order to establish their ground state values for a particular atom, Hund's rules may be applied to find the values of the quantum numbers for angular momentum that minimise the energy. Hund's rules are empirical constraints that are the consequence of minimising the Coulomb interactions between electrons and obeying the Pauli exclusion principle. They are:

1. Maximise S - thus attempting to prevent the dual occupation of any electron orbital and hence minimising the electrostatic repulsion energy.

2. Maximise L - another attempt at minimising Coulomb repulsion by assuming that electrons in orbits that rotate in the same direction are more effective at avoiding each other.

3. Find J as $|L - S|$ if an atomic shell is less than half full, and as $|L + S|$ if an atomic shell is more than half full - in an attempt to minimise the spin-orbit energy, note, however, that this rule only works well for rare earth ions.

Hund's rules assume that only the ground state of the atom is populated and cannot be applied to excited states of the atom.

2.1.2   Free ions in an applied magnetic field

In condensed matter systems, magnetic materials contain vast numbers of atoms, and any non-zero magnetic moments of unpaired electrons will tend to align in a magnetic field. The degree of alignment, called the magnetisation $\mathbf{M}$, will depend on the strength of the applied field, $\mathbf{H}$, and is defined as the moment per unit volume of a sample. However, increases in temperature will randomise the spins, and thus the magnetisation is a function of both field and temperature, and its magnitude is related to the degree of magnetic order present in a system. The measured magnetisation can also be compared to the theoretical values to try and understand the in-field behaviour of different magnets. The magnetic flux density, $\mathbf{B}$, is the field induced inside a magnetic material by the external field, and it is related to $\mathbf{M}$ by

$$\mathbf{B} = \mu_0(\mathbf{H} + \mathbf{M}) \tag{2.5}$$

where μ_0 is the permeability of free space. For linear materials, the magnetisation is proportional to the applied field, and so $\mathbf{M}$ and $\mathbf{H}$ can be related using

$$\mathbf{M} = \chi\mathbf{H} \tag{2.6}$$

where the susceptibility, χ, is a dimensionless quantity that represents the magnetic moment induced by the applied field $\mathbf{H}$ per unit volume. χ can be reported as a molar magnetic susceptibility or a mass susceptibility. For such materials, Eq. 2.5 can then be written as

$$\mathbf{B} = \mu_0(1 + \chi)\mathbf{H} = \mu_0\mu_\mathrm{r}\mathbf{H} \tag{2.7}$$

and μ_r is called the relative permeability of the material.

The energy, E, of a magnetic moment in a magnetic field, $\mathbf{B}$ is

$$E = -\boldsymbol{\mu} \cdot \mathbf{B} \tag{2.8}$$

and thus E is minimised when the moment is aligned along the applied field direction. So, using the definitions given in the previous section, the energy of an electron spin in a mag-

netic field applied along the z direction is $E = g\mu_\mathrm{B} m_s B$, which means that an applied field splits the energy levels of an electron, and this Zeeman splitting is proportional to the applied field. However, the atoms also possess orbital angular momentum, and from classical considerations of an atomic Hamiltonian in an applied magnetic field with the appropriate gauge, it can be shown that the two dominant perturbations to the original Hamiltonian are the paramagnetic and diamagnetic contributions.

Diamagnetism is a negative response to an applied magnetic field, so the moments in a sample align in a way that opposes the applied field and χ in Eq. 2.6 is negative. Diamagnetism is always present in any material, and an example of a perfect diamagnet would be a superconductor in the superconducting state. Classically this effect can be explained by Lenz's law, but it is more instructive to consider it using perturbation theory, by evaluating the first-order shift in the ground state energy due to the diamagnetic term in the Hamiltonian. The Helmholtz free energy, $F = E - TS$, can be written in terms of the partition function, Z,

$$F = -Nk_\mathrm{B}T\ln Z \tag{2.9}$$

where N is the number of particles, k_B is Boltzmanns constant with a value of 1.3807×10^{-23} JK^{-1} and T is the temperature. Using the first law of thermodynamics, the magnetisation can thus be found using

$$M = -\left(\frac{\partial F}{\partial B}\right)_{T,V}. \tag{2.10}$$

At $T = 0$ K, the first-order energy change due to the magnetic field for spherically symmetric ions (in which all shells are full) may be determined to be

$$\Delta E_0 = \frac{e^2 B^2}{12m_\mathrm{e}} \sum_{i=1}^{Z} \langle 0|r_i^2|0\rangle \tag{2.11}$$

where N is the number of ions, Z is the atomic number and $\langle r_i^2 \rangle$ is the mean radius of the ith electron squared. Thus, if V is the volume of the sample, the susceptibility of a

diamagnet can be evaluated using

$$\chi \approx \frac{\mu_0 M}{B} = -\frac{\mu_0}{B}\frac{\partial F}{\partial B} = -\frac{\mu_0}{B}\frac{N}{V}\frac{\partial \Delta E_0}{\partial B} = -\frac{N}{V}\frac{e^2\mu_0}{6m_{\mathrm{e}}}\sum_{i=1}^{Z}\langle r_i^2\rangle. \qquad (2.12)$$

At temperatures above zero, excited states of the system become gradually more important in determining the diamagnetic response of materials, but this effect is generally very weak and usually diamagnetic susceptibilities can be considered to be approximately temperature independent.

Paramagnetic systems show a positive susceptibility in an applied field. In zero field magnetic moments on unpaired electrons can be considered to be independent of each other, and thus are randomly oriented with respect to each other, so a sample would not have a net magnetic moment. In an applied field magnetic moments will tend to align along the field direction, with the degree of alignment governed by both temperature and the strength of the applied magnetic field. In high fields and at low temperatures (where there are less thermal fluctuations to oppose the alignment of the moment with the fields) all of the moments would be aligned and the magnetisation becomes saturated. A quantum mechanical derivation of paramagnetism (ignoring any diamagnetic effects, which are always present as a weak negative contribution) starts with the derivation of the partition function for a state with the total angular momentum J, which is

$$Z = \sum_{m_J=-J}^{J} \exp(m_J g_J \mu_{\mathrm{B}} B/k_{\mathrm{B}} T). \qquad (2.13)$$

The magnetisation can be derived from the Helmholtz free energy, which can be written in terms of the partition function, as shown in Eqs. 2.9 and 2.10. So after some algebra (see for example [3]), the magnetisation for any value of the total angular momentum in the general paramagnetic case can be written as

$$M = M_{\mathrm{s}} B_J(y) \qquad (2.14)$$

where

$$y = g_J \mu_{\mathrm{B}} J B/k_{\mathrm{B}} T \qquad (2.15)$$

and M_{s} is the saturation magnetisation, given by

$$M_{\mathrm{s}} = n g_J \mu_B J \tag{2.16}$$

where n is the number of magnetic moments per unit volume, and $B_J(y)$ is the Brillouin function as defined by

$$B_J(y) = \frac{2J+1}{2J} \coth \left(\frac{2J+1}{2J} y \right) - \frac{1}{2J} \coth \frac{y}{2J}. \tag{2.17}$$

In the limiting cases, $\mathbf{J} = \infty$ and $\mathbf{J} = \frac{1}{2}$, the Brillouin function reduces to the classical Langevin function and the $\tanh(y)$ function respectively. In a fully magnetised sample the magnetisation should be equal to the theoretical saturation value given by Eq. 2.16. In a single crystal sample the magnetisation can be measured along different principal crystal axes, and this can give information about the magnetic anisotropies present in the system.

For a linear magnetic material at high temperature and low magnetic fields $y = g_J \mu_{\mathrm{B}} J B / k_{\mathrm{B}} T \ll 1$ (so that $\chi \ll 1$) and using the Maclaurin expansion of $\coth y$ for small y (so $B_J(y) = (J+1)y/3J + \mathcal{O}(y^3)$), the susceptibility can be approximated by

$$\chi = \frac{M}{H} \approx \frac{\mu_0 M}{B} = \frac{n \mu_0 \mu_{\mathrm{eff}}^2}{3 k_{\mathrm{B}} T} \tag{2.18}$$

where the expected moment, μ_{eff}, on each ion can be related to the total angular momentum via

$$\mu_{\mathrm{eff}} = g_J \mu_{\mathrm{B}} \sqrt{J(J+1)} \tag{2.19}$$

and

$$g_J = \frac{3}{2} + \frac{S(S+1) - L(L+1)}{2J(J+1)} \tag{2.20}$$

is called the Landé g-factor.

Eq. 2.18 has the form of the Curie-Weiss law (which states that the magnetic susceptibility of a material is inversely proportional to the temperature), and has the form

$$\chi = \frac{C}{T - \theta_{\mathrm{CW}}} \tag{2.21}$$

Ion	Shell	S	L	J	g_J	Calculated μ_{eff} (μ_{B})
Ho^{3+}	$4f^{10}$	2	6	8	$\frac{5}{4}$	10.60
Gd^{3+}	$4f^{7}$	$\frac{7}{2}$	0	$\frac{7}{2}$	2	7.94

Table 2.1: The quantum numbers, g_J parameters and the expected moments for the Ho^{3+} and Gd^{3+} lanthanide ions.

where C is the Curie constant, $\text{C} = n\mu_0 g_J^2 J(J+1)/3k_{\text{B}}$ and θ_{CW} is the Weiss temperature. In low applied fields and at high temperatures some magnetic materials will tend to behave like paramagnets, so the effective moment (μ_{eff}) can be calculated from the Curie constant by using

$$\mu_{\text{eff}} = [3k_{\text{B}}/\mu_0 N_A \mu_B^2]^{\frac{1}{2}} \sqrt{\chi_{\text{m}} T} \tag{2.22}$$

which reduces to $\mu_{\text{eff}} = 2.827\sqrt{\chi_{\text{m}}^{\text{cgs}} T}$ when molar susceptibility in the cgs system of units is used. Accordingly, by plotting $1/\chi$ against temperature straight line graphs may be obtained and hence the values of C and θ_{CW} can be calculated from fits to the data. Their values are dependent on the material under investigation, and the value of the effective moment can be compared to the theoretical ground state effective moment, which can be calculated according to Eqs. 2.19 and 2.20 since (except for Sm and Eu, which have low-lying excited states) the lanthanide ions obey Hund's rules. For example, Ho^{3+} and Gd^{3+} have the values tabulated in 2.1. Thus the relations detailed above are useful when looking at real materials, and the practicalities of magnetisation and susceptibility measurements will be explained in Section 4.2.1.

2.1.3 Crystalline electric fields (CEF)

In condensed matter systems magnetic ions are not isolated, but are combined together in several possible ways to make crystalline solids. Crystals can be modelled as arrangements of anions and cations that are held together by long range electrostatic attractive forces and minimisation of short-range repulsion between the ions. The crystal structure determines the nearest-neighbour coordination symmetry, and thus the site symmetry of magnetic ions is often lowered from the spherical distribution. Only s orbitals are spherically symmetric, and all others have a pronounced angular dependence, and so different orbitals would

have different energy cost depending on the surrounding ions. The electrostatic interactions between neighbouring atoms thus set up an electric field which is called the crystalline electric field. The crystal field breaks the degeneracy of the J multiplets and creates small level splittings. The size and nature of the CEF effects, and hence the level splitting and energy level scheme, are directly governed by the symmetry of a magnetic ion's local environment.

For the SrLn_2O$_4$ compounds in which a central Ln^{3+} ion is surrounded by an octahedron of O^{2-} ions, see Section 2.3.1, electrostatic forces occur between the f orbital of the Ln^{3+} ions and the p orbitals of the O^{2-} ions. The f orbitals in rare earth compounds have highly anisotropic angular dependences, so in an octahedral environment some of these orbitals will be in a higher energy configuration than others. Thus the energy levels are split by the crystal field, with the amount of splitting governed by factors like the geometry of the octahedra. The effect of the crystal field on rare earth compounds, however, is mostly small since the 4f orbitals lie underneath the 5s and 5p states, but the interaction of the orbital distribution with the CEF gives rise to large single ion anisotropies observed in the lanthanides. This means that because of the crystal field there is an energetic preference for the spin to lie along a particular crystallographic direction, and this can be observed as magnetic anisotropy in some rare earth materials.

Inelastic neutron scattering is a technique that is often used to determine the position of (and the matrix elements of the transitions between) the crystal field energy levels. Once these are known, phenomenological techniques exist to fit the data and determine the crystal field schemes of materials, usually by expressing the single-ion crystal field potentials in terms of the total angular momentum states for constant **J** in the Stevens operator-equivalent notation [7]. Here, the single-ion crystal field Hamiltonian becomes

$$\hat{\mathscr{H}}_{\text{cf}}(i) = \sum_i \sum_{l,m} B_l^m O_l^m(\mathbf{J}_i) \tag{2.23}$$

where B_l^m are the crystal field parameters, and O_l^m are Stevens operators, and $\hat{\mathscr{H}}_{\text{cf}}(i)$ has the eigenfunctions $|Jm_J\rangle$. For many systems the number of crystal field parameters is usually greatly restricted by symmetry, and in practice, B_l^m are treated as adjustable parameters to fit the observed energy levels.

2.1.4 Interacting moments

So far the magnetic ions have been treated in terms of isolated magnetic moments, however, interactions between the magnetic moments on neighbouring atoms can also take place. A basic interaction that can take place between magnetic moments is the dipolar interaction. Considering the typical size, separation and degree of alignment of magnetic moments in a sample, it turns out that the dipolar interaction is a rather weak effect, and would only be important for materials that order at millikelvin temperatures.

For a lot of materials, the primary interactions between magnetic ions in matter can be described by the exchange interaction between their magnetic moments. The exchange interaction comes from electrostatic considerations as it costs energy to bring particles of the same charge into close proximity due to the Coulomb repulsion between electrons, and the Pauli exclusion principle which prohibits any two electrons to be in an identical quantum state. To obey exchange symmetry the final state under particle exchange must be a multiple of the starting state, and the operation of particle exchange must return states which are either symmetric or antisymmetric. In a simple model of a two electron system the total wave function is the product of the spatial and spin parts, and overall it must be antisymmetric which generates two possible combinations:

1. if the spatial part is symmetric, then the spin part is an antisymmetric singlet state (with $S = 0$),

2. if the spatial part is antisymmetric, then the spin part is a symmetric triplet state (with $S = 1$).

For exchange interaction to happen, the orbitals of electrons must overlap, and thus the Coulomb interaction between the electrons lifts the degeneracy of the two combinations such that there is an an energy difference between the symmetric and the antisymmetric spatial part of the wavefunction.

The energy difference between the singlet and triplet states can be parametrised using the scalar product of the moments of neighbouring spins $\mathbf{S}_i$ and $\mathbf{S}_j$, such that the Hamiltonian that describes the electrostatic interactions between magnetic ions can be replaced by an effective spin Hamiltonian. Since all of the neighbouring spins would interact

with each other via the exchange interaction, this motivates the spin Hamiltonian of the Heisenberg model:

$$\hat{\mathscr{H}} = -\sum_{ij} \mathsf{J}(ij)\mathbf{S}_i \cdot \mathbf{S}_j \tag{2.24}$$

where $\mathsf{J}(ij)$ is the exchange constant for the system and its value depends on the spin operators $\mathbf{S}_i$ and $\mathbf{S}_j$. The calculation of the exchange constant can be quite complicated, but some general properties emerge from considerations of whether the interaction is from magnetic moments on the same atom, or on different atoms. If the interaction is from the spins of electrons on the same atom, the triplet state is energetically preferable since this would reduce Coulomb repulsion by separating the electrons spatial wavefunctions (and thus satisfy Hund's first rule) by increasing their kinetic energy. So positive values of $\mathsf{J}(ij)$ imply a symmetric spin wave function so that it is energetically favourable for the spins $\mathbf{S}_i$ and $\mathbf{S}_j$ to align in parallel with respect to each other (ferromagnetic exchange). If the interaction is from the spins of electrons on the neighbouring atoms, where the electrons can save kinetic energy by forming bonds which result in a spatially symmetric wave function, $\mathsf{J}(ij)$ is likely to be negative as this implies an antisymmetric spin wave function so the spins favour an antiparallel alignment (antiferromagnetic exchange). The Heisenberg model works well for insulating materials where electrons tend to be localised. Although in Eq. 2.24 the interaction was between the spins $\mathbf{S}_i$, the Heisenberg model can also be applied to the total angular momenta $\mathbf{J}_i$, as in the case of rare-earth ions.

The process described above is usually called direct exchange since it is the consideration of the interaction between neighbouring magnetic atoms that relies on the overlap of their electron orbitals. This is rare in real systems, as the geometry of many materials prevents such overlap of the orbitals and in rare earth ions the 4f orbitals are highly localised and so no overlap can occur. The strength of the exchange interaction rapidly decreases with increasing the distance between electrons, so in many magnetic materials the moments couple indirectly through superexchange. Superexchange is mediated by a non-magnetic ion, often diamagnetic oxygen, placed between the magnetic ions. Since in ionic solids the electrons kinetic energy is reduced by being delocalised over the whole metal-oxygen-metal unit, in general there will be a preference for antiferromagnetism due

to superexchange (but there can be circumstances where this interaction is ferromagnetic). The strength of this interaction is dependent upon the degree of overlap of the orbitals and hence is very determined by the angles of the metal-oxygen-metal bonds. For the SrLn_2O$_4$ compounds this interaction is likely to be the dominant exchange mechanism since the rare earth ions are well separated from each other, and each Ln^{3+} ion has six O^{2-} nearest neighbours. For some magnetic materials next-nearest neighbour interactions may also be important, (although it is expected that these will be weaker due to the larger separation of the magnetic ions) and this means that may be necessary to be include extra exchange constants in the Hamiltonian. In any magnetic solid there may be several independent exchange paths along which magnetic ions can interact, with some being more important than others, and the contribution of each coupling mechanism will be determined by the materials crystal structure.

Other types of indirect exchange interaction in magnetic materials are possible. These include superexchange mediated by more than one intermediate ion, the anisotropic exchange interaction which is mediated by the spin-orbit coupling instead of an oxygen ion, double exchange which can occur between ions of mixed valency, and the RKKY interaction in metals where the conduction electrons mediate the exchange. These mechanisms however are less pertinent to the study of SrLn_2O$_4$ materials.

Overall, the introduction of the exchange interaction allows materials to form long-range ordered states below some critical temperature even in the absence of an applied field. There are a variety of exchange interactions, and these different correlations between magnetic moments can lead to many diverse magnetic structures, which will be discussed in Section 2.1.5. Experimentally, susceptibility measurements and inelastic neutron scattering may be used to deduce the nature of the interactions present in a magnetic system and to determine the corresponding exchange constants.

2.1.5   Ordered magnetic structures and symmetry breaking

At sufficiently low temperatures it is usually energetically favourable for conventional magnetic materials to develop some sort of long-range order when there are interactions between the magnetic moments. The leading interaction between spins in ionic crystals is

usually of the form of the exchange Hamiltonian of the Heisenberg model, and the nature
of the exchange constant depends on the preferred alignment of the magnetic moments. The
Hamiltonian that can describe basic magnetic structures in an applied magnetic field is:

$$\hat{\mathscr{H}} = \hat{\mathscr{H}}_{cf} + \hat{\mathscr{H}}_{ex} + \hat{\mathscr{H}}_{Z} \tag{2.25}$$

where the first sum is the single-ion crystal field Hamiltonian as in Eq. 2.23, the two ion
term exchange interaction term as in Eq. 2.24, and a Zeeman term

$$\hat{\mathscr{H}}_{Z} = -\sum_{j} \boldsymbol{\mu}_i \cdot \mathbf{B}_j = g\mu_{\mathrm{B}} \sum_{j} \mathbf{S}_j \cdot \mathbf{B} \tag{2.26}$$

which is just a many particle version of Eq. 2.8. Two simple ordered structures include
ferromagnetic and antiferromagnetic spin arrangements, which will be discussed from the
point of view of the Weiss model below.

Ferromagnets are the most well known magnetic structure, since, as mentioned in
the introduction, some permanent magnets (which show spontaneous magnetisation even
in the absence of an applied field) have been around since antiquity. Microscopically, in
a single-domain ferromagnet, all of the magnetic moments would be pointing along the
same preferred direction and thus $\mathsf{J}(ij)$ in Eq. 2.24 is positive. As the temperature of a
ferromagnet is increased, at the transition temperature, T_{C}, the thermal fluctuations will be
strong enough to break the magnetic order, and at $T > T_{\mathrm{C}}$ the spins will no longer have a
preferred orientation.

To solve Eq. 2.25 for a ferromagnet, (neglecting the term due to the crystal field and
assuming $L = 0$ for simplicity), it can be useful to make the approximation that there is an
effective molecular field at the ith site of

$$\mathbf{B}_{\mathrm{mf}} = -\frac{2}{g\mu_{\mathrm{B}}} \sum_{j} \mathsf{J}(ij)\mathbf{S}_j \tag{2.27}$$

which is produced by the neighbouring spins. Thus the exchange term can be rewritten in

terms of the Weiss field, so that the effective Hamiltonian for the system becomes

$$\hat{\mathscr{H}} = g\mu_{\mathrm{B}} \sum_i \mathbf{S}_i \cdot (\mathbf{B} + \mathbf{B}_{\mathrm{mf}}) \tag{2.28}$$

which looks exactly like the Zeeman term in the Hamiltonian of a paramagnet, given in Eq. 2.26, with the magnetic field replaced by $(\mathbf{B} + \mathbf{B}_{\mathrm{mf}})$. This approach assumes that the molecular field experienced by all of the magnetic ions is the same, which is only reasonable at temperatures far from the transition temperature. Since the molecular field is related to the amount of order present in the system, it can be assumed that it will be proportional to the magnetisation:

$$\mathbf{B}_{\mathrm{mf}} = \lambda \mathbf{M}. \tag{2.29}$$

The problem now reduces to the simple paramagnetic case in an applied field of $(\mathbf{B} + \mathbf{B}_{\mathrm{mf}})$, and this model can be solved almost identically to the paramagnetic case, by solving Eqs. 2.14 and 2.15, where B is replaced by $(B + \lambda M)$ simultaneously. The only difference is that at low temperatures the moments will be aligned by the internal molecular field even in the absence of an applied external field. The temperature at which this happens is called the Curie temperature, T_{C}, and is given by

$$T_{\mathrm{C}} = \frac{g\mu_{\mathrm{B}}(S+1)\lambda M_{\mathrm{s}}}{3k_{\mathrm{B}}} = \frac{n\lambda\mu_{\mathrm{eff}}^2}{3k_{\mathrm{B}}}. \tag{2.30}$$

Since the strength of the molecular field is related to the exchange interaction, assuming that it is effective over only z nearest neighbours and takes the value J, it can be deduced from Eqs. 2.25, 2.28 and 2.29 that

$$\lambda = \frac{2z\mathsf{J}}{ng^2\mu_{\mathrm{B}}^2} \tag{2.31}$$

and hence the transition temperature is given by

$$T_{\mathrm{C}} = \frac{2z\mathsf{J}S(S+1)}{3k_{\mathrm{B}}}. \tag{2.32}$$

When $L \neq 0$, such as in the case of the rare earth ions, $\mathbf{S}$ is not a good quantum number, so $\mathbf{J}$ should be used instead. Repeating the calculations for this case, means that the transition

temperature becomes

$$T_{\mathrm{C}} = \frac{2z(g_J - 1)^2 \mathsf{J} J(J + 1)}{3k_{\mathrm{B}}}. \tag{2.33}$$

The solution to the equations indicates that there is a net magnetisation for temperatures below T_{C}, and none above, and since the magnetisation is a continuous function at the Curie temperature while its gradient is not, the paramagnet to ferromagnet phase transition is of second order. Thus, in a small applied field, above the ordering (Curie) temperature a ferromagnetic material will behave like a paramagnet, and its susceptibility will be governed by the Curie-Weiss law (by setting $T_{\mathrm{C}} = \theta_{\mathrm{CW}}$ in Eq. 2.21). Upon reducing the temperature the susceptibility will tend to infinity at T_{C}, and below this temperature more complicated behaviour will occur due to the domains in the material, so the $M(H)$ curves show hysteretic behaviour. By applying a magnetic field, the sharp phase transition will be removed since in this model the direction of the applied field is not important as the magnetisation will always rotate to be in line with the applied field. This is not the case in real ferromagnets where there are magnetic anisotropies associated with the material.

Compared to ferromagnets, in the ordered (Nèel) state antiferromagnets does not have a net magnetisation in zero field because the molecular field is oriented such that the magnetic moments are all aligned antiparallel with their nearest neighbours, and thus $\mathsf{J}(ij)$ in Eq. 2.24 is negative. There are many different ways of antiferromagnetically arranging magnetic moments on a lattice (and these arrangements will also depend on the materials crystal structure) since the only constraint is that the net magnetisation must equal zero. In a simple model antiferromagnetic systems can be considered as two equal interpenetrating sublattices on one of which all of the moments are pointing up, and on the other as down. So the molecular field on each sublattice (in this case labelled "+" and "−") would be

$$B_+ = -|\lambda| M_- \text{ and } B_- = -|\lambda| M_+ \tag{2.34}$$

with λ again being the (negative) molecular field constant. In this model it can be assumed that the magnetisation on one sublattice is proportional to the other, so that except for the magnetisation direction the sublattices are equivalent and $|M_+| = |M_-| \equiv M$. By using
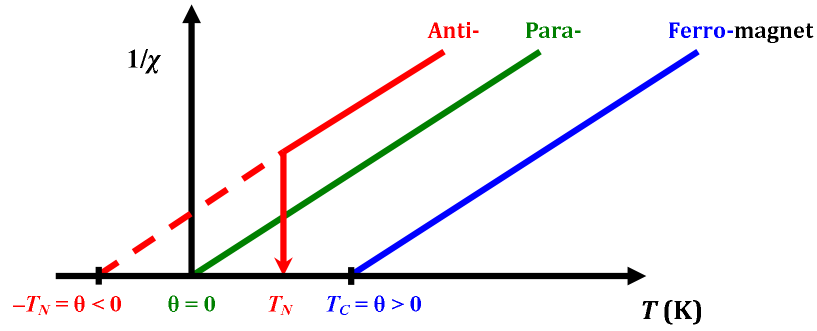
Figure 2.1: Well above ordering temperature the magnetic susceptibility is expected to follow the Curie-Weiss law, where $\chi \propto (T - \theta_{\mathrm{CW}})^{-1}$. Plotting $1/\chi$ against T gives straight line graphs, and θ_{CW} is determined by the temperature intercept. The sign of θ_{CW} gives information about the interactions present in a magnetic system, and the effective moment can be calculated from the gradient of the line.

Eq. 2.14, and setting

$$y = \frac{g_J \mu_{\mathrm{B}} J |\lambda| M}{k_{\mathrm{B}} T} \tag{2.35}$$

for the antiferromagnetic case, the equations are very similar to those used to describe ferromagnetism. Thus the molecular field on each sublattice only exists below a transition temperature temperature, T_{N}, which is defined as

$$T_{\mathrm{N}} = \frac{g_J \mu_{\mathrm{B}} (J+1) |\lambda| M_{\mathrm{s}}}{3 k_{\mathrm{B}}} = \frac{n |\lambda| \mu_{\mathrm{eff}}^2}{3 k_{\mathrm{B}}}. \tag{2.36}$$

Thus at low temperatures all of the moments are ordered antiferromagnetically. As the temperature is increased, the susceptibility would reach a well-defined maximum at T_{N}, and upon subsequent increases in temperature, $T > T_{\mathrm{N}}$, thermal fluctuations will be strong enough to break the magnetic order.

In small magnetic fields and at high temperatures, where the magnetic moments are disordered, the antiferromagnetic material behaves like a paramagnet, and the susceptibility will again have the form of the Curie-Weiss law (setting $-T_{\mathrm{N}} = \theta_{\mathrm{CW}}$ in Eq. 2.21). Accordingly, since in this regime both the ferromagnetic and antiferromagnetic materials susceptibilities follows the Curie-Weiss law, by plotting $1/\chi$ against temperature, illustrated in Fig. 2.1, straight line graphs may be obtained and from fitting the data the effective

moment, μ_{eff}, can be calculated from the Curie constant by using Eq. 2.22 and θ_{CW} is determined by the temperature intercept. The sign of θ_{CW} then gives information about the interactions present in a magnetic system, and for a paramagnet $\theta_{\text{CW}} = 0$. Positive values of the Weiss temperature indicate ferromagnetic interactions, with the expected transition temperature $\theta_{\text{CW}} = T_{\text{C}}$. Negative values indicate antiferromagnetic interactions, and the expected ordering temperature of $\theta_{\text{CW}} = -T_{\text{N}}$.

Applying a magnetic field to an antiferromagnet below T_{N} is complicated because of crystalline anisotropy as the behaviour of the susceptibility will depend upon the direction of the applied field with respect to the orientation of the magnetic moments in the sample. Since the magnetisation on the two sublattices is equal, any energy saving gained by one sublattice's moments by aligning along the field direction will be cancelled out by the energy cost on the other. A simple example would be to consider the effect of an applied field on an antiferromagnet disregarding any complications from thermal fluctuations. If the field is applied perpendicular to the direction of the spins, there will be some canting of the moments along the field direction on both sublattices, and the susceptibility would have a finite value upon decreasing the temperature. As the field is increased, the moments on both sublattices would tilt more and more until a strong enough field would rotate them all to point along the same direction. If a small field is applied parallel to the spins, the magnetisation on each sublattice is already saturated so the susceptibility falls continuously to zero with decreasing temperature. Applying a stronger magnetic field would not take the system out of the antiferromagnetic phase until a critical field is reached and it becomes energetically favourable for the system to undergo a spin-flop transition such that the moments on both of the sublattices would have some component to the magnetisation along the field direction. Even stronger fields would eventually rotate the moments to line up along the applied field direction. If there is a large magnetic anisotropy in the material, however, a single metamagnetic spin-flip transition can occur (instead of a spin-flop) at some single critical value of the applied field.

Ferromagnetism and antiferromagnetism are fairly simple forms of long-range magnetic order, but more complicated arrangements of moments also exist. Two examples are ferrimagnetic order (where the magnetic moments reside on two sublattices like in the an-

tiferromagnetic arrangement, but they do not have the same magnitude and thus there is a net magnetisation) and sinusoidally modulated spin structures such as spiral, helical and spin density waves (where the direction and/or the magnitude of the spins changes from one magnetic site to the next and the magnetic structure may not be commensurate with the crystal structure). The determination of the type of magnetic order present in a material can be made using various experimental techniques, such as magnetisation and magnetic susceptibility measurements, which are bulk properties probes; and neutron diffraction, NMR, μSR and resonant x-ray scattering measurements which are local probes. The techniques most relevant to the work presented in this thesis will be described in detail in Chapter 4.

All of the ordered magnetic phases described above, as well as other phenomena such as structural phase transitions and superconductivity, are associated with symmetry breaking. This means that as a function of an external parameter, such as temperature, pressure, or an applied field, some physical property of a material shows a marked difference above and below a critical value. Thus there will be an order parameter associated with the phase transition between the two states of the system. For example, in the case of the ferromagnet this is the formation of spontaneous magnetisation (when all of the magnetic moments choose a unique direction in which to point) below a critical temperature T_C, and thus the rotational symmetry of the system is reduced from the high temperature state where the magnetic moments could point in any direction.

The formation of order that is driven by thermal fluctuations can be readily understood from the free energy, $F = E - TS$, since to minimise F at low temperatures the system would (usually) order into the lowest possible (ground) state, and to minimise F at high temperatures the system would need to maximise S, which increases disorder. A lot of phase transitions are driven by thermal fluctuations, but other classes exist, such as quantum and topological phase transitions. Phase transitions involve a change of symmetry, and in the Ehrenfest classification, second order phase transitions, which involve no latent heat, show a discontinuity at the critical temperature in the second order derivatives of the free energy (such as the heat capacity). In contrast, first order phase transitions can be seen as discontinuities in first order derivatives of the free energy, such as volume and entropy. In real materials there may be several magnetic phase transitions as different temperature

and magnetic field conditions would allow some ordered phases to be more energetically favourable than others, so the phase diagram may be complicated.

Models of magnetic systems that provide a description of the underlying physics can be put into two broad categories: mean-field theories and microscopic models. A famous phenomenological theory is Landau's theory of second order phase transitions [8, 9]. Instead of considering the details of the interactions that govern the behaviour of the system, it arises from general symmetry considerations. Writing the free energy as a function of the order parameter of the system, and using a Taylor expansion, F can be minimised to find a solution where the order parameter goes to zero at the phase transition. For example, for a ferromagnet the Taylor expansion of the order parameter (magnetisation) cannot have any odd terms as there is no energetical difference between the spin up and spin down states, so that

$$F(M) = F_0 + a(T)M^2 + bM^4 \tag{2.37}$$

where F_0 and b are constants and $a(T)$ is the temperature dependent term that changes sign at the phase transition. Then, near the transition $a(T) = a_0(T - T_C)$, and the solutions of $\partial F/\partial M = 0$ that minimise the energy are

$$M = 0 \text{ or } M = \pm \left(\frac{a_0(T_C - T)}{2b} \right)^{\frac{1}{2}}. \tag{2.38}$$

Thus the magnetisation is zero for $T > T_C$ and proportional to $(T_C - T)^{\frac{1}{2}}$ for $T < T_C$. Mean-field theories do not include a description of correlations, but fluctuations of the order parameter become very large near phase transitions. Thus, in three or less dimensions, mean-field theories do not account well for the region around the phase transition since their underlying mean-field assumption is that all of the regions of the system are the same is invalid near a phase boundary. Microscopic models of interactions could be used instead to explain this behaviour.

To understand magnetic behaviour, several microscopic models of the magnetic interaction are available. In general, in these models the dimensionality of the magnetic moments may be different to the dimensionality of the lattice on which the spins sit. One such model is the nearest-neighbour Heisenberg model, given by Eq. 2.24, where the spins

are three dimensional vectors. A limiting case of the Heisenberg model is the Ising model. Here the exchange interaction is anisotropic, so that the interaction along one dimension (say the z axis) is much stronger than all the others, such that the moments can only align parallel or anti-parallel to the z direction, and Eq. 2.24 becomes

$$\hat{\mathscr{H}} = -\sum_{\langle ij \rangle} \mathsf{J} S_i^z \cdot S_j^z. \tag{2.39}$$

Ising spins on a one dimensional lattice would only show a transition to long range magnetic order at $T = 0$, since at any non-zero temperature it is always possible to create spontaneous defects in an infinite chain as the free energy cost is always negative and the entropy gain is infinite. Other interesting models include those of Ising spins on a two dimensional lattices, Heisenberg chains where three-dimensional spins sit on one dimensional lattices, the XY model for spins that are constrained to lie in the $x - y$ plane, and spin ladders which are systems that lie somewhere in between one- and two-dimensional magnets.

Finally, when a material undergoes a second order phase transition, there are some universal consequences of the symmetry breaking:

1. Once the symmetry is broken the system will have an energetic preference for staying in the broken symmetry state (for example in crystals this is rigidity and in ferromagnetic systems this is permanent magnetism).

2. At temperatures above $T = 0$ there will be elementary excitations in the order parameter (such as phonons in a crystal and magnons in magnetic systems, these will be discussed in Section 2.1.6).

3. Defects will occur if the symmetry breaking is not isotropic across a macroscopic sample (such as dislocations and grain boundaries in crystals and domain walls in magnetic systems).

2.1.6 Excitations

In solid state systems, below the transition temperature, several excitations are possible. In magnetic systems the most common collective excitations are phonons and magnons which

involve many interacting atoms and spins, respectively.

At temperatures above $T = 0$, the atoms that make up the lattice will not be completely static as thermal vibrations, whose energies can be quantised as phonons, will disturb the perfect crystalline order. The phonons energy, $\hbar\omega$, is related to their crystal momentum, $\hbar q$, via a dispersion relation. There can be two separate branches in the dispersion relation, called the optical and acoustic modes. Acoustic phonons have no energy gap in their excitation spectrum, so that at $q = 0$ their energy is also zero, and thus as long as $T \neq 0$ they can be thermally generated (with a very long wavelength for very low temperatures). Thus since acoustic phonons can be produced at infinitesimal energy cost, they are the 'massless' Goldstone modes of the crystal, and at low temperatures (in three dimensional crystals) they give rise to the T^3 term in the heat capacity. Optical phonons, however, do have an energy gap at $q = 0$ in their dispersion relation, and their dispersion is also often less variable with the momentum compared to acoustic phonons. The phonon contribution to the specific heat of a material can be complicated, but simplifying models exist. The two most commonly used are the Einstein and the Debye models, the details of which may be found in the literature, for example see [10].

In complete analogy to phonons, long-range ordered magnetic systems will have quantised fluctuations of the spins, called magnons (or spin waves), that propagate though the system. Magnons also have well defined characteristic dispersion relations, which are different depending on the type of magnetic order present in the system. In isotropic ferromagnets, the dispersion relation of magnons is gapless, and thus the spin waves are the Goldstone modes of the system. For an anisotropic system, however, an energy gap in the dispersion relation will appear at $q = 0$. The spin wave excitations will also contribute to the heat capacity, and, experimentally, it is possible to follow their dispersion relation using inelastic neutron scattering.

It should be noted that crystal-field excitations are also possible, but these are single-ion excitations and therefore (to a first approximation) have no dispersion.

2.2 Frustrated magnetism

In the discussion on magnetism, it has been assumed that at low enough temperatures spin systems will find a way to minimise their energy and settle into a long-range ordered state. However, for some systems this is not always possible, and thus the term *frustration* is used to describe the inability of a system to satisfy all the competing microscopic interactions in order to establish a unique global ground state. Frustration was first investigated in 1935 by Pauling in the context of water ice [11], but it was not discussed in the context of magnetic systems until the discovery of spin glasses [12, 13] in the 1970's (although the low temperature phase in these materials is due to both frustration and a high degree of structural disorder). A general consequence of frustration is the establishment of long-range order at temperatures much lower than expected from the strength of the exchange interactions, and this leads systems to exhibit some unusual properties. At very low temperatures some frustrated systems may eventually order, sometimes in very complicated spin arrangements, but others may stay disordered, for example the spin glasses mentioned above and also spin liquids [14, 15] in which the ground state is dynamic.

An empirical measure of frustration proposed by Ramirez [16] is the "frustration parameter", f, which capitalises on the fact that in the field of frustrated magnetism discrepancies between θ_{CW} and actual T_{N} are very common. The frustration parameter is defined as

$$f = \frac{\theta_{\mathrm{CW}}}{T_{\mathrm{N}}} \qquad (2.40)$$

so that $f > 1$ corresponds to frustration. The temperature regime between θ_{CW} and T_{N} thus represents a free spin in a strongly interacting environment. However, care must be taken when applying this criteria as this is almost always true for antiferromagnets [3] because in the discussion presented in Section 2.1.5, the relations used to derive the Curie-Weiss law for antiferromagnets it was assumed that the molecular field on one magnetic sublattice depends only on the magnetisation of the other. Nevertheless, f can be a useful guide if the difference between θ_{CW} and T_{N} is at least an order of magnitude, *i.e.* where $f > 10$. Such materials are said to be strongly frustrated, and they cannot be described by using the mean field theory multi-sublattice picture - instead values of $f > 10$ signify a more complicated
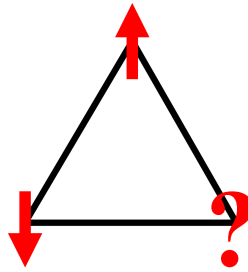
Figure 2.2: In a simple triangular lattice Ising spin system geometric frustration may be observed, since the third spin is unable to satisfy both antiferromagnetic constraints in order to minimise the ground state energy.

state that is not accessible by mean field theory [16].

In this section a few basic concepts of frustrated magnetism are presented, mostly involving a discussion of how the geometry of the underlying lattice coupled with suitable interactions can frustrate the ordering of the magnetic moments, such that frustration plays a fundamental role in establishing highly degenerate ground states and exotic low-temperature phases. Some different examples of these geometrically frustrated structures will be considered, as well as a few types of novel magnetic phenomena they support. It should be pointed out that not all frustration is geometrical - for example the spin glasses can have site randomness, where the magnetic sites are arranged randomly in a non-magnetic matrix, and bond randomness, where the material possesses more than one type of magnetic atom and the interactions between the moments are unequal - but this is not relevant to the SrLn_2O$_4$ materials, and will not be considered here.

There are vast amounts of both theoretical and experimental literature available on magnetic frustration, so only a short introduction to the subject intended here, and [16–20] are suggested as formal books and reviews of the topic.

2.2.1 Geometrical frustration

Geometrical frustration arises in systems where the interactions between the magnetic moments are incompatible with their spatial arrangement in a lattice, so that at low temperatures not all of the interaction energies can be simultaneously minimised. A simple example would be to consider an Ising spin system. On a square lattice, the energy of all the antifer-

romagnetic interactions between the spins can be minimised since it is possible to anti-align every spin with respect to its nearest neighbours; but on a triangular lattice this is impossible, as the third spin cannot be simultaneously anti-aligned to both of its nearest neighbours, and this situation is illustrated in Fig. 2.2. The spins would have to compromise, such that there will not be a unique microscopic ground state solution; and in the general macroscopic case there will be a multitude of degenerate low temperature states with the same energy (since the spins in all of these different combinations will be equally unable to minimise their energy). Frustration also tends to enhance quantum fluctuations for low-dimensional spin systems.

In the case of the simple triangular antiferromagnet considered above a non-collinear solution can be found where the moments on each triangle are pointing at $120°$ with respect to each other. However, unique ground state solutions of some frustrated magnetic materials are not always possible even for Heisenberg spins [21, 22], so these systems will never show long-range order at finite temperatures. The traditional examples are of spin glasses, where the spins eventually get 'frozen' in a random metastable state, and spin liquids where the spins are highly correlated, but fluctuate down to the lowest temperatures. The newer "spin-ice" materials [23, 24] are a particularly interesting examples of spin-liquid materials with a strong local Ising anisotropy - here one dimensional spins are arranged on a corner-sharing tetrahedral lattice and there is no unique way to minimise all of the nearest neighbour interactions (and satisfy the local two-in two-out spin rule on each tetrahedron) in order to establish a single ground state. This problem is analogous to stacking H_2O molecules to form (hexagonal) water ice [25]. Most intriguingly, it can be shown that the excitations in spin ice (the defects that break the two-in two-out rule) can freely propagate throughout the lattice and can be thought of as magnetic monopoles connected by a semi-infinite string of flipped spins [26].

For real frustrated systems that *do* manage to achieve long range order at low temperatures, there may be a multitude of extra (small) perturbations to the Hamiltonian, such as further-neighbour exchange, single-ion anisotropy, magnetic dipolar interactions, quantum fluctuations, etc., that lift the degeneracy and stabilise the formation of a unique ground state. These materials often result in a variety of interesting magnetic structures, arrived at
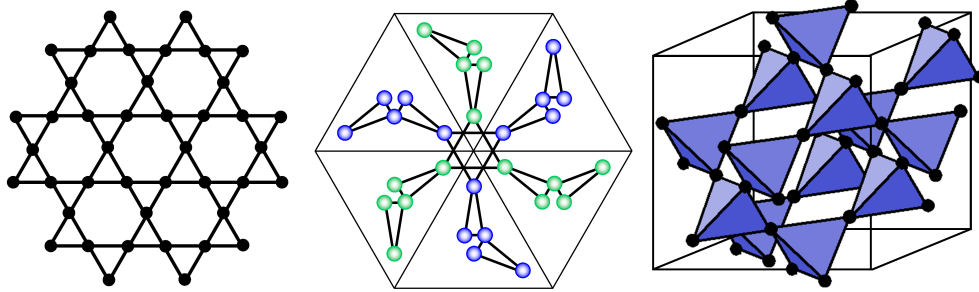
Figure 2.3: Examples of lattices based on triangles and tetrahedra include the (left) two dimensional kagomé, (middle) three dimensional garnet, and (right) pyrochlore structures.

by novel mechanisms such as order-by-disorder (driven by thermal [27] or quantum [28] fluctuations). New magnets which exhibit the effects of geometric frustration are constantly being discovered. The behaviour of these systems is often complex, with a rich variety of low-temperature properties.

2.2.2   Geometrically frustrated lattices

In the presence of antiferromagnetic exchange interactions, many magnets based on corner- or edge-sharing triangles [29] or tetrahedra [30] can exhibit geometric frustration. The corner-sharing materials are more susceptible to the effects of frustration than than edge-sharing networks. There are a large number of such systems in both two and three dimensions, and three of these are illustrated in Fig. 2.3. The two dimensional structures include the (simple) edge-sharing triangular lattice, and corner-sharing triangular networks such as the kagomé [31, 32] and honeycomb [33] structures. In three dimensions, triangular corner-sharing arrangements include the garnet [34, 35] and kagomé staircase compounds [36]; while corner-sharing tetrahedra are realised in spinels [37] and pyrochlore [30, 38] compounds. Other frustrated magnetic networks are found in square lattices with nearest and next-nearest-neighbour interactions [39], spin chains [40] and face-centered cubic lattices in three dimensions [41, 42]. Thus, there are plenty of systems where frustration can play a fundamental role in establishing the low temperature properties, and recently the SrLn_2O$_4$ family of compounds (which shall be described below) have also been suggested as lattices that could give rise to frustrated magnetism.

2.3 The Sr*Ln*$_2$O$_4$ compounds

Recently, a new family of highly anisotropic magnetic compounds, that have the formula Sr*Ln*$_2$O$_4$, where *Ln* = Lanthanide, have started to be investigated from the point of view of geometric frustration [43]. Their crystal structure, and the magnetic properties of the SrEr$_2$O$_4$, SrDy$_2$O$_4$ and SrYb$_2$O$_4$ members of the family that have been studied so far will be discussed in this section. The detailed investigation into the magnetic properties of SrHo$_2$O$_4$ and SrGd$_2$O$_4$ will be presented in Chapters 5 and 6. Some comments on the role of frustration as a function of the rare earth element for this series of compounds, in light of the findings for SrHo$_2$O$_4$ and SrGd$_2$O$_4$, is left until the concluding Chapter 7.

2.3.1 Structure of Sr*Ln*$_2$O$_4$ compounds

The Sr*Ln*$_2$O$_4$ (where *Ln* = Lanthanide) family of compounds [44], crystallise in the form of calcium ferrite [45], space group *Pnam*. All the atoms sit on the $4c(x, y, 0.25)$ positions and there are two crystallographically inequivalent sites for the rare earth ions. In this setting, the a and b axes of the unit cell are more extended than the c direction, and in fact a and b have quite similar lengths, which means that both of the rare earth ions sit in slightly different octahedral environments. In spin ice pyrochlore compounds, strong crystal field anisotropy which comes from the differences in the $Ln-$O bonds and the strong single-ion anisotropy of some rare earths combine to allow the rare earth ions behave like Ising spins. A similar situation can occur in the Sr*Ln*$_2$O$_4$ compounds since these materials also have significant differences between the $Ln-$O bond lengths.

The *Pnam* structure allows the magnetic Ln^{3+} ions to be linked in a network of triangles and hexagons, as shown in Fig. 2.4, with the inequivalent sites of the lanthanides shown in red and blue. For all the Sr*Ln*$_2$O$_4$ systems the magnetic ions form zigzag ladders that run along the c axis. The chains fall into two categories: those that couple the lanthanides sitting in the same crystallographic positions (the red and blue chains in Fig. 2.4), which have shorter $Ln^{3+} - Ln^{3+}$ separations along both the spines and across the zigzag of the ladder, and longer interconnecting chains that weakly couple the red and blue ladders together. These triangular structures can be frustrated, and are magnetically equivalent to
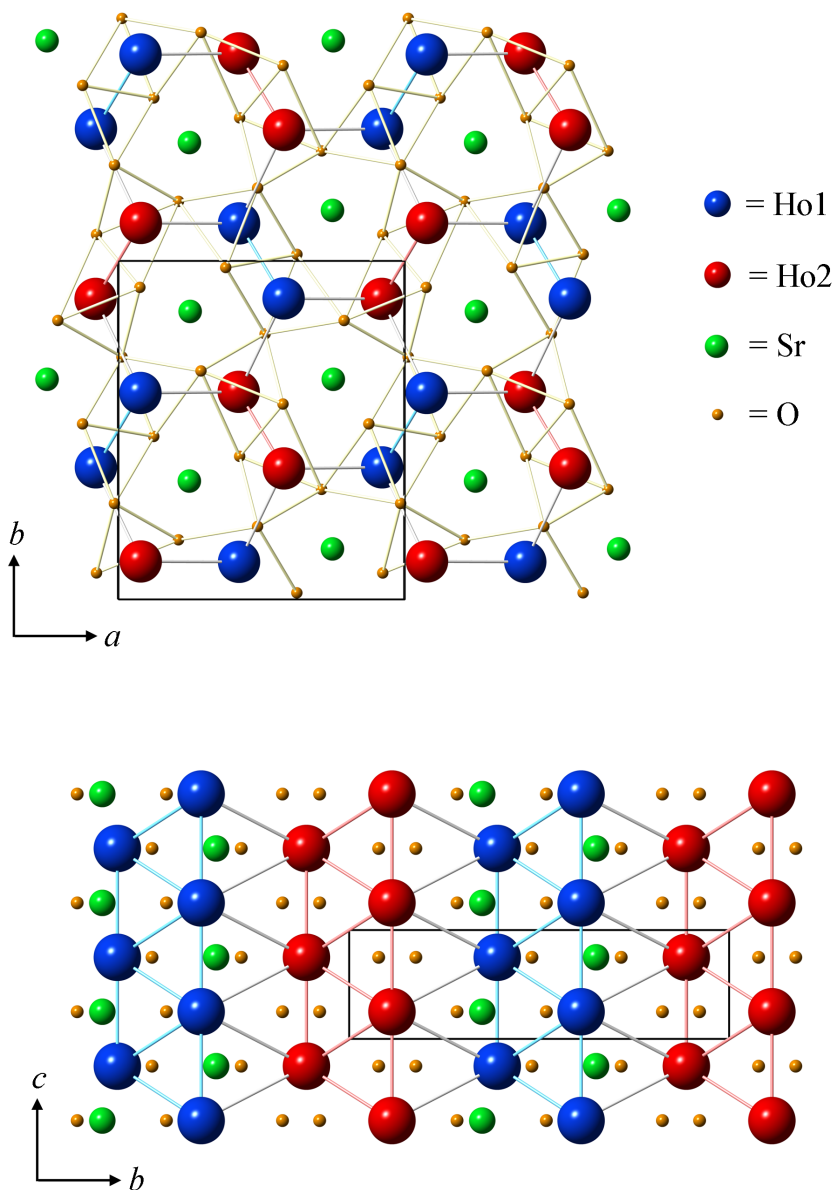
Figure 2.4: Crystal structure of the Sr*Ln*$_2$O$_4$ compounds, (top) viewed in the *a-b* plane where the isolated Sr ions are surrounded by Ho-O$_6$ octahedra, and (bottom) the zigzag chains of Ho^{3+} ions are seen along the *c* axis (the bonds between the oxygen ions have been omitted for clarity). The two crystallographically inequivalent positions for the rare earth ions are shown in blue and red. The chains fall into two categories - those that couple the lanthanides sitting in the same crystallographic positions (the red and blue chains), and the longer interconnecting chains that couple the red and blue ladders. The particular example of SrHo$_2$O$_4$ is used here, but the basic structure is appropriate for all the different rare earth compounds in this series, allowing for slight changes for the bond lengths and angles.

spin chains with first- and second-nearest-neighbour interactions. The chains of Ln^{3+} ions interconnect by forming a distorted *honeycomb* structure, a bipartite lattice made up of edge sharing hexagons, in the *a-b* plane.

The honeycomb lattice would only be frustrated if further than nearest-neighbour exchange is considered, but receives substantial theoretical interest since it has the smallest possible coordination number in two-dimensions [46–48]. Thus for these systems quantum fluctuations are expected to have a much larger effect on the stability of magnetic order than, for example, for square or triangular lattices. A number of honeycomb lattice structures have been identified experimentally, including the spin-$\frac{1}{2}$ compound $InCu_{\frac{2}{3}}V_{\frac{1}{3}}O_3$ [49, 50], the spin-$\frac{3}{2}$ systems $Bi_3Mn_4O_{12}(NO_3)$ [51, 52] and $\beta-CaCr_2O_4$ [53, 54] as well as other systems with larger spins like $BaLn_2O_4$ [55], $EuLn_2O_4$ [56] and $SrLn_2O_4$ [43].

Overall, the spin ladder and honeycomb-like arrangement of the rare earth ions makes the $SrLn_2O_4$ compounds suitable candidates to study the effects of geometric frustration since the rare earth ions are likely to be predominantly coupled with antiferromagnetic superexchange interactions.

2.3.2 Properties of SrLn_2O$_4$ compounds

The magnetic properties of the $SrLn_2O_4$ family of compounds recently began to be investigated. Karunadasa *et al.* [43] reported on the bulk property measurements of magnetic susceptibility and magnetisation, and some neutron diffraction results for several powder samples of the $SrLn_2O_4$ materials. In this early characterisation, a study of the magnetic susceptibility, $\chi(T)$, measured on powder samples of all the $SrLn_2O_4$ compounds has revealed a disparity in the measured Curie-Weiss constants, θ_{CW}, and the lack of long-range order down to 1.8 K [43]. Such anomalous behaviour is usually a sign of frustration, as discussed in Section 2.2, and this could lead the $SrLn_2O_4$ materials to show a variety of unusual magnetic properties.

Since the work of Karunadasa *et al.*, three members of the $SrLn_2O_4$ family, where $Ln =$Er, Dy and Yb, have been studied in detail. Single crystals of these oxides have been grown [57], and measurements of the low-temperature susceptibility and heat capacity have revealed that $SrEr_2O_4$ orders at T_N = 0.75 K [58, 59], with the transition seen as a cusp in

$\chi(T)$, and a λ-anomaly in the specific heat. For $SrYb_2O_4$, a λ-anomaly is also observed in the specific heat at $T_N = 0.92$ K [60]. In contrast, $SrDy_2O_4$ does not show any anomalies in $\chi(T)$ down to 0.5 K [59], and no indications of transitions to long-range order have been observed in heat capacity measurements down to 0.39 K in zero applied field [61]. The application of a magnetic field along the principal crystal axes of all of these compounds also induces a variety of in-field transitions. The crystals are highly anisotropic, and for $SrEr_2O_4$ and $SrDy_2O_4$ plateaux in the magnetisation curve appear to be stabilised for certain values of the applied field along the a and b principal crystal axes, respectively.

Neutron diffraction on powder samples of $SrDy_2O_4$ reveals only broad diffuse scattering peaks and thus further corroborates the apparent lack of long-range order at least down to 20 mK for this compound [62]. Low-temperature neutron diffraction studies of $SrYb_2O_4$ point to unusual magnetic behaviour, where the two inequivalent sites of the Yb^{3+} ion do not appear to have the same value of the ordered moment [60]. The magnetism in $SrEr_2O_4$ is equally unconventional since powder neutron diffraction measurements indicate that the transition to Nèel order involves only half of the Er^{3+} sites (either the red or blue sites in the notation of Fig. 2.4) [58]. Furthermore, polarised neutron studies on single crystals of $SrEr_2O_4$ suggest that the long-range ordered $\mathbf{k} = 0$ magnetic structure coexists with a shorter-range incommensurate ordering that has a pronounced low-dimensional character at temperatures below $T_N = 0.75$ K [63]. Applied magnetic fields tend to destroy the $\mathbf{k} = 0$ ordered phase in $SrEr_2O_4$ [64], but, in contrast, $SrDy_2O_4$ only appears to order in the presence of a magnetic field [62].

In this thesis the results of an investigation into the nature of the magnetism in powder and single crystal samples of another two members of the $SrLn_2O_4$ family, with Ln = Ho and Gd, will be presented. In these compounds the magnetic ions Ho^{3+} and Gd^{3+} have rather different electronic structures, with Ho^{3+} known to display Ising like properties in certain crystal field environments, and Gd^{3+} is almost isotropic in the ground state where its $L = 0$. Thus, the magnetic behaviour of $SrHo_2O_4$ and $SrGd_2O_4$ is expected to be relatively disparate, and where possible, comparisons will also be drawn with the other members of the $SrLn_2O_4$ series.

Chapter 3

Structure and scattering theory

This chapter outlines the basics of structure and scattering theory (with emphasis on neutron scattering in particular), which are most relevant to the data presented in this thesis. It is by no means an exhaustive coverage of the subjects and only a few salient equations and concepts are shown, and some reference texts, such as [65–67], cover the material in a far more complete manner. The treatment begins with a brief review of crystal and magnetic structures, and the principles of diffraction. Neutron scattering, a powerful tool that can be used to give information about magnetism on a microscopic scale, is described in more detail, including the review of the elastic, magnetic and polarised, and inelastic scattering techniques. The chapter concludes with a summary of the methods for neutron production.

3.1 Crystal and magnetic structures

In the solid state, the three dimensional crystal lattice is an infinite periodic structure that can be fully described by three basis vectors. Usually, structures are described with reference to a unit cell, which is the smallest parallelepiped that will replicate the crystal lattice using only translation operations. The lattice parameters are the lengths of the sides of this parallelepiped (denoted by a, b and c), and the angles between them (α, β, γ). Constraints on these parameters define seven different crystal systems, for example the SrLn_2O$_4$ compounds fall into the orthorhombic group where $a \neq b \neq c$ and $\alpha = \beta = \gamma = 90°$. If the unit cell has the same volume as the space associated with a single lattice point, as in the case of

SrLn_2O_4 systems, it is called primitive. However, the lattice systems can also be combined with face-, body- or side-centred unit cells, and this gives rise to the 14 Bravais lattices. The full symmetry of a crystal may be described by one of 230 the space groups, which are the combination of four point group (rotation axes, mirror planes, rotoinversion axes and a centre symmetry) and two translational (screw axes and glide planes) symmetries with the Bravais lattices. The full crystal structure of a material would then be described by the convolution of the lattice with a basis, (a set of atomic positions). Further information on the formalism of the crystal structure can be found in [65] and [68].

In a similar manner to the crystal structure, the magnetic structure of a material—the quasi-static configuration of ordered magnetic moments—can be described by a periodic repetition of a magnetic unit cell. In an antiferromagnet, the magnitude and direction of the spin on each site must be defined, but there are different possibilities of arranging magnetic moments. Thus, to establish a magnetic unit cell, the group and symmetry operators that generate the magnetic atoms positions and spin directions must be found. There are many more magnetic space groups than crystallographic groups due to the addition of the time reversal symmetry. Defining magnetic unit cells can be cumbersome, and by applying group theory methods it is instead possible to describe the magnetic structure using the nuclear unit cell and a propagation vector $\mathbf{k}$ that defines a relationship between the orientations of the magnetic moments of symmetrically equivalent magnetic atoms in different nuclear unit cells [69]. Thus, if the basis vector of the moment orientation is known in the zeroth cell, using the propagation vector would allow one to calculate the spin on any other symmetrically equivalent site. For example, if the crystallographic and magnetic unit cells coincide, the propagation vector is $\mathbf{k} = (0,0,0) \equiv 0$, and if the magnetic cell is doubled along the c axis compared to the nuclear cell for a single antiferromagnetic spin, the propagation vector is $\mathbf{k} = (0, 0, \frac{1}{2})$.

3.2 Diffraction

By elastically scattering of beams of radiation, such as x-rays, electrons and neutrons, crystal (and magnetic) structures of a material may be determined. In order to achieve adequate

$$n\lambda = 2d\sin(\theta)$$
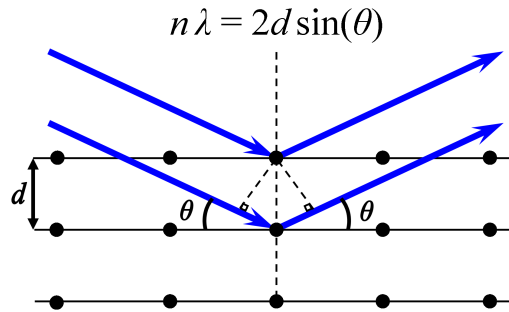
Figure 3.1: The incident radiation can be modelled as set of plane waves scattering from lattice planes separated by d. Peaks are observed in the diffraction pattern when the Bragg condition (that the path difference between the scattered waves is equal to an integer number of wavelengths) is satisfied.

resolution, the wavelength of the radiation must be smaller than the interatomic spacing. In a simple representation of this type of scattering, the incident radiation is modelled as plane waves hitting the surface at an angle θ, shown in Fig. 3.1. When the Bragg condition

$$n\lambda = 2d_{hkl}\sin(\theta), \text{ where } n = \text{integer} \tag{3.1}$$

is satisfied for a crystal, peaks are seen in the diffraction pattern due to the coherent scattering of radiation by the crystalline planes since the path difference between the scattered waves is equal to an integer number of wavelengths. The intensity of a Bragg peak is thus a sum of all the amplitude and phase information for the different scattered waves. The intensity of a reflection can also be calculated by considering the structure factor $|F(hkl)|^2$, for nuclear reflections or the magnetic structure factor for Bragg scattering from ordered magnetic moments.

Single crystal and polycrystalline diffraction—using both x-rays and neutrons—have been used for the work in this thesis. It should be noted that some difficulties of single crystal scattering, such as multiple scattering and extinction, do not arise in powder diffraction, but in general, in polycrystalline measurements, there is a much bigger 'phase' problem, since experimentally only the magnitude and not the phase of the structure factor can be measured. One way to overcome the phase problem, is to only compare the moduli of the observed and calculated diffraction patterns, such as employed in Rietveld refinement

methods (see Section 4.1.3).

Neutron diffraction will be described in more detail in the following section, but x-ray diffraction will be briefly considered here. Two distinct mechanisms are available for x-ray production in a laboratory. Firstly, beams of electrons can be fired at metal targets, and their deceleration would produce electromagnetic radiation over a range of wavelengths. In the Laue diffraction method, this beam of white x-rays is exploited to allow the Bragg condition to be simultaneously satisfied for different reflections. Secondly, electrons colliding with the atoms in a target, can knock out one of the inner electrons, and when another electron falls to fill in the gap, it emits a photon characteristic of the transition. These beams of x-rays can be exploited in powder diffractometers, since in a (finely ground) powder the Bragg condition will be satisfied for many different planes. Ultimately, x-ray scattering relies on the electrical interaction between the incident radiation and the electrons in a sample, and thus they are scattered more strongly by heavier elements.

3.3 Neutron scattering

Neutron scattering is a very useful tool for studying both the structural properties and dynamic processes of materials. The de Broglie wavelength of neutrons, at energies appropriate for experiments, is comparable to that of interatomic distances, and thus neutrons can be used for diffraction. Neutrons penetrate deeply into the materials because they have no net electrical charge, and thus, unlike x-rays (which are scattered by the electron cloud around an atom), neutrons interact with atomic nuclei and are scattered via the strong nuclear force. Consequently, the neutron scattering cross-sections are not strongly related to the atomic number, such that the lightest elements can be investigated, and isotopes of a material can have vastly different scattering lengths. Neutrons also have a spin angular momentum of $\frac{\hbar}{2}$, which allows them to interact with any unpaired magnetic moments in a material via the electromagnetic dipolar interaction. Thus, neutron scattering can be used to determine a material's nuclear and magnetic structures. Furthermore, inelastic neutron scattering can be used to study both the phonon and magnetic excitations.

The interaction between neutrons and matter is weak, and thus may be treated us-
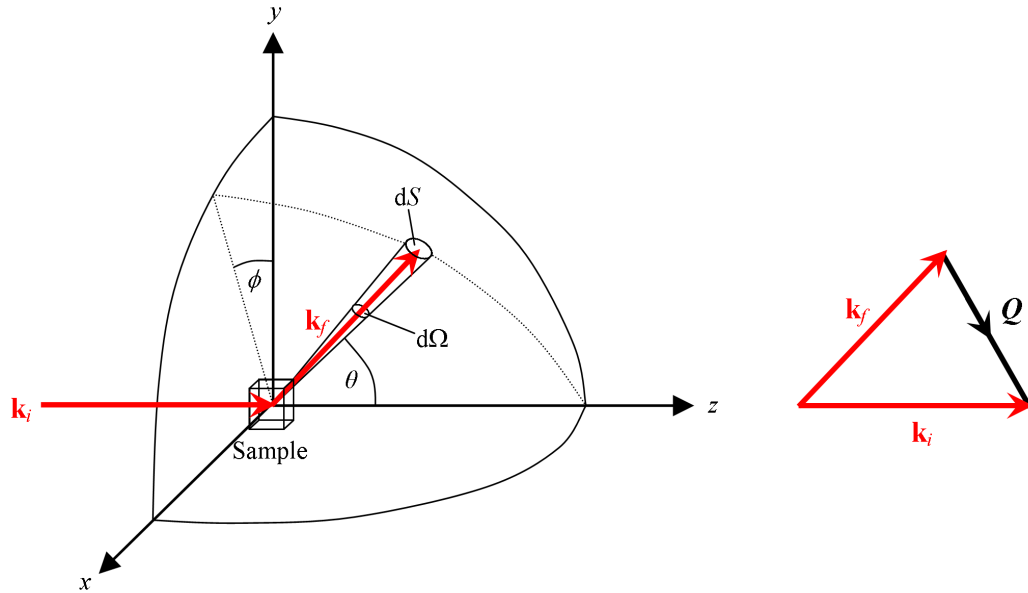
Figure 3.2: The geometry of a scattering experiment and the scattering triangle. The incident neutrons with wavevector $\mathbf{k}_i$ are scattered by the sample in the direction θ, ϕ with the final wavevector $\mathbf{k}_f$. $\mathbf{Q}$ is the scattering vector. Figure made with reference to Fig. 1.2 in [67].

ing first-order perturbation theory of the Born approximation, where it is assumed that the incident and scattered neutrons behave like plane and spherical waves, respectively. This is good because it greatly simplifies the expressions for the scattering cross-sections and thus theory and experiments can be compared in a relatively straightforward way, however, it also means that in order to get good statistics in a reasonable amount of time the sample sizes must be large.

The theory of neutron scattering will be briefly discussed in the following sections, with the caveat that other authors have covered the material presented in a much more rigorous and systematic fashion, for example, see [66, 67, 70]. Emphasis will be placed on some specific scattering techniques that have been used to carry out the work presented in this thesis, the experiments, including the instruments utilised, will be described in Chapter 4.

3.3.1 Basics

In this section only the nuclear interactions of neutrons will be considered, and a discussion of magnetic neutron scattering is left until Section 3.3.2. In a neutron scattering experiment,

a simple geometry of which is shown in Fig. 3.2, neutrons with initial energy, E_i, and momentum $\mathbf{k}_i$, are scattered by a sample into a new state with energy, E_f, and momentum $\mathbf{k}_f$. If $\mathbf{k}_i = \mathbf{k}_f$, energy is conserved, so the process is called elastic, and this allows to probe the structure of matter. The scattering vector, $\boldsymbol{Q}$, (shown on the right in Fig. 3.2) is given by

$$\boldsymbol{Q} = \mathbf{k}_i - \mathbf{k}_f \tag{3.2}$$

and the momentum transfer is $\hbar\boldsymbol{Q}$. If $\mathbf{k}_i \neq \mathbf{k}_f$, energy and momentum are not conserved, and the process is inelastic, which allows for the investigations of dynamic phenomena and excitations. The inelastic case will be considered separately in Section 3.3.4. The number of neutrons scattered per second in all directions divided by the incident neutron flux, Φ, is called the total differential cross-section, σ_{tot}. During an experiment, only a part of the solid angle will be covered by the detectors, so the number of neutrons scattered per second into a small solid angle $\mathrm{d}\Omega$ in the direction of (θ, ϕ) divided by the incident neutron flux, Φ, is given by the partial differential cross-section, $\left(\frac{\mathrm{d}\sigma}{\mathrm{d}\Omega}\right)$.

The incident neutrons can be modelled as plane waves, $\phi_i = e^{ikr}$, and a single atom would provide a weak perturbation, such that the scattered wave would be spherically symmetric, $\phi_f = -be^{ikr}/r$, and its amplitude will be given by the scattering length b with r being the radius of the scattered wave. The scattering length is related to the total scattering cross-section, σ_{tot}, via

$$\sigma_{\text{tot}} = \frac{\text{scattered flux}}{\text{incident flux}} = 4\pi b^2, \tag{3.3}$$

and it is usually determined from experiments, a list can be found in [71]. The scattering length depends on the atom, isotope and the relative orientation of the nuclear and neutron magnetic moments. Thus even if the scattering is coming from a single element, there will be a variety of scattering lengths in the sample and the scattered neutrons will have different phases, which gives rise to two terms—the coherent, σ_{coh}, and incoherent, σ_{incoh},—in the total scattering cross-section. Coherent scattering arises from an average scattering length of the system, and the incoherent scattering comes from the variation of the scattering lengths about this value. For example, during a powder diffraction experiment, the recorded pattern will be the sum of the coherent scattering seen as Bragg peaks, as well as

some non-zero incoherent background. These cross-sections are defined as:

$$\sigma_{\mathrm{coh}} = 4\pi\bar{b}^2 \tag{3.4}$$

and

$$\sigma_{\mathrm{incoh}} = 4\pi(\overline{b^2} - \bar{b}^2). \tag{3.5}$$

The differential cross-section can thus be written in terms of the coherent and incoherent cross-sections which are expressed in terms of the scattering length b, and the standard derivation may be found in [67].

To extract the structural information from the Bragg scattering due to an array of nuclei, n, the differential cross-section, can be used, and it is defined as:

$$\frac{\mathrm{d}\sigma}{\mathrm{d}\Omega} = \left| \sum_n b_n \exp(\mathrm{i}\boldsymbol{Q} \cdot \mathbf{r}_n) \right|^2 \tag{3.6}$$

where $\mathbf{r} = x\mathbf{a} + y\mathbf{b} + z\mathbf{c}$ gives the position of the interacting nucleus in terms of the lattice parameters. Diffraction occurs when Bragg's law, (which can be re-written as $\boldsymbol{Q} = 2|\mathbf{k}|\sin\theta$, and states that the nuclear scattering peaks occur when the scattering vector is equal to the reciprocal lattice vector) is satisfied, and thus $\frac{\mathrm{d}\sigma}{\mathrm{d}\Omega}$ is given by

$$\frac{\mathrm{d}\sigma}{\mathrm{d}\Omega} = N^2 |F(hkl)|^2 \tag{3.7}$$

where N is the number of unit cells, and the structure factor is defined as

$$F(hkl) = \sum_n b_n \exp[2\pi\mathrm{i}(hx_n + ky_n + lz_n)] \tag{3.8}$$

and, as before, the intensity of the Bragg scattering will be proportional to $|F(hkl)|^2$.

Finally, it is important to note that if a monochromatic beam of neutrons is incident on a powder sample, the scattered neutrons for each wavevector $\mathbf{k}_f$ would lie on a Debye-Scherrer cone of diffraction due to the random orientation of the crystallites, as illustrated in Fig. 3.3.
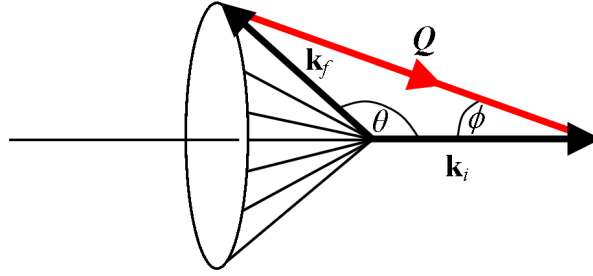
Figure 3.3: The relationship between Q, $\mathbf{k}_i$ and $\mathbf{k}_f$ in reciprocal space for an elastic scattering experiment using monochromated neutrons, and the Debye-Scherrer cones for Bragg scattering from a polycrystalline sample. Figure made with reference to Fig. 3.9 in [67].

3.3.2 Magnetic scattering

Neutron diffraction (in virtue of the neutrons magnetic moment) can also take place from an ordered arrangement of the magnetic moments [66, 67]. During a scattering event, the neutron's dipole moment will interact with the electromagnetic fields generated by the orbital moments, and the spins of any unpaired electrons in the material. The strength of this interaction is comparable to that of coherent scattering by nuclei, which allows for the simultaneous measurement of both nuclear and magnetic structures using neutron scattering. Magnetic scattering is highly dependent on the position in reciprocal space because the neutrons scatter from electrons in atomic orbitals, which have a large spatial interaction volume, so the scattering is weaker at higher angles, and the intensity of magnetic correlations falls dramatically for high Q values. Thus, measurements of magnetic order are usually restricted to low momentum transfers. This dependence of the magnetic scattering is described by the magnetic form factor, f_M, which can be considered as the Fourier transform of the magnetisation density, $\rho(r)$:

$$f_\mathrm{M} = \int \rho(r) \exp(i\mathbf{k}r)\mathrm{d}r. \tag{3.9}$$

The magnitude of the magnetic scattering can be defined analogously to the nuclear case, using a magnetic scattering length, p:

$$p = \left(\frac{e^2 \mu_n}{m_e c^2}\right) \mathbf{S} f_\mathrm{M} \tag{3.10}$$

where e and m_e are the mass and charge of an electron, μ_n is the neutron's magnetic moment, c is the speed of light and $\mathbf{S}$ is the spin. Hence, from similar consideration to the nuclear structure factor, the magnetic structure factor is a Fourier transformation of the magnetic distribution in a material, and for collinear magnetic structures it can be defined by:

$$F_{\mathrm{M}} = \sum_j f_{\mathrm{M},j}(\boldsymbol{Q})\mu_j \exp(i\boldsymbol{Q} \cdot \boldsymbol{r}_j) \tag{3.11}$$

where μ_j is the magnetic moment on site j. It is important to note that the dot product encodes the fact that the magnetic scattering is dependent upon the orientation, since the dipole interaction between moments is a directionally dependent quantity. Thus, magnetic scattering can only occur from the components of the magnetic moments which are perpendicular to the scattering vector. The magnetic scattering intensity is proportional to $|F_{\mathrm{M}}|^2$.

3.3.3 Polarised scattering

In a magnetic material, any disordered moments will give rise to paramagnetic diffuse scattering, which is generally much weaker than Bragg scattering. By using polarised neutrons, it is possible to separate the nuclear, magnetic and spin-incoherent cross-sections of paramagnets and powders of collinear antiferromagnets, and full details and derivations of the "XYZ-difference method" method may be found in [72–74].

For the polarisation analysis, the X and Y polarisation directions are fixed with respect to the instrument and only the Z polarisation is parallel and perpendicular to the wavevector transfer. The angle, α, between the X polarisation axis and Q is called the Schärpf angle. Compared to the polarisation of the incident neutrons, the polarisation of the scattered neutrons will either be the same (non-spin-flipped, NSF) or reversed (spin-flipped, SF) by the interaction with the sample. Thus, in total, six different configurations of the detected neutron states are possible, and all of them must be recorded for the full polarisation measurement: $\left(\frac{\mathrm{d}\sigma}{\mathrm{d}\Omega}\right)^z_{\mathrm{nsf}}$, $\left(\frac{\mathrm{d}\sigma}{\mathrm{d}\Omega}\right)^z_{\mathrm{sf}}$, $\left(\frac{\mathrm{d}\sigma}{\mathrm{d}\Omega}\right)^x_{\mathrm{nsf}}$, $\left(\frac{\mathrm{d}\sigma}{\mathrm{d}\Omega}\right)^x_{\mathrm{sf}}$, $\left(\frac{\mathrm{d}\sigma}{\mathrm{d}\Omega}\right)^y_{\mathrm{nsf}}$ and $\left(\frac{\mathrm{d}\sigma}{\mathrm{d}\Omega}\right)^y_{\mathrm{sf}}$. The dependence of these differential cross-sections on the nuclear, magnetic and spin incoherent cross-sections expressed in terms of the angle α can be derived following [73, 74], and by choosing appropriate linear combinations of the XYZ NSF and SF cross-sections the

$\left(\frac{d\sigma}{d\Omega}\right)_{nuc}$, $\left(\frac{d\sigma}{d\Omega}\right)_{mag}$ cross-sections can be found:

$$\left(\frac{d\sigma}{d\Omega}\right)_{nuc} = \frac{1}{6}\left[2\left(\frac{d\sigma}{d\Omega}\right)_{Tnsf} - \left(\frac{d\sigma}{d\Omega}\right)_{Tsf}\right] \tag{3.12}$$

where the subscripts Tnsf and Tsf refer to the total non spin flip and total spin flip components, and

$$\left(\frac{d\sigma}{d\Omega}\right)_{mag} = 4\left(\frac{d\sigma}{d\Omega}\right)^z_{nsf} - 2\left(\frac{d\sigma}{d\Omega}\right)^x_{nsf} - 2\left(\frac{d\sigma}{d\Omega}\right)^y_{nsf}$$

$$\text{or} \tag{3.13}$$

$$\left(\frac{d\sigma}{d\Omega}\right)_{mag} = 2\left(\frac{d\sigma}{d\Omega}\right)^x_{sf} + 2\left(\frac{d\sigma}{d\Omega}\right)^y_{sf} - 4\left(\frac{d\sigma}{d\Omega}\right)^z_{sf}.$$

Thus the magnetic scattering may be separated from the nuclear Bragg peaks.

There are, however, some limitations to this method when single crystals with directional spin components, such as ordered antiferromagnets, are investigated, because the angle α in general will not be known and the relations used to derive Eqs. 3.12 and 3.13 will not hold.

3.3.4   Inelastic scattering

If there is an energy change involved in the scattering process, where the neutrons gain or lose energy to the sample, the process is defined as inelastic, and the double differential cross-section, $\left(\frac{d^2\sigma}{d\Omega dE_f}\right)$ where E_f is the final energy of the neutron, is measured by an analyser. The method relies on the energy and momentum conservation relations, so for coherent inelastic scattering from a single excitation, the momentum transfer is still $\hbar\boldsymbol{Q}$, but the energy transfer is now defined as

$$\hbar\omega = E_i - E_f = \frac{\hbar^2}{2m}(k_i^2 - k_f^2). \tag{3.14}$$

The scattering function, $S(\boldsymbol{Q}, \omega)$ contains all of the information about the system, and is related to the double differential cross-section via

$$\left(\frac{d^2\sigma}{d\Omega dE_f}\right) = \frac{k_f}{k_i}S(\boldsymbol{Q}, \omega). \tag{3.15}$$

The measured energy spectrum shows a set of peaks which can be associated with transitions between different CEF levels, phonon scattering, and other magnetic excitations. In an inelastic spectrum magnetic modes are easily identified because of the decay in their intensity along increasing Q with the magnetic form factor.

3.4   Neutron production

Neutron flux for scattering experiments can be produced in two different ways: using a research nuclear reactor or from a spallation source. The experiments that have been carried out on $SrHo_2O_4$ and $SrGd_2O_4$ took place at the ISIS spallation source at the Rutherford Appleton Laboratory, UK, and the nuclear reactor sources in Institute Laue Langevin (ILL), France, and at the Helmholtz Zentrum Berlin (HZB), Germany.

At reactor sources, the continuous neutron flux is produced by a fission process, and the neutrons are subsequently slowed down by a moderator to maintain the fission process and provide the neutrons needed for experiments at appropriate energies. Moderation by water at 300 K allows for the production of 'thermal' neutrons, whereas moderation by deuterium, which is kept at 25 K, produces 'cold' (low-energy) neutrons, and finally, moderation by graphite, which is kept at 2400 K, produces 'hot' (high-energy) neutrons. The neutrons are guided from the moderator to the instruments via reflective wave guides, and since the reaction is constant, neutrons are continuously produced with a variety of energies. Neutron beams at reactor sources are often monochromated before the instrument in order select a narrow wavelength range for the experiment. Heat dissipation is often a big problem at reactor sources, and since the power needed to run a spallation source is often much lower, the nuclear fission reactors for making neutrons for research are slowly being superseded.

Spallation sources produce neutrons by initially accelerating short bursts of protons to high energies using a synchrotron and then colliding them with a target made out of heavy metallic elements, such as tungsten. The energy distribution of these neutrons is therefore broad, and the neutron flux is not continuous (with a frequency of 50 Hz at ISIS), but this can be exploited in the time-of-flight technique which removes the need for

monochromatisation, however the average flux is still much lower than that of a reactor source. In time-of-flight experiments, a white beam of neutrons is used to scatter off the sample. Since the time taken for neutrons to travel a flight path of a known distance can be measured, the final wavevectors $\mathbf{k}_f$ can be determined. The neutrons are moderated to suitable energies for scattering experiments by water (300 K), liquid methane (100 K) or liquid hydrogen (20 K) before being guided to instruments.

Chapter 4

Experimental techniques

This chapter outlines the experimental methods and techniques used to carry out the research presented in this thesis. The basics of sample preparation and single crystal growth, bulk properties characterisation methods and neutron scattering techniques will all be described in detail below.

4.1 Sample preparation

All the samples used in the experiments carried out for this thesis were made at Warwick.

4.1.1 Powder preparation

The powder samples were prepared from high purity starting compounds $SrCO_3$ and Ln_2O_3, in an off-stoichiometric ratio 1 : 0.875. This ratio was found to be optimal for all the $SrLn_2O_4$ compounds made, as initially when powders were mixed in a stoichiometric ratio the final materials were found to contain a large ($\sim$15 %) impurity phase of Ln_2O_3. The powders were ground together and heated in air at 1350°C for a total of 48 hours in an alumina crucible at ambient pressure, since it is well documented [43, 44, 57] that these compounds can be synthesised via a simple process of solid state diffusion. In general, one intermediate re-grinding was used to ensure homogeneity of the mixtures.

4.1.2 Compositional analysis

Powder x-ray diffraction was used to ascertain the composition of the synthesised compounds. The Panalytical X'Pert Pro Multipurpose x-ray diffraction and the Brucker D5005 diffractometers with monochromated Cu K_α ($\lambda = 1.5418$ Å) radiation were most frequently used to record the x-ray diffraction spectra in reflection mode. When the Bragg condition is satisfied, peaks are seen in the recorded pattern due to the coherent scattering of x-rays by crystalline planes. The purity of the synthesised powder samples were subsequently checked by performing a Rietveld refinement (which is described below) on the x-ray diffraction data, using the TopasRuns software [75]. This usually indicated the final purity of the compounds to be greater than 99 %.

4.1.3 Rietveld refinement

In order to determine a model that is compatible with the observed diffraction data, a Rietveld refinement may be performed. In the Rietveld method, a crystal (and/or magnetic) structure for powder samples is refined by minimisation of the square of the difference between the observed pattern and the calculated profile by adjustments of the parameters in the model [76, 77]. For single crystal data, the model is instead fit to the integrated intensities of the Bragg peaks. The model is based on an extensive set of parameters: the unit cell and space group (which are used to calculate the Bragg reflection positions), the atomic positions, temperature factors and site occupancies (which are used to calculate the intensity information), peak shapes, the FWHMs, background, the instrumental information, such as detector flight paths and angles, as well as any extra parameters, such as peak broadening, absorption and extinction. The maximum number of these parameters is determined by the quality of the data, but an upper limit will be set by the intrinsic line broadening [78]. The function M, which has to be minimised with respect to the parameters [78] is

$$M = \sum_{i=1}^{N} w_i [y_i(obs) - y_i(calc)]^2 \qquad (4.1)$$

where $\sum_i$ is the sum over the independent observations, $y_i(obs)$ is the measured intensity at a point i, w_i is its weight, and $y_i(calc)$ is the calculated intensity. Assuming the background

48

to be zero, and the only source of error in $y_i(obs)$ being the counting statistics, then the weight would be written as $w_i = [y_i(obs)]^{-1}$. The calculated profile can be found using

$$y_i(calc) = s \sum_{k=k_1}^{k_2} m_k L_k |F_k|^2 G_i k \tag{4.2}$$

where s is the overall scale factor, which ensures that $sy(calc) = y(obs)$, m_k is the multiplicity of the reflection k, L_k is the Lorentz factor (which defines the angular dependence of the integrated intensity), F_k is the structure factor, and $G_i k$ is the peak shape function (which can be Gaussian, Lorentzian or a mix of the two, called Pseudo-Voigt).

The R-factors allow to assess how well the proposed model fits the data, and the R-factors that are quoted for all of the refinements presented in this thesis are the profile R-factor, R_P, the weighed profile R-factor, R_{WP}, the expected weighed profile factor, R_{EXP}, and the goodness-of-fit, χ^2, which are defined as:

$$R_P = \frac{\sum_i |y_i(obs) - y_i(calc)|}{\sum_i y_i(obs)}$$
$$R_{WP} = \left[\frac{\sum_i w_i |y_i(obs) - y_i(calc)|^2}{\sum_i w_i y_i^2(obs)} \right]^{\frac{1}{2}}$$
$$R_{EXP} = \left[\frac{N}{\sum_i w_i y_i^2(obs)} \right]^{\frac{1}{2}}$$
$$\chi^2 = \left(\frac{R_{WP}}{R_{EXP}} \right)^2$$

$$\tag{4.3}$$

where N in the expression for R_{EXP} is the number of degrees of freedom (number of observations minus the number of refined parameters).

In order to be able to carry out a refinement, the space group of the material must be known so that a partial diffraction pattern can be calculated. This can be found by profile matching, simulated annealing or symmetry considerations. The full structure and all of the other parameters mentioned above can then be refined, but since it is an iterative process, it is usually necessary to have a pretty good estimate of what the model should be! Programs such as TopasRuns [75] and FullProf [79] may be used to carry out refinements. Finally, it is important to remember that the Rietveld method is a structure refinement method, and does not give a structure solution, just a model compatible with the data.
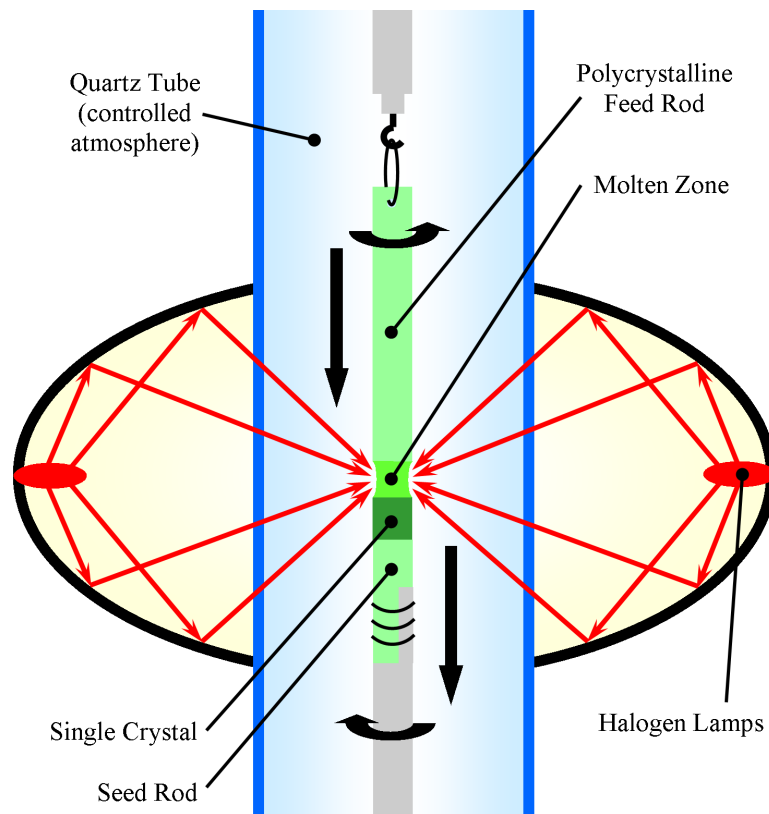
Figure 4.1: Illustration of the floating zone crystal growth technique. A pair of counter-rotating seed and feed rods is brought close together in the centre of the furnace. The ellipsoidal mirrors focus the heat into a narrow hot spot, such that a molten floating zone between the two rods is formed. The floating zone is moved vertically and a crystal is obtained as the material cools.

4.1.4 Single crystal growth

The crystal growth technique that has been used to make a sample of $SrGd_2O_4$ is called the floating-zone method. This technique is based on the principle of epitaxial growth to produce large, high quality single crystals which are suitable for most bulk property characterisation measurements and neutron scattering experiments. In order to produce crystals in this manner, initially, high purity starting compounds have to be prepared (as described above). These powders are subsequently isostatically pressed into rods of $\sim$7 mm diameter and $\sim$80 mm in length, and sintered in air at 1100°C for 24 hours. Since no previous $SrGd_2O_4$ crystals existed, to start the growth, one rod was used as a "seed" and the other rod was used as a "feed". To begin with, a "feed" rod of powdered $SrGd_2O_4$
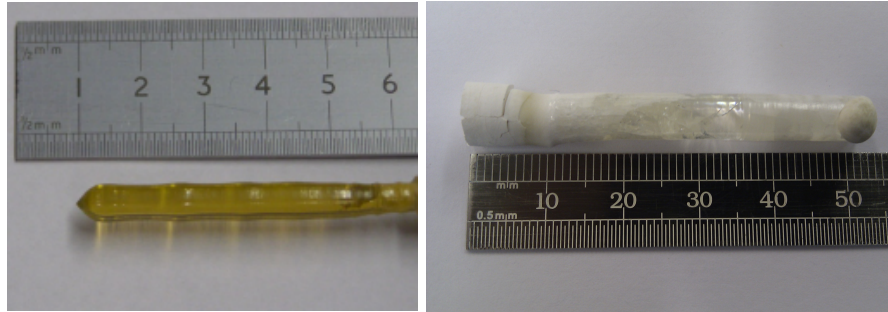
Figure 4.2: The boules of (left) $SrHo_2O_4$ [57] and (right) $SrGd_2O_4$ grown using the floating zone method, and used for all single crystal experimental work presented in this thesis. For $SrGd_2O_4$, only the central translucent region of the crystal was aligned and used in subsequent experiments.

is suspended above the above the "seed" near the middle of an image furnace. For the growth of $SrHo_2O_4$ and $SrGd_2O_4$ a high temperature optical furnace (Crystal Systems Inc. Optical Floating Zone Furnace Model FZT-12000-X-VI-VP) equipped with four Xe arc lamps focused by four ellipsoidal mirrors was used. The four mirror configuration gives a more homogeneous central hot-spot than a two mirror furnace.

Once the lamps are on and the four elliptical mirrors focus the heat of the system into a narrow hot spot, the "seed" and "feed" rods are moved closer together into this region. The starting materials begin to melt and form a molten ("floating") zone that is held between the two solid rods by its own surface tension. The feed and seed rods are counter-rotated at 10-20 rpm in order to homogeneously mix the molten material. The floating zone region is then moved vertically, at speeds ranging from 3 to 6 mm h^{-1}. This allows the crystal to form as the material cools and solidifies when it is moved away from the localised radiation focus. The grown crystal is expected to take on the atomic structure of the seed piece. A diagram of this process can be seen in Fig. 4.1. Several atmospheres were tried for the growth of $SrGd_2O_4$, but the best results were obtained for growths carried out in air at ambient pressure.

It should be noted that many different attempts at growing a single crystal of $SrGd_2O_4$ have failed. Various attempts using different atmospheres, growth speeds and temperatures were performed. Since none had produced a good single crystal, no single crystal "seeds" could be used. A lot of the growth attempts produced an amalgamation of small bits of
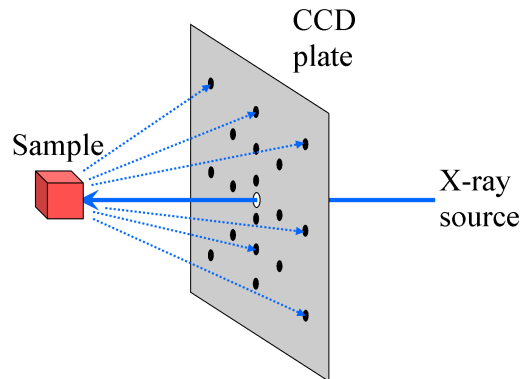
Figure 4.3: The back scattering x-ray Laue geometry, where an incident Bremsstrahlung beam is allowed to back scatter off the sample such that the Bragg condition to be satisfied for different lattice planes. The diffracted signal is detected at the CCD plates.

crystal with large polycrystalline regions. The final few boules of $SrGd_2O_4$ that were grown produced mostly clear crystals and these also tended to develop facets as they grew. The best attempts were transparent to light for several cm of the crystal length. However, all of the grown boules of $SrGd_2O_4$ developed cracks upon cooling even for the slowest growth speeds that were attempted. Eventually, a crystal was obtained using the procedure described above, this grown crystal had only a $\sim$2 cm region of clear translucent crystal, but it was the least cracked and large usable single crystal pieces could be isolated. Photos of the grown boules of $SrHo_2O_4$ and $SrGd_2O_4$ shown in Fig. 4.2. (The crack-free single crystal of $SrHo_2O_4$ was prepared using a similar method prior to the start of my research. The details of the procedure can be found in Ref. [57].) The large high quality single crystals that are obtained in this manner then need to be cut and aligned for further experimental study.

4.1.5 Laue diffraction

A single crystal sample first needs to be aligned along the principal axes before any bulk property and neutron scattering measurements can be made. A backscattering x-ray camera was used to align the crystal, with the setup shown in Fig. 4.3. Here, the sample is mounted onto a triple-axis goniometer, which is remotely controlled by the computer. When the sample is in position, an incident Bremsstrahlung beam (a broad distribution of x-ray energies) passes through the small central hole in the charge-coupled device (CCD) plates
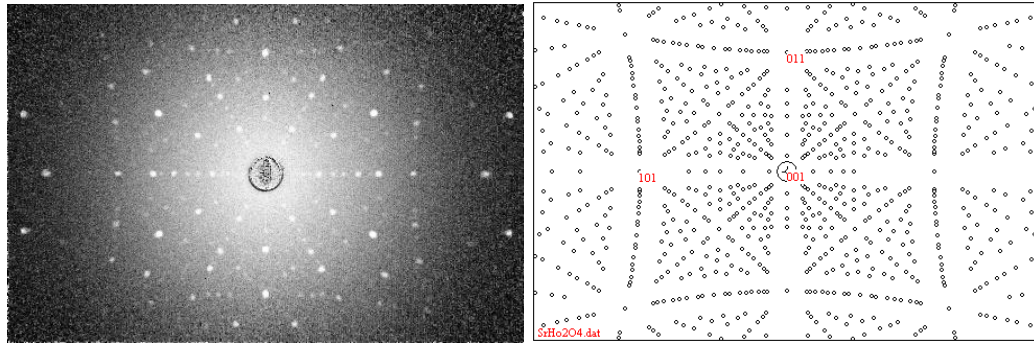
Figure 4.4: A typical x-ray Laue diffraction image (left) and the OrientExpress [81] simulation (right) of a well-aligned sample of $SrHo_2O_4$ oriented along the c axis. The exposure time was 10 seconds.

and is allowed to back scatter off the sample. The micro-focussed x-ray source and electronic detection means that the diffraction patterns can be obtained and recorded in much shorter times compared to conventional film-based methods. This wide range of wavelengths present in the incident radiation allows for the Bragg condition to be satisfied for different lattice planes, and the diffracted signal is detected at the CCD plates which are connected to a computer. When dealing with long-range ordered periodic structures (such as the single crystals) coherent elastic scattering takes place. The data collection is handled using the Image-Pro Express software [80], where exposure times and number of images recorded can be manipulated. An example of a well-aligned sample of $SrHo_2O_4$ along the c-direction is shown on the left hand side of Fig. 4.4.

To identify the different crystal orientations from the acquired Laue images a program called OrientExpress [81] was used. This software uses the space group and the unit cell parameters appropriate to the sample in order to calculate the expected diffraction pattern. The version of OrientExpress used does not simulate the experimental intensity of the Bragg spots, only their allowed positions, and hence more spots can be seen in the simulation than in the Laue image in Fig. 4.4. The Laue simulation allows for this pattern to be viewed for different directions in reciprocal space. Comparison of the simulation and the images acquired allows the crystal orientations to be determined. Once the three main crystallographic directions are identified, the crystal can be cut along planes perpendicular to them. This is achieved by carefully glueing the crystal to another goniometer and then

cutting using a low speed diamond wheel saw. To make it easier to apply demagnetisation corrections, most of the crystal pieces used for bulk property measurements presented in this thesis were box-shaped, with each face perpendicular to a principal crystallographic axis.

4.2 Bulk property measurements

Measurements of the magnetic susceptibility, magnetisation and the heat capacity can tell us about the macroscopic behaviour of magnetic systems. These studies can often give us some insight into what is happening in the material and this information can be used to effectively plan the neutron scattering experiments.

4.2.1 Static magnetic susceptibility and magnetisation

To investigate how magnetic susceptibility varies with temperature and how magnetisation varies with an applied magnetic field several different techniques are available. Some common examples of these include extraction magnetometry, torque magnetometry and vibrating sample magnetometry (VSM) [3]. The susceptibility and magnetisation measurements presented in this thesis have been made using the Quantum Design MPMS-5S and MPMS-XL magnetometers. These comprise of a second-order gradiometer detection coils connected to a Superconducting QUantum Interference Device (SQUID) and use the inductive method to measure a magnetic signal [82]. The principles of SQUID magnetometry are illustrated in Fig. 4.5. To perform a measurement, samples (attached to non-magnetic holders) are moved in a series of steps through the pick-up coil in a homogeneous magnetic field produced by a superconducting magnet. By Faraday's law, this motion changes the magnetic flux in the gradiometer coils, and hence a current is induced that is proportional to the magnetisation of the sample. The detection coil is wound in the manner of a second order gradiometer, shown in Fig. 4.5, in order to reduce the noise in the detection circuit caused by fluctuations in the magnetic field of the superconducting magnet.

The induced current is not directly measured, and instead the gradiometer coils are inductively coupled to a SQUID device, which is made up of a ring of superconduct-
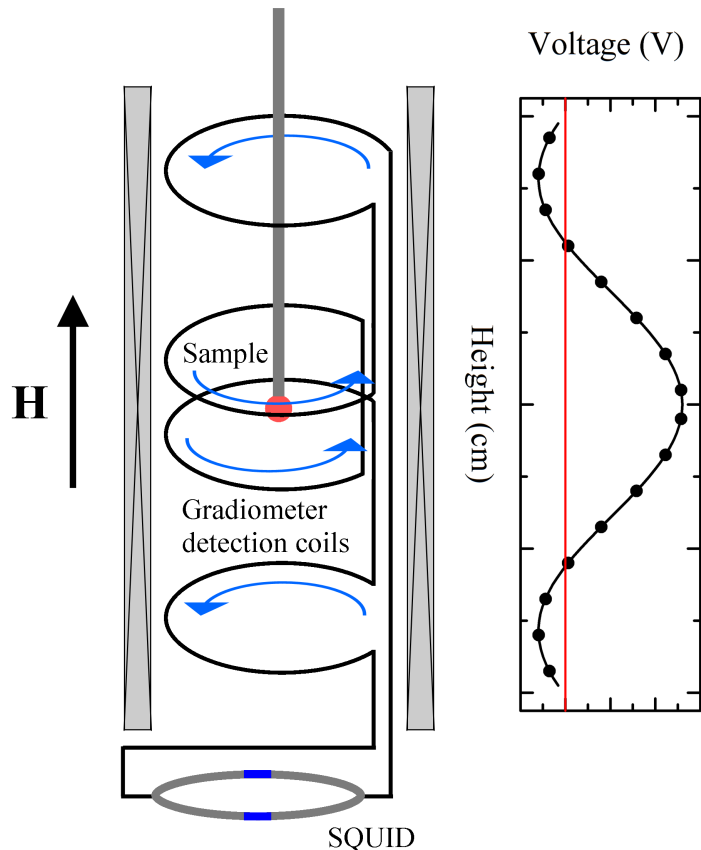
Figure 4.5: Basic components of a SQUID magnetometer. To carry out a measurement, the sample is moved through the gradiometer pick-up coils in an applied magnetic field. This movement induces a current proportional to the magnetisation of the sample. The change in current can be detected by a SQUID - a pair of Josephson junctions on a superconducting ring - and converted to a voltage. Fitting the voltage allows the value magnetisation to be computed. Figure made with reference to [82].

ing material with a pair Josephson junctions that act like tunneling barriers for Cooper pairs. The SQUID acts as a very sensitive current to voltage converter because the magnetic flux through the superconducting ring has to be a multiple of the magnetic flux quantum, $\Phi_0 = h/2e = 2.068 \times 10^{15}$ Wb [82], so that small changes in the ring current can be accurately detected. In fact, signals as small as 5×10^{-8} emu for the magnetic moment can be measured. As the SQUID is highly sensitive, it is positioned well below the sample space that is situated inside the magnet, and protected by superconducting shielding.

The SQUID is calibrated using a sample of a known magnetic susceptibility. Thus when a new sample is measured the voltage response is fitted to obtain a signal in electro-

magnetic units (emu). The external field must be homogeneous for the whole region of the measurement (the sample is typically moved through 4 cm), and the two magnetometers used for the work in this thesis have a field uniformity of 0.01%. Magnetisation measurements using the MPMS-5S can be made in a temperature range of 1.8 to 300 K and a field range of ± 5 T; and using the MPMS-XL, in the temperature range of 1.8 to 400 K and a field range of ± 7 T.

The MPMS-XL magnetometer can also be connected to an iQuantum (IQ2000-AGHS-2RSO ^{3}He system) refrigerator insert [83], which allows the temperature range that can be investigated to be extended down to $\sim$0.5 K. This is useful when studying crystals that only order magnetically at very low temperatures not accessible when using only liquid ^{4}He. To use the ^{3}He system, samples (attached to small tufnol holders) are placed inside a thermal shield in contact with a thermometer and heater that sit at the end of the sample rod. The sample rod is placed inside the main pipe, which fits inside the usual MPMS sample space. When data is being collected, the main pipe contains the liquid ^{3}He and the whole pipe is moved by the RSO motor connected at the top of the main pipe. The main pipe is connected to the gas handling system using the bellows, and this is all sealed in a vacuum like the usual MPMS sample space.

The sample stick, main pipe and bellows are assembled and connected into the MPMS at room temperature, and the system is only cooled down once everything is sealed and the vacuum conditions are met, in order to avoid contamination of the ^{3}He gas. Once the system reaches low temperature, an auxillary pump maintains the MPMS at 1.6 K, the temperature at which the ^{3}He gas is condensed. After this stage is complete, the liquid ^{3}He can be pumped and the base temperature of $\sim$0.5 K can be reached. The flow of ^{3}He is continuously controlled by the needle valve, and the software allows for automated data collection of both $\chi(T)$ and $M(H)$. The temperature rise during each scan is typically no higher than a few mK.

Usually, $\chi(T)$ is measured on warming in a Zero-Field-Cooled (ZFC) regime, where the sample is first cooled to the lowest desired temperature, and then a magnetic field is applied and data is subsequently collected upon warming the sample. However, some of the data presented in this thesis was also measured in the Field-Cooled (FC) warming regime,

where the cooling to the lowest experimental temperature happens after the magnetic field is applied to the system (again the data is collected while warming). The ZFC and FC datasets sometimes need to be differentiated because they are not always identical, and can depend on the nature of the magnetic order of the system studied. As an example, differences in the susceptibility between ZFC and FC data can occur for spin glass materials below their spin freezing transition temperature [13].

Finally, it is important to note that the applied field ($\mathbf{H}_\mathrm{a}$) can be very different to the internal field ($\mathbf{H}_\mathrm{i}$) inside the sample. In general, for irregularly shaped magnets, $\mathbf{H}_\mathrm{i}$ will depend on the position inside the sample in which it is measured. In the particular case of ellipsoidal samples (and this includes the special cases of a sphere and a flat plate), $\mathbf{H}_\mathrm{i}$ may be defined throughout the sample if the field is applied along one of the principal axes of the ellipsoid, such that

$$\mathbf{H}_\mathrm{i} = \mathbf{H}_\mathrm{a} - N\mathbf{M} \tag{4.4}$$

and N is called the demagnetising factor [3]. Demagnetisation corrections must be performed if the magnetisation is large compared to the applied field. All of the samples used for bulk property measurements presented in this thesis were made to approximate thin plates. Corrections to the data to take into account demagnetisation effects were made using the equation found in [84]. This method was found to agree with the results obtained by approximating all of the plates to similarly sized cylinders and using the tables in [85] to obtain N. The demagnetising field was found always to be less than 5% (typically 2%) of the applied field.

4.2.2 Specific heat measurements

Heat capacity is related to the internal energy (U) of a system and can be derived from the first law of thermodynamics, so that $dQ = dU + dW$ where Q is the amount of heat added to a substance and W is the external work done (normally assumed to be compression or expansion, so that $dW = PdV$). Hence the heat capacity at constant pressure (C_P) can be defined as

$$C_P = \left(\frac{dQ}{dT}\right)_P \approx \left(\frac{\delta Q}{\delta T}\right)_P \tag{4.5}$$

i.e. the amount of heat required to raise the temperature (T) of a substance a given amount during a quasi-static isobaric process. Since entropy (S) is defined as

$$dQ = TdS \tag{4.6}$$

changes in the energy of the system have an associated entropy change. Thus, the entropy can be calculated from absolute zero to an arbitrary temperature T_f by using

$$S(T_f) = \int_0^{T_f} \frac{dQ}{T} = \int_0^{T_f} \frac{C(T)}{T} dT \tag{4.7}$$

From experimental data, the temperature dependence of the magnetic entropy can be calculated as an area under the $C(T)/T$ curve (which is normally linearly extended down to $T = 0$ K) once the phonon and the free electron contributions have been subtracted. The magnetic entropy is associated with spin disorder, and can be compared to the expected entropy of a magnetic ion with the total angular momentum **J**, which is

$$S = R\text{ln}(2J + 1) \tag{4.8}$$

here, R is the molar gas constant ($R = 8.314$ J mol^{-1} K^{-1}).

In general, the heat capacity of insulating samples is dominated by the lattice and magnetic contributions. For a magnet at low temperatures, the lattice contribution to the heat capacity decays with T^3, and hence the heat capacity is a useful quantity to measure when investigating magnetic properties. At a phase transition there is a large change in the in the internal energy of a sample in a small temperature range. Peaks in heat capacity can be a useful indicator of phase transitions and are called λ-anomalies. In order to convert from heat capacity to the specific heat, the amount of material must be taken into account. Thus, overall, the specific heat is a useful measurement to carry out in order to look at lattice properties, for phase transitions and Schottky anomalies.

Specific heat can be measured as a function of temperature and of magnetic field on both polycrystalline and single crystal samples. The Quantum Design Physical Prop-
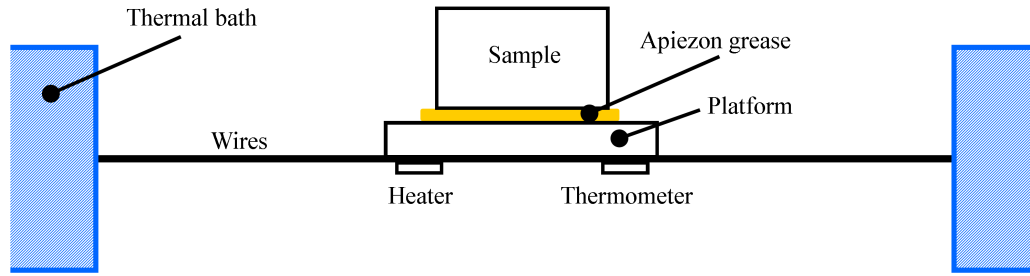
Figure 4.6: Sample environment for making specific heat measurements using the relaxation technique. The sample is held using Apiezon grease on a small platform which contains a heater and a thermometer. Once the sample puck is inserted into the PPMS for heat capacity measurements, the sample environment is held at high vacuum. Figure made with reference to [87].

erties Measurement System (PPMS) has been used to make specific heat measurements at constant pressure using the two-tau model relaxation technique. The PPMS can take measurements in the temperature range of 1.9 to 400 K and the field range of ± 9 T [86]. In order to collect data at lower temperatures, down to ~ 0.35 K, a closed cycle ^{3}He insert was also used for some of the measurements [87]. The system uses a pump line and a return line so that uninterrupted operation of the insert can continue down to 0.5 K (as long as the PPMS holds the sample chamber at 1.9 K). The temperature is lowered by a turbo pump, connected to the pump line, that pumps on the liquid ^{3}He, and the return line allows the ^{3}He to continuously flow back and condense into the reservoir in the base of the probe. This reservoir is thermally linked to the sample platform, and the temperature can be controlled by varying the pump speed (to get different ^{3}He vapour pressures) and using the sample platform heater. To get down to ~ 0.35 K, a "one-shot" mode is automatically activated by shutting off the flow to the return line. To use this insert, only electrical connections have to be made and the refrigerator has to be mounted inside the sample chamber. ^{3}He condensation can begin once the PPMS sample chamber reaches 1.9 K because the system comes pre-charged with ^{3}He. Thermal anchoring baffles along the probe assist in cooling and maintaining the probe at the 1.9 K base temperature. All of the pumping system valves, temperature and data collection are subsequently controlled by the software.

Both of the materials I have studied have been insulators, and hence in order to make accurate measurements of the heat capacity very thin samples (~ 0.1 mm) of the ma-

terials had to be made in order to minimise temperature gradients across the sample. Ideally, the samples used would also have a large surface area in order to ensure the largest possible contact between the sample and platform. To perform the measurements [87], the thin plate-like samples are mounted using the N (low temperature) or H (high temperature) Apiezon grease onto the puck platform to ensure that good thermal contact is maintained. The platform is suspended inside a "puck" on thin wires in order to isolate it from thermal contact with the rest of the system. The wires also provide electrical contacts for the platform heater and thermometer. The puck is connected to the cold finger of the refrigerator and plugs into a 12-pin connector, which provides electrical access to the measurement hardware at the bottom of the PPMS sample chamber. (A reference temperature of the system is measured by a separate thermometer not in contact with the platform.) The sample chamber is held at high vacuum during measurements to ensure that heat is not lost via the exchange gas. The basics of the sample environment are illustrated in Fig. 4.6.

Preliminary heat capacity measurements using just the platform and grease are run over the entire temperature range required to produce addenda files, so that the all of the background signal may be subtracted for the data collected with the sample. For some measurements even a small discrepancy in the amount of grease in addenda measurements can produce significant inaccuracies in the data. With the sample in place, the heat capacity can be measured at the desired temperature and field. Once a particular temperature is deemed stable, a small amount of heat (usually 2 to 5% of the reference temperature) is applied to the platform. The system records the heater power, the initial temperature rise and subsequent relaxation of the sample and platform, and the data is fitted to a two-tau model, described in more detail in [88]. This method assumes that the sample is not completely thermally coupled to the platform, and hence two time constants are used to fit the data: τ_1 for the relaxation of the whole system of the platform with the thermal bath, and τ_2 for the time for equilibrium of the sample with the sample stage. If the sample is sufficiently thin, or a good thermal conductor, 100% coupling is assumed and the data is instead fitted to a one-tau model. The software automatically selects whether to use the one-tau or two-tau model, and a typical relaxation technique pulse is illustrated in Fig. 4.7.

The total heat capacity is a sum of the phonon, electronic and magnetic contribu-
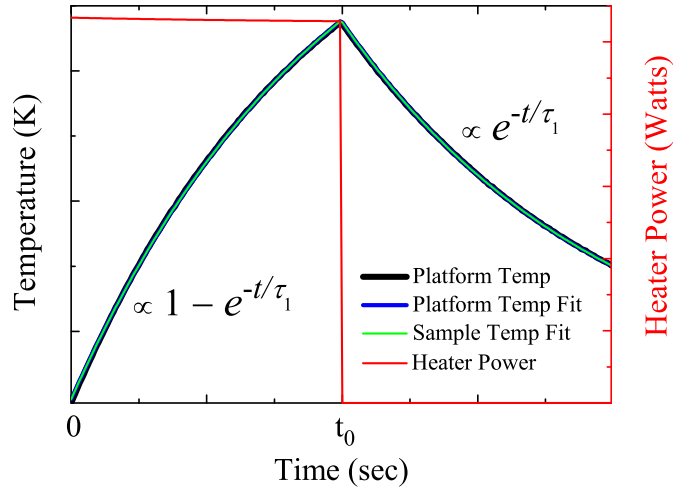
Figure 4.7: A relaxation technique heating and cooling pulse. Sometimes, two time constants are needed to fit the data: τ_1 is the time for equilibrium of the platform and sample with the thermal bath. τ_2 is the time for equilibrium of the sample with the platform. (Note, sample coupling has to be pretty good in order to achieve accurate results.)

tions. In order to try and separate out the magnetic (spin disorder) part, a phonon blank can be measured. This is usually a compound of the same crystal structure as the sample, but with all of the magnetic ions replaced by non-magnetic analogues in order to have as accurate representation as possible of the magnetic compounds phonon and electronic contributions to the heat capacity. Thus if the phonon blank is subtracted from the specific heat data, a purely magnetic signal is expected to remain. For the SrLn_2O$_4$ systems both SrY$_2$O$_4$ and SrLu$_2$O$_4$ may be used as phonon blanks. SrY$_2$O$_4$ will be lighter than the magnetic SrLn_2O$_4$ compounds investigated, and hence its use would slightly underestimate the phonon and electronic contributions to the heat capacity. SrLu$_2$O$_4$ will instead be heavier and hence overestimate the contributions. Overall, at low temperature, it is expected that this correction will be small.

4.3 Neutron Diffraction

The neutron diffraction techniques that have been used to investigate the magnetic structure of SrHo$_2$O$_4$ will be described below. The basics of neutron scattering theory have already

been discussed in Section 3.3.1. Diffraction measurements have been performed using both polarised and unpolarised neutrons on powder and single crystal samples of $SrHo_2O_4$ in order to establish the materials magnetic structure.

Due to the vast neutron absorption cross-section of naturally abundant Gadolinium of 49700 barns [71], and the prohibitive expense of the ^{160}Gd isotope (which has a small absorption cross-section of 0.77 barns [71]), a single diffraction experiment using "hot" (high-energy) neutrons was attempted on $SrGd_2O_4$. Since the absorption is not a linear function of the incident neutron energy, at high energies there occurs a minimum in the absorption curve for Gd. Due to the magnetic form factor, strong magnetic reflections are usually observed only at low Q, so trying to investigate magnetic correlations using hot neutrons is quite challenging. Due to these limitations and the early termination due to equipment failure of the only diffraction experiment undertaken on $SrGd_2O_4$, it will be described separately in Section 6.3.

4.3.1   Neutron Laue: Orient Express, ILL

The neutron diffraction Laue machine at the Institute Laue-Langevin [89] has been used to check and align some of the crystals that were to be used in other diffraction experiments, for example on D7 and D10. The system works on principles similar to the x-ray Laue described in Section 4.1.5, but uses a white beam of thermal neutrons instead of photons. The big advantage of the neutron Laue is that the bulk of the crystal is sampled, and not just the surface like with the x-ray set-up.

The Laue system is composed of a goniometer (which has two tilt stages mounted on an ω-rotation plate) and a scintillator-detector which captures diffracted neutrons and covers an angular range of 180°. The sample-to-detector distance can be varied from 32 to 220 mm. All the motors of the diffractometer can be controlled manually or through the MAD program. Before the neutrons are allowed to scatter off the sample, the crystal is optically aligned to sit in the centre of the incident beam using a video camera.

The diffraction patterns are collected electronically, using two high performance image intensified CCD cameras that are coupled to a large-area (252×198 mm^2) neutron scintillator. The neutron scintillator provides high neutron capture efficiency, and the cam-
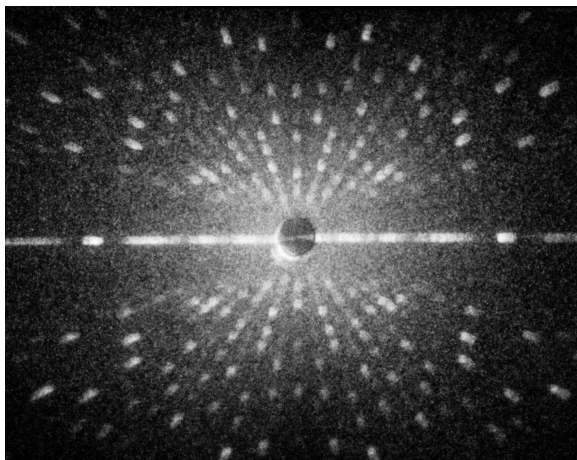
Figure 4.8: A neutron Laue diffraction image of a well-aligned sample of $SrHo_2O_4$ oriented along the b axis. The figure was created by averaging together five individual images, the exposure time for each image was 30 seconds.

eras use f/0.95 lenses to achieve high sensitivity. The two cameras are synchronised to take images simultaneously, and exposure times of a few ms to many minutes are possible. A single image of the diffraction pattern is reconstructed by the Image Pros Plus software [80], which also controls the cameras' operation. The software allows the user to adjust the binning, exposure time, and intensifier gain in order to optimise the frame rate, resolution, sensitivity, image size and dynamic range. As an example, Fig. 4.8 shows the diffraction pattern collected for a well aligned sample of $SrHo_2O_4$ oriented along the b axis. The image was constructed by averaging five 30 second exposures, in order to avoid saturating the detector. As with the x-ray Laue images, the determination of the orientation matrix of the diffraction patterns can be performed using OrientExpress [81].

4.3.2 Powder neutron diffraction: GEM, ISIS

The GEneral Materials diffractometer (GEM), a "multi-bank" Time-of-Flight (TOF) instrument at the ISIS neutron facility, has been used to study the nuclear and magnetic diffraction from a powder sample of $SrHo_2O_4$. The basics of powder diffraction were discussed in Section 3.3.1, and perhaps it is only useful to restate that for a specified neutron wavelength Bragg scattering from a powder sample will lie on Debye-Scherrer cones. Powder diffractometers are well suited for neutron pulses because these have a relatively constant time-

resolution over a broad range of wavelengths. The GEM instrument is briefly described below, but more details can be found in [90, 91].

GEM is not like the early powder diffractometers, which had very long primary flightpaths and detectors that were positioned on a geometrically focussed locus so that individual detector elements had equal resolution and could be grouped to produce a single diffraction pattern. Instead, GEM uses electronic focusing, which allows the detector banks to be designed with varying Q resolution and positioned at various diffraction angles. GEM uses ZnS/^{6}Li scintillator-detectors, where the absorption of a neutron in the detector produces a flash of light. Reasonable resolution in Q is achieved by the small effective width (5 mm) of the individual detector elements, and these are also highly stable (showing a variation of 0.12% per degree for the detector efficiency with temperature). The detector elements are grouped in parallel into modules, which are arranged tangentially to DebyeScherrer cones of diffraction. The modules are organised into banks that cover a limited range in the scattering angle (2θ), and, importantly, within each bank the individual elements are approximately resolution focussed. In total, there are eight detector banks on GEM, and their schematic position and scattering angle parameters are presented in Fig. 4.9. Thus GEM covers a broad Q-range because the detector array covers a very large area (7.270 m^2) which translates to a wide range in scattering angles of $1.21° < 2\theta < 171.40°$.

In early powder diffractometers the detectors were arranged only in the equatorial plane. The GEM detector array, however, covers a very large solid angle of 3.860 steradians because the detectors extend over wide range in azimuthal angle ϕ (mostly of $\phi \approx \pm45°$). This means that the detectors cover more than 30% of all the possible scattering directions from the sample. Overall, 7270 individual detector elements make up the detector array on GEM, allowing it to have a high count rate.

In order to achieve good resolution in reciprocal space, particularly in the backscattering geometry, GEM has a 17 m long primary flightpath from the moderator to the sample. (Longer flightpaths reduce the TOF contributions to the resolution, which distort the Bragg peaks shape). Having the best possible resolution is also advantageous in order to achieve the best possible separation of the Bragg peaks in the diffraction pattern. However, it should be noted that longer flightpaths also significantly reduce the incident neutron flux. To pre-

Bank #	Scattering angle 2θ (°)
0	1.21–3.18
1	5.32–12.67
2	13.44–21.59
3	24.67–45.61
4	50.07–74.71
5	79.07–106.60
5X	106.02–114.19
6	142.50–149.72
7	149.98–171.40
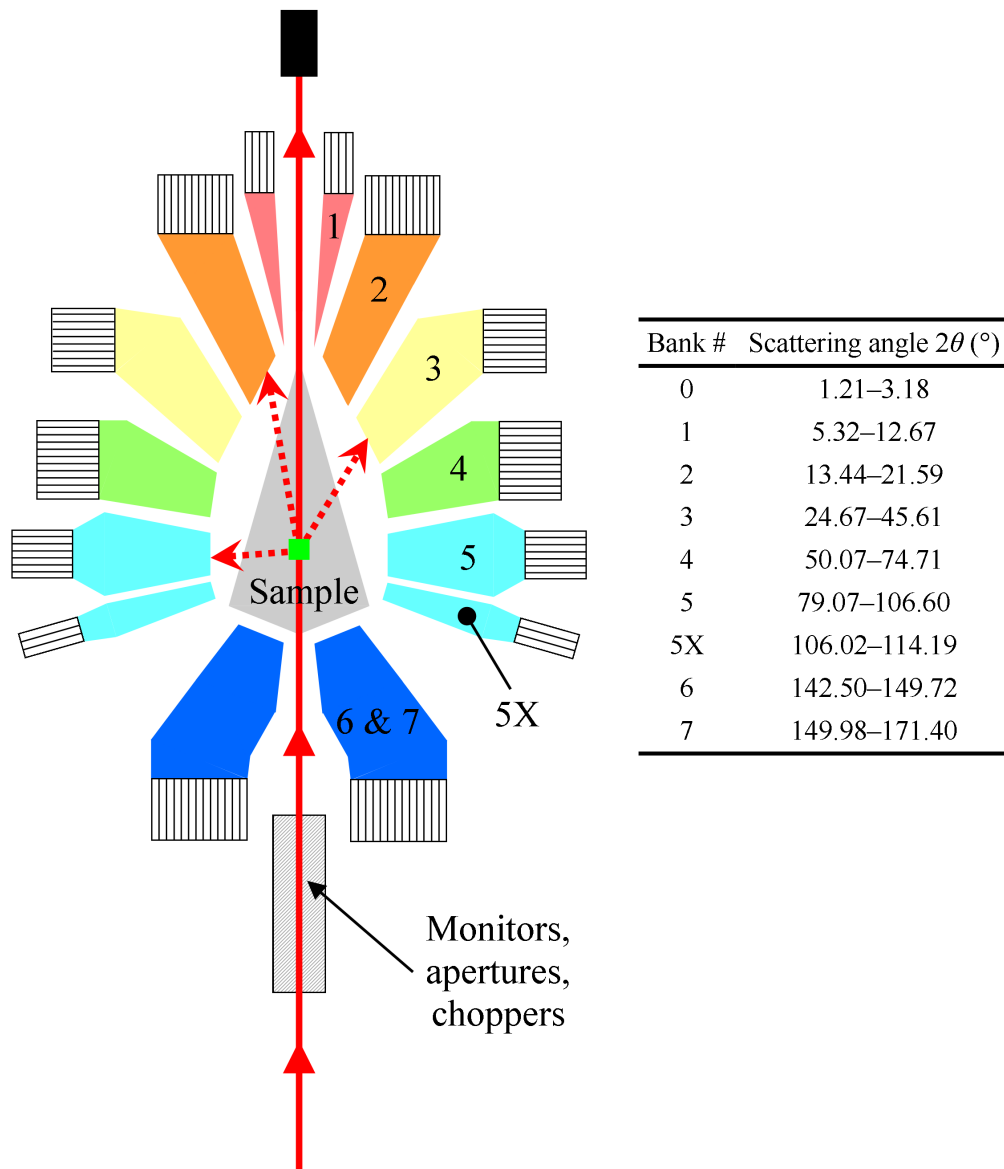
Figure 4.9: Two-dimensional schematic of the GEM instrument at ISIS, UK. The different detector banks are shown in different colours (Bank 0 is not shown). This figure was made with reference to Figs. 1 and 2 in [91].

vent the attenuation of the neutron beam by air scattering, GEMs primary flight path and sample tank are kept under vacuum (the detectors are located outside the sample tank), and a sequence of horizontal and vertical slits define the beam's dimensions. Two disc choppers are used to prevent frame overlap problems caused by fast neutrons from one pulse catching up to the slow neutrons from the previous pulse, and this allows to define the wavelength range for GEM of 0.05 to 3.40 Å. If lower Q data are required, this range can be shifted to longer wavelengths. Also, a nimonic chopper reduces the background by removing the fastest neutrons from each neutron pulse, and the neutron flux is monitored at four stages along the primary flightpath. Just before the sample position is a final aperture (called a beam-scraper) that accurately defines the dimentions of the incident neutron flux. Further reductions in the background are achieved by using an oscillating radial collimator in the sample tank for the diffracted neutrons.

For GEM, the $\Delta Q/Q$ resolution in reciprocal space is mostly good, with the best value of 0.34% in backscattering. This means that at high momentum transfers good real space resolution is achieved, which is important for structural studies. The resolution at low-Q (which is important for magnetism) is, however, relatively low (several %) and is dominated by the geometrical factor. Using GEM, experiments that probe both the crystal and magnetic structures are possible by simultaneously using several banks. This means that GEM is of great use for a wide variety of studies of ordered crystalline materials. Many different sample environments are available on GEM, including a dilution cryostat and a magnet. The diffraction data collected using the GEM instrument must be refined in order to determine the crystal and magnetic structures. A description of the data refinement analysis for the experiment on a powder sample of $SrHo_2O_4$ is given in Section 5.1.3.

4.3.3 Single crystal neutron diffraction: WISH, ISIS

The WISH (Wide-angle In a Single Histogram) instrument [92] is a relatively new cold neutron multidetector diffractometer at the ISIS facility, Rutherford Appleton Laboratory, UK. It is primarily intended for the study of powder samples, but can be adapted to look at single crystals (provided that these are carefully aligned beforehand). The single crystal diffraction is possible using WISH due to its large continuous detector array. WISH is

located at Target Station 2, which has much lower frequency neutron pulses than instruments like GEM at Target Station 1. WISH uses a solid methane moderator that operates at 40 K to produce a high flux of cold neutrons. Due to the low frequency of the neutron pulses, the natural bandwidth of the instrument is 9.4 Å. A supermirror guide allows the beam to travel the 40 m from the moderator to the sample position. Selection of the bandwidth of the instrument and prevention of frame overlap is handled by a system of choppers along the guide. The divergence of the beam can be controlled by five sets of slits positioned in the guide. So for low-resolution mode, all of the slits would be open, and in high-resolution mode only a $0.2°$ divergence is transported by the guide, giving a nearly constant $\Delta Q/Q = 0.3$ % resolution at high diffraction angles. Thus, depending on the experimental requirements the WISH instrument resolution and flux can be tuned to deliver high quality data in a broad Q range. The WISH diffractometer is currently equipped with a large continuous array (760 tubes) of position sensitive ^{3}He detectors that are arranged on a cylindrical locus and cover an angular range of $10° < 2\theta < 170°$, and $\pm 15°$ out of plane. In high resolution mode, each tube covers a horizontal angle that matches the beam divergence. The continuous array means that that there are no gaps between the tubes, and this provides the substantial Q-space coverage required for single crystal experiments. The engineering layout of WISH can be found in Fig. 1 in [92].

Any of the standard sample environment options can be accommodated on WISH, and for the $SrHo_2O_4$ experiment a dilution fridge and a recondensing superconducting magnet were used. This is a vertical magnet with a $340°$ in-plane opening and an asymmetric horizontal opening of $15°$. The scattering from the aluminium sample environment is designed to prevent any shadowing from the support pillars, and is further reduced by an oscillating radial collimator for an area in the centre of the sample space. This means the instrument has a low background, which allows for studies of magnetic diffuse scattering. Once the sample-to-detector space is filled with argon the air scattering will be further minimised.

Neutron diffraction measurements on $SrHo_2O_4$ were made in the $(hk0)$ scattering plane in a range of temperatures from 0.05 to 1.5 K and a range of fields of 0 to 2.5 T. A 0.9 g sample of $SrHo_2O_4$, aligned using the backscattering Laue technique and cut perpen-
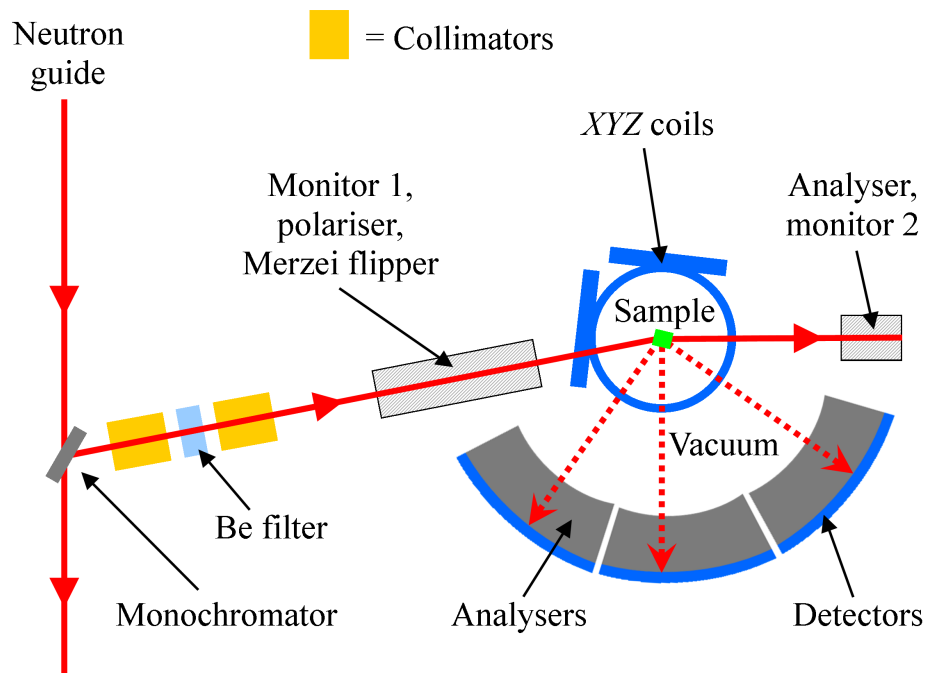
Figure 4.10: Schematic of the D7 instrument at a thermal neutron guide at ILL, France. This figure made with reference to the D7 page in [89] and Fig. 2 in [74].

dicular to the crystal's c axis within an estimated accuracy of $1°$, was fixed to an oxygen free copper sample holder using Kwikfill resin. The data collection was done in two configurations on WISH: the histogram and event modes. The histogram format is akin to other powder diffractometers, where the wide angular range of the data collected is focussed into a single histogram (or several histograms for each bank on GEM), and then displayed. The event mode, instead, is able to bin the data collected in (almost) real time. All of the data processing was subsequently handled using the Mantid software [93].

4.3.4 Polarised neutron diffraction: D7, ILL

D7 is a cold neutron diffuse scattering diffractometer that is equipped with *XYZ* polarisation analysis at the Institut Laue-Langevin in Grenoble, France [73, 74, 89, 94]. D7 can be used in two separate configurations: *XYZ* polarisation analysis and uniaxial polarisation analysis (used for looking at scattering from non-magnetic samples and non-collinear magnets). Below, only the polarisation analysis configuration will be described. On D7, Q resolution is

relaxed in order to gain flux to look at diffuse scattering which is not expected to have any sharp features. The background is kept as low as possible because the diffuse features are also, in general, expected to be much weaker than Bragg scattering. Measurements of the *XYZ* polarisation cross-sections described in Section 3.3.3 allow for the unambiguous separation of nuclear, magnetic, nuclear-spin-incoherent and isotope incoherent contributions to the scattering function simultaneously over a large range of scattering vector Q.

The wavelength of the incident neutrons on D7 is selected by moving the entire instrument to access three different angles of the vertically and horizontally focusing pyrolytic graphite monochromators, which translate into incident wavelengths of 3.1, 4.7 or 5.8 Å. A Beryllium filter is used to suppress higher order contamination. Polarisation is achieved on D7 using a polariser, flipper and a *XYZ* alignment coil assembly. First, the incident neutron beam is polarised with high efficiency in the Z direction using a focusing Schärpf supermirror bender, and a small guide field of $\sim$20 G ensures that this polarisation is effectively transmitted through the instrument. A Mezei-type flipper (not used for the non-spin-flip measurements) is a rectangular coil that produces a well defined horizontal magnetic field, and when calibrated for the correct neutron λ it rotates neutron spin polarisation by π radians with respect to the guide field. A set of three orthogonal field coils around the sample position rotate the beam polarisation in the X, Y or Z directions, and thus define the incident neutron spin polarisation. It should be noted that the X, Y and Z polarisation directions are fixed with respect to the instrument, and only the Z polarisation direction is parallel and perpendicular to the wavevector **Q**. The Schärpf angle α, discussed in Section 3.3.3, is then the angle between **Q** and the X polarisation axis. The neutrons scattered by the sample are analysed by more supermirror benders that are situated in front of an array of 132 ^{3}He detectors arranged in three banks, which can be moved around, and these allows D7 to cover a significant angular range of $4° < 2\theta < 145°$. The sample space to detector/supermirror analyser banks is encased in a vacuum box to reduce air scattering, and a schematic of the instrument layout is shown in Fig. 4.10. By measuring the amount of neutrons that have been spin-flipped (SF) and non-spin-flipped (NSF) by the sample for the three separate coordinate axes (*i.e.* six separate measurements) it is possible to carry out a full *XYZ* polarisation analysis to isolate the coherent nuclear, incoherent nuclear, spin

incoherent and magnetic contributions to the scattering.

Before each experiment, several calibration measurements have to be performed. A vanadium standard is used for normalising the detector efficiency (and analyser transmission) of the instrument because it is a purely incoherent (isotropic) scatterer. Vanadium calibration also allows the intensity to be converted to absolute units. A quartz (amorphous silica) standard was used for normalising the polarisation efficiency because its scattering is perfectly coherent, and hence any scattering in the SF channel will arise from non perfect polarisation. An empty sample holder must also be run in order to determine the background. Scans with the sample are performed by rotating the crystal about the vertical axis, typically in steps of $1°$. The reciprocal space maps are then constructed in the usual manner using standard D7 data reduction functions [95].

For the single crystal $SrHo_2O_4$ experiments carried out on D7, 0.9 g samples of $SrHo_2O_4$ (one for the $(hk0)$ and one for the $(h0l)$ scattering planes) were aligned using the backscattering x-ray Laue technique and cut perpendicular to the principal crystal axes, within an estimated accuracy of $2°$. The samples were fixed to oxygen free copper sample holders using Kwikfill resin, and equivalent sample mountings used for background measurements. Cold neutrons monochromated to a wavelength of 3.1 Å were used in order to look at the magnetic reflections at the lowest scattering angles, resulting in Q-space coverage of 0.14 to 3.91 Å^{-1}. The polarisation ratio was found to be 0.95 for the zero-field diffraction experiments, and 0.85 for the experiment with a cryomagnet. During the experiments, the samples were rotated in steps of $1°$, and different detector positions, separated by $4.5°$ were used (to cover the "dead" angles between the detector banks). The $SrHo_2O_4$ experiments required dilution fridge temperatures, and $360°$ planes were measured at 0.055, 0.75 and 4.5 K in zero field. For the zero-field experiment, six measurements required to carry out full *XYZ* polarisation analysis were performed at each temperature for both sample orientations, and 36 hours were required to measure each plane at each temperature with good statistics. For the in field measurements, $360°$ planes were also measured in fields of 0.1, 0.6, 0.8, 1.2 and 2.0 T at the lowest reached temperature of 0.15 K. With the cryomagnet, only the Z polarisation SF and Z NSF cross-sections can be collected, because the large magnet severely depolarises the neutron beam.

Figure 4.11: Schematic of the D10 instrument at a thermal neutron guide at ILL, France. This figure made with reference to the D10 page in [89].

4.3.5   4-circle diffraction: D10, ILL

D10 [89] is a high-flux single-crystal diffractometer located on a thermal neutron guide at the Institute Laue-Langevin in Grenoble, France. Exceptionally good **Q** resolution and low background make this instrument very useful for careful studies of both nuclear and magnetic scattring from small single crystal samples. Additionally, the optional energy analysis mode allows to restrict the incident neutron energy range and an even greater reduction in the background is achieved, which is useful when investigating diffuse scattering. Four different configurations of the instrument are possible, and these are standard four-circle, standard two-axis, four-circle with energy analysis and two-axis with energy analysis. For the experiment performed on $SrHo_2O_4$, D10 was used in the four-circle dilution refrigerator mode and in four-circle with energy analysis mode to collect precise neutron scattering data.

Many incident energies may be selected on D10, and for the $SrHo_2O_4$ experiment a vertically focusing pyrolytic graphite (002) monochromator that gave an incident wavelength of 2.36 Å was chosen. The half-wavelength contamination was suppressed by a PG filter. For the $SrHo_2O_4$ measurements, single crystal samples of $SrHo_2O_4$ (weighing 0.3 g and 0.1 g) were fixed to oxygen free copper pins using Stycast resin. The sample pins are attached to the Eulerian cradle (which allows for three separate axes of rotation for the crystal) inside a helium flow cryostat with the dilution option to allow scanning along all reciprocal lattice directions at low temperature. Measurements on $SrHo_2O_4$ were made in the temperature range 0.15 to 10 K. Air cushions underneath the sample and the analyser tables allow them to move indepentently. In the diffraction configuration of D10 the detector rotates around the sample position, and two different detectors can be used - a 80×80 mm microstrip detector and a single ^{3}He detector. The out of plane coverage on D10 can be increased by inclining the detector by up to $30°$. In order to create an orientation (UB) matrix using the positions of the nuclear reflections from the sample, the detector is placed at a value of 2θ which satisfies the Bragg condition for a reflection from (hkl), and then rotating the crystal while measuring the scattered intensity. Once several strong reflections are measured, the UB matrix may be found and hence the sample can be easily moved to any required position in Q. For the $SrHo_2O_4$ experiment an analyser was used to give improved resolution and suppressed background for some of the measurements. The two-dimensional area detector was used for all the measurements except for those made with the energy analyser, where the single ^{3}He detector was used instead. The basic layout and the main features of the D10 instrument are shown in Fig. 4.11.

D10 is controlled via a command lines from a computer. The data analysis includes the usual routines for integrating Bragg reflections, fitting peak profiles and plotting the scattering profiles. From the data collected during the $SrHo_2O_4$ experiment, the integrated intensity of the magnetic diffuse scattering around the nuclear Bragg peaks was extracted in the usual manner [96]. However, the plane like diffuse scattering features often had a broad intensity profile which covered a large proportion of the two-dimensional D10 detector. This meant that the selection of the integration box for these features required a compromise between getting adequate resolution and the correct representation of the diffuse scattering
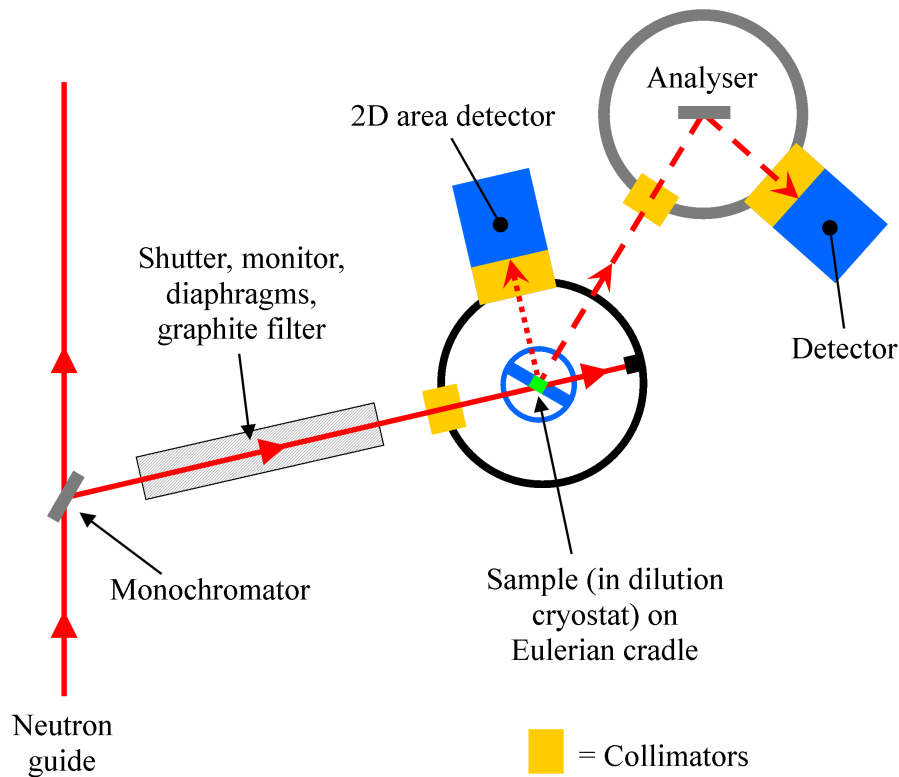
Figure 4.12: Schematic of the IN4 instrument at a thermal neutron guide at ILL, France. This figure made with reference to the IN4 page in [89].

profile.

4.4 Neutron spectroscopy

The theory of the CEF and inelastic neutron scattering were presented in sections 2.1.3 and 3.3.4 respectively. The time-of-flight inelastic neutron scattering instruments, IN4 and IN5, that have been used to to investigate the magnetic excitations in powder samples of $SrHo_2O_4$ will be discussed below.

4.4.1 Time-of-flight, powder spectroscopy: IN4 and IN5, ILL

IN4 [89, 97] is a TOF spectrometer located at the Institute Laue-Langevin in Grenoble, France, that is used to study excitations in the thermal neutron energy range of 10 to 100 meV. The instrument is designed to have a high flux and signal-to-noise ratio with good resolution, by using improved focussing optics, background suppression by the chop-

per system and a large area detector respectively. A diagram emphasising the main elements of IN4 is shown in Fig. 4.12, and will be described below.

On IN4, the incoming neutron beam first passes through an Al shield, that protects the beam tube, and this shield is one of the main losses of flux for the instrument. After the shield, two background choppers act as a low-bandpass filter, and eliminate the fast neutrons and gamma rays that give rise to noisy spectra. A large area (440 cm^2) double-curvature monochromator is used to select a specific incident neutron energy and focus the beam and thus give a high incident flux at the sample position. The variable curvature of the monochromator in both the horizontal and vertical planes allows to trade intensity for resolution by using variable take-off angles and a time focussing technique. The monochromator assembly allows for four separate crystals, PG(002), PG(004), Cu(111) and Cu(220), to be used for a selection of incident wavelengths. For the SrHo$_2$O$_4$ experiment, both the Cu and PG monochromators on IN4 were used to get wavelengths of 1.1, 1.5, 2.2 and 3.4 Å. The best energy resolution is obtained at the longer wavelengths, with minimum $\Delta E_i/E_i \approx 2\%$. A Fermi chopper transforms the incident beam into a set of short pulses required for the TOF technique. Varying the speed of this chopper changes the time resolution.

Standard sample environment options are available on IN4, and a radial collimator is used to minimise the scattering from this equipment. The instrument has a large detector bank made up of 300 ^{3}He detector tubes which cover 120° in 2θ, and an additional ^{3}He multidetector is used to observe forward scattering. The sample to detector space is kept under vacuum to avoid air scattering. The recorded TOF spectra are used to obtain the $S(Q, \omega)$ scattering function of the sample using the standard IN4 data reduction techniques in the LAMP software [98]. Standard calibrations to vanadium and empty cells are be performed, and a measurement of a phonon blank for a magnetic system (in order to separate out the dynamic lattice contribution to the scattering) is also usually carried out. During the SrHo$_2$O$_4$ experiment, SrLu$_2$O$_4$ was used as the non-magnetic analogue. Thus, information can be obtained from the energy dependent scattering measured on IN4, and particularly the crystal field excitations of magnetic systems.

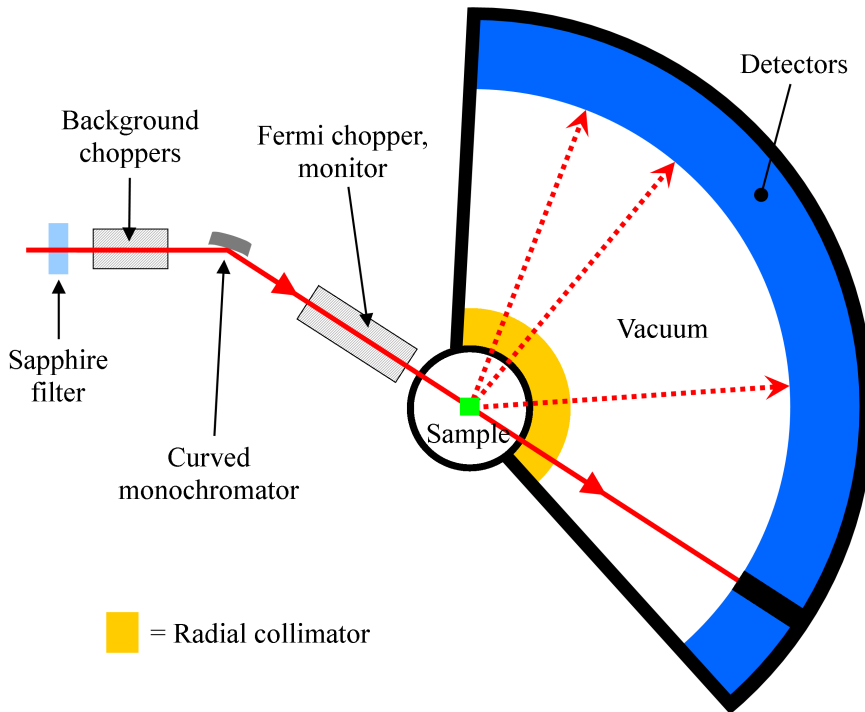IN5 [89, 99, 100] is a high precision TOF spectrometer located at the ILL, that is
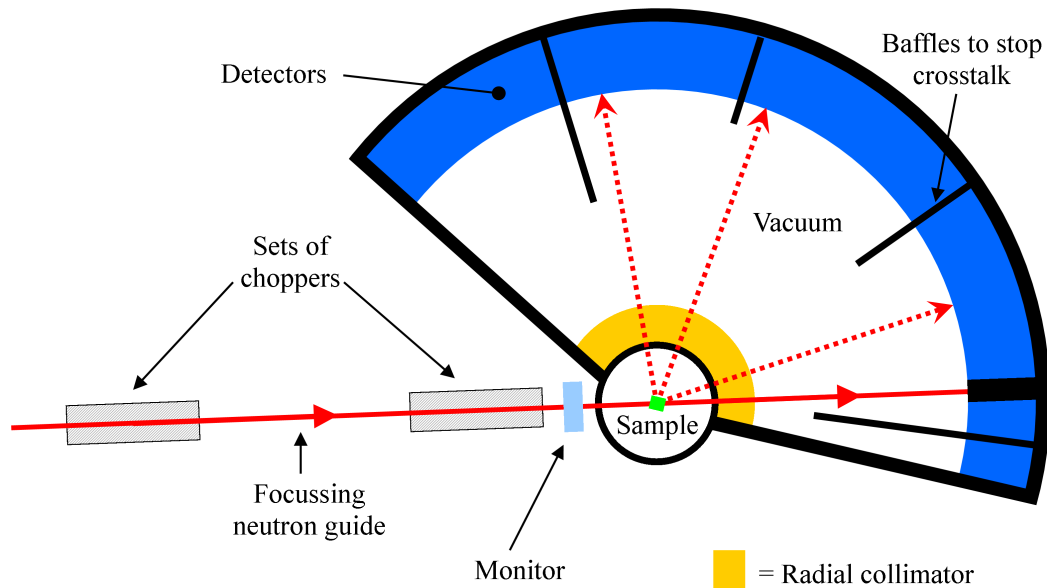
Figure 4.13: Schematic of the IN5 instrument at a thermal neutron guide at ILL, France. This figure made with reference to the IN5 page in [89].

also used to study excitations in the cold neutron energy range of 0.1 to 100 meV. IN5 is a direct geometry instrument that has a flexible wavelength and chopper speed selection to measure a large range of energy and momentum transfers, with $\sim 1\%$ for the best energy resolution. IN5 has a high flux due to focussing the source beam on the sample position, and its good resolution is due to a short neutron pulse time and a long neutron guide. A diagram emphasising the main elements of IN5 is shown in Fig. 4.13. On IN5, the incident neutron beam passes through several sets of choppers situated inside a vertically focusing neutron guide. The guide is made out of both nickel and supermirriors, to achieve a large neutron flux at the sample position. One chopper is used to remove frame overlap, another to remove background contamination, and two sets of counter-rotating choppers are used for making TOF pulses and monochromating the pulses. To achieve the best energy resolution, both the TOF and monochromating choppers have to have fast chopping speeds (fastest speed available are close to 17000 rpm), and to be separated as far as practicably possible (8 m on IN5). The elastic line resolution remains nearly gaussian as it is well defined by the chopper system at short wavelengths (highest chopper speeds). At longer wavelengths it tends to be dominated by the uncertainties in the flightpaths of the neutrons scattered by the sample.

Wavelengths of 3.4, 5.0 and 8.0 Å were used during the experiment on a powder sample of $SrHo_2O_4$.

The sample space of IN5 is large and can accommodate a wide range of cryostats and magnets. For the $SrHo_2O_4$ experiment, a dilution fridge was used to achieve a base temperature of ~ 100 mK. The scattered neutrons pass through a radial collimator, before travelling through a vacuum chamber to the detectors on IN5. These detectors consist of a cylindrical array of 384 position sensitive ^{3}He tubes that cover an angular range of $-11.5° < 2\theta < 140°$. The detectors continuously cover a very large area (30 m^2) with very good spacial resolution. The detector height allows to measure out of the horizontal scattering plane, and this can be useful for single crystal measurements. The post data collection processing allows to bin the detectors into Debye-Scherrer cones for powder samples, and standard IN5 data reduction functions in the LAMP software can subsequently be used.

The inelastic scattering results for powder samples of $SrHo_2O_4$, from data collected using both the IN4 and IN5 spectrometers, are presented in Section 5.5.

Chapter 5

Magnetic properties of SrHo$_2$O$_4$

This chapter is devoted to the study of the magnetic properties of the frustrated antiferro-magnet SrHo$_2$O$_4$, in both its polycrystalline and single crystal form. An introduction to the SrLn_2O$_4$ (where Ln = Lanthanide) family of compounds was given in Section 2.3, and as discussed previously, their crystallographic structure has been known for some time [44]. The compounds crystallise in the form of calcium ferrite [45] (space group *Pnam*) which allows the magnetic Ln ions to be linked in a network of triangles and hexagons (see Section 2.3.1). The positions of the magnetic ions in SrHo$_2$O$_4$ are shown in Fig. 5.1, with two crystallographically inequivalent sites of the rare earth ions shown in red and blue. For all the SrLn_2O$_4$ systems the magnetic ions form zigzag chains that run along the c axis. These triangular ladders can be frustrated if the dominant exchange is antiferromagnetic. The ladders are magnetically equivalent to one-dimensional chains with first- and second-nearest-neighbour interactions.

The magnetic properties of this family of compounds, however, have only recently begun to be investigated. Karunadasa *et al.* [43] reported on the bulk property measurements of magnetic susceptibility and magnetisation, and some neutron diffraction results for several powder samples of the SrLn_2O$_4$ materials. The main results of their investigation into the magnetic susceptibility of SrLn_2O$_4$ compounds suggest that even in the presence of strong exchange interactions (assessed by noting the large values for the Curie-Weiss constants), no features indicating the transition to long range order could be detected for any of the compounds down to 1.8 K. Such anomalous behaviour is usually a sign of frustration,
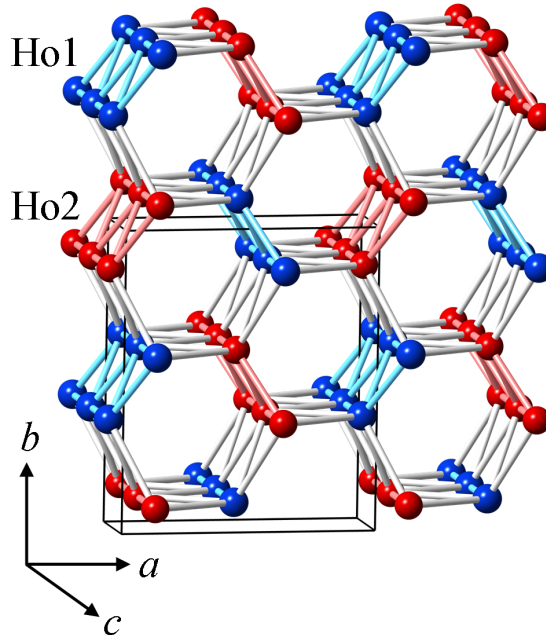
Figure 5.1: The positions of the magnetic ions in SrHo$_2$O$_4$, with the two crystallographically inequivalent positions of the rare earth ions shown in different colors. When viewed in the a-b plane, honeycombs of the Ho^{3+} ions are visible. Zigzag chains running along the c axis connect the honeycomb layers and give rise to geometric frustration. The box indicates the dimensions of the unit cell.

as discussed in Section 2.2, and this could lead the SrLn_2O$_4$ materials to show a variety of unusual magnetic properties. Currently, three of the members of the SrLn_2O$_4$ series of compounds have been investigated in detail: SrEr$_2$O$_4$, SrDy$_2$O$_4$ and SrYb$_2$O$_4$; and a short introduction to their magnetic phases was given in Section 2.3.2.

The research into the magnetic properties of SrHo$_2$O$_4$ presented in this thesis began with the extension of the earlier work by [43]. Initially, high quality powder samples of SrHo$_2$O$_4$ were prepared, and the susceptibility and magnetisation in an extended range of temperatures were measured. These experiments gave an indication that in this compound some kind of ordering transition takes place at $T = 0.7$ K. Powder neutron diffraction experiments, conducted at dilution refrigerator temperatures, subsequently allowed for the solution of the low temperature magnetic structure of SrHo$_2$O$_4$ which forms below 0.7 K. The powder neutron scattering data had also revealed the coexistence of two magnetic phases in this material: an ordered commensurate phase and a short-range ordered, low-dimensional

phase which persists at temperatures much higher than 0.7 K.

The first large single crystal of $SrHo_2O_4$ was grown prior to the start of my PhD, and the details have been published in [57]. The magnetic susceptibility was measured along each of the principal axes of $SrHo_2O_4$ in different applied fields down to 0.5 K, and a magnetic ordering transition was observed at 0.62 K. Magnetisation curves have revealed a variety of field-induced phase transitions at low temperatures for $SrHo_2O_4$. A magnetisation plateau at approximately one third of the saturation value can be seen when the field is applied along the b axis of $SrHo_2O_4$, and this is usually indicative of the stabilisation of a collinear two-spins-up one-spin-down (uud) structure. Specific heat measurements have been used to further characterise the $SrHo_2O_4$ crystal, but their usefulness is limited as the low temperature magnetism is completely masked by the huge nuclear Schottky contribution. Overall, the bulk property measurements on single crystal sample of $SrHo_2O_4$ point towards a rich $\mu_0 H - T$ phase diagram for this material.

In order to further investigate the magnetic phase diagram of $SrHo_2O_4$ and to determine the nature of the low-dimensional diffuse scattering seen in the powder neutron diffraction data, several single crystal neutron diffraction experiments using both polarised and unpolarised neutrons have been conducted on $SrHo_2O_4$. The most unusual finding is that for the single crystal samples of $SrHo_2O_4$ no long-range order was found down to 0.05 K. Instead, at low-temperature there appears to be two distinct types of short-range magnetic order (which can be inferred from single crystal diffraction data) coexisting in this material, which has no chemical instability or phase separation. The highly unusual coexistence of the two types of diffuse scattering in $SrHo_2O_4$ is likely to be the result of the presence of two crystallographically inequivalent sites for Ho^{3+} in the unit cell. In the $(hk0)$ plane the diffuse scattering is most noticeable around the $\mathbf{k} = 0$ positions and its intensity rapidly increases at temperatures below 0.7 K. In addition, planes of diffuse scattering at $Q = (hk \pm \frac{l}{2})$ are visible at temperatures as high as 4.5 K. These planes coexist with the broad peaks of diffuse scattering in the $(hk0)$ plane at low temperatures. Both types of diffuse scattering are strongly correlated, with the associated correlation lengths of several hundreds of Å, and appear to be elastic in nature.

The diffraction measurements were repeated in an applied field, and the findings

can be correlated with the single crystal magnetisation data. When the field is applied along the c axis, only one transition was expected, and the diffuse scattering around the $\mathbf{k} = 0$ positions seen in zero field is suppressed, and even larger fields induce the system to long-range order. At low temperature, when the field is applied along the b axis where the magnetisation plateau appears, the planes of one-dimensional scattering are split into a new diffuse phase for a range of values of the applied field. Eventually, as the field strength is increased further, this diffuse phase is also suppressed and new Bragg peaks appear in the diffraction pattern.

In order to better understand the highly anisotropic behaviour of $SrHo_2O_4$, a series of measurements of the crystalline electric field have been recently completed. The data and the initial analysis are presented, and the unusual behaviour of the CEF levels is discussed. Fitting the crystal field for this compound is quite challenging, and this is currently underway. The results of the research into the magnetic behaviour of $SrHo_2O_4$ will be described in detail in the rest of this chapter, the final section of which is devoted to conclusions and a careful comparison of the magnetic properties of $SrHo_2O_4$ with that of the other members of the SrLn_2O_4 family.

5.1 Polycrystalline SrHo$_2$O$_4$

As discussed in Section 2.3.1, the crystallographic structure of the SrLn_2O_4 compounds was well established a long time ago [44]. The polycrystalline $SrHo_2O_4$ samples, used for all subsequent measurements, were prepared from high purity starting compounds as described in Section 4.1.1. The x-ray diffraction data were collected at 300 K using the process discussed in Section 4.1.2. The purity of the $SrHo_2O_4$ powder was checked by performing a Rietveld refinement (see Section 4.1.3) using x-ray diffraction data, and the TopasRuns software [75] was used to fit the data.

An example dataset for $SrHo_2O_4$, as well as its fit from the refined model and the difference plot are shown in Fig. 5.2. The space group is *Pnam* and the unit cell parameters were found to be $a = 10.06798(6)$ Å, $b = 11.91296(7)$ Å, and $c = 3.40923(2)$ Å, with $\alpha = \beta = \gamma = 90°$. These unit cell parameters, as well as the atomic position parameters are
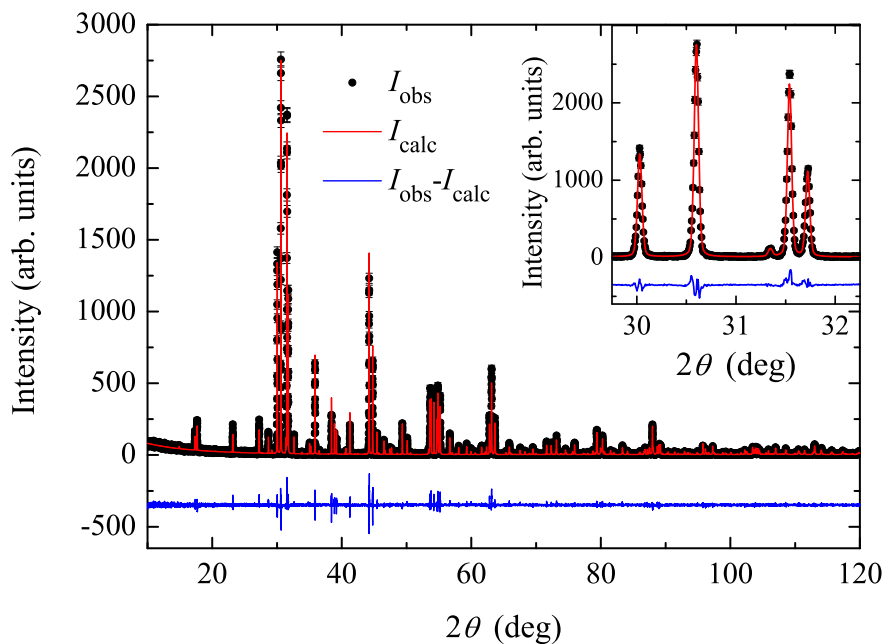
Figure 5.2: X-ray diffraction data collected at 300 K (I_{obs}), Rietveld refined model (I_{calc}), and the difference ($I_{\mathrm{obs}} - I_{\mathrm{calc}}$) plot for a powder sample of $SrHo_2O_4$. Inset: A smaller data range to show the largest crystallographic peaks in the $SrHo_2O_4$ spectrum. The data were collected and analysed as described in Sections 4.1.2 and 4.1.3. The fit parameters are $\chi^2 = 1.291$, $R_{\mathrm{P}} = 16.61\%$ and $R_{\mathrm{WP}} = 21.29\%$.

very close to those published in [43]. The final purity of $SrHo_2O_4$ was found to be 99.5%, and a small impurity phase of 0.5% was found to be the starting compound Ho_2O_3. The fit parameters are $\chi^2 = 1.291$, $R_{\mathrm{P}} = 16.61\%$ and $R_{\mathrm{WP}} = 21.29\%$. The large R factors are probably not the result of a particularly poor model, but from having very high quality and very low background data, which tends make imperfections more obvious, thus giving rather large discrepancy indices. For a discussion of this low background effect on the R factors in Rietveld analysis, please see [101], and especially Fig. 1 therein.

5.1.1 Bulk properties

Karunadasa, *et al.* [43] were the first to investigate the magnetic properties of powder samples of the SrLn_2O_4 compounds, with Ln = Gd, Dy, Ho, Er, Tm, and Yb. For $SrHo_2O_4$, they reported a large difference between the Curie-Weiss temperature, $\theta_{\mathrm{CW}} = -16.9(5)$ K, and
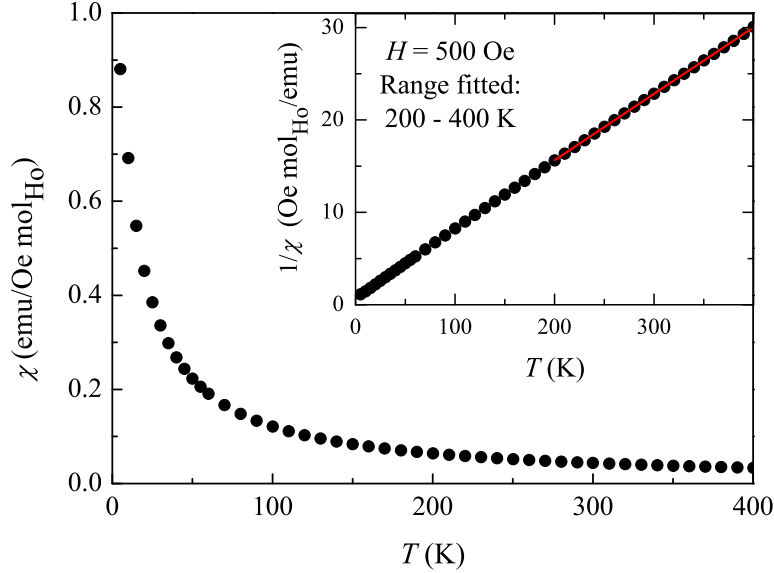
Figure 5.3: High temperature magnetic susceptibility for a powder sample of $SrHo_2O_4$. Inset: The inverse susceptibility as a function of temperature, and the fit to the data between 200 - 400 K (red line). From the fit, the effective moment is calculated to be $\mu_{\text{eff}} = 10.54(2)\ \mu_B$, and the Curie-Weiss constant is $\theta_{\text{CW}} = -17.2(4)$ K.

the lack of any indications of phase transitions in the magnetic susceptibility down to 1.8 K. To compare to published data in [43], the high temperature magnetic susceptibility versus temperature was measured in 500 Oe for a 10.3 mg polycrystalline sample of $SrHo_2O_4$ using a SQUID magnetometer (see Section 4.2.1), and the data is shown in Fig. 5.3. The high temperature dependence of the inverse susceptibility is presented in the inset of Fig. 5.3. In the high temperature range, where the $1/\chi(T)$ curves follow a paramagnetic Curie-Weiss behaviour, the data are fitted with least-squares regression lines, in the temperature range

	μ_{eff} (μ_{B})	θ_{CW} (K)
From Ref. [43]	10.50(1)	$-16.9(5)$
From Fig. 5.3	10.54(2)	$-17.2(4)$
Hund's Rules [3]	10.60	

Table 5.1: The μ_{eff} and θ_{CW} parameters of powder $SrHo_2O_4$ and a comparison to the published data and the Hund's rules prediction for a Ho^{3+} ion.
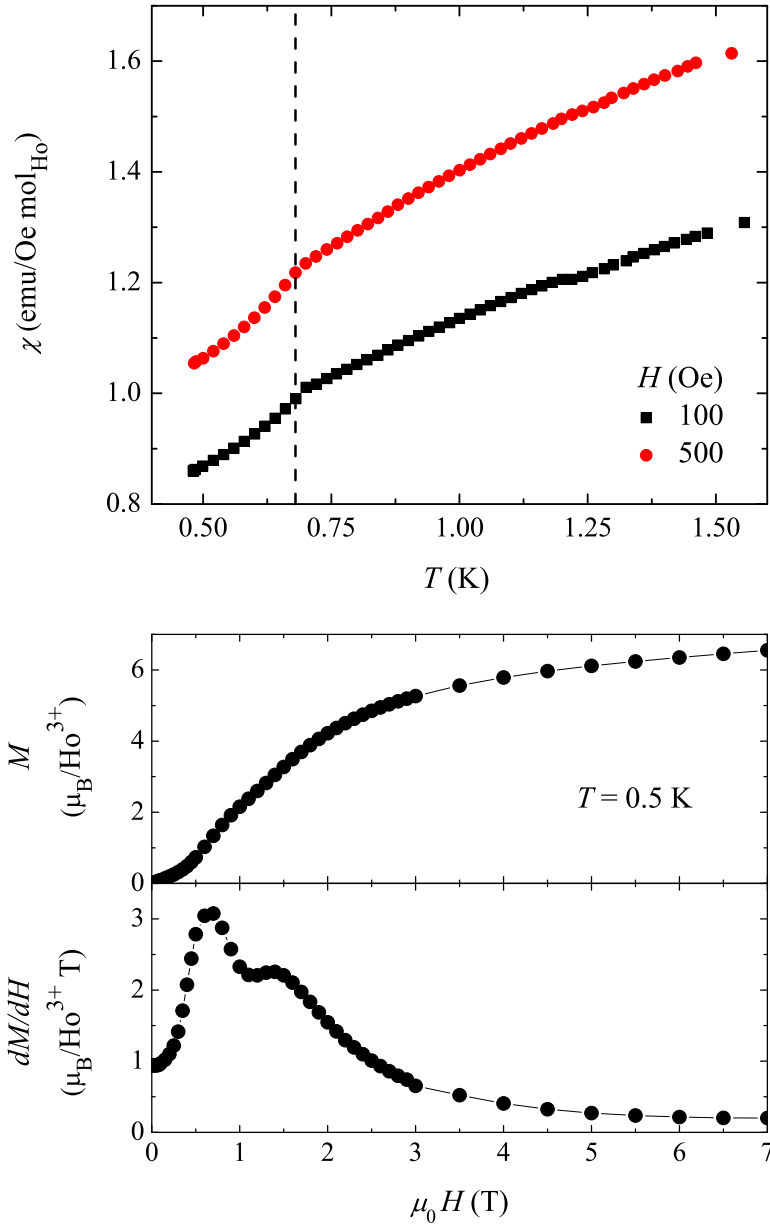
Figure 5.4: (Top) Magnetic susceptibility measured in 100 and 500 Oe for a powder sample of $SrHo_2O_4$. The dashed line indicates 0.7 K, the temperature at which a cusp is observed in the susceptibility, which suggests at the presence of a phase transition at this temperature. (Bottom) Field dependent magnetisation and the derivative of magnetisation with respect to the applied field at 0.5 K for a powder sample of $SrHo_2O_4$. The data is comparable to that shown in [43] which was recorded at 1.8 K, with the only difference being that the double peak in dM/dH is much more pronounced at the lower temperature.

of 200 to 400 K. The parameters of this fit, the Curie-Weiss constant and the calculated effective moment per Ho^{3+} ion (see Section 2.1.5), are given in Table 5.1, and the values obtained by Karunadasa, *et al.* [43] are also listed for comparison.

The measurements in [43] were limited in temperature to 1.8 K, the base of the SQUID magnetometer. So to extend the measurable temperature range down to 0.5 K, a ^{3}He insert (see Section 4.2.1) was used. In the low temperature magnetic susceptibility measurements on powder $SrHo_2O_4$, shown in the top panel of Fig. 5.4, a cusp can be seen at 0.7 K, and this suggests the presence of a phase transition. This points to a moderately large frustration parameter of 24.5 for this compound. Usually, specific heat measurements can be made to confirm the presence of phase transitions, but measurements on the powder samples of $SrHo_2O_4$ (not shown) indicated that below $\sim$1.5 K the heat capacity is dominated by the nuclear contribution which completely masks the magnetic signal.

The field dependent magnetisation $M(H)$ and its derivative dM/dH at 0.5 K are shown in the bottom panel of Fig. 5.4. The double peak in dM/dH is much more pronounced at this temperature than in the data published for $SrHo_2O_4$ in [43], which was recorded at 1.8 K. No complete saturation of magnetisation is observed, as the dM/dH values remain nonzero even at 7 T. This implies that the spins are still not fully aligned at this field, and the observed value of magnetisation remains much lower than expected from Hunds rules predictions for Ho^{3+} ions [3].

5.1.2 GEM neutron diffraction measurements

The GEM instrument, which was described in Section 4.3.2, was used to collect neutron scattering data on a powder sample of $SrHo_2O_4$ in a range of temperatures from 0.045 to 10 K. The $SrHo_2O_4$ sample weighed 3.53 g, and was compressed into a Cu cylinder (which had 3.5 cm usable length, 0.6 cm diameter) to aid thermal conductivity at low temperatures. Longer counting times were used to collect data at the base temperature of the dilution cryostat, temperatures around 0.7 K (where a cusp was observed in magnetic susceptibility measurements) and for the 10 K background runs.

Fig. 5.5 shows the magnetic scattering in GEM bank 2 for five neutron diffraction patterns from $SrHo_2O_4$ collected in the temperature range 0.25 to 1.42 K. The mag-
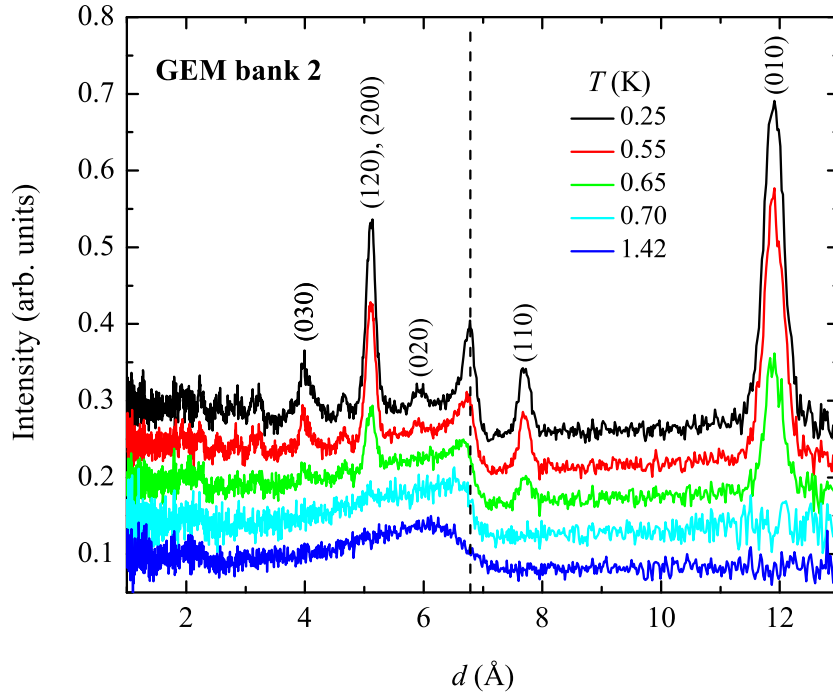
Figure 5.5: Temperature evolution of the magnetic scattering of SrHo$_2$O$_4$ (curves have been offset for clarity). The magnetic diffraction pattern is isolated by subtracting a 10 K background from the low temperature runs. Below 0.7 K resolution-limited **k** = 0 peaks can be seen indicating the presence of long-range order. Some of the largest magnetic reflections have been indexed for clarity. At all temperatures short-range correlations around $d \approx 6.8$ Å (denoted by the dashed line) are also observed. The magnetic peak due to these short-range correlations gets sharper upon decreasing the temperature.

netic scattering was isolated by subtracting a 10 K background from the data collected at the lower temperatures. Resolution limited peaks, which were assessed by comparing the FWHM of these peaks with that of the nuclear reflections at appropriate Q, begin to appear below 0.7 K, indicating the onset of long-range order. The peaks become more intense upon lowering the temperature, but in reciprocal space their positions remain the same. The magnetic reflections are commensurate with the lattice and can be indexed with a single propagation vector **k** = 0 and thus the magnetic structure may be described within the crystallographic unit cell. Fig. 5.6 again shows the magnetic scattering in bank 2, (the data in bank 2 was chosen because it spans the appropriate range in 2θ that shows the lowest Q and
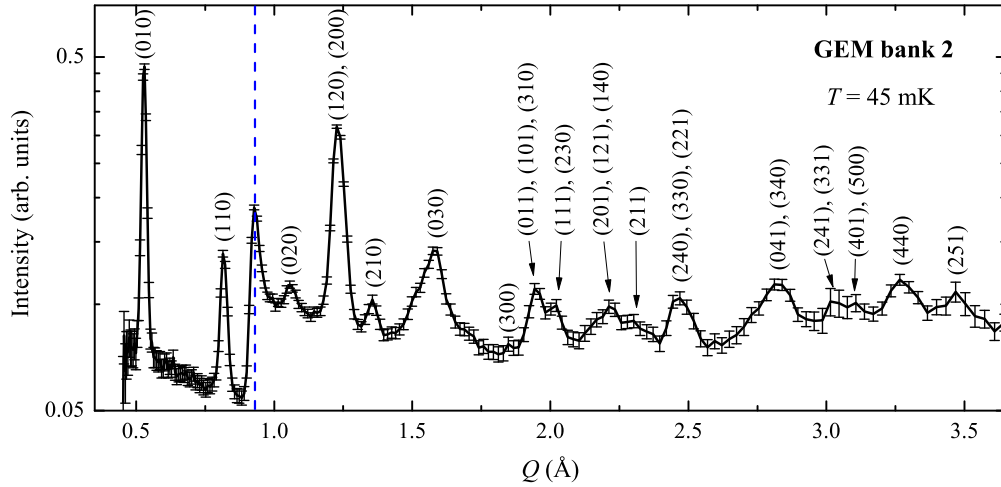
Figure 5.6: The magnetic scattering from $SrHo_2O_4$ isolated by subtracting a 10 K background from the data collected at T = 45 mK. All the peaks have been indexed for clarity. Dashed line indicates the position of $Q = (00\frac{1}{2})$.

strongest magnetic scattering) at the lowest temperature of 0.045 K and the reflections are labelled with the appropriate (hkl) indices. Temperature dependence of the integrated magnetic intensity for the two strongest magnetic peaks (010) and (120) is shown in Fig. 5.7. The **k** = 0 magnetic scattering shows second-order phase transition type behaviour.

From looking at Fig. 5.5, which shows the temperature dependence of the magnetic scattering, it is obvious that in addition to the **k** = 0 phase, there exist some broad diffuse scattering features, around $d \approx 6.8$ Å (which corresponds to $Q = (00\frac{1}{2})$), and at symmetry related positions, that persists at temperatures well above 0.7 K. Fig. 5.8, shows the diffuse scattering at T = 1.42 K and T = 5.00 K, isolated by subtracting a 10 K background from data collected at the lower temperatures. These diffuse scattering features have the characteristic powder profile of a low-dimensional magnetic structure, and hint at the development of short-range magnetic correlations in $SrHo_2O_4$. It is useful to note that the magnetic scattering shown in Fig. 5.8 is practically identical to the magnetic scattering shown in Fig. 16 in the paper by Karunadasa *et al.* [43]. There the data were obtained by subtracting the 5.05 K background from the data collected at 1.72 K, as well as looking at the broad distribution of magnetic scattering at slightly higher temperatures.

The coexistence of a low dimensional magnetic structure with a second type of
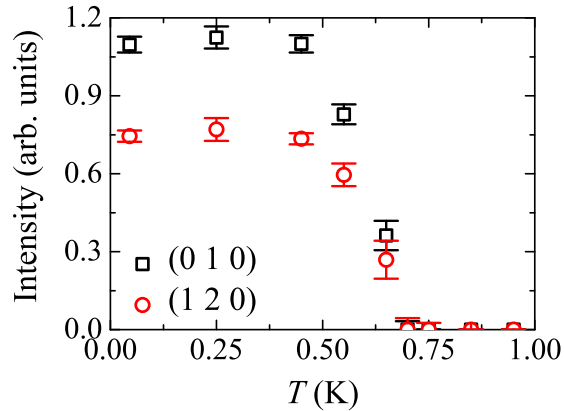
Figure 5.7: Temperature dependence of the integrated magnetic intensity of (010) and (120), the two strongest magnetic peaks in the $SrHo_2O_4$ neutron powder diffraction profile.

magnetic ordering is not confined to $SrHo_2O_4$, but is also found in the isostructural compound $SrEr_2O_4$ [63]. This coexistence of two magnetic phases well below T_N is thought to arise because one of the two crystallographically inequivalent Er^{3+} sites orders in a long-range three-dimensional structure, whereas the other Er^{3+} partially orders in a short-range magnetic phase.

5.1.3 Magnetic structure refinement

The FULLPROF software suite [79] was then employed to refine the nuclear and magnetic structure of $SrHo_2O_4$ using the neutron powder diffraction data, in collaboration with L. C. Chapon (ISIS Facility, Rutherford Appleton Laboratory). The Rietveld refinement technique was discussed in Section 4.1.3, and the first step in refinement is the indexing of the pattern, which was reported in the previous section. The initial input parameters were the $SrHo_2O_4$ space group and the unit cell dimensions which were known from the x-ray analysis at room temperature (and also given in [43]) and the Cu (sample holder) unit cell symmetry and dimensions. For the powder $SrHo_2O_4$ a model for the nuclear structure, the background and the background Bragg peaks from the Cu sample holder were then refined using data collected at 10 K, in the paramagnetic state of the material. Once the nuclear structure and the background are known, they are usually kept fixed during the magnetic part of the refinement.
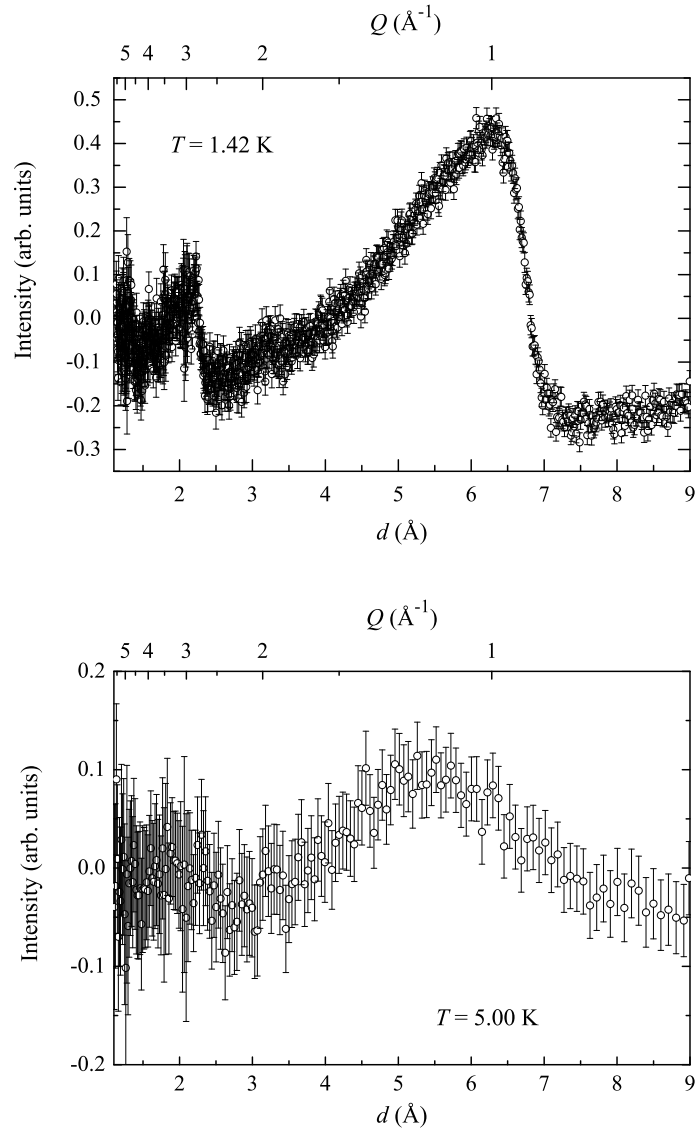
Figure 5.8: Broad peaks associated with the low dimensional magnetic scattering at (top) $T = 1.42$ K and (bottom) $T = 5.00$ K, isolated by subtracting a 10 K background from data collected at the lower temperatures. These data are comparable to that published in Fig. 16 in [43].
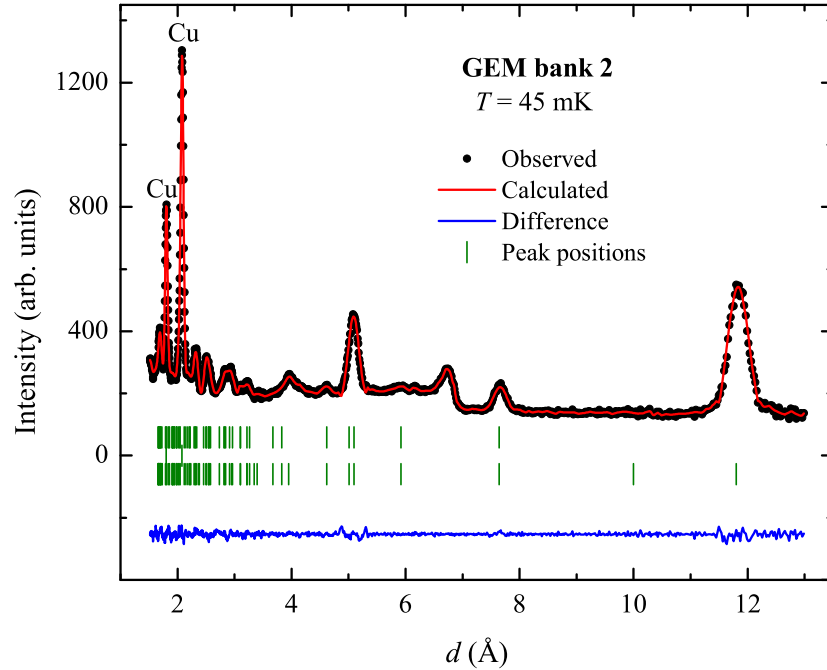
Figure 5.9: Refined model of $SrHo_2O_4$ using the powder neutron diffraction data collected in detector bank 2 on the GEM instrument at $T = 45$ mK. Data points and fit are shown in the upper curve, the difference between the observed and calculated pattern is shown in the lowest curve. Three sets of vertical tick marks (from top to bottom) correspond to the expected positions for nuclear peaks from $SrHo_2O_4$, reflections from the copper sample container and magnetic peaks from $SrHo_2O_4$ respectively. The peaks coming from the copper sample holder are labelled for clarity. The low-dimensional scattering was treated as background.

To begin the magnetic part of the refinement, the propagation vector and the symmetry of the magnetic cell must be known. For $SrHo_2O_4$, all of the magnetic peaks can be indexed with the propagation vector $\mathbf{k} = 0$, as discussed in the Section 5.1.2, and representation analysis was used to find the symmetry of the magnetic cell using the program BasIreps in the FULLPROF software suite. By putting in certain constraints, BasIreps calculates the basis functions of the irreducible representations of the propagation vector group for the magnetic unit cell, and this allows to obtain the magnetic moments on each crystallographic site occupied by magnetic atoms. During the refinement of the $SrHo_2O_4$
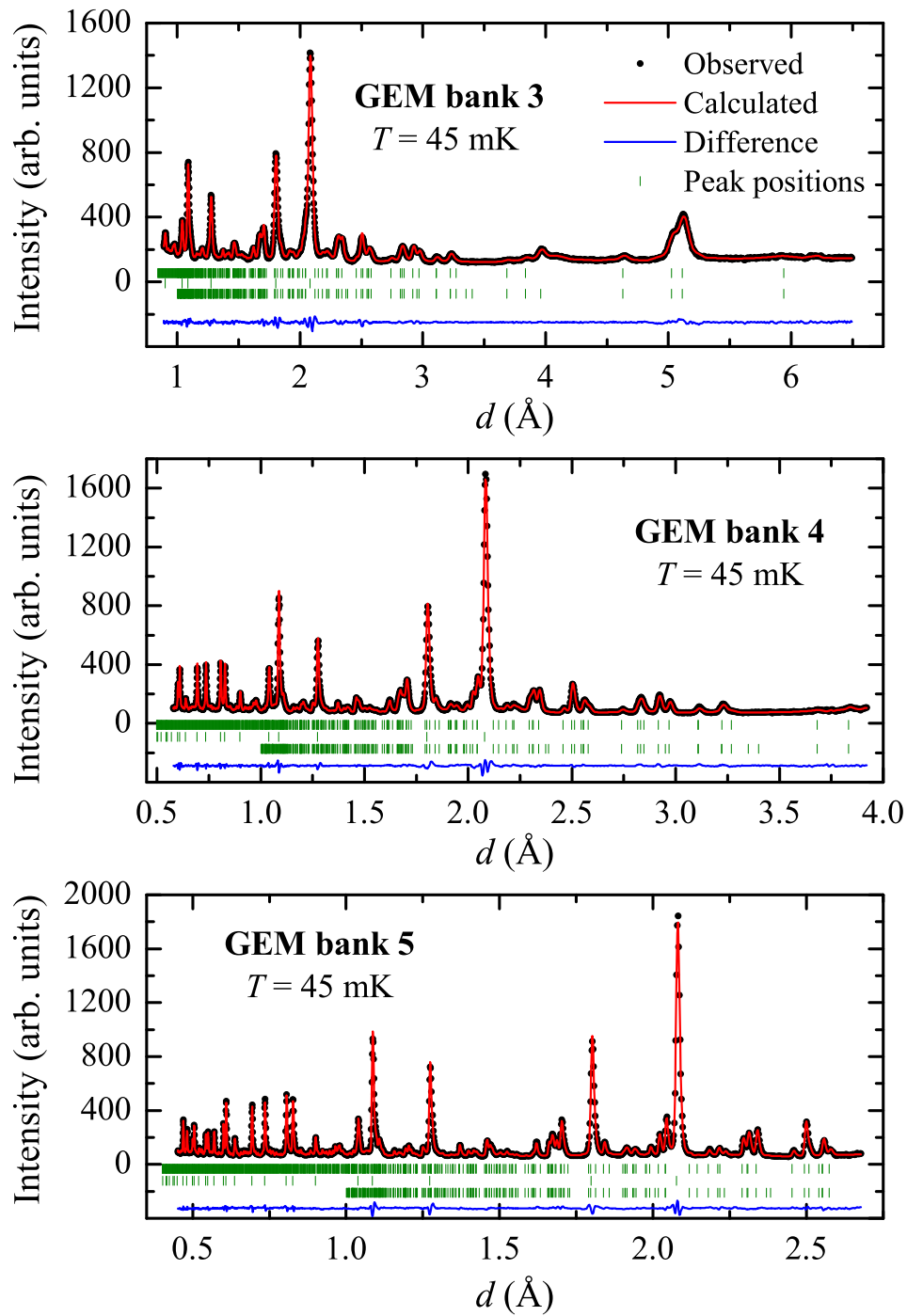
Figure 5.10: Refined model of SrHo$_2$O$_4$ using the powder neutron diffraction data collected in detector banks 3, 4, 5 on the GEM instrument at $T = 45$ mK. The large (background) Cu peaks are the least well fit.

	x	y	B_{iso}	Magnetic Moment (μ_B) only along c
Sr	0.7513(1)	0.6492(1)	0.71(3)	
Ho1	0.4222(1)	0.1122(1)	-0.20(1)	5.06(2)
Ho2	0.4215(2)	0.6104(2)	-0.20(1)	0.21(1)
O1	0.2140(4)	0.178(1)	0.46(2)	
O2	0.1284(5)	0.4795(1)	0.75(2)	
O3	0.5136(1)	0.7815(3)	0.58(1)	
O4	0.4258(2)	0.4215(2)	0.38(1)	

Table 5.2: The low temperature refined parameters for SrHo$_2$O$_4$, all of the atoms sit on $4c$ $(x, y, 0.25)$. Refinements were performed using the FULLPROF software suite.

data, all possible combinations of the symmetry operators suggested by BasIreps were tried, but only one gave a model which seemed to fit the experimental data well. (The simulated annealing method was also briefly tested to try and determine the magnetic structure of SrHo$_2$O$_4$, but did not produce any sensible results.)

The Rietveld refinement procedure can then again be used to solve the details of the magnetic structure, such as the magnitude and direction of the spin magnetic moments that give the best fit to the experimental data. The full model for the nuclear and crystal of SrHo$_2$O$_4$ (and the background) contains many parameters that have to be refined in order to get a good fit. The background, atomic positions, unit cell dimensions, scale factors, isotropic temperature corrections and the magnetic moment parameters had the most impact on the goodness of fit during the refinement analysis done using the SrHo$_2$O$_4$ data. A table of these is shown in 5.2, and the refined unit cell parameters are a = 10.048923 Å, b = 11.871435 Å and c = 3.401167 Å.

The FULLPROF refinement was performed using data collected in detector banks 2 to 5 of the GEM instrument simultaneously, since these banks gave data which had the best balance between seeing the magnetic reflections, high count rates and good Q-resolution. Fig. 5.9 shows the magnetic structure refinement of the data collected in detector bank 2 at 45 mK, since in this detector bank all of the low Q magnetic reflections from SrHo$_2$O$_4$ are visible. The diffuse scattering, seen around $Q = (00\frac{1}{2})$ was treated as part of the background in the structure refinement as the limited information from powder data does not allow for a complete solution of this component of the magnetic scattering.
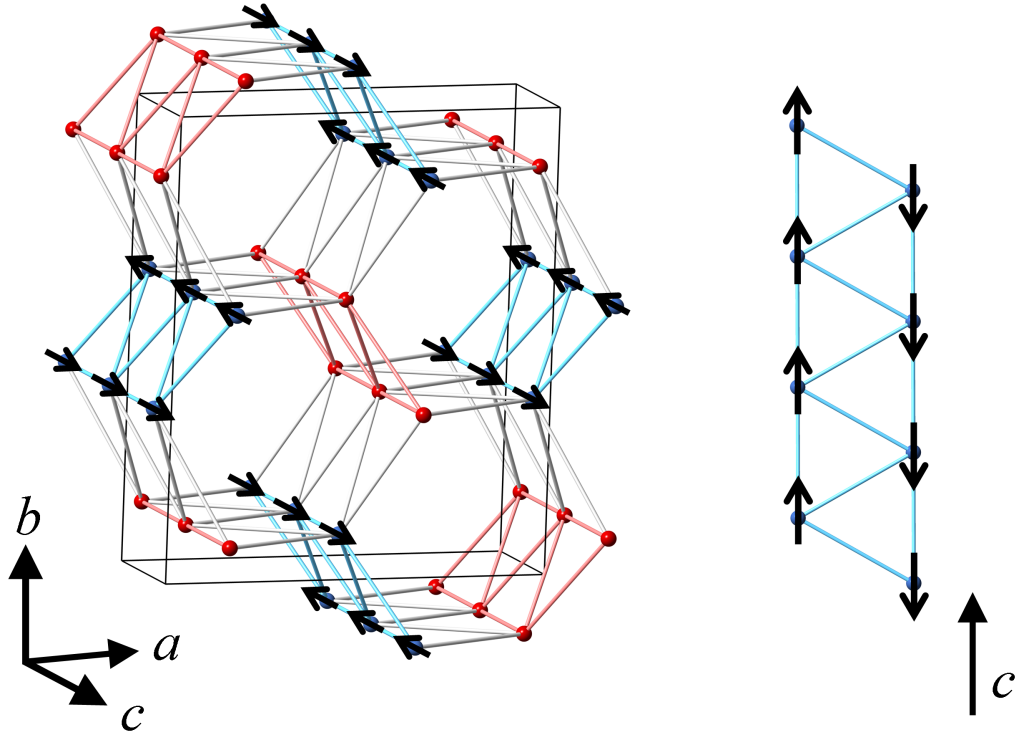
Figure 5.11: Magnetic structure of SrHo$_2$O$_4$ at T = 45 mK determined from a Rietveld refinement performed using the neutron scattering data collected on GEM (ISIS). The two crystallographically inequivalent Ho^{3+} sites are shown in different colours as only one (blue) carries a significant magnetic moment of about 5 μ_B (the second Ho^{3+} has no more than 0.2 μ_B). All of the moments point along the c axis, in ferromagnetic chains, with neighbouring chains coupled antiferromagnetically. Swapping the moments between the red and blue sites has a negligible impact on the quality of the refinement.

The agreement factors for the nuclear and magnetic phases in the detector bank 2 shown in Fig. 5.9 are R_{nuc} = 2.21% and R_{mag} = 1.32%. The data in the other banks is shown as three panels in Fig. 5.10. No adjustments had to be made for the background in these banks as the contribution from the low dimensional structure at $Q = (00\frac{3}{2})$ and higher orders was fairly small. The agreement factors for the nuclear and magnetic phases for the detector banks 3, 4, 5 are R_{nuc} = 2.21% and R_{mag} = 1.62%, R_{nuc} = 3.52% and R_{mag} = 6.48%, and R_{nuc} = 5.68% and R_{mag} = 7.71% respectively.

The proposed magnetic structure of SrHo$_2$O$_4$ that appears below 0.7 K is shown in Fig. 5.11. The moments are aligned along the c axis, since no (00l) reflections were observed. The moments are coupled ferromagnetically in chains running along the c direc-

tion, with neighbouring chains in the same ladder coupled antiferromagnetically. Only one of the crystallographically inequivalent sites of the Ho^{3+} ions carries a significant magnetic moment of ~5 μ_B, the second has no more than 0.2 μ_B. Swapping the moments between the sites in this model has a negligible impact on the quality of the refinement.

Within the refined magnetic structure there is a large difference between the values of the Ho^{3+} moments that sit on crystallographically inequivalent sites. This is probably due to the coexistence of two separate magnetic structures in this material, where only one of the sites would contribute to the $\mathbf{k} = 0$ order, and the second to the short-range ordered, low-dimensional structure that develops well above 0.7 K (the scattering from which had to be treated as part of the background during the refinement). Further zero-field neutron scattering experiments on single crystals of $SrHo_2O_4$, are discussed in Section 5.3, and these give greater insight into the nature of the low-dimensional, magnetic features inferred from the powder data.

5.2 Single crystal bulk property measurements

The $SrHo_2O_4$ single crystal samples, used for all of the bulk property measurements, were grown by the floating zone method, with details of the procedure used reported in Section 4.1.4 and in Ref. [57]. The samples were aligned along the principal crystal axes to within an estimated accuracy of 2° using the backscattering x-ray diffraction Laue technique detailed in 4.1.5. The samples were cut into thin rectangular plates (with faces perpendicular to a, b and c) that weighed ~20 mg for high temperature magnetisation and magnetic susceptibility measurements, and ~10 mg for measurements made with the ^{3}He insert. In order to minimise the effects of demagnetisation, the field was applied parallel to the longest side of the plates. Corrections to all of the single crystal data to take into account this effect were made following [84] as discussed in Section 4.2.1 and the demagnetising field was found always to be less than 5% (typically 2%) of the applied field.

The temperature dependence of the magnetic susceptibility, $\chi(T)$ in the range of 0.5 to 400 K, and the field dependence of the magnetisation, $M(H)$ in the range of 0 to 7 T, were measured using a Quantum Design SQUID magnetometer, following the procedure

	$H \parallel a$	$H \parallel b$	$H \parallel c$	Mean	Expected
$\mu_{\mathrm{eff}}(\mu_{\mathrm{B}})$	10.57(2)	10.10(4)	10.72(8)	10.45(5)	10.54(2) [powder]
θ_{CW} (K)	-72.4(5)	22.3(7)	-2(1)	-17.5(5)	-17.2(4) [powder]

Table 5.3: The μ_{eff} and θ_{CW} parameters for the field applied along the principal axes of a single crystal sample of $SrHo_2O_4$, their average values and a comparison to the data collected for a powder sample of $SrHo_2O_4$.

described in Section 4.2.1, for the fields applied along each of the principal crystallographic directions. The specific heat measurements (described in Section 4.2.2) on $SrHo_2O_4$ were made on very thin samples that weighed under 0.5 mg in zero field, and with the field applied along the c axis. The heat capacity measurements with $H \parallel c$ were made only in a limited range of fields and at higher temperatures since earlier heat capacity measurements on the powder samples of $SrHo_2O_4$ showed that below $\sim$1.5 K the magnetic signal is completely obscured by the nuclear Schottky anomaly of Ho^{3+} ions.

5.2.1 High temperature susceptibility

The magnetic susceptibility versus temperature in 1 kOe for fields applied along each of the three principal axes for a single crystal sample of $SrHo_2O_4$ is shown in in the top panel of Fig. 5.12. The high temperature dependence of the inverse susceptibility for these data are presented in the bottom panel of Fig. 5.12. In the high temperature range of 100 to 400 K, where the $1/\chi(T)$ curves follow a paramagnetic Curie-Weiss behaviour (see Section 2.1.5), the data are fitted with least-squares regression lines. The parameters of these fits, the Curie-Weiss constants, θ_{CW}, and the calculated effective moments per magnetic ion, μ_{eff}, are listed in Table 5.3. From considering Fig. 5.12 it is immediately obvious that there is a large anisotropy in the Curie-Weiss temperatures (θ_{CW} is negative along a and positive along b) for the three principal crystal directions of $SrHo_2O_4$. The large differences in the Curie-Weiss temperatures observed for the three principal crystal directions usually point to the presence of low-lying crystalline electric field (CEF) levels. The CEF levels in the $SrHo_2O_4$ system derived from inelastic neutron scattering measurements will be discussed in Section 5.5. The average value of θ_{CW}, however, is in agreement with that presented earlier in Section 5.1.1 for a polycrystalline $SrHo_2O_4$ sample. The high temperature sus-
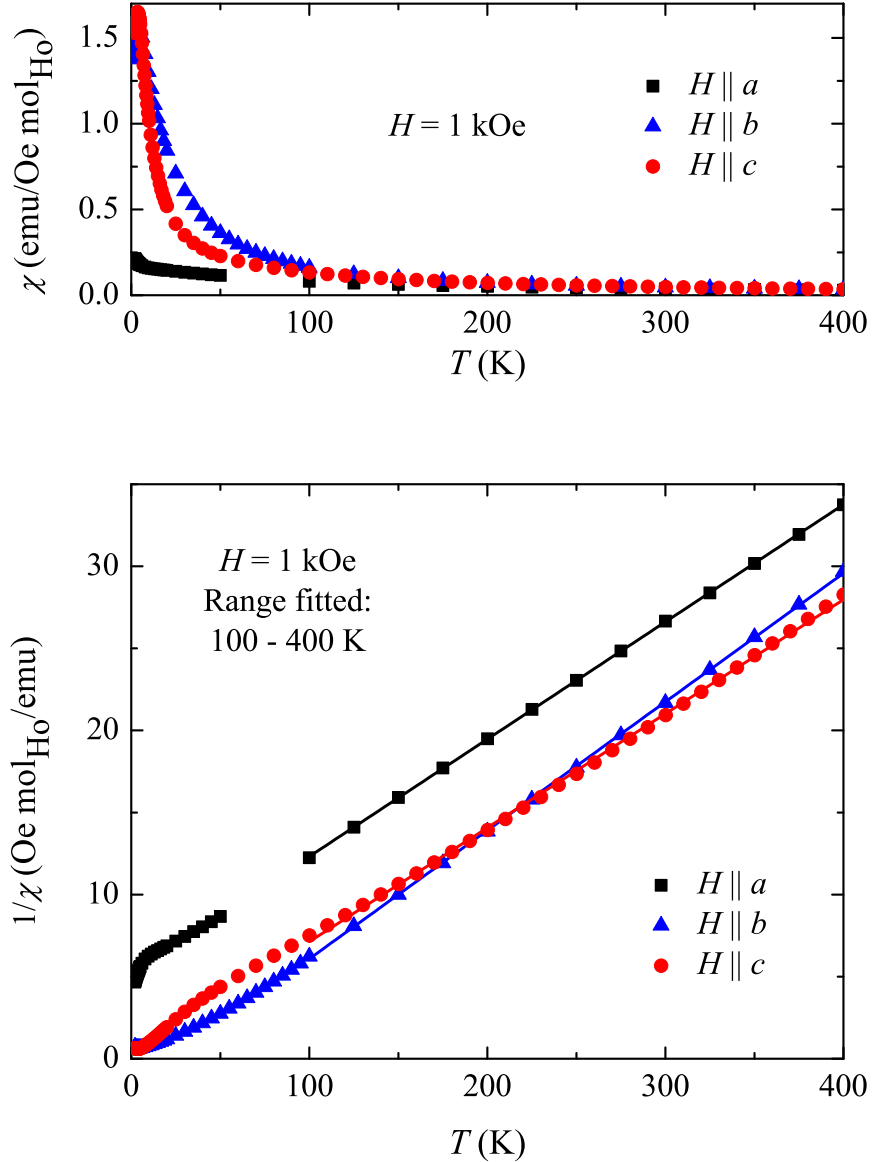
Figure 5.12: (Top) High temperature magnetic susceptibility versus temperature in an applied field of 1 kOe in the temperature range of 2 to 400 K for the field applied along the three principal axes of a single crystal sample of SrHo$_2$O$_4$. (Bottom) Reciprocal of the molar susceptibility versus temperature and the least-squares regression fits to the data (using the Curie-Weiss model). From the fits, the average effective moment is calculated to be $\mu_{\text{eff}} = 10.47(3)$ μ_B, and the average Curie-Weiss constant is $\theta_{\text{CW}} = -17.5(5)$ K, the individual values for each axes are given in Table 5.3.

ceptibility curves imply that the magnetic anisotropy in $SrHo_2O_4$ is of the hard-axis type for the entire temperature range studied, with the b and c axes being the easier directions for magnetisation.

5.2.2 Low temperature susceptibility

A summary of the main results of low-temperature susceptibility measurements on the single crystal $SrHo_2O_4$ samples is presented in Fig. 5.13 for fields of 100 Oe and 1 kOe applied along the a, b, and c directions. When a field of 100 Oe is applied along the different principal crystal axes, a cusp in the susceptibility at 0.62 K suggests the presence of a phase transition. In Section 5.1.1, a cusp was observed in the low temperature susceptibility at 0.7 K for the powder sample of $SrHo_2O_4$. Demagnetisation factor corrections make no impact on the position of the phase transition, but simply scale the data depending on $\mathbf{H_i}$, as defined in Eq. 4.4. It is possible that the difference in temperature where the cusp in $\chi(T)$ appears between the powder and the single crystal $SrHo_2O_4$ may be due to slight non-stoichiometry of the samples resulting from the crystal growth process.

In low applied fields such as 100 Oe, below the transition temperature, there is also a noticeable difference between the data obtained on warming after cooling in field (FC) and the zero-field-cooled warming (ZFC) data, (see Section 4.2.1). The observed difference is due to incomplete spin order (which is deduced from the single crystal neutron diffraction data discussed in Section 5.3.1); and thus the original partially ordered state does not recover if the field is cycled up and then down, as shown later for a couple of magnetic reflections from $SrHo_2O_4$ in Fig. 5.34. A moderate field of 1 kOe applied to $SrHo_2O_4$ suppresses the cusp in the $\chi(T)$ curves, shown in the bottom panel in Fig. 5.13. The higher-field data also appear to be almost insensitive to sample history, since there is very little difference between ZFC and FC susceptibility measurements.

5.2.3 Magnetisation

The summary of the results of the field dependent magnetisation $M(H)$ and its derivative dM/dH, with H applied along the a, b, and c axes of $SrHo_2O_4$ at 2 K and 0.5 K are shown in Fig. 5.14. These single crystal magnetisation measurements reveal the highly anisotropic
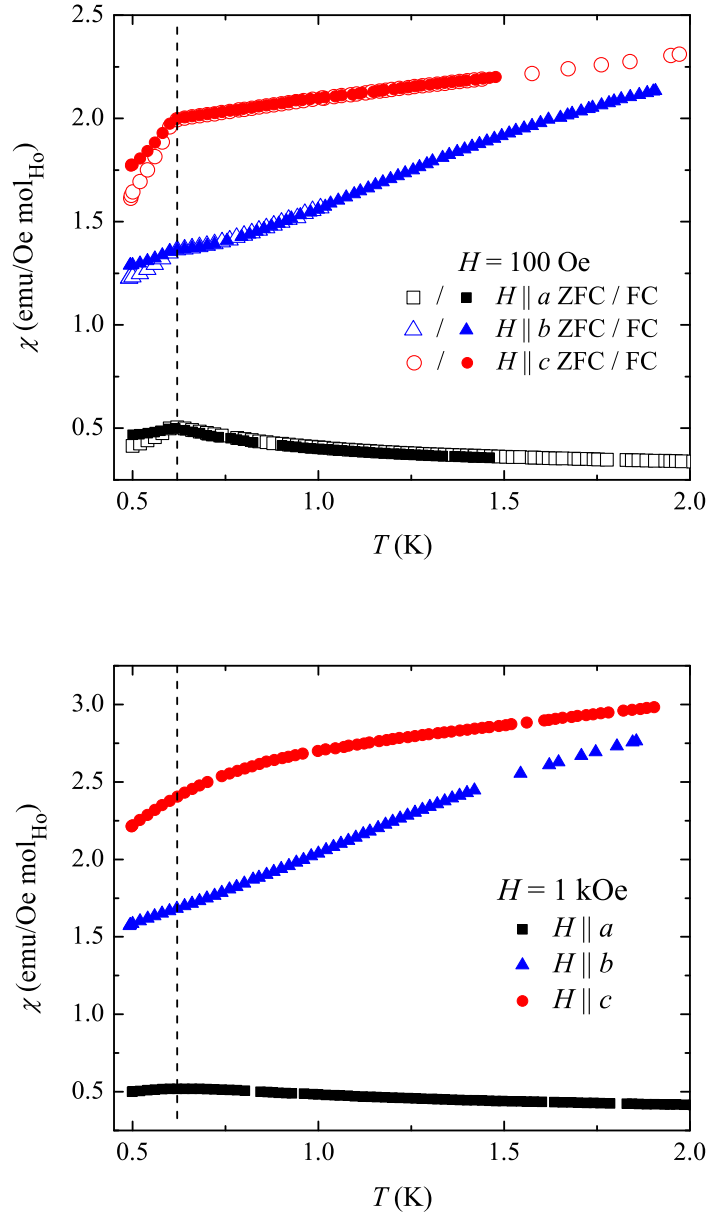
Figure 5.13: Low temperature magnetic susceptibility obtained in the temperature range of 0.5 to 2 K for the three principal axes of $SrHo_2O_4$ in applied fields of (top) 100 Oe and (bottom) 1 kOe. Dashed line represents 0.62 K, where a cusp is observed in the susceptibility at low fields, and also the temperature at which a difference between Zero-Field-Cooled (ZFC) and Field-Cooled (FC) measurements becomes apparent. In higher applied fields, there is very little difference between ZFC and FC $\chi(T)$ measurements for $SrHo_2O_4$.
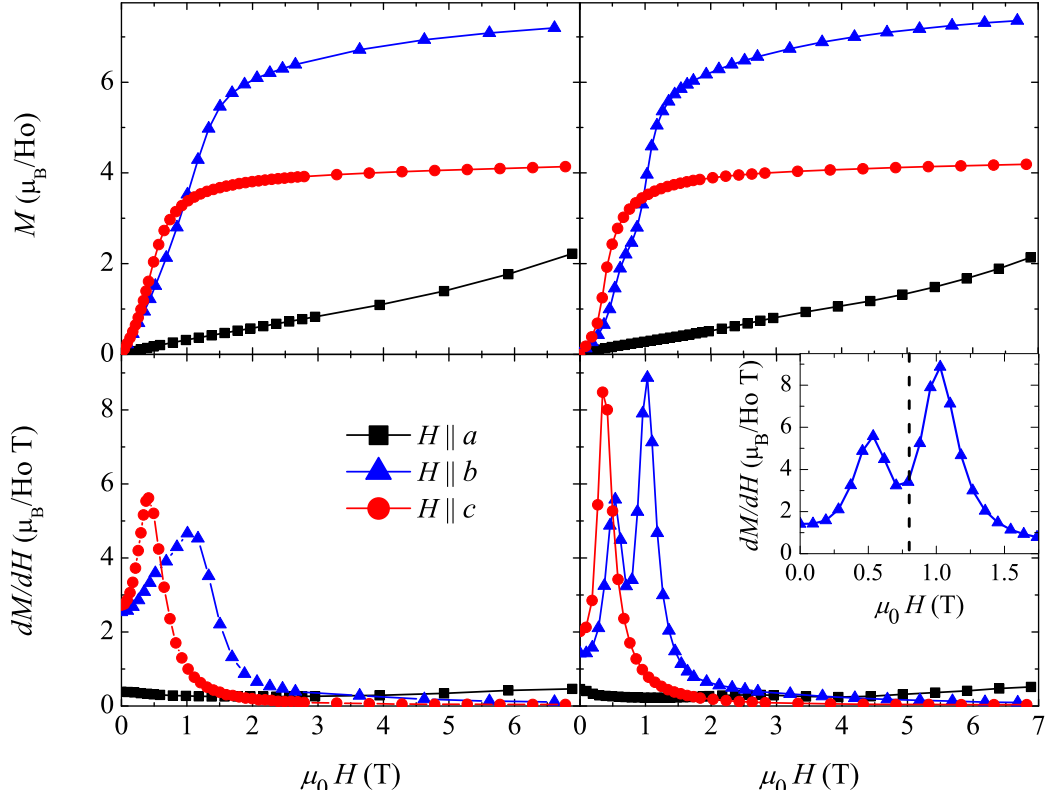
Figure 5.14: Field-dependent magnetisation curves (top panels) for SrHo$_2$O$_4$ obtained at 2.0 K (left) and 0.5 K (right) in the field range of 0 to 7 T. (Bottom panels) The field derivatives of the magnetisation at 2.0 K (left) and 0.5 K (right). Inset: the low field part of the 0.5 K dataset for the field applied along the b axis in more detail. The dashed line indicates 0.8 T, the value of the field around which the plateau in dM/dH is observed at approximately one third of the value for the fully saturated moment. In this case, this observation suggests that a collinear *two-spins-up-one-spin-down* (uud) structure is being stabilised around 0.8 T when the field is applied along the b axis.

nature of this rare-earth oxide.

The a axis is clearly a hard magnetisation direction, and dM/dH for a field applied along this direction remains small and nearly flat at all fields and at all measured temperatures. At 0.5 K, for $H \parallel b$, initially, the magnetisation rises sharply with a maximum in dM/dH at $\mu_0 H_{c1} \approx 0.59$ T, and so for a small region of the applied field the magnetisation shows much slower growth (with a minimum in dM/dH seen at 0.8 T), and then another sharp rise up to a second maximum in dM/dH at $H_{c2} \approx 1.2$ T. H_{c1} and H_{c2} thus confine a narrow plateau with an average magnetisation value of 2.5 μ_B, which equates to roughly a third of the saturation magnetisation value observed above H_{c2}. These types of plateaux are a sign of a field induced stabilisation of a collinear *two-spins-up-one-spin-down* (uud) magnetic structure, in which on each triangle of spins, two are pointing up along the field and the third spin pointing down anti-parallel to the field direction [102, 103]. On warming the sample above 0.5 K the magnetisation plateau between H_{c1} and H_{c2} for $H \parallel b$ gradually disappears, and by 2 K, shown in the lefthand panels of Fig. 5.14, dM/dH only shows a single broad maximum. This temperature behaviour implies that on further cooling below 0.5 K, the plateau in magnetisation is expected to become even better defined and perhaps occupy a more extensive region between H_{c1} and H_{c2}.

For $H \parallel c$, at 0.5 K, the magnetisation process is characterised by a single transition (seen as a sharp maximum in dM/dH) at $\mu_0 H_c = 0.4$ T. The nature of this field-induced transition cannot be known using only magnetisation measurements, and instead will be discussed in Section 5.4.1 which reports the relevant single crystal neutron scattering data. Upon raising the temperature, the maximum in dM/dH for $H \parallel c$ gradually becomes less pronounced. By 2 K, this maximum is significantly broader and shifts in field to 0.5 T.

Above 4 T the magnetisation curves for the a, b and c axes of $SrHo_2O_4$ look rather featureless, however, no complete saturation of magnetisation is observed at any temperature for any of the directions studied, as the dM/dH values remain nonzero even in the highest applied field of 7 T. This implies that the spins are still not fully aligned at this field, which is not surprising given the fact that the observed values of magnetisation remain much lower than what is expected from Hunds rules predictions for Ho^{3+} ions [3]. No hysteresis with the applied field is observed for the field applied along any of the prin-

cipal crystal axes of $SrHo_2O_4$. The demagnetisation corrections only have a small impact on the position of the field-induced phase transitions in $SrHo_2O_4$, limited to shifts of a few percent at most.

5.2.4 Heat capacity

Specific heat measurements were performed using a Quantum Design PPMS calorimeter as described in Section 4.2.2. The temperature dependence of the specific heat of $SrHo_2O_4$ in zero applied field is shown in Fig. 5.15. The lattice contribution to the specific heat of $SrHo_2O_4$ was estimated by measuring the heat capacity of two single crystal non-magnetic isostructural compounds: SrY_2O_4 and $SrLu_2O_4$, and is also shown in Fig. 5.15.

At low temperature, and especially for temperatures below 10 K, the lattice contribution to the specific heat of $SrHo_2O_4$ is negligible, but a broad peak centred around 3 K is observed. This type of feature could potentially be caused by a low-lying crystal field level, but is more likely to be associated with the onset of low-dimensional magnetic correlations seen in the powder neutron diffraction data, which were discussed in Section 5.1.2. Above $\sim$10 K the heat capacity begins to rise again, but only some of this rise is likely to be the result of the lattice contribution, and to try and estimate this the differences in specific heat $C_{SrHo_2O_4} - C_{SrLu_2O_4}$ and $C_{SrHo_2O_4} - C_{SrY_2O_4}$, are plotted in the inset to the top panel of Fig. 5.15. Unlike the broad peak at low temperatures, it is likely that this additional contribution to $C(T)$ is probably caused by the low-lying crystalline electric field levels present in $SrHo_2O_4$. A more detailed analysis of the crystal field levels will be discussed in Section 5.5.

Fig. 5.16 shows the temperature dependence of the specific heat divided by temperature (in zero applied field) in the region of 0.4 to 1.6 K for three different samples of $SrHo_2O_4$. These measurements were taken using the ^{3}He insert for the PPMS (see Section 4.2.2). No immediately obvious sharp λ-type anomalies, which correspond to a magnetic phase transitions are observed, and the specific heat steadily rises due to the nuclear contribution from the Ho^{3+} ions. The first dataset had too large a step size in temperature to try and observe the transition at 0.62 K, which was seen as a cusp in single crystal magnetic susceptibility measurements. Subsequent attempts to look at the temperature region of in-
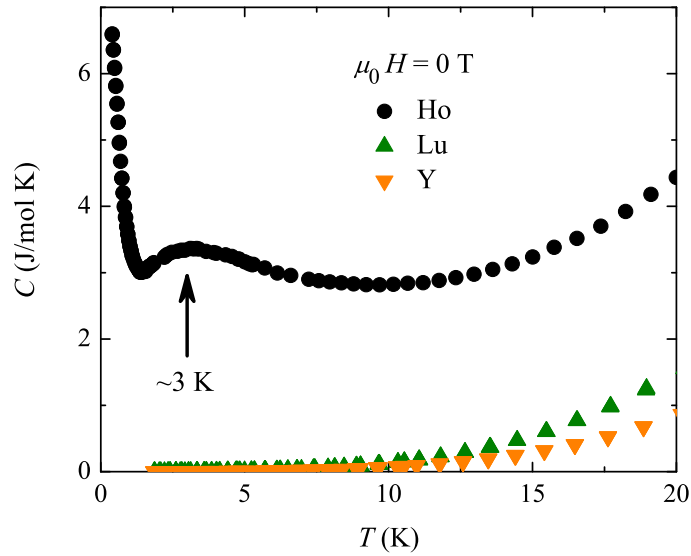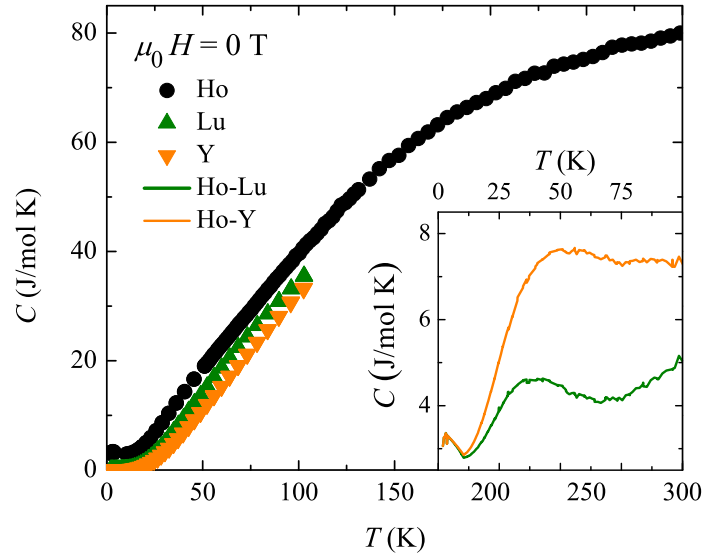
Figure 5.15: Temperature dependence of the specific heat of $SrHo_2O_4$ and of the nonmagnetic isostructural compounds $SrLu_2O_4$ and SrY_2O_4 measured on single-crystal samples for the full temperature range (top) and the low temperature range (bottom). A broad peak in the specific heat at $\sim$3 K is associated with short-range magnetic correlations.
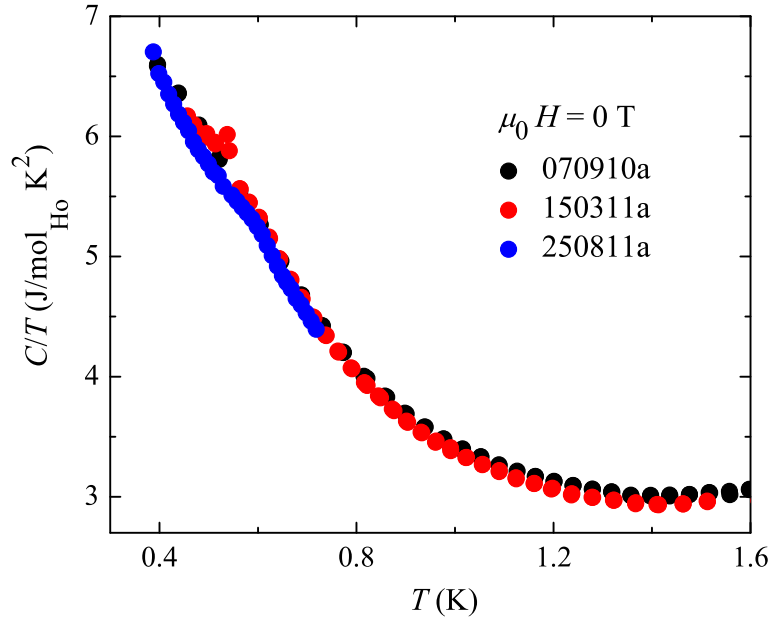
Figure 5.16: Temperature dependence of the specific heat divided by temperature for several single crystal samples of $SrHo_2O_4$. Due to the large contribution to the heat capacity from the nuclear Schottky anomaly of Ho^{3+} it is difficult to tell whether there is a transition in the specific heat at 0.62 K (the temperature at which a cusp is observed in the single crystal susceptibility measurements).

terest were plagued by temperature instabilities, but even with a good dataset, it is still very hard to tell whether a phase transition is happening because the nuclear contribution completely overwhelms any magnetic signal. The temperature dependence of entropy, which is usually calculated as an area under the $C/T(T)$ curve which has been extended linearly down to $T = 0$ K, cannot be calculated as there is not enough data to accurately subtract the nuclear Schottky anomaly. Thus any integration performed on the data presented is likely to be misleading like the data presented in the inset to Fig. 3 in Ref. [104].

Due to the problems of the nuclear contribution, the specific heat in an applied field was measured only for the fields applied along the c axis for $SrHo_2O_4$, and the data is shown in the top panel of Fig. 5.17. The broad peak due to the short range correlations seems to be suppressed with the application of higher fields. Measurements in fields higher than $\sim$2 T could not be completed as the sample tended to come off from the sample holder, due to the
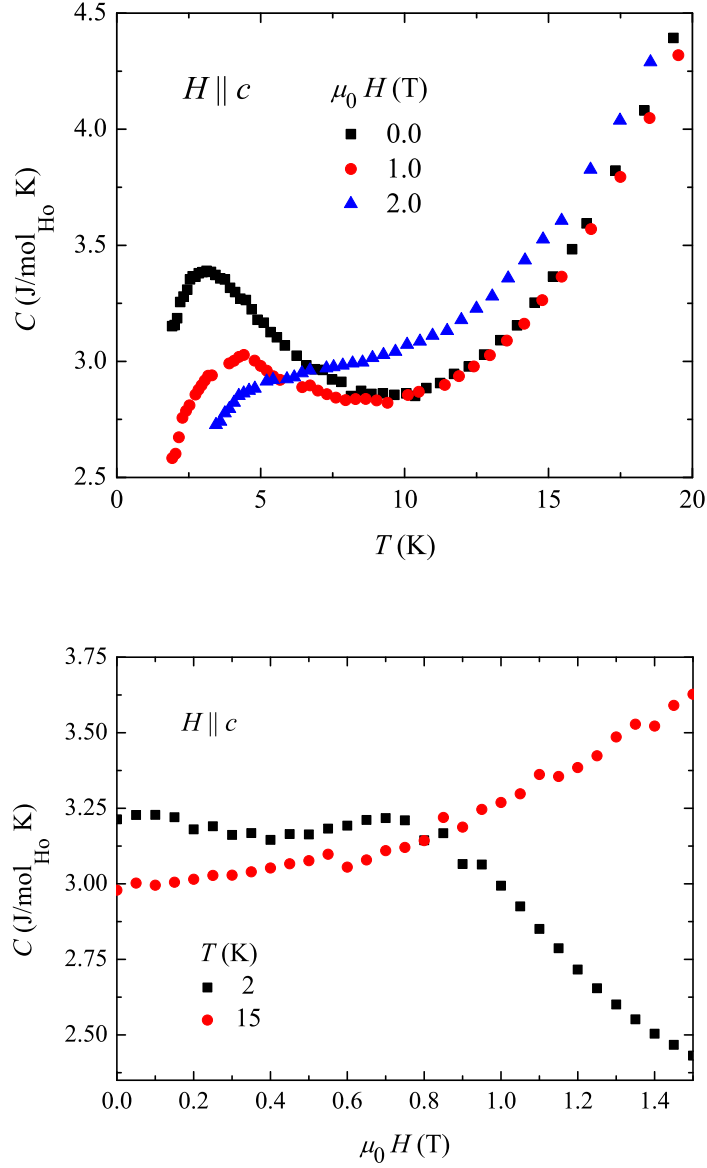
Figure 5.17: (Top) Temperature dependence of the specific heat of $SrHo_2O_4$ in several fields applied along the c axis of a single-crystal sample. The broad peak associated with short-range magnetic correlations seen in the specific heat at ~ 3 K in zero field is suppressed with increasing values of the applied field. (Bottom) Field dependence of the specific heat at two temperatures for a single crystal sample of $SrHo_2O_4$, when the field is applied along the c axis. The differences in specific heat $C_{SrHo_2O_4} - C_{SrLu_2O_4}$ and $C_{SrHo_2O_4} - C_{SrY_2O_4}$, are plotted in the inset to the top panel.

significant torque generated by the large moment of the Ho^{3+} ions as the easiest axis rapidly changes from c to b above 1 T, see Fig. 5.14. The specific heat measured as a function of field was also measured for $H \parallel c$, and this is shown in the bottom panel of Fig. 5.17. The high temperatures the $C(H)$ curve is pretty featureless, but at 2 K there seems to be a change in the specific heat above 0.75 T, but which does not look like a phase transition.

5.3 Diffraction in zero field

The neutron diffraction patterns for three orthogonal directions in the reciprocal space of single crystal $SrHo_2O_4$ were measured. The diffraction measurements in the $(hk0)$ scattering plane were made using the cold neutron WISH instrument at the ISIS facility, which was described in Section 4.3.3. The diffuse scattering spectrometer D7 at the Institut Laue-Langevin (see Section 4.3.4) with *XYZ* polarisation analysis was used to collect neutron scattering data for both $(h0l)$ and $(0kl)$ scattering planes. The high-flux single-crystal diffractometer D10 at the Institute Laue-Langevin, described in Section 4.3.5, was also used in the four-circle dilution refrigerator mode to collect precise neutron scattering data. A vertically focussing PG analyser was employed on D10 to give improved resolution and suppressed background for some of the measurements.

The results indicate that in $SrHo_2O_4$ *two* distinct types of *short-range* magnetic order arise from the two sites for the Ho^{3+} ions. In the $(hk0)$ plane, the first type of diffuse magnetic scattering appears around positions with the propagation vector $\mathbf{k} = 0$ below 0.7 K (with no long-range order present in contrast to previous measurements on powder samples of $SrHo_2O_4$). Whereas the second type of diffuse scattering appears as planes of scattering intensity at $(hk \pm \frac{l}{2})$. These planes are seen as "rods" of scattering intensity in both the $(h0l)$ and $(0kl)$ planes in reciprocal space at $Q = (00\frac{1}{2})$ and symmetry related positions. Therefore the second type of short-range order present in this material is one-dimensional in real space. Thus two members of the Sr*Ln*$_2O_4$ series, $SrHo_2O_4$ and $SrEr_2O_4$, both show the coexistence of two types of magnetic ordering at low-temperatures, but $SrEr_2O_4$ has long- and short-range components, whereas in $SrHo_2O_4$ both types of magnetic correlations are short-ranged.
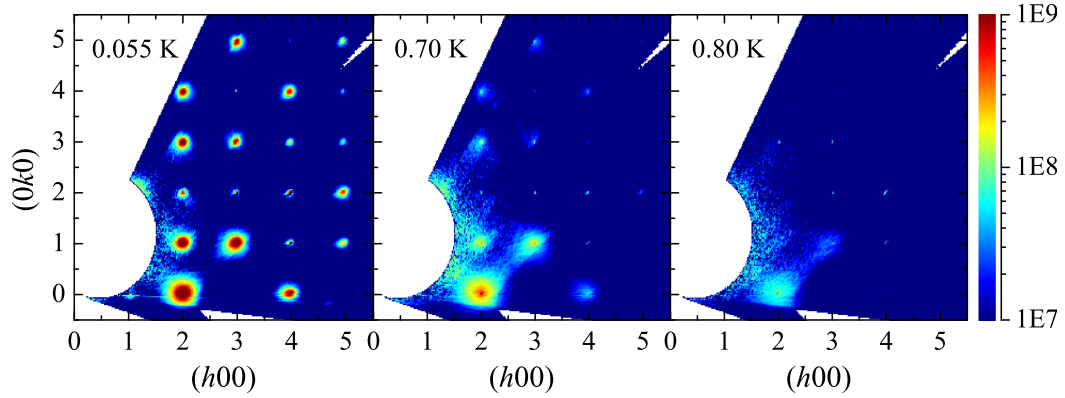
Figure 5.18: The magnetic contribution to the scattering from $SrHo_2O_4$ in the $(hk0)$ plane at 0.055, 0.70 and 0.80 K. The magnetic component was isolated by subtracting a 1 K background from the single crystal neutron diffraction data collected using WISH, ISIS.

Careful studies of the correlation lengths (L) in $SrHo_2O_4$ indicate that the diffuse scattering that appears around the $\mathbf{k} = 0$ positions is correlated to $L \approx 150$ Å in the a-b plane at 0.18 K, and to $L \approx 190$ Å along the c axis at 0.16 K. The scattering is mostly isotropic in reciprocal space. The diffuse intensity planes have a correlation length of $L \approx 230$ Å along the c axis at 0.15 K. Finally by utilising an energy analyser it is possible to deduce that the diffuse scattering in the $(hk0)$ plane is purely elastic, while the diffuse scattering that appears in planes along $(00\frac{l}{2})$ is mostly elastic. The exposition of the zero-field diffraction measurements, starting with the data collected in the $(hk0)$ scattering plane of $SrHo_2O_4$, is presented below.

5.3.1 Measurements of the ($hk0$) plane

From earlier measurements on a powder sample of $SrHo_2O_4$, that were described in Section 5.1.2, $\mathbf{k} = 0$ magnetic Bragg peaks were expected in the $(hk0)$ scattering plane, similar to what has previously been observed for $SrEr_2O_4$ [63]. However, after cooling down a single crystal sample of $SrHo_2O_4$ to 0.055 K, no long-range order was found in the measurements made using the WISH diffractometer. Fig. 5.18 shows the observed magnetic scattering intensity (which was isolated by subtracting a 1 K background from the low-temperature data). From the single crystal data it is apparent that in the $(hk0)$ plane diffuse magnetic scattering appears around the $\mathbf{k} = 0$ positions and that its intensity increases
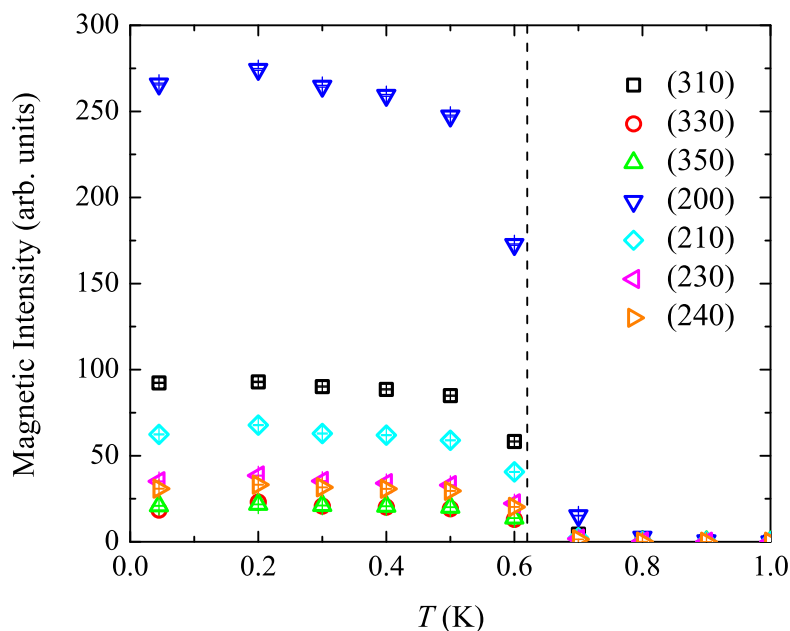
Figure 5.19: Temperature dependence of several diffuse peaks intensities in the ($hk0$) plane as a function of temperature. The magnetic intensity was isolated by subtracting a 1 K background from data collected using WISH, ISIS.

rapidly below 0.7 K. Waiting at low-temperature for a long time ($\sim$5 hours) for the sample to thermalise made no measurable difference to the intensity or width of the diffraction patterns.

The positions of the observed broad diffuse scattering peaks in the ($hk0$) scattering plane are in agreement with the positions previously reported for a $\mathbf{k} = 0$ structure obtained from the powder refinement. However, from the single crystal experiment no long-range order is actually observed even though the onset of the diffuse scattering in the ($hk0$) plane appears to go through a second-order phase transition (see Fig. 5.19 and Fig. 5.23), and was also observed as a clear cusp in low temperature single crystal magnetic susceptibility measurements described in Section 5.2.2. It is important to note that in $SrHo_2O_4$ at temperatures below 0.7 K the diffuse scattering forms the same *lozenge* pattern that is seen at low-temperatures in $SrEr_2O_4$ [63]. This is a result of very similar positions of the magnetic Ln^{3+} ions in the respective unit cells for both compounds.
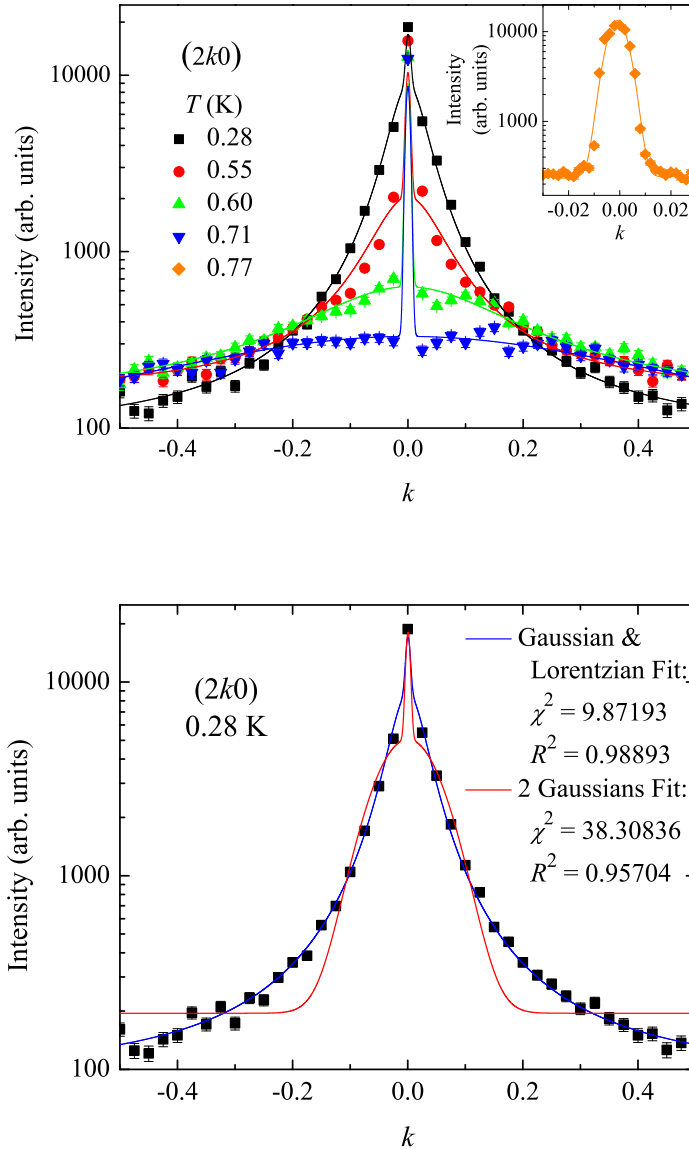
Figure 5.20: (Top) Temperature dependence of the scattering intensity of the (200) reflection from SrHo$_2$O$_4$. This is an allowed reflection in *Pnam* symmetry. The data are fitted using Gaussian (nuclear) and Lorentzian (magnetic) components, and was collected on the D10 instrument at the ILL. The inset shows the data collected for the nuclear (200) peak at high temperature with high resolution and the fitted Gaussian distribution. (Bottom) Comparison of two different fits, Lorentzian and Gaussian, to the magnetic part of the scattering intensity of the (200) reflection at 0.28 K (the same Gaussian component that was fit to a high temperature scan across the (200) reflection is used to fit the nuclear component in both of the fits).
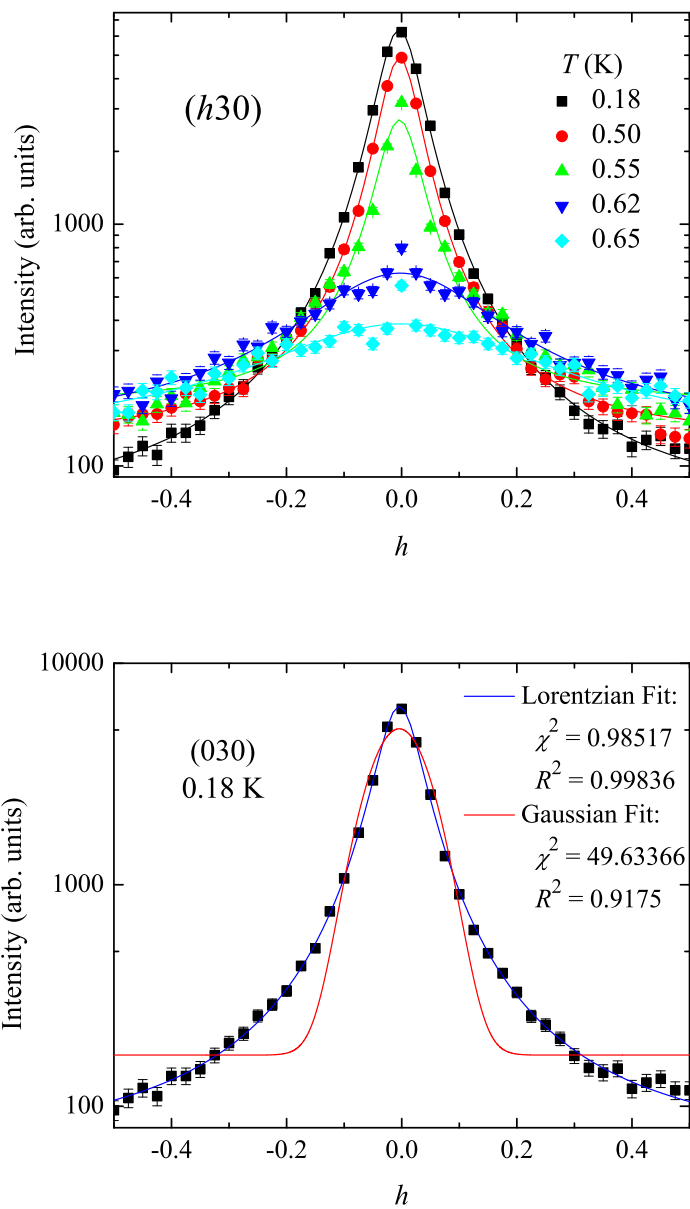
Figure 5.21: (Top) Temperature dependence of the scattering intensity of the (030) reflection from SrHo$_2$O$_4$. This is a forbidden reflection in *Pnam* symmetry. The data are fitted using the Lorentzian distribution and was collected using the D10 instrument at the ILL. (Bottom) Comparison of two different fits, Lorentzian and Gaussian, to the scattering intensity of the (030) reflection at 0.18 K.

Figure 5.22: (Top) Temperature dependence of the scattering intensity of the (200) reflection from $SrHo_2O_4$. The data are fitted using two Gaussian components (one for nuclear and one for magnetic contributions) at all temperatures. The data were collected using the D10 instrument at the ILL. (Bottom) Comparison of two different fits, Lorentzian and Gaussian, to the magnetic part of the scattering intensity of the (200) reflection at 0.16 K (the same Gaussian component is used to fit the nuclear part of the scattering in both of the fits).

Although the Q resolution of WISH is good the sample was kept stationary during the experiments and in order to measure the correlation lengths associated with the diffuse scattering features more accurately, high resolution scans across the nuclear and magnetic reflections in the $(hk0)$ plane were performed using the D10 instrument, which was described in Section 4.3.5. Temperature dependence of the scattering intensity for two different types of reflections in the $(hk0)$ plane of SrHo$_2$O$_4$, one compatible with *Pnam* symmetry and one forbidden by it, are shown in Fig. 5.20, Fig. 5.21 and Fig. 5.22. The data in Fig. 5.20 have been fitted with Gaussian and Lorentzian components, to account for the nuclear (temperature independent) and magnetic scattering. The nuclear (Gaussian) component was fitted to data collected for (200) at higher temperature with high resolution, and this is shown in the inset to Fig. 5.20. The data in Fig. 5.21 have been fitted using the Lorentzian distribution only, since this is a forbidden reflection in *Pnam* symmetry, and purely magnetic scattering is expected. The data in Fig. 5.22 have been fitted using two Gaussian components (one for nuclear and one for magnetic contributions) at all temperatures. Since the scattering intensity is much narrower, and no higher resolution scans were measured in the paramagnetic regime to obtain a good fit for the nuclear intensity for the scan along l, the agreement factors for the fits are worse than for the scans along h and k.

No assumptions were made about the nature of the magnetic scattering distribution when fitting the data, with the end goal of only fitting the data well in order to calculate the relevant correlation lengths. It may ultimately prove quite difficult to work out the nature of the peak distributions since the data were collected in two sample orientations in order to overcome the limitations of D10's poor vertical resolution. The choice of the integration box when looking at the diffuse scattering profiles would also affect the quality of the fits. To fit the magnetic contribution to the scattering intensity, the Lorentzian or Gaussian fitting functions were chosen because they gave the best fit to the data, assessed by comparing the value of R^2 and reduced χ^2 for the different fits, and as an example the bottom panels of Figures 5.20 to 5.22 show the comparison of the different fitting functions and the appropriate agreement factors.

From the FWHM of the fitted Lorentzian curves to the diffuse scattering, the correlation lengths were estimated using L (Å) = 2π(FWHM (Å^{-1}))$^{-1}$ [105, 106]. (Another
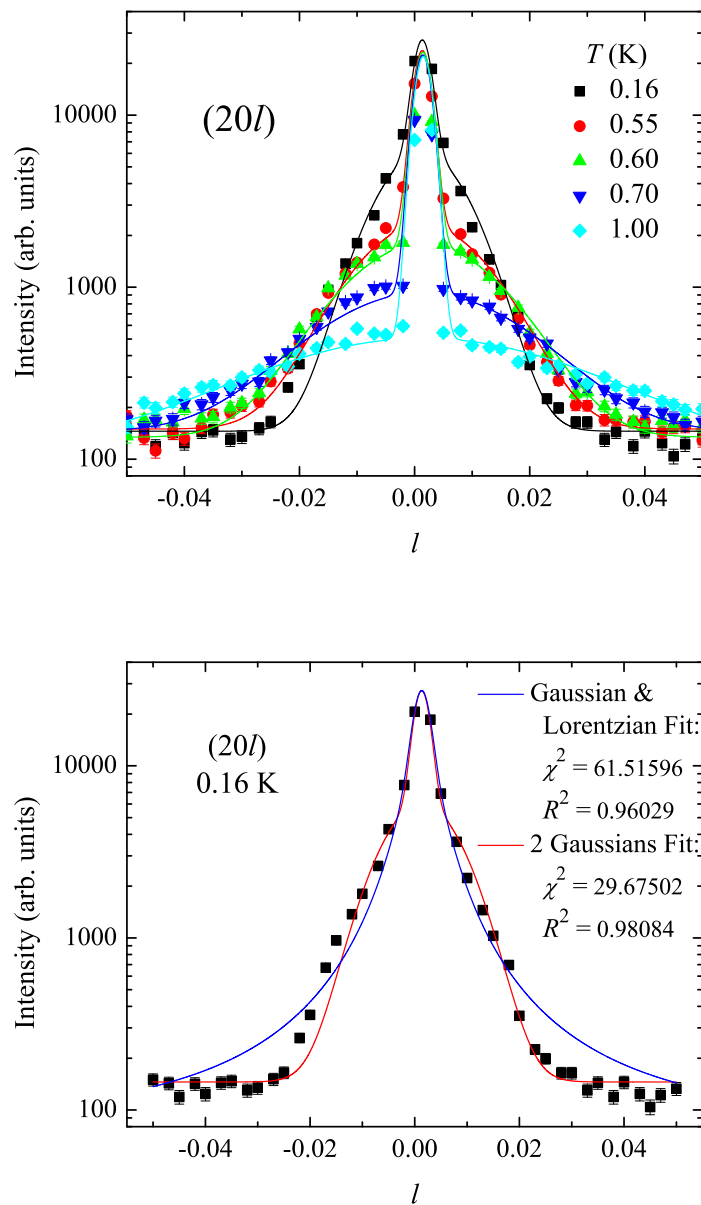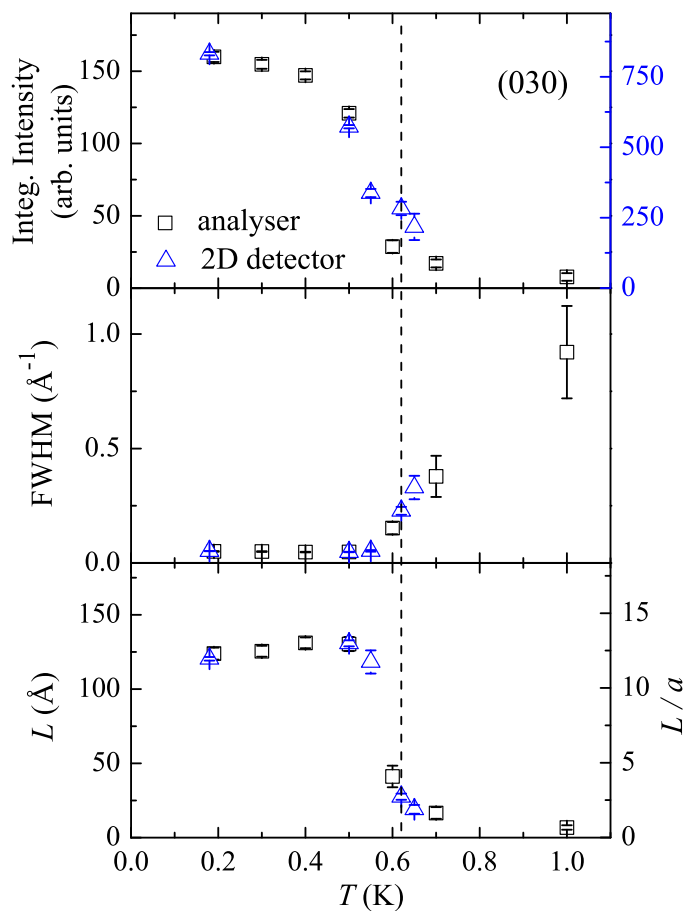
Figure 5.23: Temperature dependence of the integrated intensity and the FWHM along h of the (030) reflection from $SrHo_2O_4$, as well as the calculated correlation length, L, along the a axis. The integrated intensity and the FWHM were extracted by fitting a Lorentzian distribution to data collected using the D10 instrument at the ILL in both the area detector and the energy analyser configurations. For the top panel, the righthand axis shows the intensity scale for the area detector instrument configuration. The righthand axis of the bottom panel is a conversion to how many unit cells the magnetic order is correlated to. The dashed line indicates 0.62 K - the temperature at which a cusp is observed in single crystal magnetic susceptibility measurements.

common definition of the correlation length is L (Å) $= 2$(FWHM (Å^{-1}))$^{-1}$ [17], and differs by a factor of π to the one used throughout this thesis.) o Taking into account the instrument resolution by estimating the correlation lengths using $L = 2\pi(W_{\mathrm{peak}}^2 - W_{\mathrm{ref}}^2)^{-\frac{1}{2}}$, where W_{peak} and W_{ref} are the full widths at half maximum in Q space for the Lorentzian peak in question and a reference (resolution-limited) Bragg peak obtained on the same instrument resulted in a difference in the calculated correlation length of less than 1 % for the lengths along the a and b axes. The instrument resolution is more important for the calculations of correlation lengths along the c axis where the scattering profile is much narrower.

At the lowest temperature, the magnetic order is correlated to $L \approx 150$ Å in the a-b plane, and to $L \approx 190$ Å along the c axis. The integrated intensity and FWHM along h, and the calculated correlation length along the a axis of the (030) reflection is plotted as a function of temperature in Fig. 5.23. The data for the (030) reflection in Fig. 5.23 were collected using both the two-dimensional detector and energy analyser D10 instrument configurations, as described in Section 4.3.5. A detailed comparison of these two types of measurements is presented later, see Section 5.3.3. Overall, the diffuse scattering in the ($hk0$) plane shows second-order phase transition type behaviour, with a marked increase in correlation length below 0.62 K - the temperature at which a cusp was observed in single crystal magnetic susceptibility measurements.

Finally, it is important to note that with the improved instrumental resolution offered by D10, it is possible to see that there is a small amount of scattering intensity at positions forbidden by the *Pnam* symmetry at all temperatures (although at the lowest temperatures it tends to be masked by the magnetic intensity). This suggests that the proposed space group is not entirely appropriate for the Sr*Ln*$_2$O$_4$ family of compounds, although the relative intensity of the "forbidden" peaks is systematically low compared to the intensity of the allowed nuclear peaks reflections, therefore much more accurate collection of the intensity of all the peaks is required in order to solve the crystal structure.

5.3.2 Measurements of the (*h0l*) and (*0kl*) planes

The main conclusions of the single crystal neutron diffraction experiments to investigate the second type of diffuse scattering present in SrHo$_2$O$_4$, can be summarised by looking

at the measurements carried out using the D7 instrument at the ILL, which was described in Section 4.3.4. The Z polarisation intensity maps of neutron scattering data in the ($h0l$) and ($0kl$) scattering planes (in a range of temperatures from 0.055 to 4.5 K) are shown in Fig. 5.24 and Fig. 5.25 respectively.

The polarised neutron experiments were configured to measure two independent components of the scattering function, here called the Non-Spin-Flip (NSF) and Spin-Flip (SF) channels. The Z polarisation direction in our measurements coincides with the vertical axis, and hence the sum of Z NSF and Z SF measurements is what would be observed in unpolarised neutron experiments. The standard data reduction formulas utilising all of the *XYZ* polarised measurements to calculate the purely magnetic contribution to the scattering [74, 94] cannot be applied to the $SrHo_2O_4$ system, because it is not an isotropically magnetic crystal at low-temperatures. Instead, Fig. 5.24 shows the intensity measured in the ($0kl$) plane Z NSF and SF measurements (here, the Z polarisation direction coincides with the a axis). No extra magnetic features associated with the ($hk \pm \frac{l}{2}$) planes are observed in the Z NSF cross-section for this sample orientation. Fig. 5.25 shows the data for the ($h0l$) plane Z NSF and SF measurements (here, the Z polarisation direction coincides with the b axis). Similarly, no extra magnetic features due to the ($hk \pm \frac{l}{2}$) planes are observed in the Z SF cross-section for the second sample orientation, (only the diffuse peaks that belong to the $\mathbf{k} = 0$ magnetic phase can be seen in the Z SF channel).

Fig. 5.26 shows the purely magnetic contribution to the scattering intensity in the ($h0l$) plane that is only due to the one dimensional spin structure. The magnetic intensity in the ($h0l$) plane calculated using the expression $(\frac{d\sigma}{d\Omega})_{mag} = 2\left[\left(\frac{d\sigma}{d\Omega}\right)_z^{nsf} - \left(\frac{d\sigma}{d\Omega}\right)_{nuc}\right]$, where the nuclear contribution is obtained following J. R. Stewart, *et al.* [74], using all six *XYZ* components measured with polarised neutrons. This method of separating the magnetic intensity ignores the contribution of components of the moments orthogonal to the Z axis, however there is no scattering information on this magnetic structure is in the Z SF channel (see Fig. 5.25).

Measurements of the ($h0l$) and ($0kl$) scattering planes reveal broad "rod"-like features at half-integer positions along the l-axis observed at all measured temperatures. The position of the rods along l suggests that the unit cell for this magnetic structure is doubled

Figure 5.24: Intensity maps of the scattering from $SrHo_2O_4$ in the $(0kl)$ plane at different temperatures, made from data collected using the D7 instrument at the ILL. (Top) The Z polarisation Non-Spin-Flip (NSF) scattering and (Bottom) the Z polarisation Spin-Flip (SF) scattering intensity in the $(0kl)$ plane. "Rods" of scattering intensity at $(0k\frac{1}{2})$ and symmetry related positions are visible at low temperature. In the $(0kl)$ plane at 0.055 K diffuse magnetic peaks associated with the $\mathbf{k} = 0$ structure are also visible. No scattering due to the $(hk \pm \frac{l}{2})$ planes can be seen in the NSF channel, which means that the spins that participate in the low-dimensional structure are orthogonal to the a axis.

Figure 5.25: Intensity maps of the scattering from $SrHo_2O_4$ in the $(h0l)$ plane at different temperatures, made from data collected using the D7 instrument at the ILL. (Top) The Z polarisation NSF scattering and (Bottom) the Z polarisation SF scattering intensity in the $(h0l)$ plane. "Rods" of scattering intensity at $(h0\frac{1}{2})$ in the Z NSF measurement and symmetry related positions are visible at low temperature. Except the diffuse peaks that belong to the $\mathbf{k} = 0$ magnetic phase, no scattering due to the $(hk \pm\frac{l}{2})$ planes can be seen in the Z SF channel, which means that the spins that participate in the low-dimensional structure are collinear with the b axis.
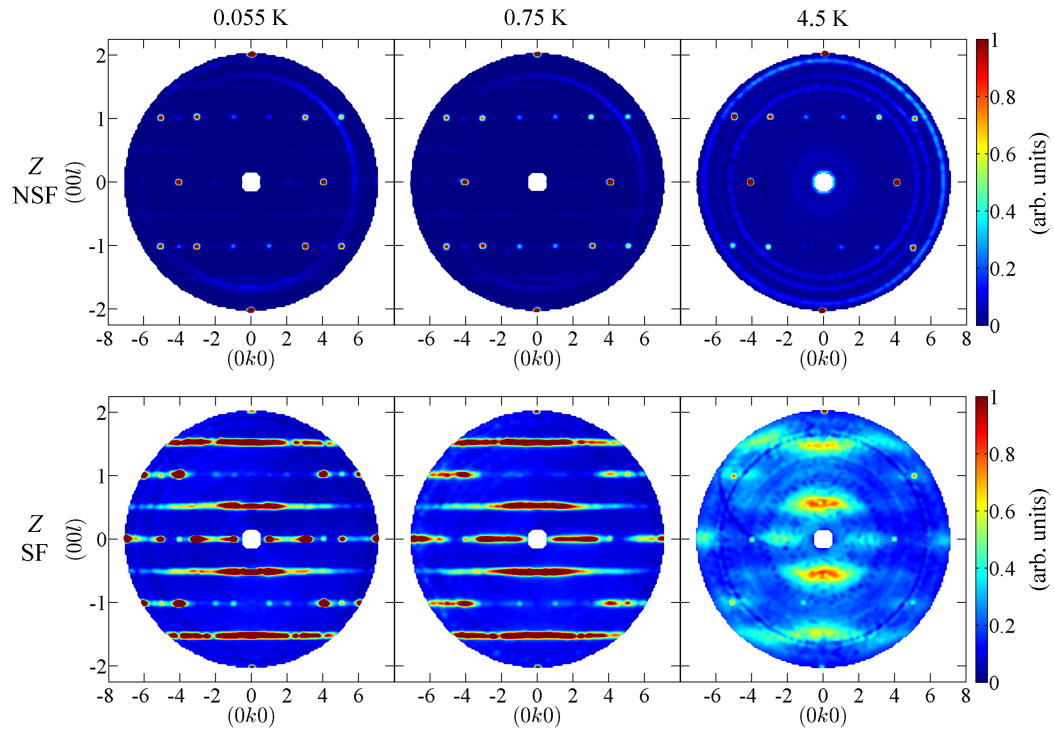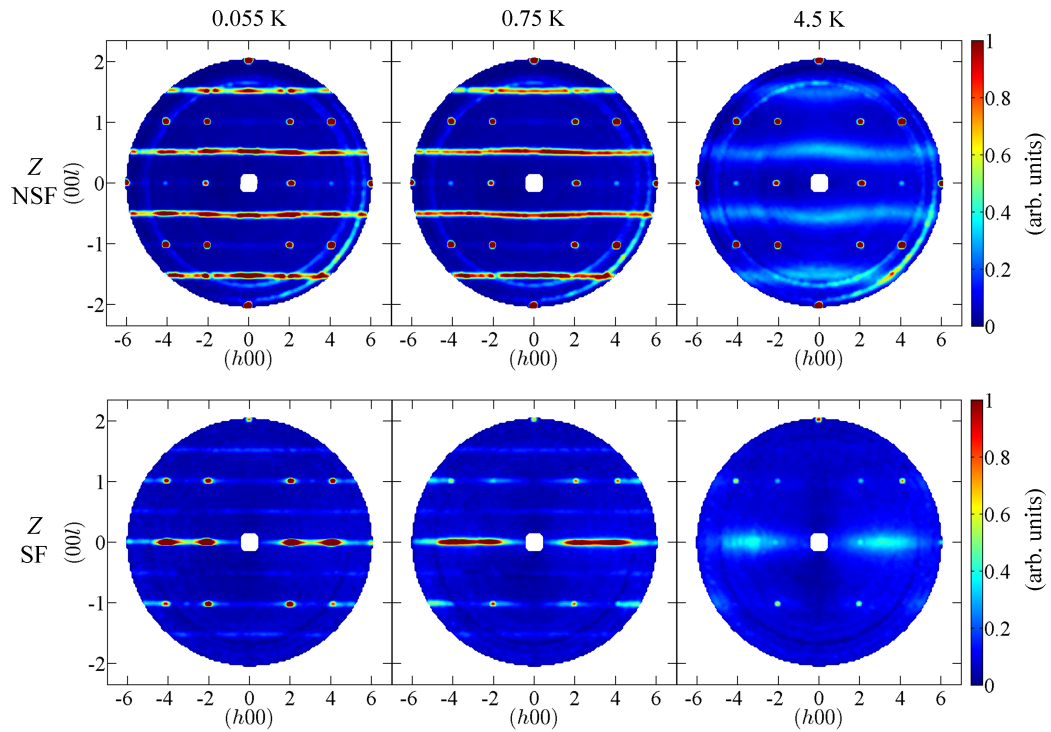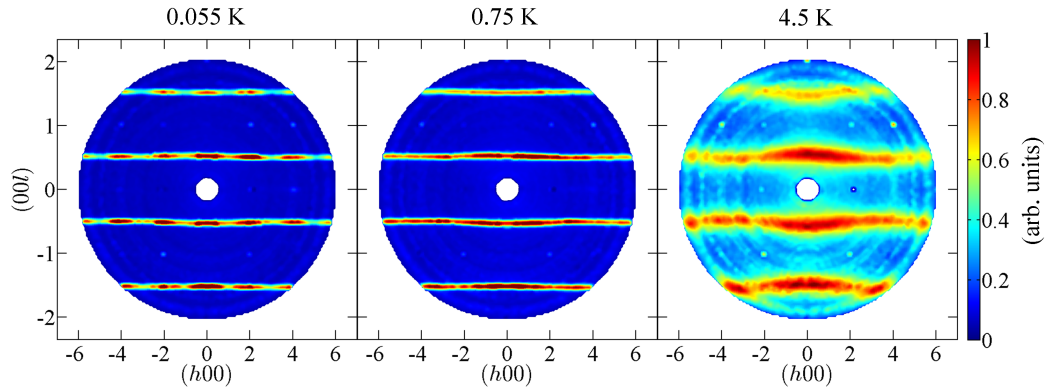
Figure 5.26: Intensity maps of the magnetic scattering from SrHo$_2$O$_4$ in the $(h0l)$ plane at different temperatures, made from data collected using the D7 instrument at the ILL. "Rods" of scattering intensity at $(h0\frac{1}{2})$ and symmetry related positions are visible at low temperature. The method of calculating the magnetic intensity in the $(h0l)$ plane is described in the text.

along the c axis. In the $(h0l)$ plane, the rods extend along the h-direction which implies that the magnetic moments are only weakly correlated along the a axis. Also, in the $(0kl)$ plane, the rods extend along the k-direction, so the magnetic moments are only weakly correlated along the b axis. The presence of the "rods" along two orthogonal directions means that the diffuse scattering is a two-dimensional structure in reciprocal space. Hence the correlations of this type of short-range order in SrHo$_2$O$_4$ are *one*-dimensional in real space.

At the lowest temperature of 0.055 K the "rods" of diffuse scattering are most intense and approximate straight lines perpendicular to the l-direction. In the $(h0l)$ plane areas of greater intensity along the rod can also be seen at even integer h. There is no pronounced decay of intensity for the "rods" with increasing h, k or l. On warming the system to 0.75 K the one-dimensional scattering in both the $(h0l)$ and $(0kl)$ planes is still very intense, and for the $(0kl)$ plane it is little different to what is observed at base temperature. However, in the $(h0l)$ plane there is no longer any modulation of the intensity along the rods. Thus the onset of the diffuse scattering in the $(hk0)$ plane below 0.7 K seems to only affect the modulation of the intensity along the rods in the $(h0l)$ plane, with no other effect on the diffraction pattern of the second diffuse phase. If each of the crystallographically inequivalent Ho^{3+} sites in SrHo$_2$O$_4$ contributes to only one of the two coexisting magnetic structures, it would explain this small coupling between the two types of short-range order-

ing. At much higher temperatures, $T = 4.5$ K, there is still some intensity in the diffuse component of the total scattering, for example shown in the righthand panels of Fig. 5.24 and Fig. 5.25. The "rods" are now much wider along the l-direction, and they appear to be a lot less straight. The one-dimensional order persists over a wide temperature range, and the onset of these correlations may be observed with bulk heat capacity measurements (as the broad peak around $\sim$3 K shown in the bottom panel of Fig. 5.15.

From the Z polarisation direction NSF and SF data, some conclusions can be drawn about the nature of this diffuse magnetic scattering. In the $(0kl)$ measurement the diffuse scattering appears at the $(0k\frac{1}{2})$ and symmetry equivalent positions only in the SF channel. This demonstrates that the spin structure has no components parallel to the Z direction which coincides with the crystallographic direction a in this measurement, $i.e.$ all of the magnetic moments lie in the b-c plane. In the $(h0l)$ measurement the diffuse scattering appears at the $(h0\frac{1}{2})$ and symmetry equivalent positions only in the NSF measurement, which indicates that in this low-dimensional magnetic structure all of the spins lie *parallel* with the b axis.

The diffuse scattering peaks associated with the **k** = 0 magnetic structure are only visible in the Z SF data for both the $(h0l)$ and $(0kl)$ scattering planes. This means that all of the spins that give rise to the **k** = 0 scattering are *parallel* with the c axis. This is in agreement with the previously proposed magnetic structure (see Section 5.1.3) that was established from a refinement performed using powder neutron diffraction data. Single ion anisotropy, due to the crystal field, may be responsible for the magnetic moments on the two crystallographically inequivalent sites pointing along two orthogonal principal axes.

The Q resolution of D7 does not allow for the precise investigation of the structure of the planes of diffuse scattering, so the D10 diffractometer (see Section 4.3.5) was used to further examine the "rod" like features. Scans along the rods at 0.15 K indicate that there is a pronounced Q-dependence to the scattering intensity, and to illustrate this, data for the $(h0\frac{1}{2})$ rod is shown in Fig. 5.27. At the lowest temperature the scattering appears to be most intense near the integer values of h. Upon raising the temperature the Q-dependence becomes less pronounced, but the scattering intensity remains measurable above background even at temperatures as high as 1.8 K, as expected from the D7 measurements. In order to
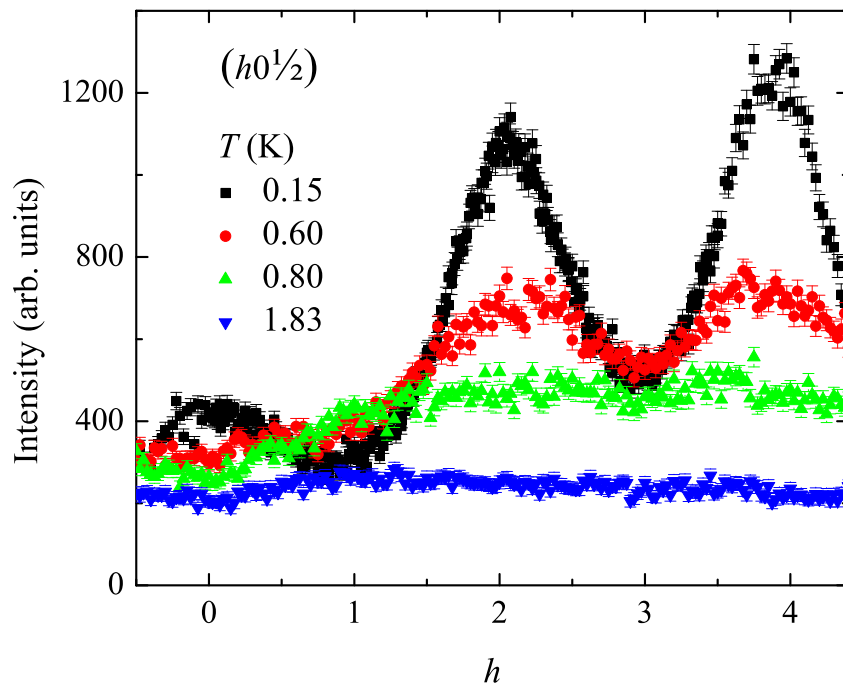
Figure 5.27: Q-dependence of the scattering intensity along one of the "rods" in the $(h0l)$ plane measured at different temperatures for the SrHo$_2$O$_4$ crystal using the D10 instrument at the ILL. At the lowest temperature of 0.15 K, the scattering is most intense at even integer values of h. As the temperature is increased to 1.83 K, the diffuse scattering is still measurable above background, but the Q-dependence of the scattering intensity along the "rod" is no longer present.

have a complete picture of the one-dimensional scattering, scans across the "rods" along the l-direction were also performed. The temperature dependence of the integrated intensity of the diffuse magnetic scattering across $(20l)$ and $(30l)$ are shown in Fig. 5.28 as examples. At the lowest temperature the moments are highly correlated around $l = \frac{1}{2}$. Upon raising the temperature the scattering becomes less intense and less symmetrical about $l = \frac{1}{2}$. Unlike the *lozenge*-type diffuse scattering seen in the $(hk0)$ plane, the diffuse scattering intensity seen in the $(h0l)$ and $(0kl)$ planes appears to be a smooth function of temperature, with no well-defined transition, just a gradual building-up of one-dimensional correlations.

From the FWHM of the fitted Lorentzian curves to the diffuse scattering, the correlation lengths were estimated as described above. Taking into account the instrument reso-
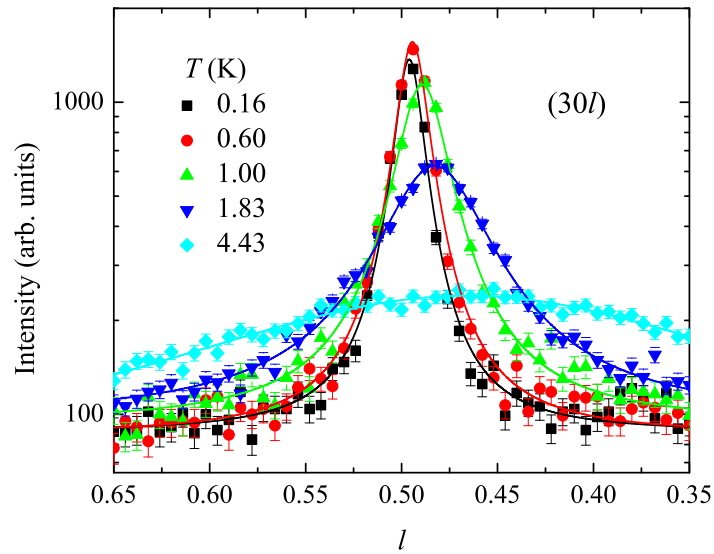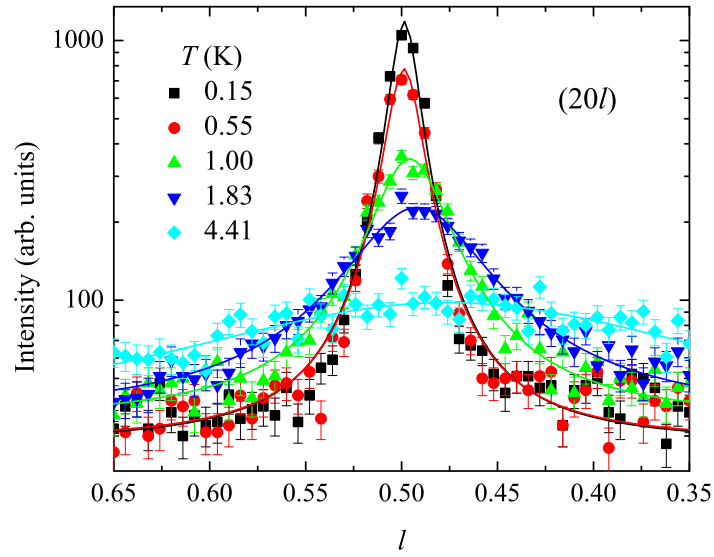
Figure 5.28: Temperature dependence of the integrated intensity of the diffuse magnetic scattering around (top) the $(20\frac{1}{2})$ and (bottom) the $(30\frac{1}{2})$ positions in reciprocal space, measured using the D10 instrument at the ILL. The data have been fitted using a Lorentzian distribution.
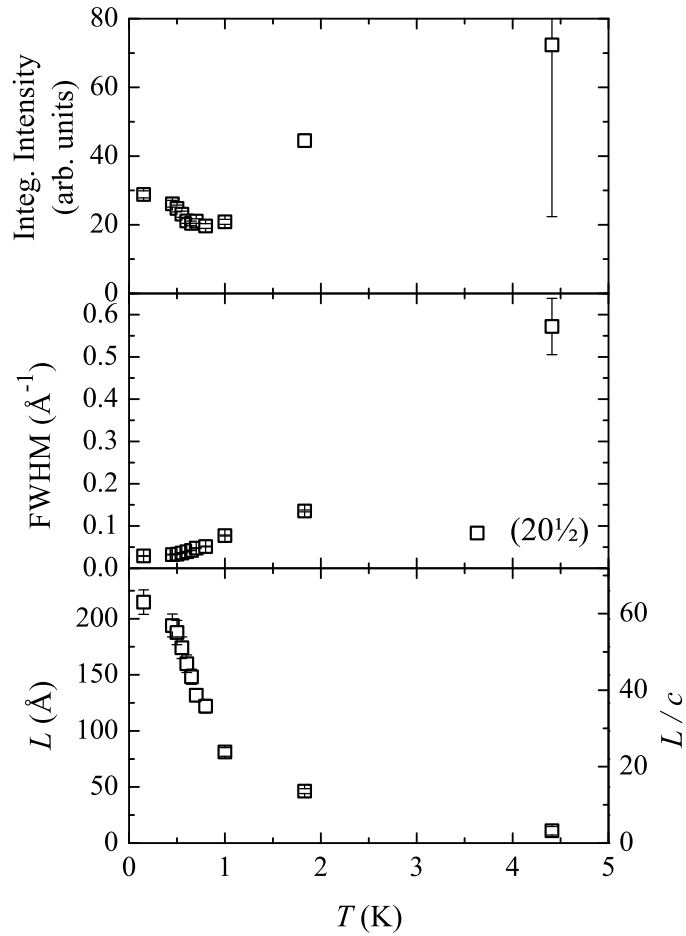
Figure 5.29: Temperature dependence of the integrated intensity and the FWHM along l of the $(20\frac{1}{2})$ reflection from SrHo$_2$O$_4$. The calculated correlation length, L, along the c axis is shown in the bottom panel, with the righthand axis giving a conversion to how many unit cells the magnetic order is correlated to. The integrated intensity and the FWHM were extracted by fitting a Lorentzian distribution to data collected using the D10 instrument at the ILL.

lution again did not result in a significant difference to the calculated correlation lengths. At the lowest temperature, the $(hk \pm \frac{l}{2})$ planes of diffuse scattering are correlated to $L \approx 230$ Å along the c axis. The integrated intensity and FWHM along l, and the calculated correlation length along the c axis of the $(20\frac{1}{2})$ and the $(30\frac{1}{2})$ reflections are plotted as a function of temperature in Fig. 5.29. The diffuse scattering does not show any abrupt transition, demonstrating a gradual build-up of correlations with decreasing temperature.

It is interesting to note that this type of diffuse scattering was expected from the previously collected diffraction data on powder samples of $SrHo_2O_4$, as described in Section 5.1.2 and in Ref. [43]. In those measurements, broad features were seen at $Q = (00\frac{1}{2})$ and symmetry related positions. However, from the powder data alone it could not be established whether the diffuse scattering was one- or two-dimensional.

5.3.3 Energy analysis

Using the D10 instrument with the vertically focussing PG analyser, see Section 4.3.5, both types of diffuse scattering found in $SrHo_2O_4$ were investigated. Comparison of the data collected with the analyser and with the 2-dimensional area detector data for the (030) magnetic reflection at the lowest temperature is shown in the top panel of Fig. 5.30. The statistics are much lower for the data collected in the analyser configuration. The peaks are fitted with a Lorentzian distribution, and the resulting FWHM for the two datasets is in reasonable agreement. This indicates that the diffuse scattering that appears around the peaks in the $(hk0)$ plane is elastic within the energy resolution of the analyser, which is $\delta E = 0.073$ meV (and is calculated for this experiment from the thermal neutrons used with $\lambda = 2.36$ Å, and the relative energy resolution of D10, which is $\delta E/E$ of 5×10^{-3}).

Scans along $(00l)$ at several integer positions of h were performed to check the diffuse scattering profile of the planes with an improved energy resolution. The comparison of the data collected using the 2-dimensional area detector and that using the analyser configuration for the $(20\frac{1}{2})$ reflection at 0.60 K is shown in the bottom panel of Fig. 5.30. Here, the FWHM is fairly close for both datasets, taking into account that the statistics for data collected with the analyser configuration are significantly lower. This indicates that the diffuse scattering that appears in planes at $(hk \pm \frac{l}{2})$ is mostly elastic within the energy
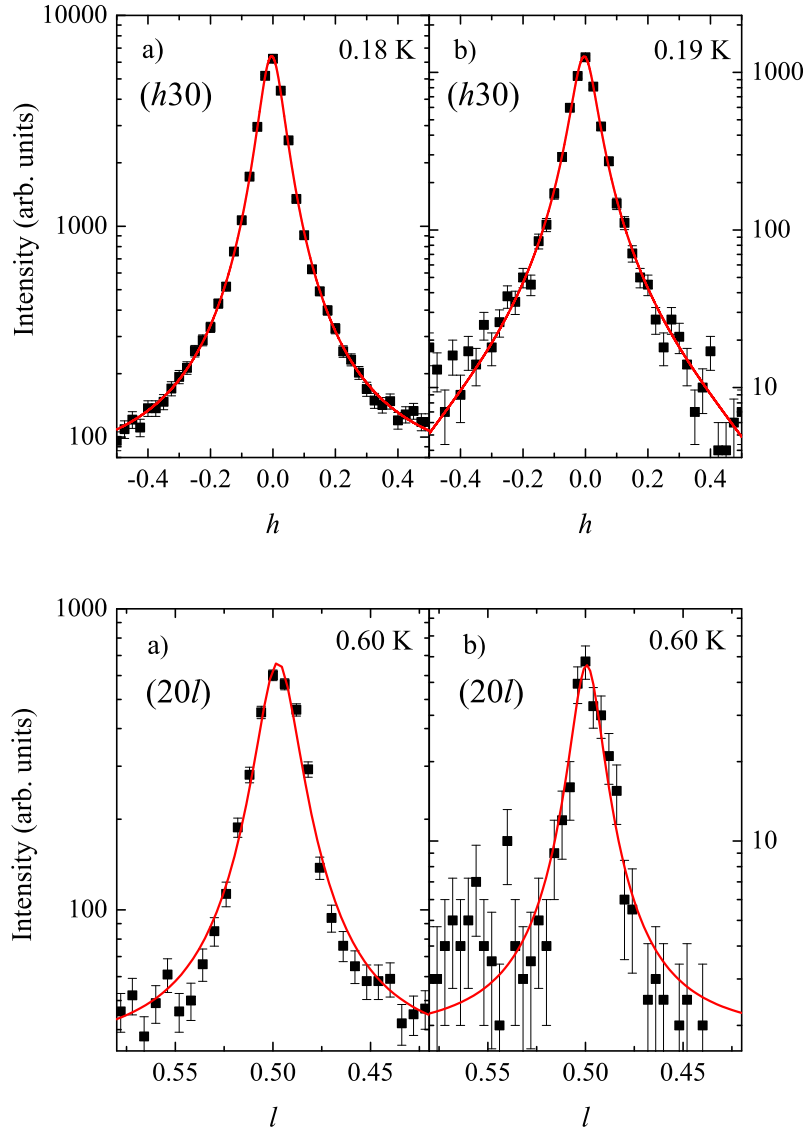
Figure 5.30: Comparison of the magnetic contribution to the scattering from $SrHo_2O_4$ when scanning across in a) 2-dimensional area detector configuration and b) energy analyser configuration for (top) the (030) peak and (bottom) along (20l). The (030) peaks are fitted with a Lorentzian distribution, where the FWHM are a) 0.052(1) Å^{-1} and b) 0.049(1) Å^{-1}. The data for (20$\frac{1}{2}$) are also fitted with a Lorentzian distribution, where the FWHM are a) 0.039(2) Å^{-1} and b) 0.029(3) Å^{-1}.

resolution of the analyser.

5.4 Diffraction in non-zero field

To investigate the field dependent behaviour of the two short range ordered spin structures seen in single crystal $SrHo_2O_4$ zero applied field, neutron diffraction patterns for two orthogonal directions in reciprocal space were measured. These were the $(hk0)$ and $(h0l)$ scattering planes, with measurements made using the WISH and D7 instruments respectively (see Sections 4.3.3 and 4.3.4). On D7, due to the high beam depolarisation during field dependent experiments, only the Z polarisation NSF and Z SF datasets were collected.

The results indicate that at low temperatures when a field applied along the c axis the diffuse magnetic scattering that appears around positions with the propagation vector $\mathbf{k} = 0$ in the $(hk0)$ plane is suppressed, and that a phase transition, which is consistent with ferromagnetic order, occurs above $\mu_0 H = 0.4$ T. Reversing the magnetic field back down to zero does not reproduce the original scattering pattern, which can only be achieved by warming up to temperatures above 0.7 K, and cooling back down. To investigate the changes to the scattering pattern from the one-dimensional spin structure in $SrHo_2O_4$, the field was applied along the b axis (since from magnetisation measurements a is the hard axis of the system, and a magnetisation plateau appeared to be stabilised when the field was applied along the b axis). At low fields, planes of scattering intensity at $(hk \pm \frac{l}{2})$ are visible, similar to those observed during the zero-field experiments, but as the field is increased, the planes split and a new diffuse scattering profile appears. From the previous polarised neutron measurement on D7 we know that the spins that participate in this structure are antiferromagnetically coupled and are pointing along the b direction, and in the new structure stabilised by the applied field this is also the case. Even larger fields suppress all of the diffuse scattering and new Bragg peaks are seen in the Z NSF cross-section, as well as new Bragg components that are orthogonal to the b direction (seen as peaks in the Z SF scattering pattern). However, by applying a field along the b direction the diffuse scattering intensity around the $\mathbf{k} = 0$ positions remains unchanged.

To further quantify the in-field behaviour of $SrHo_2O_4$, the reverse Monte Carlo

(RMC) simulations [107] are currently being carried out (in collaboration with the Goodwin group at Oxford University) to see what spin arrangements would be consistent with the observed in-field scattering patterns. Unlike conventional Monte Carlo simulations, such as those used for finding an appropriate form of the interactions between the spins that can then be used to reproduce the scattering pattern of $SrEr_2O_4$ [63], the RMC method relies on trying to minimise the difference between the data and the scattering pattern generated at every stage of the RMC refinement. The use of an extra constraint attempts to select the simplest possible spin configuration during the procedure. However, modelling the diffuse scattering a non-trivial exercise, and at this stage of the work it is too preliminary to be included in the thesis.

5.4.1 (*hk*0) plane

Measurements of the field dependence of the scattering in the $(hk0)$ plane from $SrHo_2O_4$, at 0.055 K and in a magnetic field range of 0 to 1.6 T, were made using the WISH diffractometer (see Section 4.3.3). Fig. 5.31 shows the observed magnetic scattering intensity (which was found by subtracting a 1.5 K background, collected in zero applied field, from the low-temperature datasets). To a first approximation it was assumed that the background and the nuclear peaks do not have a pronounced temperature and field dependence, however, it *does* appear to overestimate these contributions to the scattering intensity when progressively higher values of the applied field are used, and this can be seen as the oversubtraction in Fig. 5.32 and top panel of Fig. 5.33. It is apparent that when a field applied along the c axis, the diffuse magnetic scattering appears around the $\mathbf{k} = 0$ positions in the $(hk0)$ plane is suppressed, and for some reflections a new Bragg component appears above $\mu_0 H = 0.4$ T, that suggests that a transition occurs to a high field state. These new peaks are consistent with peaks which would appear if only half of the Ho^{3+} sites ordered ferromagnetically, which can be calculated by finding the positions of the nuclear peaks from $SrHo_2O_4$ if either one or the other of the crystallographically inequivalent sites was not present. The change in behaviour above 0.4 T for fields applied along the c axis in $SrHo_2O_4$ was also observed as a clear peak in the low temperature magnetisation measurements described in Section 5.2.3.
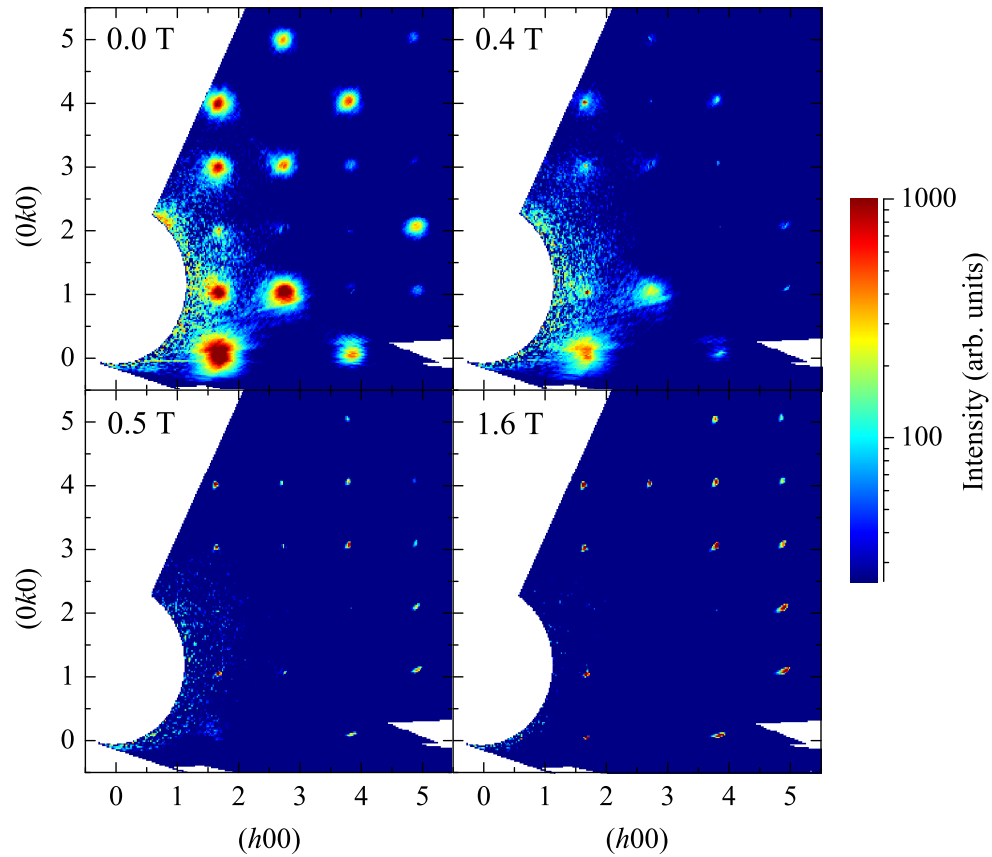
Figure 5.31: The magnetic contribution to the scattering from SrHo$_2$O$_4$ in the $(hk0)$ plane at 0.055 K in several applied fields. The magnetic component was isolated by subtracting a 1.5 K background from the low-temperature single crystal neutron diffraction data collected using WISH, ISIS.

Datasets to illustrate the field evolution of the magnetic scattering intensity for different types of reflections from SrHo$_2$O$_4$ are presented in Fig. 5.32 and the top panel of Fig. 5.33. For reciprocal space positions in the $(hk0)$ plane that had diffuse magnetic intensity in zero field, the field dependence of the scattering intensity for two different types of reflections are shown in Fig. 5.32, where (310) is forbidden by the crystal *Pnam* symmetry, and (240) is compatible with it. Reflections such as (310) lose all of their diffuse intensity upon increasing the field up to 0.5 T, and subsequent increases of the applied field do not change their magnitude. For a lot of the magnetic reflections, the diffuse scattering is suppressed by a fields of 0.5 T, with peaks such as (240) initially losing intensity, but
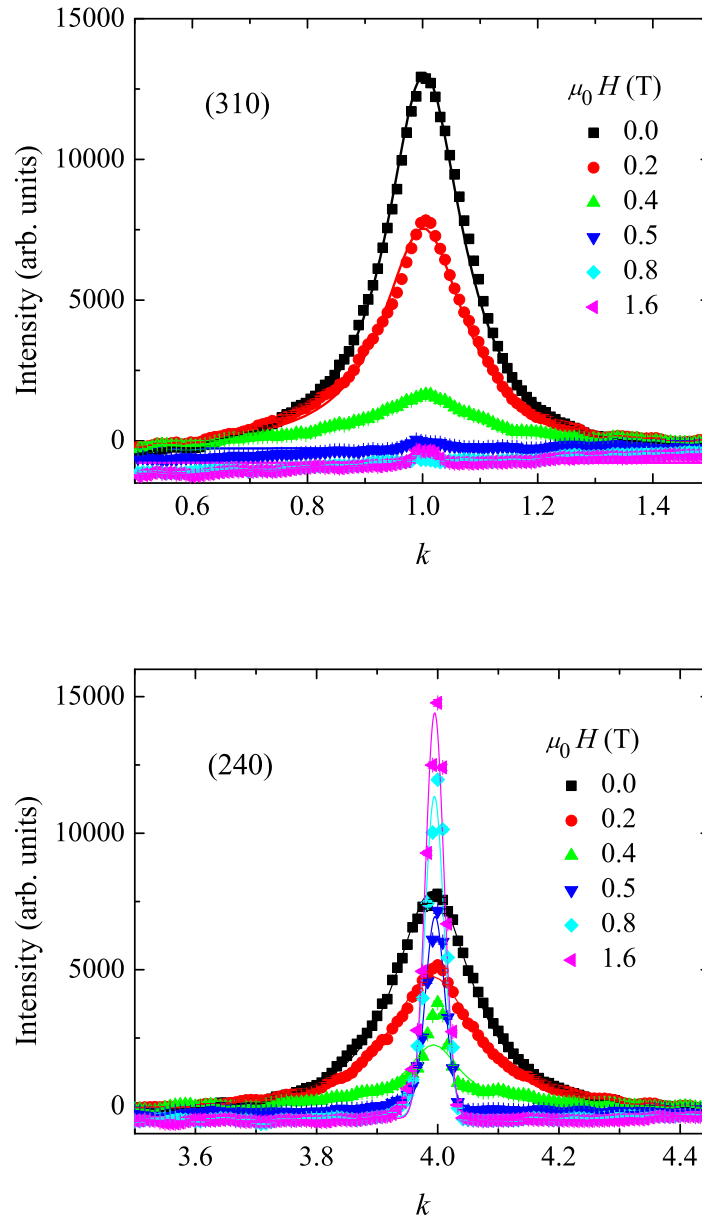
Figure 5.32: Field dependence of the magnetic scattering intensity of (top) the (310) and (bottom) the (240) reflections from SrHo$_2$O$_4$, isolated by subtracting a 1.5 K background that was measured in $\mu_0 H = 0$ T. Data were collected using the WISH instrument, ISIS. (310) is a forbidden reflection in *Pnam* symmetry, so only magnetic scattering is seen at low temperatures, and the data have been fitted using a Lorentzian distribution. (240) is an allowed reflection in *Pnam* symmetry, and here the data have been fitted using a Lorentzian distribution for $\mu_0 H \leq 0.4$ T, and using a Gaussian distribution for $\mu_0 H \geq 0.5$ T. For both peaks, the diffuse scattering that is seen at in zero field gets suppressed upon the application of higher fields, and then is completely gone by 0.5 T. For (240) above 0.5 T, a new magnetic Bragg-like component develops.
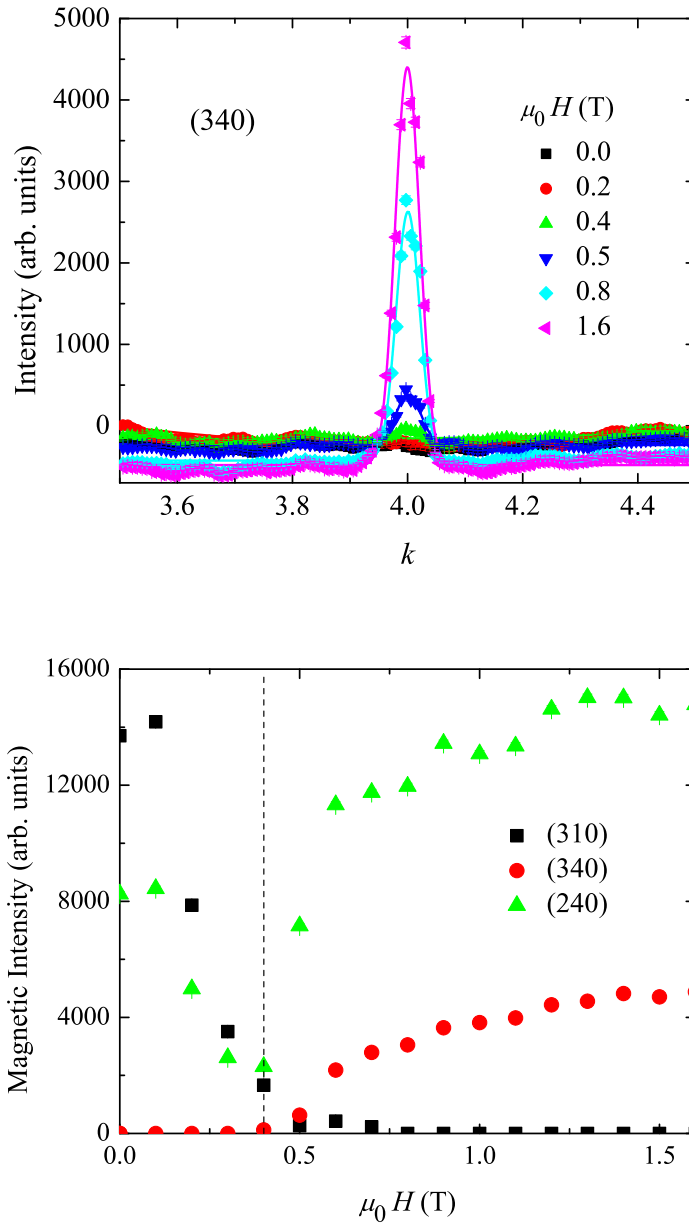
Figure 5.33: (Top) Field dependence of the magnetic scattering intensity of the (310) reflections from SrHo$_2$O$_4$, isolated by subtracting a 1.5 K background that was measured in $\mu_0 H = 0$ T. Data were collected using the WISH instrument, ISIS. Originally, (340) does not have a magnetic component, but in applied fields above 0.5 T, a large component consistent with a ferromagnetic phase starts to develop, and the data have been fitted using a Gaussian distribution. (Bottom) The summary of the temperature dependence of the magnetic intensities of the three different reflections from SrHo$_2$O$_4$.

then developing strong (and likely ferromagnetic) components. Reflections such as (340), whose field dependence is shown in the top panel of Fig. 5.33, did not have any diffuse magnetic intensity in zero field, and only develop Bragg intensities in applied fields above 0.4 T. The intensities of the new Bragg peaks that are stabilised by an applied field do not saturate, so it can be assumed that the spins are not yet completely aligned by the field. From magnetisation measurements, it is cleat that the saturation value for $H \parallel c$ is above 7 T (the highest applied field that $SrHo_2O_4$ has been measured in). Throughout, the diffuse scattering features and the ferromagnetic peaks have been fitted using Lorentzian and Gaussian distributions respectively. The field dependence of the magnitude of the magnetic intensity for the different reflections is summarised in the bottom panel of Fig. 5.33.

The one-dimensional structure does not appear to be affected by applying the field along the c axis. The highest value of the applied field used during the experiment (1.6 T) is not enough to fully align these spins along the field direction, and the situation is likely to be similar to $SrEr_2O_4$ [58], where it is shown that saturation of the moments is not achieved even in fields of 27 T. The application of the field along the c axis is not a reversible operation, as demonstrated in Fig. 5.34, where data are shown in zero field before any field is applied and for going to high field before remeasuring at 0 T. The zero field diffuse scattering intensity profile is readily recovered, however, if the sample is warmed up above 0.7 K, and cooled back down in zero field. It is important to note that this non-reversible behaviour with the applied field also occurs for $SrEr_2O_4$ at low temperatures [64], where upon cycling the field up then down the long-range order (seen as $\mathbf{k} = 0$ Bragg peaks in the $(hk0)$ plane) is destroyed and only diffuse scattering remains. In both compounds this behaviour in an applied field can be related to the single crystal susceptibility experiments where a difference can be seen between ZFC and FC measurements [59].

5.4.2 ($h0l$) plane

From the lowest temperature magnetisation measurements on a single crystal $SrHo_2O_4$ sample, it is conjectured that an up-up-down collinear spin state appears to be stabilised when a field of around 0.8 T is applied along the b axis. This state can be inferred from the location of the plateau observed in $M(H)$, a minimum in dM/dH, at a third of the value expected
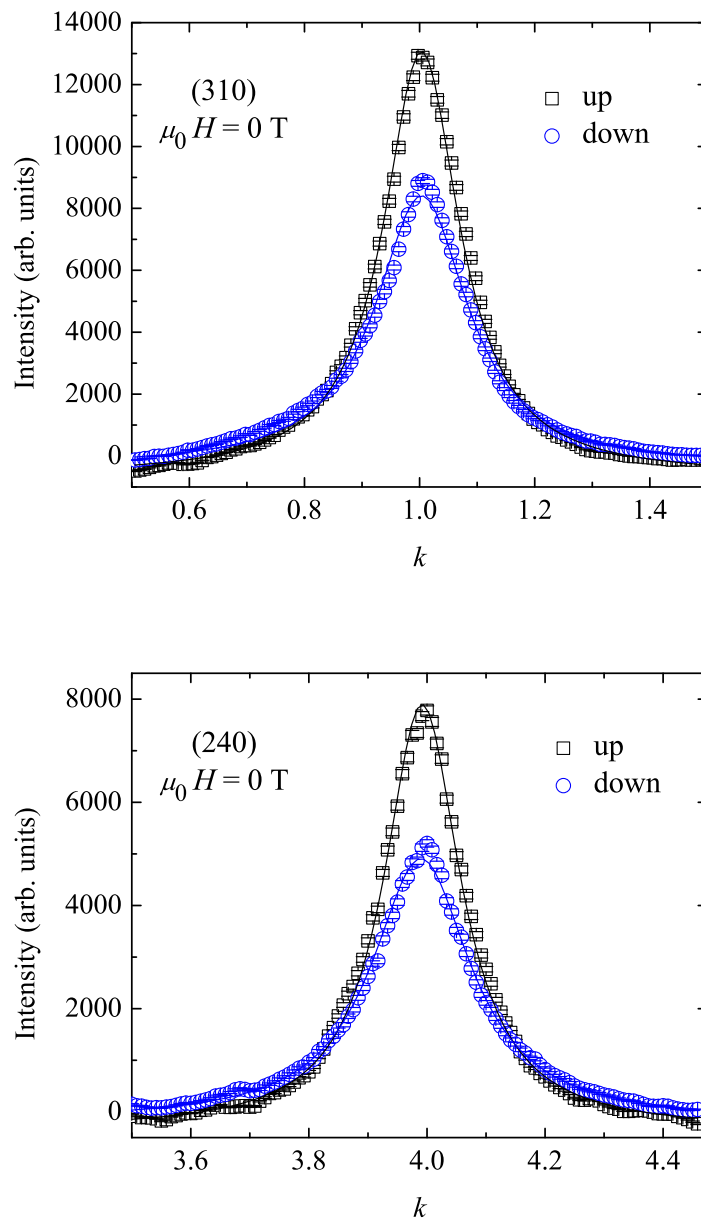
Figure 5.34: The scattering intensity of (top) the (310) and (bottom) the (240) reflections from $SrHo_2O_4$ in zero applied field. The original intensity (before switching on the field), entitled "up", and then the intensity measured after going to 1.6 T before setting the field back to 0 T, called "down". The diffuse scattering profile never recovers, and this can also be seen as a difference in the ZFC and FC susceptibility measurements, shown in Section 5.2.2.
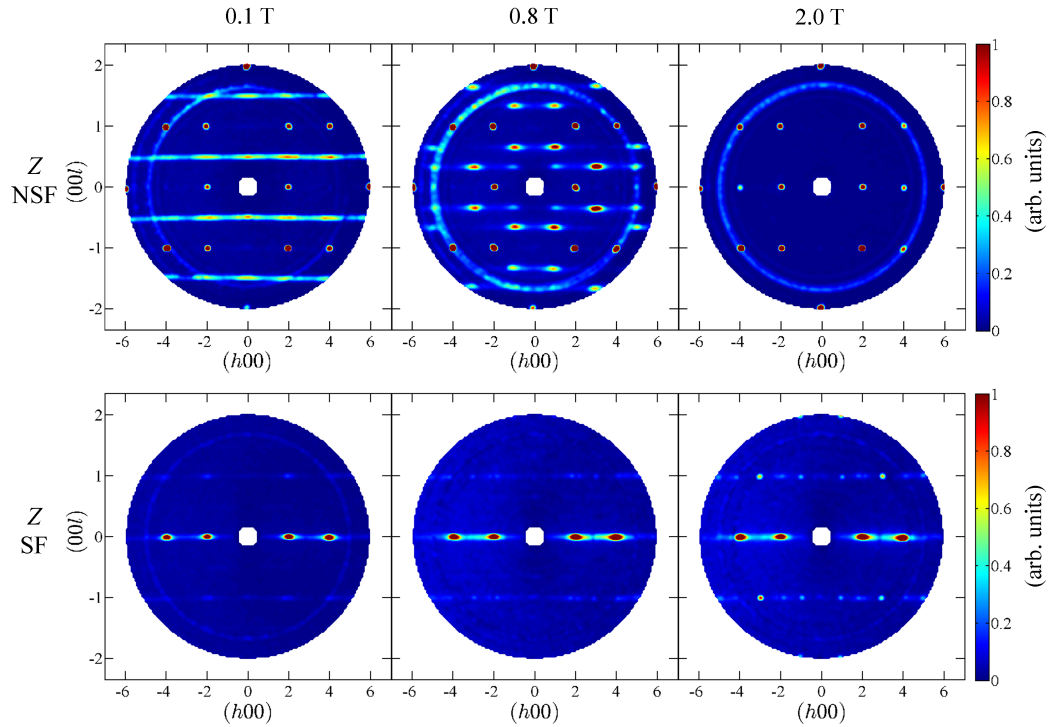
Figure 5.35: Intensity maps of the scattering from $SrHo_2O_4$ at different fields, collected at 125 mK using the D7 instrument at the ILL. In three applied fields along the b axis of 0.1, 0.8 and 2.0 T, the top row panels show the Z polarisation NSF scattering intensity and bottom row panels show the Z polarisation SF scattering contribution. The sample was cooled in field, so at 0.1 T the rods of scattering due to the $(hk \pm \frac{l}{2})$ planes, are less intense, but their structure shows relatively little difference compared to the scattering seen in the zero field measurements. By 0.8 T the rods split up into "spots", for example at $(10\frac{1}{3})$ and $(10\frac{2}{3})$, and symmetry related positions. By 2.0 T all of the diffuse scattering disappears and only intense Bragg spots are seen in the diffraction pattern, with for example a new Bragg spot at (400) in the NSF measurement. This field dependence closely follows what was expected from the bulk magnetisation measurements. The diffuse magnetic peaks associated with the $\mathbf{k} = 0$ structure are also visible in the SF measurement, and these do not appear to be affected by the field applied along the b axis. The backgrounds were measured in 0.1 T, and thus the subtraction at higher fields is not perfect so powder "rings" due to the cryomagnet and the sample environment can be seen in the data.
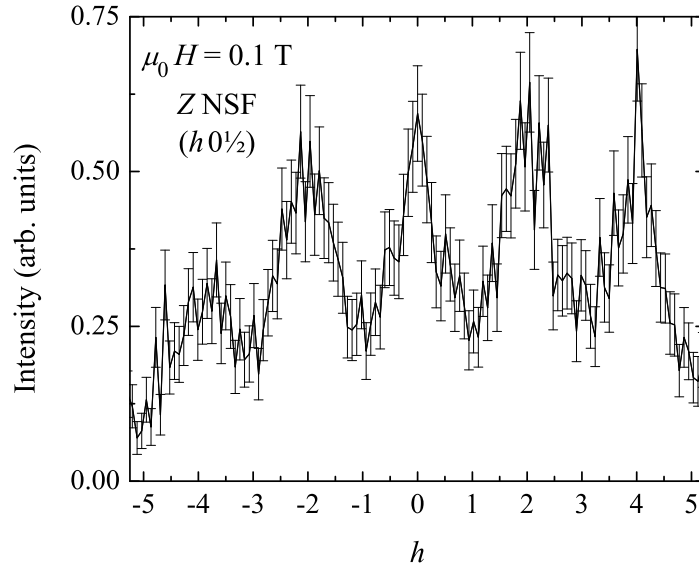
Figure 5.36: Q-dependence of the intensity of the magnetic diffuse scattering from SrHo$_2$O$_4$ along $(h0\frac{1}{2})$ in 0.1 T, extracted from the Z polarisation NSF measurement. For the rods of scattering at $(00\frac{1}{2})$ and symmetry related positions in 0.1 T there is relatively little difference in the scattering compared to zero field measurements, see Fig. 5.27, as again the scattering is most intense at even integer values of h.

for the fully saturated moment. Thus in order to investigate the field induced changes to the one-dimensional diffraction pattern from SrHo$_2$O$_4$, the field was applied along the vertical b axis (which also coincides with the Z polarisation direction) and the scattering in the $(h0l)$ plane was measured at 125 mK in the magnetic field range of 0.1 to 2.0 T using the D7 instrument (see Section 4.3.4). The top and bottom panels of Fig. 5.35 show the scattering intensity in the Z polarised NSF and SF channels, as defined previously, in applied fields of 0.1, 0.8 and 2.0 T. The background that can be attributed to scattering from the cryomagnet, dilution fridge and the copper sample holders used in the experiment was measured in 0.1 T. The background correction appears to works less well for higher fields, which means that there are some residual powder lines in the diffraction patterns in Fig. 5.35.

As in the zero field measurements, in low applied fields of 0.1, 0.3 and 0.6 T, there are rods of scattering intensity at $(00\frac{1}{2})$ and symmetry related positions in the NSF measurement. The experiment is directly comparable to the zero-field data, since the sample
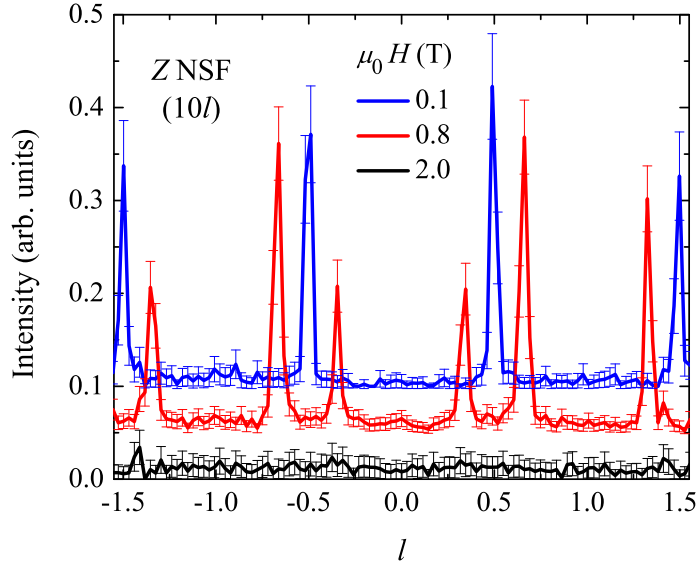
Figure 5.37: Intensity of the magnetic diffuse scattering from $SrHo_2O_4$ along $(10l)$ in three applied fields, extracted from the Z NSF measurements, with the curves offset for clarity. At 0.1 T there are rods of scattering intensity at $(00\frac{l}{2})$ and symmetry related positions, which by 0.8 T are split up into "spots" of diffuse intensity at $(10\frac{1}{3})$ and $(10\frac{2}{3})$, where the intensity at $(10\frac{2}{3})$ is twice that at $(10\frac{1}{3})$. Along $(10l)$ no new Bragg features appear and all of the diffuse scattering is gone in an applied field of 2.0 T.

is the same as the one used for the previous D7 measurements, and the only difference is that this time the sample has been FC and the data collected in a small field of 0.1 T. Thus, the structure of the magnetic scattering is similar, but it is not as intense as in the zero field pattern. To compare, a cut along $(h0\frac{1}{2})$ is shown in Fig. 5.36, again shows the pronounced Q-dependence to the scattering intensity, where maxima of intensity occur near the integer values of h. Again, no extra magnetic features due to the $(hk \pm \frac{l}{2})$ planes are observed in the spin flip channel, and only the diffuse scattering intensity along $(h00)$ is clearly visible in the measurements, which is due to the $\mathbf{k} = 0$ type structure.

By 0.8 T the rods split up into "spots", for example at $(10\frac{1}{3})$ and $(10\frac{2}{3})$, and symmetry related positions, as shown in Fig. 5.35. This scattering pattern for the up-up-down spin state is also visible in 1.0 T, however by 1.2 T the diffuse spots have lost some intensity. Fig. 5.37 shows the cuts through $(10l)$ in three fields along the l-direction. Upon increasing the applied field above 1.2 T, all of the diffuse scattering disappears and only intense new

Bragg peaks are measurable in both the Z NSF and Z SF datasets. For example, in the 2.0 T dataset is shown in Fig. 5.35 a new Bragg spot at (400) appears in the NSF measurement. Overall, there is good correlation between what was seen in the neutron scattering pattern and the critical field positions that were expected from bulk magnetisation measurements for the field applied along the b axis of SrHo$_2$O$_4$. It should be noted that for the diffuse scattering intensity due to the $\mathbf{k} = 0$ type structure (seen in the Z F channel) there is relatively little difference in the scattering pattern for all applied fields compared to zero field measurements. Complimentary measurements with unpolarised neutrons using the E2 instrument [108] at HZB also show no new information on the changes to the magnetic scattering when $H \parallel b$ compared to the D7 results.

Finally, it is interesting to note that the diffraction patterns of the field dependence of the scattering from SrHo$_2$O$_4$ for $H \parallel b$ (along which a plateau in magnetisation is stabilised) closely resemble those seen at low temperatures for the isostructural SrEr$_2$O$_4$ compound in the $(0kl)$ scattering plane in an applied field of 0.4 T [109]. (For SrEr$_2$O$_4$ the uud plateau is stabilised along the a axis.) Since SrDy$_2$O$_4$ also shows uud type of behaviour in the bulk magnetisation [59], it is likely that the up-up-down spin state is a common feature of these SrLn_2O$_4$ materials.

5.5   Inelastic scattering

As discussed in Section 2.1.3, an important factor in the study of magnetic materials is the crystalline electric field. In order to try and understand the highly anisotropic behaviour of SrHo$_2$O$_4$, inelastic neutron scattering was used to determine the positions of CEF levels. The experiments were performed on powder samples of SrHo$_2$O$_4$, using the IN4 and IN5 spectrometers, described in Section 4.4, to map out a large energy range. The CEF of SrHo$_2$O$_4$ is very complicated due to the presence of 4 Ho^{3+} ions on each of the two crystallographically inequivalent positions in a unit cell. Since Holmium is a non-Kramers ion, and the symmetry of the sites is quite low, a large number of CEF levels are expected. Previously, some inelastic neutron scattering data has been published [104, 110], but so far no crystal-field scheme has been established for this material.
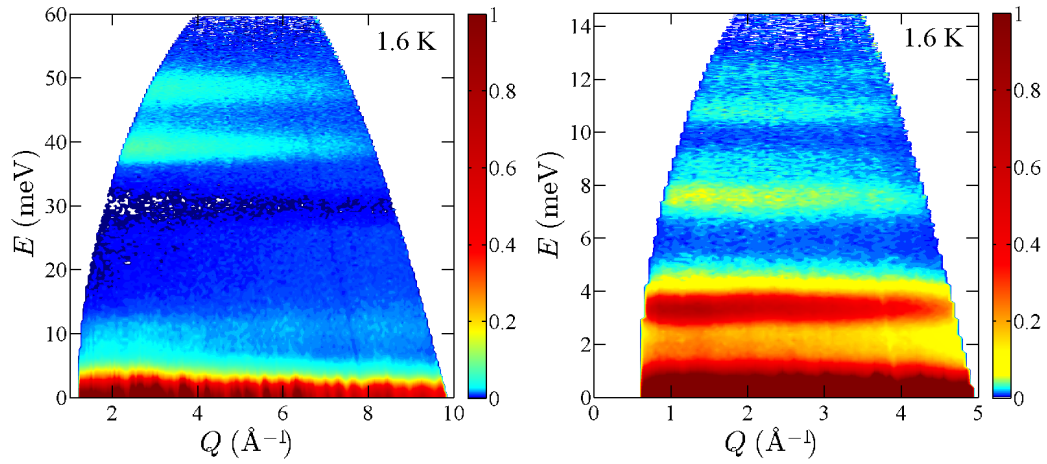
Figure 5.38: $S(Q, \omega)$ for (left) $\lambda = 1.1$ Å and (right) $\lambda = 2.2$ Å, at 1.6 K. The data have been collected using the IN4 instrument.

In SrHo$_2$O$_4$ a broad peak in the specific heat at $\sim$3 K is associated with short-range magnetic correlations, which have been seen as the formation of $(hk \pm \frac{l}{2})$ diffuse scattering planes using neutron diffraction (Section 5.3.2). As the temperature is lowered, these diffuse features get sharper, and below 0.7 K, a second set of diffuse peaks appear and coexist with the one-dimensional spin structure. We have recently started collaborating with a theory group from the University of Birmingham regarding the physics of SrHo$_2$O$_4$, and they have suggested that at temperatures above which the one-dimensional correlations become very strong, the local field would be nearly random, but below $\sim$3 K the spins will feel a static exchange field which pins them in place, and the crystal field levels will be shifted by this exchange field as the spins begin to short-range order in the one-dimensional structure. So the crystal field levels associated with the one-dimensional short-range ordered system will shift up by the exchange-interaction energy as the temperature is lowered, while the position of the crystal field levels that correspond to the **k** = 0 short-range ordered structure would not change their position with temperature. By carefully studying the changes in CEF as a function of temperature it should possible to resolve some of the complex outstanding issues about the CEF for this material, and would explain why previous investigations have been insufficient to fully solve the CEF of SrHo$_2$O$_4$.

The higher energy excitations have been measured on a powder sample of SrHo$_2$O$_4$

Figure 5.39: Temperature dependence of the inelastic scattering from $SrHo_2O_4$, constructed from integrating over all of the $S(Q, \omega)$ data collected using the IN4 spectrometer, for (top) $\lambda = 1.1$ Å and (bottom) $\lambda = 2.2$ Å, here the datasets for different temperatures have been offset for clarity. Note that, for example, the ~48.1 meV and the ~7.5 meV crystal field levels change position with temperature, whereas the 38.1 meV and 10.8 meV levels do not.

using the IN4 spectrometer, and the $S(Q, \omega)$ are shown in Fig. 5.38, with the integration over all Q shown in Fig. 5.39. The low temperature data collected at 1.1 Å appear to be much the same as the 5 K data shown in [110], except that since the temperature dependence was measured it is obvious that some of the CEF levels do shift to higher energies as the temperature is lowered. For example, from Fig. 5.39, the $\sim$48.1 and $\sim$7.5 meV levels change position with temperature, whereas other levels such as 38.1, 10.8, and 12.2 meV do not. Measurements of a non-magnetic analogue, $SrLu_2O_4$, allowed us to estimate the phonon contribution to the scattering. This was found to be not significant to the higher energy data (the inelastic CEF levels are easy to see in $SrHo_2O_4$ due to its large magnetic moment) and below 15 meV no optical phonon modes can be seen.

The data for lower energies were collected using the IN5 instrument, with the lowest temperatures reached using a dilution refrigerator, in order to map out the temperature dependence of the CEF and see what changes occur as the temperature is lowered beyond the second short-range ordering temperature of $\sim$0.7 K. The some of the data are shown in Figs. 5.40$-$5.43, and it is obvious that there are a large number of low energy CEF modes, a lot of which have a pronounced temperature dependence. The data collected at 1.6 K on IN5 is broadly comparable to that published in [104]. However, the CEF level scheme presented in [104] is incorrect because even at 1.6 K the crystal field levels are not in their ground state positions, and in fact there are small *distinct* levels, such as at 0.75, 0.94, 1.06, and 2.71 meV that can only be visible at the lowest temperature when the thermal shift and broadening of the CEF levels is at a minimum. Again, from the measured temperature dependence of the inelastic scattering from $SrHo_2O_4$ it is obvious to see that some CEF levels do, and some do not shift in energy as the temperature is lowered, which has never been established from previous measurements by other experimental teams.

Another important observation about the CEF excitations in $SrHo_2O_4$ which has never been reported is that as the temperature is lowered between 20 K and 1.6 K (the temperatures between which the one-dimensional scattering becomes strongly correlated) some of the crystal field excitations become dispersive along Q. An example of this behaviour for the 3.53 meV CEF level is shown in Fig. 5.40. The minimum of the dispersion for this level corresponds to the location of the $(00\frac{1}{2})$ peak observed in the elastic scattering data. The
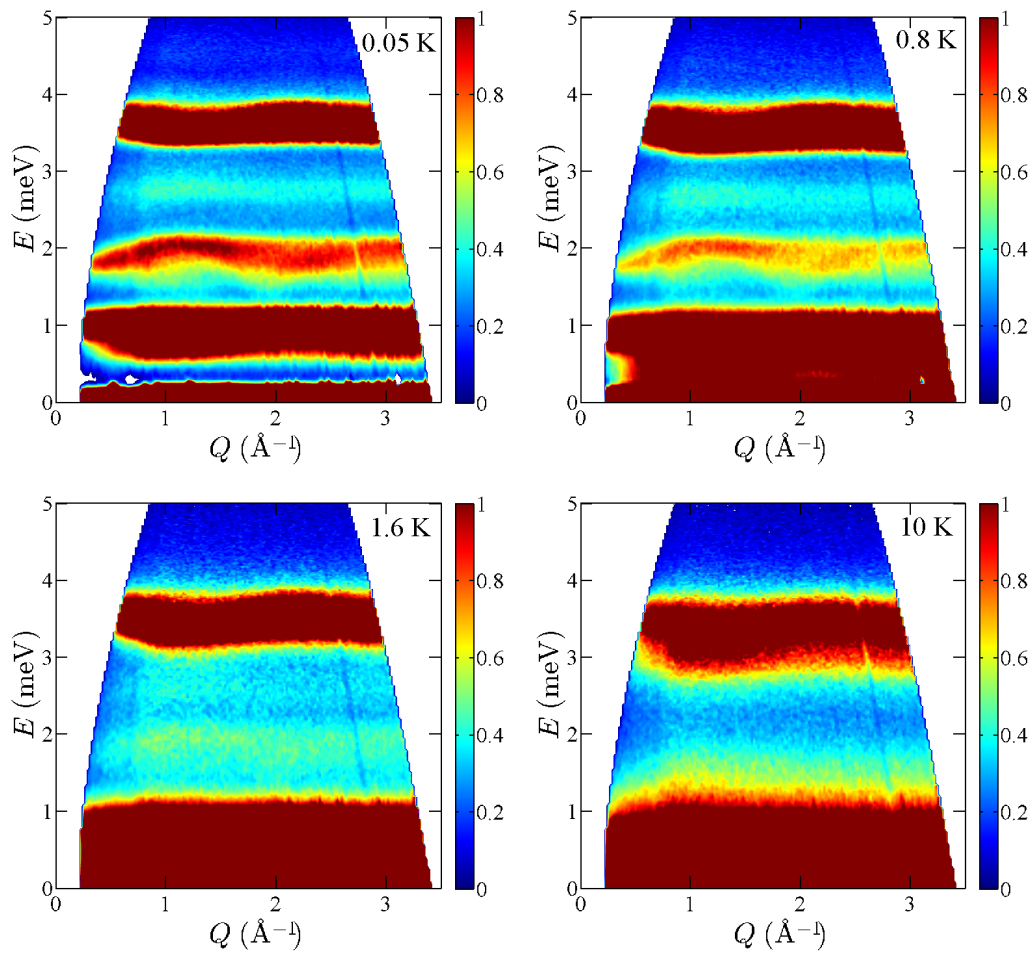
Figure 5.40: $S(Q, \omega)$ for $\lambda = 3.4$ Å at several temperatures. Note that not only do some of the CEF levels shift to higher energy with decreasing temperature, but the there is also a change in the *dispersion* of some of the levels as well, for example the 3.53 meV crystal field level. The data have been collected using the IN5 instrument.
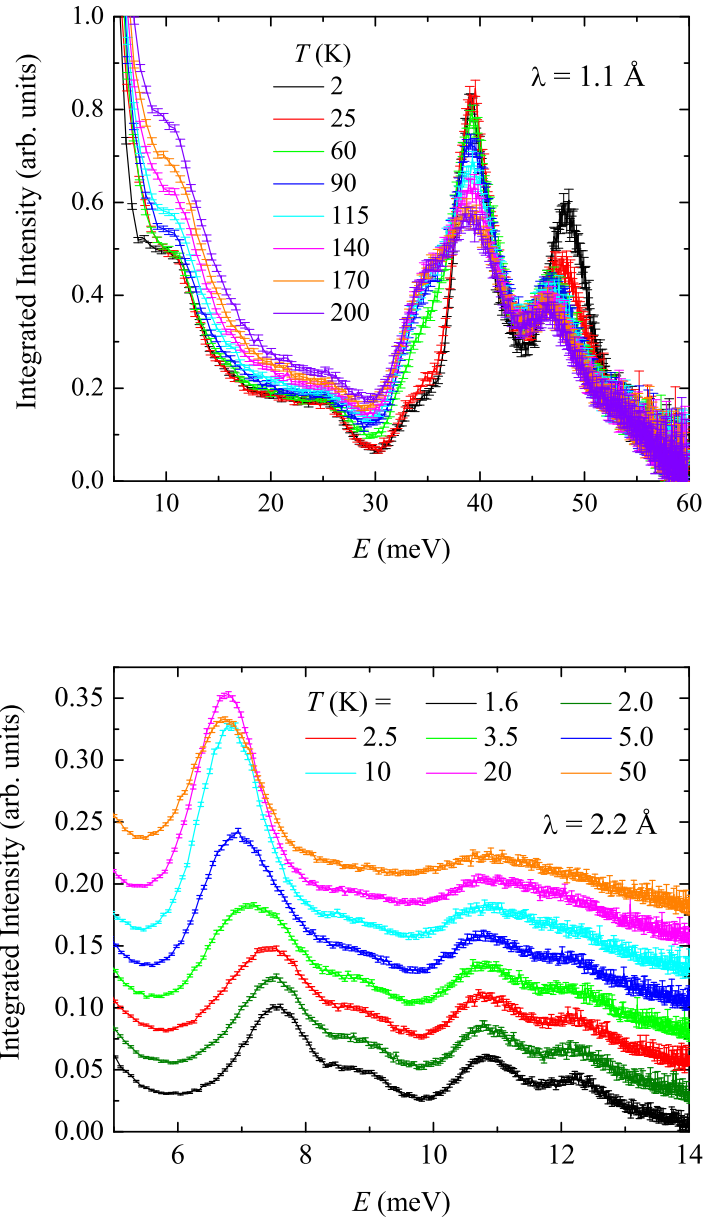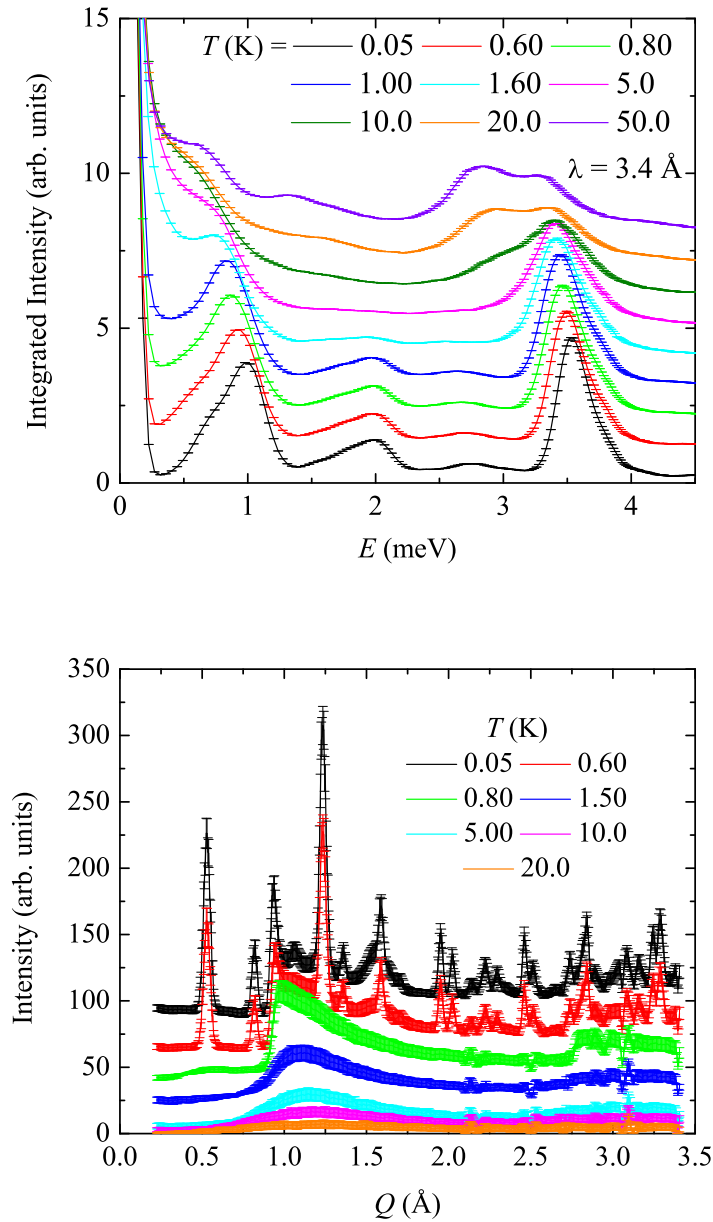
Figure 5.41: (Top) Temperature dependence of the inelastic scattering from $SrHo_2O_4$, constructed from integrating over all of the $S(Q, \omega)$ data collected using the IN5 spectrometer for $\lambda = 3.4$ Å. The curves have been offset for clarity. (Bottom) Temperature evolution of the magnetic scattering of $SrHo_2O_4$ (curves have been offset for clarity), isolated by subtracting a 50 K background from the low temperature runs. Below 0.7 K resolution-limited $\mathbf{k} = 0$ peaks can be seen which are directly comparable to the data collected on GEM (see Fig. 5.5).
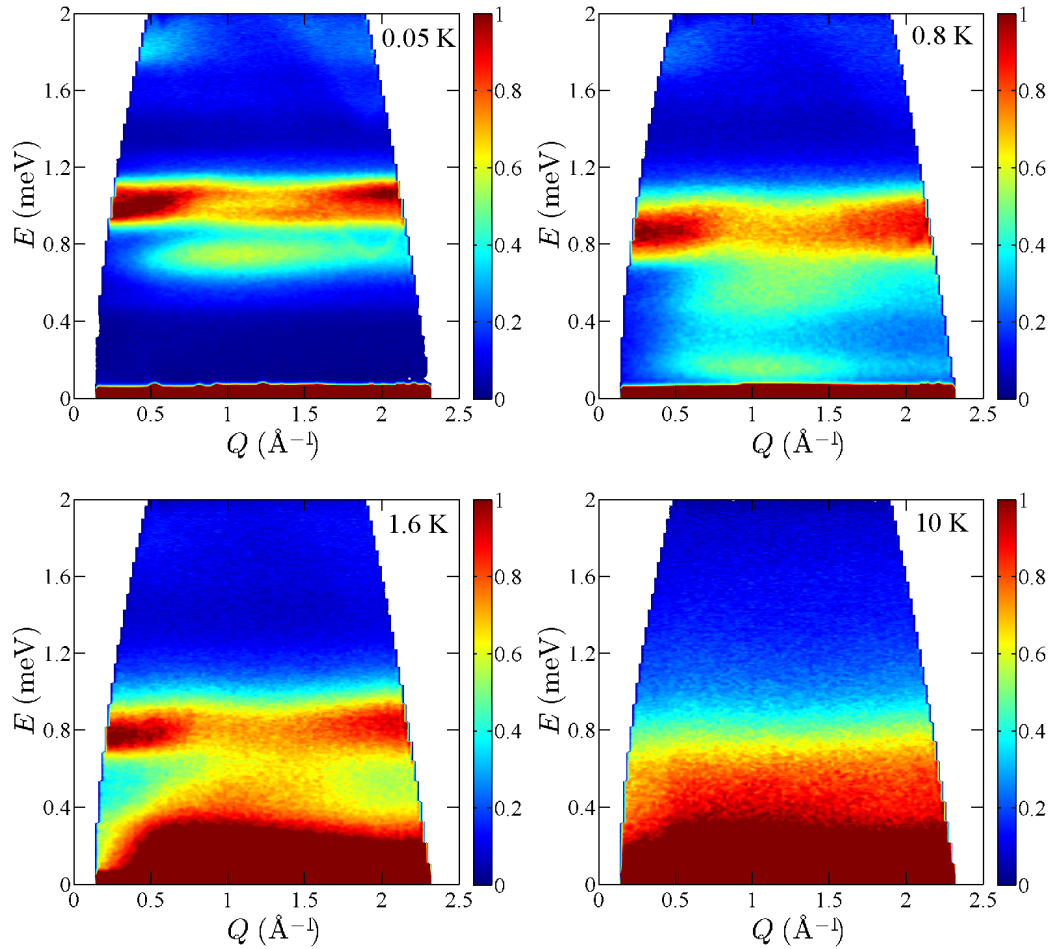
Figure 5.42: $S(Q, \omega)$ for $\lambda = 5.0$ Å at several temperatures. Again, the CEF levels shift and become dispersive upon changing the temperature, and new thermally excited features (that are not present at the lowest temperature) are also seen only above 0.7 K - the temperature at which the diffuse scattering is seen at **k** = 0 positions. The data have been collected using the IN5 instrument.
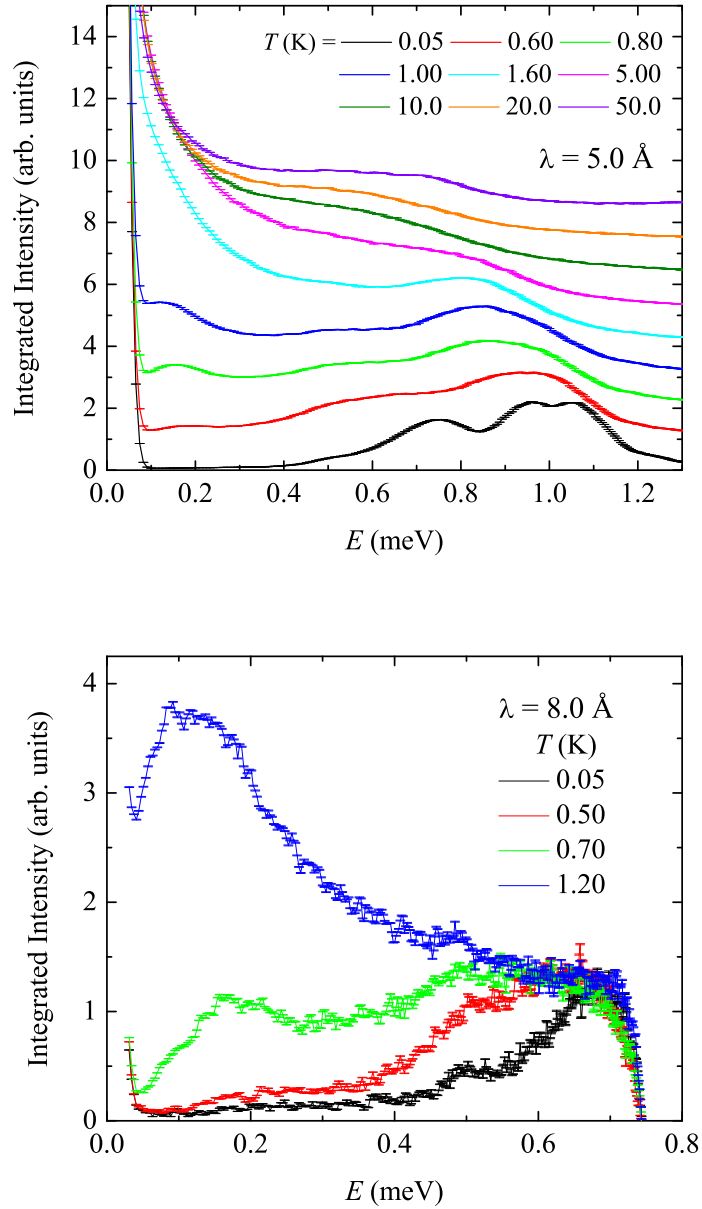
Figure 5.43: Temperature dependence of the inelastic scattering from $SrHo_2O_4$, constructed from integrating over all of the $S(Q, \omega)$ data collected using the IN5 spectrometer, for (top) $\lambda = 5.0$ Å, the datasets for different temperatures have been offset for clarity. (Bottom) Data collected with $\lambda = 8.0$ Å to look at the thermally excited feature.

$E = 0$ elastic line for the $\lambda = 3.4$ Å data are shown in the bottom panel of Fig. 5.41, and these are directly comparable to the data collected using the GEM instrument on a powder sample of $SrHo_2O_4$, shown in Fig. 5.5. Again, the magnetic peaks that appear below 0.7 K are resolution limited.

The thermal occupation of the CEF levels changes, but from the temperature dependence it is possible to work out which inelastic features are enhanced by temperature and hence compensate for this in any CEF analysis. Also a new thermally excited mode at 0.12 meV, which may be related to transitions between crystal field levels, only appears above 0.7 K as shown in Figs. 5.42 and 5.43, and thus can be excluded from the CEF scheme. At the lowest temperature of 0.05 K, the positions of the CEF levels in the $SrHo_2O_4$ system derived from inelastic neutron scattering measurements are 0.75, 0.94, 1.06, 1.53, 1.91, 2.71 and 3.53 meV; and several more possible levels at 0.55, 1.15 and 3.85 meV (these are small, and from powder data alone it is difficult to judge whether these shoulders are peaks in their own right); as well as the 7.5, 8.9, 10.8, 12.2, 38.1 and 48.1 meV higher-energy levels which have only been measured at 1.6 K. From all of the measurements carried out at all the different incident wavelengths used during the experiments we have observed a possible total of 16 crystal field levels, with another thermally excited feature at ~0.12 meV. The detailed coverage of the temperature dependence of the inelastic spectrum has been used to separate out which CEF levels belong to which Ho^{3+} subsystem, and now it may be possible to try to fit the the CEF parameters for each subsystem separately.

Overall, it is clear that the measurements have helped to make progress in order to ascertain the nature of the crystal field of $SrHo_2O_4$. Currently work in underway on a theoretical interpretation of the crystal field scheme for this material and the anomalous Q dependence behaviour that develops for some of the CEF levels, as well as the fitting of the contributions to the CEF from the two different Ho^{3+} sites separately.

5.6   Discussion

An investigation into the magnetic properties of the frustrated antiferromagnet $SrHo_2O_4$ has been presented in this this chapter. In order to facilitate the research, polycrystalline

samples have been produced using solid state reactions, and these have been assessed to be of high purity by refining a structural model using x-ray diffraction data. The higher temperature measurements of magnetic susceptibility and magnetisation of $SrHo_2O_4$ are directly comparable to the data published in [43] that shows no long-range order down to 1.8 K, but the data collected at lower temperatures indicate that some kind of ordering transition takes place below 0.7 K. The high temperature susceptibility follows the form of the Curie-Weiss law, and the value obtained for the effective moment, 10.54(2) μ_B, is in agreement with that given in [43], of 10.50(1) μ_B, and Hund's rules predictions for the Ho ion, calculated to be 10.60 μ_B. Also, the Weiss temperature of $-17.2(4)$ K indicates the presence of fairly strong antiferromagnetic exchange, and this is again in line with the value obtained in [43] of $-16.9(5)$ K.

At temperatures above 1.8 K, neutron diffraction measurements on powder samples of $SrHo_2O_4$, are directly comparable those in [43], where short-range scattering which has the profile of a low dimensional spin structure is seen. However, as the temperature is reduced below 0.7 K, additional magnetic scattering peaks are visible, and these peaks are resolution limited on GEM (found by comparing the FWHM of these peaks with that of the nuclear reflections at appropriate Q). This two component diffraction pattern is similar to that observed for $SrEr_2O_4$ [58] at the lowest temperature, although in the case of $SrEr_2O_4$, the scattering from the low-dimensional structure appears to be weaker and it is visible at much lower temperatures compared to $SrHo_2O_4$. The magnetic structure of $SrEr_2O_4$ could not be refined using the data at the lowest temperature where the diffuse scattering was strongest [58], but the structure proposed is identical to that of $SrHo_2O_4$, where only half of the spins are coupled in ferromagnetic chains with each chain coupled antiferromagnetically to its neighbours, as shown in Fig. 5.1.3. Overall, it is important to note that both $SrEr_2O_4$ and $SrHo_2O_4$ show a clear coexistence of two distinct antiferromagnetic components to the zero-field magnetic structure at low temperatures, and this is a consequence of the two different sites for the Ln^{3+} ions in the unit cell.

Bulk property measurements of magnetic susceptibility (and magnetisation) on single crystal samples have revealed that there is a large anisotropy in the behaviour of $SrHo_2O_4$ when the field is applied along the different principal axes. The susceptibility curves were

142

fitted to the Curie-Weiss law for $SrHo_2O_4$ between 100 and 400 K, and most of this temperature region lies in between the 12.2 and 38.1 meV CEF levels, so the behaviour of $\chi(T)$ here is mostly linear. Large anisotropies in the high-temperature susceptibility curves are also observed for the $SrEr_2O_4$ and $SrDy_2O_4$ [59], and it seems likely that this would be the result of low-lying crystal field levels in all of the compounds, such as those described in Section 5.5 for $SrHo_2O_4$, and some preliminary reports of low-energy CEF levels for $SrEr_2O_4$ and $SrDy_2O_4$ exist in [111] and [110] respectively.

In both $SrHo_2O_4$ and $SrEr_2O_4$ a cusp in low-temperature susceptibility measurements indicates a transition to long-range order, which correlates to the development of a $\mathbf{k} = 0$ component seen in the powder neutron diffraction data. For $SrEr_2O_4$ this transition temperature can be observed as a sharp λ-anomaly in the specific heat [58], but for $SrHo_2O_4$ the situation is somewhat complicated by the large nuclear Schottky anomaly, which needs to be carefully modelled before any further conclusions can be drawn from the data. In the specific heat measurements, however, there is also an indication of the development of short-range correlations, which is not evident from the susceptibility data, for the $SrLn_2O_4$ compounds. At temperatures higher than the observed transition temperatures for $SrHo_2O_4$ and $SrEr_2O_4$, broad peaks are seen in the specific heat. For $SrHo_2O_4$ (see Section 5.2.4) this occurs around $\sim$3 K, and can be correlated with the development of strong low-dimensional scattering intensity in the neutron diffraction data. A similar broad peak centred around 1.3 K, in the specific heat is also observed for $SrEr_2O_4$ [58], which can also be correlated with the onset of low-dimensional scattering most easily seen at the lowest temperatures in the powder data.

Further investigation into the unusual low-temperature magnetic structure of $SrHo_2O_4$ was achieved by measuring the neutron diffraction patterns in three planes orthogonal to the principal axes of the crystal, so that it would be easier to isolate the two magnetic components. It was found that these are in fact two distinct types of *short-range* magnetic order, one of which can be seen as diffuse peaks that appears around the $\mathbf{k} = 0$ positions in the $(hk0)$ scattering plane at temperatures below 0.7 K, and the Ho^{3+} spins that participate in this short-range structure are antiferromagnetically coupled and are collinear with the c axis. The second type of magnetic order forms nearly perfect planes of diffuse scattering which

143

appear as "rods" of scattering intensity seen in both the $(h0l)$ and $(0kl)$ planes in recipro-cal space at $Q = (00\frac{1}{2})$ and symmetry related positions. This observation suggests that the second type of short-range order present in $SrHo_2O_4$ is almost perfectly one-dimensional in nature. From the *XYZ*-polarised neutron measurements it is obvious that the spins that par-ticipate in this second structure are antiferromagnetically coupled and point along the b axis. The planes of diffuse scattering have internal structure, with maxima of intensity occurring at even integer h positions at the lowest temperature. Both types of diffuse scattering in $SrHo_2O_4$ appear to be elastic within the energy resolution of the analyser.

The coexistence of two distinct types of magnetic scattering in $SrHo_2O_4$, arising from the two crystallographically inequivalent sites for the Ho^{3+} ions in the unit cell, is similar to what is observed in zero applied field and at low-temperatures in $SrEr_2O_4$ [63]. Both compounds have a magnetic component with the propagation vector $\mathbf{k} = 0$ in the $(hk0)$ plane below a well-defined transition temperature, as well as the one-dimensional scattering that is observed at much higher temperatures. In $SrEr_2O_4$ a simple zigzag ladder model with nearest neighbour interactions and small coupling between the ladders is compatible with the observed diffuse scattering data [63]. This type of zigzag ladder model would also seem to be appropriate for $SrHo_2O_4$, and preliminary calculations (for Ising-like spins) using mean-field methods [112] show that optimised ratios of exchange constants correctly reproduce the form of the magnetic diffuse scattering patterns from $SrHo_2O_4$ [113]. It is still too early to fully describe the work here, but it appears that the data are consistent with a model of two independent magnetic sublattices of zigzag ladders with strong coupling along the the ladders and weak inter-ladder coupling. This weak coupling can be achieved in multiple ways that give very similar results for the position of the diffuse scattering features but vary in their relative intensities, and this is the focus of current investigations.

A final consideration of the zero-field diffraction data would be to try and under-stand whether there is a real difference between the powder and single crystal behaviour of $SrHo_2O_4$, since the data collected using the GEM instrument (and the cut of the elastic line from data collected using the IN5 spectrometer), the $\mathbf{k} = 0$ peaks that appear below 0.7 K appear to be as sharp as the nuclear Bragg reflections, but in the single crystal data these are broad *diffuse* peaks. During the high-resolution study of $SrHo_2O_4$ using the D10 instru-

ment, no mosaic spread was detected for any of the reflections and there was no shoulders or spread to the patterns so it can be assumed with some confidence that the single crystal samples are of single domain. The correlation length of the scattering in the $(hk0)$ plane have been found to be $L \approx 150$ Å at 0.18 K, which is not larger than the crystallite size of the powder which has been estimated to be $\sim$1500 Å by applying Scherrer's formula to a substantial collection of reflections from the $SrHo_2O_4$ x-ray diffraction data. So, perhaps it is just the resolution of the powder neutron scattering instruments that may not be high enough to distinguish between true long-range order and the strongly correlated diffuse scattering present in $SrHo_2O_4$.

At low temperatures and in an applied field, for $SrHo_2O_4$ the a axis is a hard magnetisation direction, but for an applied field (of $\sim$0.8 T) along the b axis a uud state is stabilised, and when the field is applied along the c axis, only a single transition takes place. This magnetisation processes appear to be quite similar to those in $SrEr_2O_4$ and $SrDy_2O_4$, where there is one hard direction for magnetisation, and then a uud plateau is stabilised when the field is applied along another axis, and with the c axis only showing a single transition in these compounds [59]. It is likely that the reason that the hard axis ($H \parallel b$) and the uud axis ($H \parallel a$) in $SrEr_2O_4$ compared to the hard axes ($H \parallel a$) and the uud axes ($H \parallel b$) for $SrHo_2O_4$ and $SrDy_2O_4$ are swapped around is due to the distortion of the 4f charge density for the different rare earth ions as induced by the crystal field. The distortion is associated with a magnetic anisotropy, thus leading to an easy direction of magnetisation which in an almost identical environment of the Ln ions would be orthogonal for Er compared to Ho and Dy from simple electrostatic considerations. It is also quite likely that the uud state, which appears to be a common feature of the $SrLn_2O_4$ compounds, is due to the fact that on a triangular spin ladder it is quite easy to arrange spins into a uud structure. A couple of points are currently impeding further comparative analysis of the magnetisation process in the $SrLn_2O_4$ compounds. Firstly, neutron diffraction indicates that two short-range magnetic components coexist in $SrHo_2O_4$, a scenario similar to that found in $SrEr_2O_4$ where a long-range ordered component coexists with a short-range low-dimensional spin structure, and that the spins that participate in these structures are constrained to point along two separate crystal axes. However, the low-temperature magnetic structure of $SrDy_2O_4$ is as

yet unknown, so no comparisons may be drawn, but preliminary powder neutron diffraction measurements indicate that no long-range order is present in this compound down to at least 20 mK in zero field, but some long-range components to develop in an applied field [62, 114]. Secondly, whereas for $SrEr_2O_4$ (and from preliminary work for $SrHo_2O_4$) a reliable model for the strength and the sign of the magnetic interactions present appears to be based on a zigzag ladder model, but no such descriptions exist for $SrDy_2O_4$.

The magnetisation measurements can be directly correlated with single crystal neutron scattering data collected for both $SrHo_2O_4$ and $SrEr_2O_4$. In both compounds the field was not applied along the hard axis of magnetisation, but both $H \parallel c$ and H applied along the suspected uud axis were measured. With $H \parallel c$ there is evidence of only a single in-field transition in $SrHo_2O_4$ above 0.4 T, such that the diffuse scattering around the $\mathbf{k} = 0$ positions is suppressed and then peaks consistent with a ferromagnetic arrangement appear. In $SrEr_2O_4$ a similar situation occurs when the field is applied along the c axis, where small applied fields initially destroy the long-range order and produce a diffraction pattern similar to that of the lozenge arrangement in zero-field $SrHo_2O_4$, before also appearing to a long-range ordered arrangement that is different to the zero-field phase, but about which nothing else is currently known [64]. The similarity of the behaviour of $SrHo_2O_4$ and $SrEr_2O_4$ with $H \parallel c$ is probably the result of the similar positions of the magnetic Ln^{3+} ions in these compounds and similar exchange interactions between the magnetic ions along the zigzag chains. If the field is reduced to zero the original long-range order of $SrEr_2O_4$ is not recovered, and only diffuse scattering persists, rather like in $SrHo_2O_4$ where if the field is increased and then decreased, the diffuse scattering intensity is not recovered. Both in $SrHo_2O_4$ and $SrEr_2O_4$ the largest difference between ZFC and FC data appears when $H \parallel c$.

In $SrHo_2O_4$ with $H \parallel b$, and $SrEr_2O_4$ with $H \parallel a$, the double peak seen in dM/dH confines a plateau in the magnetisation for certain values of the applied field. This new state can be seen in the single crystal neutron diffraction data, as the "rods" of low-dimensional scattering visible in zero and low fields disappear, and a new diffuse scattering profile can be observed. This structure does not have the profile of a one-dimensional phase, as the diffuse scattering is concentrated into distinct "spots" of intensity, and this is likely to be the uud phase stabilised by an applied field. The modelling of the interactions consistent

146

with this diffraction pattern is currently underway, and once this is achieved some Monte-Carlo simulations can be performed to look at the spin correlations in real space. As well as this, RMC calculations are also being attempted in order to fit the $SrHo_2O_4$ data. Applying even stronger magnetic fields along the uud axis suppress all of the diffuse scattering and new Bragg peaks are seen in the diffraction patterns. For both $SrHo_2O_4$ and $SrEr_2O_4$ the scattering due to the $\mathbf{k} = 0$ type structure in which the spins are aligned along the c direction, and which can be seen as peaks along $(h00)$ seems mostly unaffected by applying the field along the b axis. Unfortunately no single crystal data in zero or in applied fields exists for $SrDy_2O_4$, but since this compound also shows similar behaviour to $SrHo_2O_4$ and $SrEr_2O_4$ in the bulk magnetisation [59], it is likely that the up-up-down spin state is a common feature of these SrLn_2O_4 materials.

On the whole, it seems that for $SrHo_2O_4$ and $SrEr_2O_4$ the two sites of the rare earth ions act almost independently, and the magnetic moments on these two sites are constrained to lie along two separate principal crystallographic directions. This seems rather surprising, given that the environments of the two Ln^{3+} sites in a unit cell are almost identical, but a reasonable explanation for the origins of the highly anisotropic behaviour would likely be due to the crystal field. In $SrHo_2O_4$, in particular, both of the Ho^{3+} sites appear to have strong Ising-like characteristics due to CEF, similar to what is found for Holmium in other families of compounds, such as the pyrochlore titanates. In order to try and understand how this may be the case, the CEF of $SrHo_2O_4$ was investigated. Since, Ho is a non-Kramer's ion, this is not a trivial problem and a lot of CEF levels were expected (since any degeneracy would be accidental). A possible way to try and simplify this problem and separate which crystal field levels belong to which Ho^{3+} sub-system, as suggested by the theory group, would be to see which levels were shifted to higher energies as the temperature was lowered below the temperature where the one-dimensional correlations become particularly strong (and this was estimated from the specific heat and the diffraction measurements to be $\sim$3 K). At present, for $SrHo_2O_4$, the fitting of the CEF levels is being carried out, and further theoretical analysis on the nature of the dispersion of the CEF levels (which also occurs below $\sim$3 K) is ongoing. Also, the results of powder inelastic scattering measurements on $SrHo_2O_4$ would merit further experimental study using triple axis neutron diffraction on

single crystal samples. For $SrEr_2O_4$, some data on the inelastic scattering data is already available [111], but so far no crystal field scheme could be fitted. Overall, a complete description of the CEF levels would definitely be helpful in understanding the origins of the highly anisotropic behaviour found in these $SrLn_2O_4$ compounds as well as in identifying the roots of the dramatic differences exhibited in the magnetisation process.

In summary, $SrHo_2O_4$ is a complex system with several competing magnetic interactions. The spins behave as one-dimensional entities, embedded in a low-dimensional spin chain system with only small interactions between the chains, and no long-range order down to the lowest measured temperatures. The diffraction work on $SrHo_2O_4$ is essentially complete, but it remains to finish modelling the interactions and spin arrangements that can give rise to the observed diffuse scattering patterns in both zero and applied magnetic fields. There is also some possible extensions to the work presented here, and recently some of these avenues have started to be explored by measuring the inelastic spectra from $SrHo_2O_4$. Compatible crystal field schemes and theoretical explanations for this data are currently being sought, and the interpretation may be aided by further single crystal inelastic scattering experiments.

Chapter 6

Magnetic properties of SrGd$_2$O$_4$

This chapter is dedicated to the study of the magnetic properties of the insulating rare earth antiferromagnet SrGd$_2$O$_4$, in both its polycrystalline and single crystal form. The crystal structure, and hence the arrangement of the magnetic Gd^{3+} ions of SrGd$_2$O$_4$ is very similar to that of the other Sr*Ln*$_2$O$_4$ compounds, discussed in Section 2.3 and the beginning to Chapter 5. Previous investigations did not report that SrGd$_2$O$_4$ was moisture sensitive, and this was found upon attempting to remeasure some of the data. Since these findings, all of the SrGd$_2$O$_4$ samples have been carefully stored and handled with minimal exposure to air.

First data on the magnetic susceptibility and magnetisation of a powder sample of SrGd$_2$O$_4$ was reported by Karunadasa *et al.* [43]. The data (in [43]) suggest that in the presence of relatively strong exchange interactions, no features indicating the transition to long range order could be detected for SrGd$_2$O$_4$ down to 1.8 K. Measuring $\chi(T)$ and $M(H)$ data for a powder sample of SrGd$_2$O$_4$, however, indicated that there *are* transitions in this compound at 2.8 K in $\chi(T)$ and around 1.9 T in $M(H)$. These transitions were probably missed by [43] from having too large a step size in H and T during their data collection. The measurements on the powder samples were extended to look at the heat capacity of SrGd$_2$O$_4$, and in zero field the experiments indicate that in addition to the transition seen in the magnetic susceptibility measurements at 2.8 K, another transition at an even lower temperature of 0.47 K is also observed.

To investigate the magnetic properties of SrGd$_2$O$_4$ in more detail, a single crystal of this material was grown using the floating zone technique under the guidance of

Prof. G. Balakrishnan. Many crystal growth attempts failed and the difficulties in obtaining a single crystal of $SrGd_2O_4$ were described in Section 4.1.4. Once the crystal was produced, several samples were aligned and cut along the principal axes. Low temperature measurements of $\chi(T)$ for the fields applied along each of the principal axes, show that below 2.8 K (the transition temperature detected in the powder samples) the most dramatic changes in the susceptibility occur when the field is applied along the c axis. The ^{3}He insert used with the SQUID magnetometer is limited by the base temperature of 0.5 K, and thus the second transition temperature of 0.47 K of $SrGd_2O_4$ established from specific heat measurements on powder samples could not be definitively observed. Low temperature $M(H)$ data indicates that the magnetisation processes along the a and b axes is quite uneventful, but that there are several in-field transitions when H is applied along the c axis. Specific heat measurements on the single crystal of $SrGd_2O_4$ were performed in zero field, and $C(T)$ in several fields and $C(H)$ in a range of temperatures were also measured for fields applied along the c axis. A $H - T$ phase diagram could then be constructed from the information gathered using bulk property probes to investigate the phase transitions in single crystal $SrGd_2O_4$ when the field is applied along the c axis.

Only one high-energy neutron diffraction experiment on $SrGd_2O_4$ was attempted using the D9 instrument at ILL to investigate a single crystal sample. High energy neutrons were needed so that a wavelength of the incident neutron flux that corresponds to the minimum in the absorption curve of naturally abundant Gd could be selected. The use of short neutron wavelengths, however, does not allow access to low Q reflections in reciprocal space, and this makes looking for magnetic scattering quite challenging. The D9 experiment on $SrGd_2O_4$ could not be completed due to equipment failure, and so the data presented towards the end of this chapter only detail the successful part of the experiment and the few experimental conclusions reached for $SrGd_2O_4$. The concluding section of this chapter is reserved for the discussion of the magnetic properties of $SrGd_2O_4$ in relation to those of the other members of the SrLn_2O_4 family of compounds.
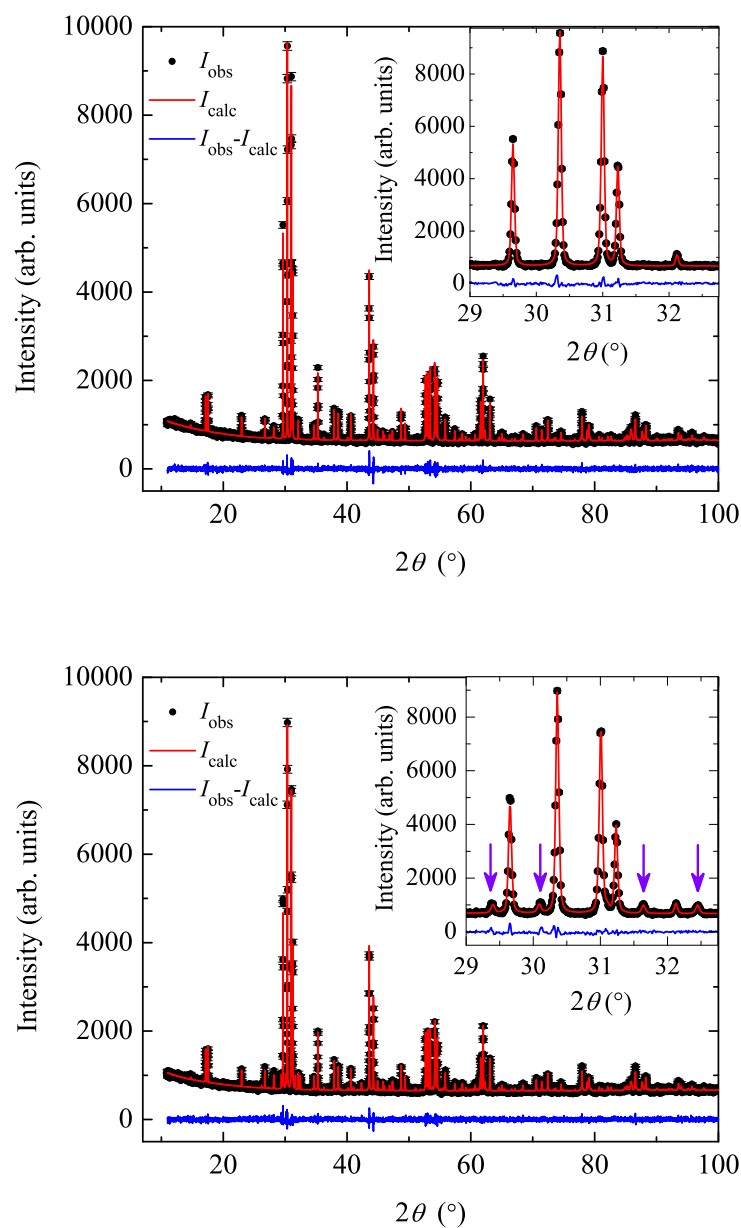
Figure 6.1: Powder SrGd$_2$O$_4$ x-ray diffraction data collected at 300 K (I_{obs}), Reitveld refined model (I_{calc}), and the difference ($I_{\text{obs}} - I_{\text{calc}}$) plot for (top) a sample prepared in an off-stoichiometric ratio of 1 : 0.875, where the deficiency is of the starting compound Gd$_2$O$_3$ and (bottom) a sample exposed to air. Insets: Smaller data ranges to show in detail some of the Gd$_2$O$_3$ impurity peaks, which are highlighted with arrows in the bottom dataset, and are absent in the clean sample. The data were collected as described in Section 4.1.2, and the refined model suggests that the SrGd$_2$O$_4$ compound prepared in an off-stoichiometric ratio is pure, and the sample left in air has an impurity phase of 3.5% of the starting compound Gd$_2$O$_3$. The goodness of fit parameters for both samples are given in the text.

6.1 Powder bulk properties

The crystallographic structure of the SrLn_2O_4 compounds, including SrGd$_2$O$_4$, was well established a long time ago [44] (see Section 2.3.1). The polycrystalline SrGd$_2$O$_4$ samples were prepared from high purity starting compounds as described in Section 4.1.1. Mixing the starting compounds in a stoichiometric ratio did not result in a pure SrGd$_2$O$_4$ sample, and a substantial impurity of the Gd$_2$O$_3$ starting compound was found in the material. Thus, an off-stoichiometric ratio of 1 : 0.875 of the starting compounds had to be used to make SrGd$_2$O$_4$, with an initial deficiency in Gd$_2$O$_3$. Initially, the SrGd$_2$O$_4$ samples were thought to be stable in air, since there have been no reports to the contrary, but upon trying to remeasure data on old samples similar results were not obtained. This observation led to remeasuring the x-ray diffraction spectra of all the samples, and subsequently to all the SrGd$_2$O$_4$ samples used for the bulk property experiments to be carefully handled and stored in a desiccator to prevent contamination. The x-ray diffraction data for different SrGd$_2$O$_4$ samples were collected at 300 K using the process discussed in Section 4.1.2, and are shown in Fig. 6.1. The purity of the SrGd$_2$O$_4$ powder was checked by performing a Rietveld refinement (see Section 4.1.3) using x-ray diffraction data, and allowing for two phases in the material - the desired SrGd$_2$O$_4$ and an impurity phase of the starting compound Gd$_2$O$_3$. The models suggest that the SrGd$_2$O$_4$ sample that was prepared in an off-stoichiometric ratio is pure, and the sample left in air has an impurity phase of 3.5%. The fit parameters for the clean sample are $\chi^2 = 1.158$, $R_P = 3.321\%$ and $R_{WP} = 4.248\%$, and for the contaminated sample are $\chi^2 = 1.121$, $R_P = 3.195\%$ and $R_{WP} = 4.079\%$. The atomic positions for the pure SrGd$_2$O$_4$ sample are given in Table 6.1, and the refined unit cell parameters are $a = 10.1321(1)$ Å, $b = 12.0614(1)$ Å and $c = 3.47566(2)$ Å, in the orthorhombic space group *Pnam*.

The results of the investigation on powder samples of SrGd$_2$O$_4$ are presented in the following sections. The temperature dependence of the magnetic susceptibility, $\chi(T)$ in the range of 1.8 to 400 K, and the field dependence of the magnetisation, $M(H)$ in the range of 0 to 5 T, were measured using a Quantum Design SQUID magnetometer, using the procedure described in Section 4.2.1, on samples weighing between 10 and 20 mg. Specific heat measurements (described in Section 4.2.2), were also carried out on small SrGd$_2$O$_4$

	x	y
Sr	0.7506 (5)	0.6489(4)
Gd1	0.4270(4)	0.1127(3)
Gd2	0.4161(4)	0.6110(3)
O1	0.220(3)	0.181(2)
O2	0.135(3)	0.479(3)
O3	0.510(3)	0.785(2)
O4	0.423(4)	0.420(2)

Table 6.1: The refined structural parameters for a clean sample of $SrGd_2O_4$, all atoms sit on $4c$ $(x, y, 0.25)$. Refinements were performed using the TopasRuns software.

	μ_{eff} (μ_B)	θ_{CW} (K)
From Ref. [43]	8.02(2)	$-9.0(6)$
From Fig. 6.2	7.68(1)	$-9.8(3)$
Hund's Rules [3]	7.94	

Table 6.2: The μ_{eff} and θ_{CW} parameters of powder $SrGd_2O_4$ and a comparison to the published data and the Hund's rules prediction for a Gd^{3+} ion.

samples (weighing between 12.5 and 0.14 mg) in the temperature range of 0.05 to 400 K in zero field.

6.1.1 High temperature susceptibility

Karunadasa, *et al.* [43] were the first to investigate the magnetic properties of powder samples of the $SrLn_2O_4$ compounds, including the case of Ln = Gadolinium. To compare to published data in [43], the high temperature magnetic susceptibility versus temperature was measured in 0.1 T for a 12.66 mg polycrystalline sample of $SrGd_2O_4$ using a SQUID magnetometer (see Section 4.2.1), and the data is shown in Fig. 6.2. The temperature dependence of the inverse susceptibility is presented in the inset of Fig. 6.2. In the high temperature range of 100 to 400 K, where the $1/\chi(T)$ curve follows a paramagnetic Curie-Weiss behaviour (see Section 2.1.5), the data are fitted with a least-squares regression line. The parameters of this fit, the Curie-Weiss constant and the calculated effective moment per Gd^{3+} ion, are given in Table 6.2. The values obtained by Karunadasa, *et al.* [43] and the Hund's rules prediction for the effective moment of Gd^{3+} are also listed for comparison.
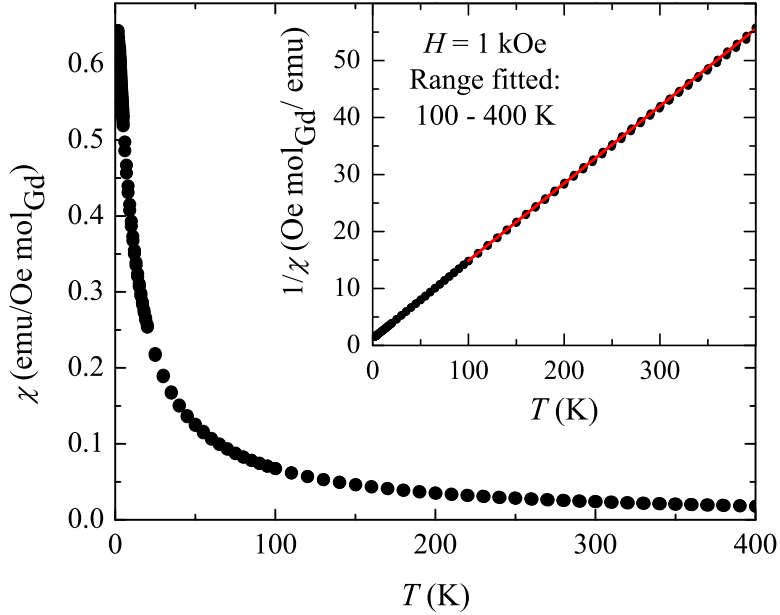
Figure 6.2: High temperature magnetic susceptibility for a powder sample of $SrGd_2O_4$. Inset: The inverse susceptibility as a function of temperature, and the linear fit to the data between 100 and 400 K (red line). From the fit, the effective moment is calculated to be $\mu_{\text{eff}} = 7.68(1)\,\mu_B$, and the Curie-Weiss constant is $\theta_{CW} = -9.8(3)$ K.

The data obtained for the $SrGd_2O_4$ sample appear to be largely consistent with the values published in [43] and Hund's rules predictions.

6.1.2 Low temperature susceptibility

For $SrGd_2O_4$, Karunadasa, *et al.* [43] reported a difference between the Curie-Weiss temperature, $\theta_{CW} = -9.0(6)$ K, and the lack of any indications of phase transitions in the magnetic susceptibility down to 1.8 K. The measurements of low temperature susceptibility were carried out on a pure $SrGd_2O_4$ sample using a SQUID magnetometer (see Section 4.2.1), and some of the data are shown in the top panel of Fig. 6.3. A cusp at 2.8 K (indicated by a dashed line in the figure) suggests the presence of a phase transition. (This indicates a small frustration parameter of 3.5 for $SrGd_2O_4$.) This phase transition was missed in the data published for $SrGd_2O_4$ in [43], because the step size used for their low
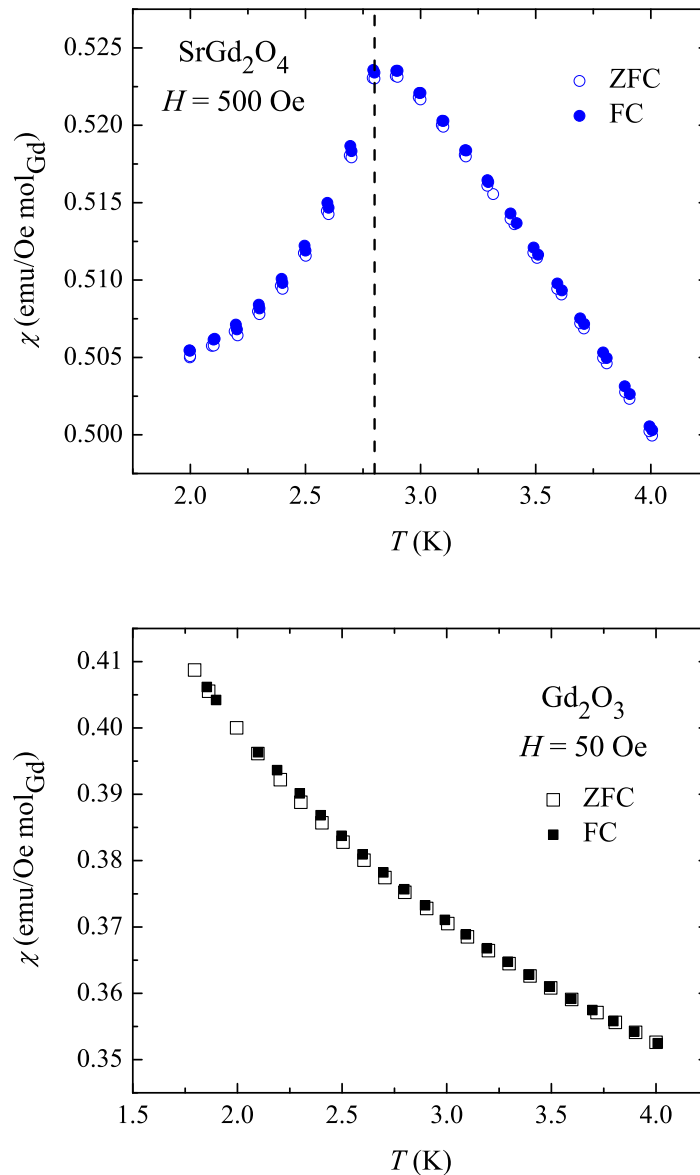
Figure 6.3: (Top) Magnetic susceptibility measured in 500 Oe for a powder sample of SrGd$_2$O$_4$ between 2 and 4 K. The dashed line indicates 2.8 K, the temperature at which a cusp is observed in the susceptibility, which indicates the presence of a phase transition. No differences are observed between data obtained using ZFC and FC regimes. (Bottom) The magnetic susceptibility measured in 50 Oe for a powder sample of Gd$_2$O$_3$, shows no discontinuities. The starting compound for the synthesis of SrGd$_2$O$_4$ was measured because it was deemed to be the most likely impurity (see discussion in Section 6.1).

temperature measurements of susceptibility was too large. Around the transition temperature, in all applied fields (for example 500 Oe shown in the top panel of Fig. 6.3) there is no noticeable difference between the data obtained on warming after cooling in field (FC) and the zero-field-cooled warming (ZFC) data, (see Section 4.2.1). This suggests that the magnetic susceptibility of $SrGd_2O_4$ is insensitive to sample history. For $SrGd_2O_4$ higher applied fields do not suppress the cusp $\chi(T)$, but move it to lower temperatures. Also, the transition temperature of $SrGd_2O_4$ is much higher than that of the other members of the $SrLn_2O_4$ series of compounds.

The most likely impurity phase in $SrGd_2O_4$ samples was found to be Gd_2O_3 (see discussion in Section 6.1), whether a result of the $SrGd_2O_4$ sample left in air, or a non-optimal ratio of the starting compounds was used to make the powder. Thus, magnetic susceptibility data for a powder sample of Gd_2O_3 were taken to check if there is a transition in this compound around 2.8 K, and the results are shown in the bottom panel to Fig. 6.3. Since no discontinuities are observed in $\chi(T)$ for Gd_2O_3 in the temperature range of interest, it is suggested that the cusp observed in $\chi(T)$ for powder $SrGd_2O_4$ is not an impurity issue and that the transition at $\sim$2.8 K only happens in the $SrGd_2O_4$ compound.

6.1.3 Magnetisation

The field dependent magnetisation $M(H)$ and its derivative dM/dH at 1.8 and 5 K are shown in Fig. 6.4. For the data collected at temperatures above 2.8 K (the transition temperature seen in the susceptibility data), the $M(H)$ and dM/dH curves are completely featureless. For the data collected at temperatures below 2.8 K, such as that shown for 1.8 K in Fig. 6.4, a broad peak in dM/dH is observed around 1.9 T. This phase transition was missed in the data published for $SrGd_2O_4$ in [43], because their step size was too large at fields above 1 T. No hysteresis is observed at any temperatures, as the data collected with increasing and decreasing field lie on top of each other. Complete saturation of magnetisation is not observed for $SrGd_2O_4$, as the dM/dH values remain nonzero even in an applied field of 7 T, but the magnetisation reaches nearly 6.5 μ_B. This implies that the spins are not fully aligned at this field, but the observed value of magnetisation becomes a large fraction to what is expected from Hunds rules predictions for Gd^{3+} ions [3].

156
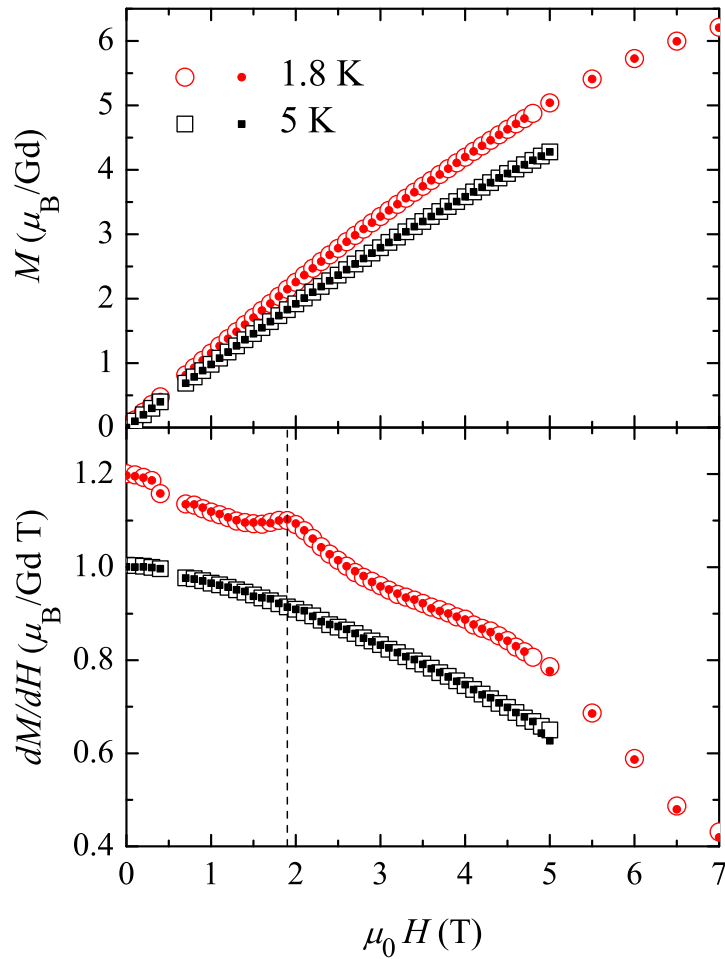
Figure 6.4: (Top) Field dependent magnetisation and (bottom) the derivative of magneti-sation with respect to the applied field at 1.8 and 5 K for a powder sample of $SrGd_2O_4$. The data collected with increasing (decreasing) field are shown as empty (filled) symbols, and demonstrate that no hysteresis is observed. For the data collected below at 1.8 K (be-low the transition temperature observed in magnetic susceptibility measurements), a peak in dM/dH appears around 1.9 T, highlighted by the dashed line. No features in $M(H)$ and dM/dH are observed at higher temperatures.
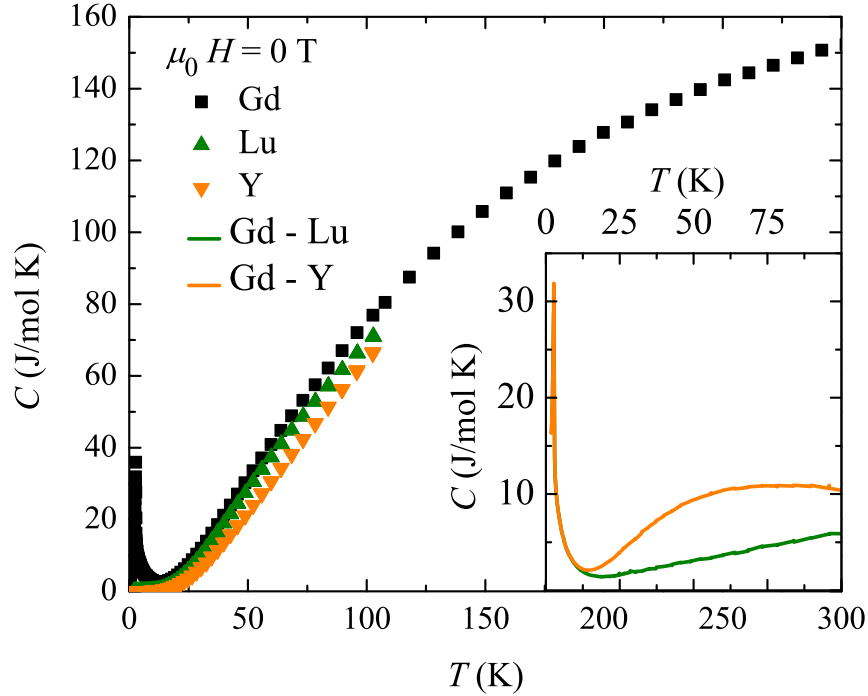
Figure 6.5: Temperature dependence of the specific heat of polycrystalline $SrGd_2O_4$ and of the nonmagnetic isostructural compounds $SrLu_2O_4$ and SrY_2O_4 measured on single-crystal samples between 0.4 and 300 K in zero field. At temperatures below $\sim$10 K, the lattice contribution to the heat capacity is negligible. The inset shows the differences in specific heat of $C_{SrGd_2O_4} - C_{SrLu_2O_4}$ and $C_{SrGd_2O_4} - C_{SrY_2O_4}$.

6.1.4 Heat capacity

Specific heat measurements on powder samples of $SrGd_2O_4$ were performed using a Quantum Design PPMS calorimeter as described in Section 4.2.2. The temperature dependence of the specific heat of $SrGd_2O_4$ in zero applied field is shown in Fig. 6.5. The lattice contribution to the specific heat of $SrGd_2O_4$ can be estimated by measuring the heat capacity of two single crystal non-magnetic isostructural compounds: SrY_2O_4 and $SrLu_2O_4$, and is also shown in Fig. 6.5. As can be seen from the figure, at temperatures below $\sim$10 K, the lattice contribution to the specific heat of $SrGd_2O_4$ is negligible. Above $\sim$10 K the heat capacity begins to rise again, but only some of this rise is likely to be the result of the lattice contribution, and to try to estimate this the differences in specific heat $C_{SrGd_2O_4} - C_{SrLu_2O_4}$
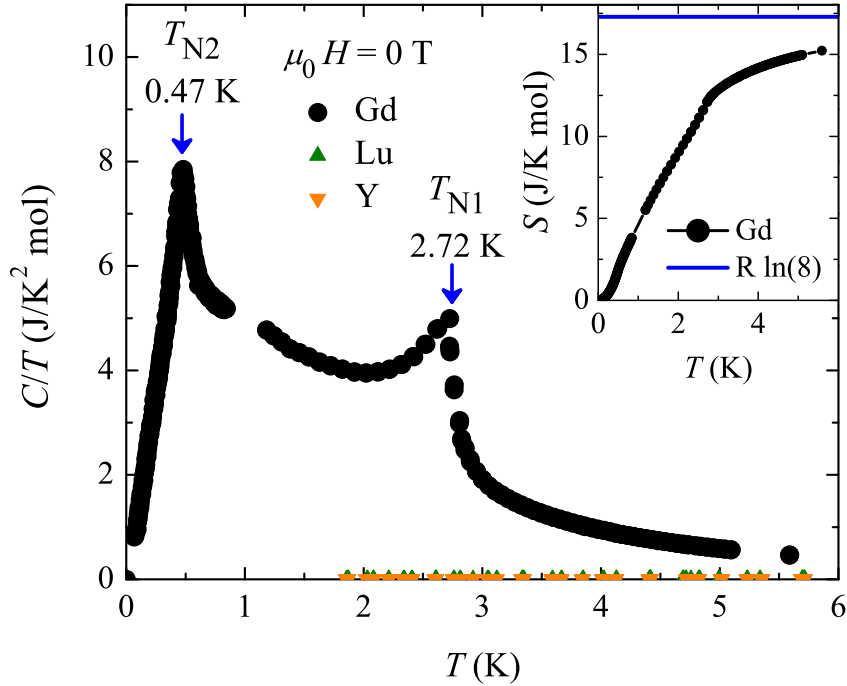
Figure 6.6: Temperature dependence of the specific heat divided by temperature for poly-crystalline $SrGd_2O_4$ in zero field. Two λ-anomalies, with $T_{N1} = 2.72$ K and $T_{N2} = 0.47$ K, are observed indicating the the complex nature of the low temperature ordering in this compound. Inset: Magnetic entropy at low temperature found by integrating the $C/T(T)$ curve, which has been linearly extended down to 0 K. The solid line corresponds to the magnetic contribution to the entropy expected for the all-spin Gd^{3+} system.

and $C_{SrGd_2O_4} - C_{SrY_2O_4}$, are plotted in the inset to Fig. 6.5. At low temperatures, when Gadolinium is in the ground state, the orbital angular momentum is equal to zero due to Hund's rules, so that there are no distortions of the electronic charge density for this ion and hence no CEF effects. Thus, the additional contribution to $C(T)$ at low temperatures, should not be caused by low-lying CEF levels like in $SrHo_2O_4$.

Fig. 6.6 shows the low temperature dependence of the specific heat divided by temperature for a powder sample of $SrGd_2O_4$ in zero field. From the figure it is immediately obvious that *two* λ-anomalies which correspond to transitions to long-range magnetic order are observed at $T_{N1} = 2.72$ K and $T_{N2} = 0.47$ K. A dilution insert for the PPMS was used to extend the temperature range of the measurements down to 0.05 K, so check that below

T_{N2} $C(T) \to 0$ as $T \to 0$ K, and that no more low temperature transitions are present in the material down to the calorimeters lowest achievable temperature. At low temperature, and especially for temperatures below 6 K, the lattice contribution to the specific heat of $SrGd_2O_4$ is negligible, so below this temperature an estimate of the magnetic entropy can be made by calculating the area under the $C/T(T)$ curve which has been extended linearly down to $T = 0$ K. The temperature dependence of the magnetic entropy of $SrGd_2O_4$ is shown in the inset to Fig. 6.6, and $\sim$90% of the entropy expected for the $SrGd_2O_4$ system is recovered by 6 K.

6.2 Single crystal bulk properties

A single crystal sample of $SrGd_2O_4$ was grown using to the floating zone technique described in Section 4.1.4. The crystal was aligned along the principal axes using the backscattering Laue method (see Section 4.1.5), and the diffraction patterns and OrientExpress simulations are shown in Fig. 6.7. The samples were cut into thin rectangular plates (with faces perpendicular to a, b and c within an estimated accuracy of 3°) that weighed $\sim$15 mg for the static magnetic susceptibility and magnetisation measurements, and $\sim$1 mg for the specific heat studies. Corrections to account for demagnetisation effects were made as detailed in Section 4.2.1.

A Quantum Design SQUID magnetometer (see Section 4.2.1) was used to measure the magnetic susceptibility and magnetisation along each of the principal crystallographic directions in the ranges of $0.5 < T(\text{K}) < 400$ and $0 < \mu_0 H(\text{T}) < 7$. These measurements revealed that for $SrGd_2O_4$ the magnetisation processes are rather uneventful, except for when the field is applied along the c axis. Specific heat measurements (see Section 4.2.2) on single crystal samples were carried out both in zero field, and for the fields applied along the c axis. Based on all of the bulk property measurements, a $H - T$ phase diagram for $H \parallel c$ was constructed for $SrGd_2O_4$.
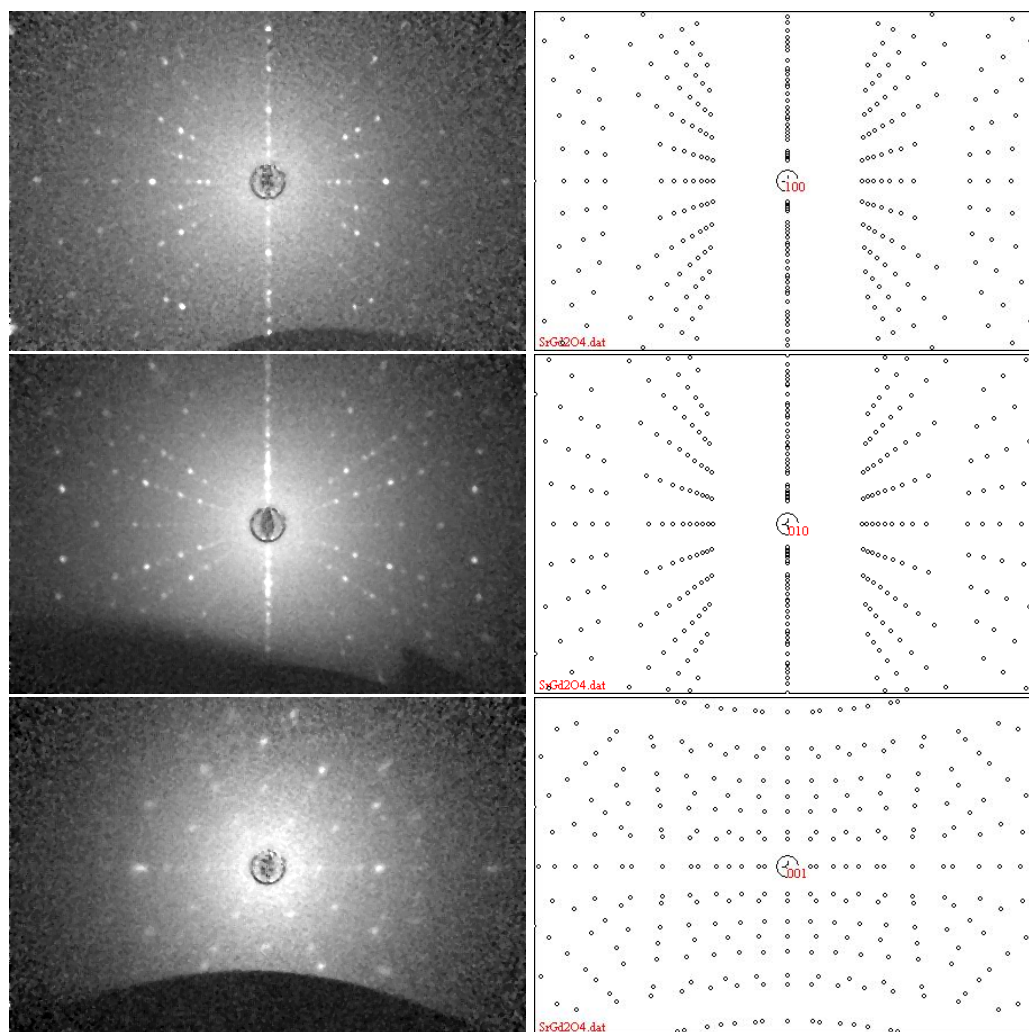
Figure 6.7: Laue diffraction images (left) and the OrientExpress simulations (right) of well-aligned samples of $SrGd_2O_4$ oriented along the (top) a, (middle) b, and (bottom) c axes. The exposure time for each image was 30 seconds.
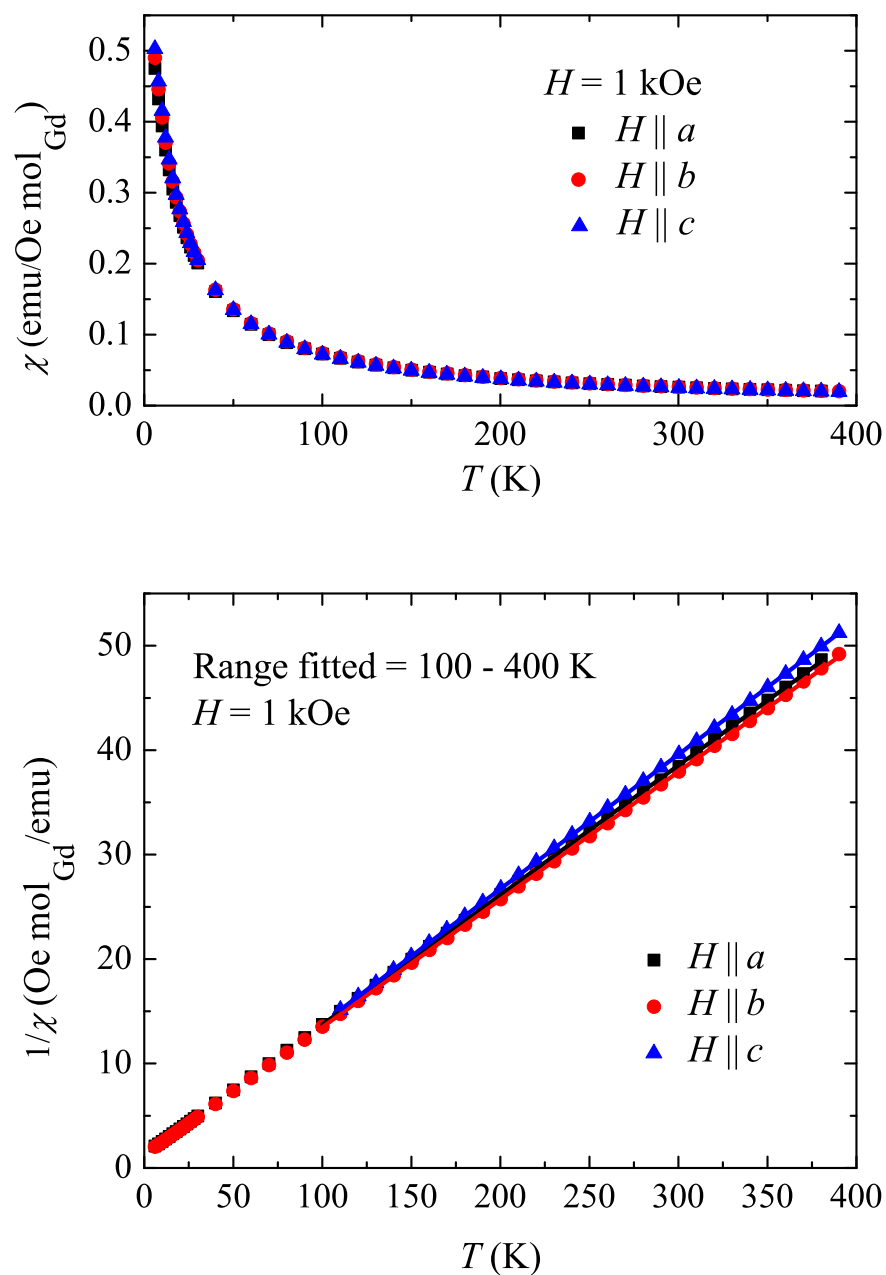
Figure 6.8: (Top) High temperature magnetic susceptibility versus temperature in an applied field of 1 kOe in the temperature range of 6 to 400 K for the for the field applied along the three principal axes of a single crystal sample of $SrGd_2O_4$. (Bottom) Reciprocal of the molar susceptibility versus temperature and the least-squares regression fits to the data (using the Curie-Weiss model). From the fits, the average effective moment is calculated to be $\mu_{\text{eff}} = 8.00(3)\ \mu_B$, and the average Curie-Weiss constant is $\theta_{\text{CW}} = -10.3(2)$ K, the individual values for the field applied along each axis are given in Table 6.3.

	$H \parallel a$	$H \parallel b$	$H \parallel c$	Mean	Expected
$\mu_{eff}(\mu_B)$	8.03(8)	8.10(5)	7.88(2)	8.00(3)	7.68(1) [powder]
θ_{CW} (K)	-11.0(6)	-7.4(2)	-12.3(1)	-10.3(2)	-9.8(3) [powder]

Table 6.3: The μ_{eff} and θ_{CW} parameters for the fits of the data collected with the field applied along each of the principal axes of a single crystal sample of $SrGd_2O_4$, their average values and a comparison to the data collected for a powder sample of $SrGd_2O_4$.

6.2.1 High temperature susceptibility

The top panel of Fig. 6.8 shows the magnetic susceptibility versus temperature in 1 kOe, for field applied along each of the three principal axes for a single crystal sample of $SrGd_2O_4$. The bottom panel of Fig. 6.8 shows the high temperature dependence of the inverse susceptibility. In the temperature range of 100 to 400 K the data are fitted with least-squares regression lines, since at high temperatures the $1/\chi(T)$ curves follow the Curie-Weiss law (see Section 2.1.5). The parameters of these fits, the Curie-Weiss constants, θ_{CW}, and the calculated effective moments per magnetic ion, μ_{eff}, are listed in Table 6.3.

From considering Fig. 6.8 and the data in Table 6.3 it is immediately obvious that unlike $SrHo_2O_4$ there is no large differences in the Curie-Weiss temperatures or the effective moments for the three principal crystal directions of $SrGd_2O_4$. This is because in the ground state Gadolinium has a pure spin magnetic moment, and thus there is no distortion of the spherical $4f$ charge density due to the spin-orbit coupling, and hence no corresponding crystal field anisotropy.

6.2.2 Low temperature susceptibility

The low-temperature susceptibility measurements on the single crystal samples of $SrGd_2O_4$ are presented in Fig. 6.9 for field of 0.01 T applied along the a, b, and c directions. When a field of 0.10 Oe is applied along the different principal crystal axes, a cusp in the susceptibility at 2.7 K for the a and b axes, and a large decrease $\chi(T)$ along the c axis suggests the presence of a phase transition, with the region of interest highlighted in the inset to Fig. 6.9. These observations are consistent with the data presented in Section 6.1.2 for the powder sample of $SrGd_2O_4$, where a cusp was observed in the low temperature susceptibility at
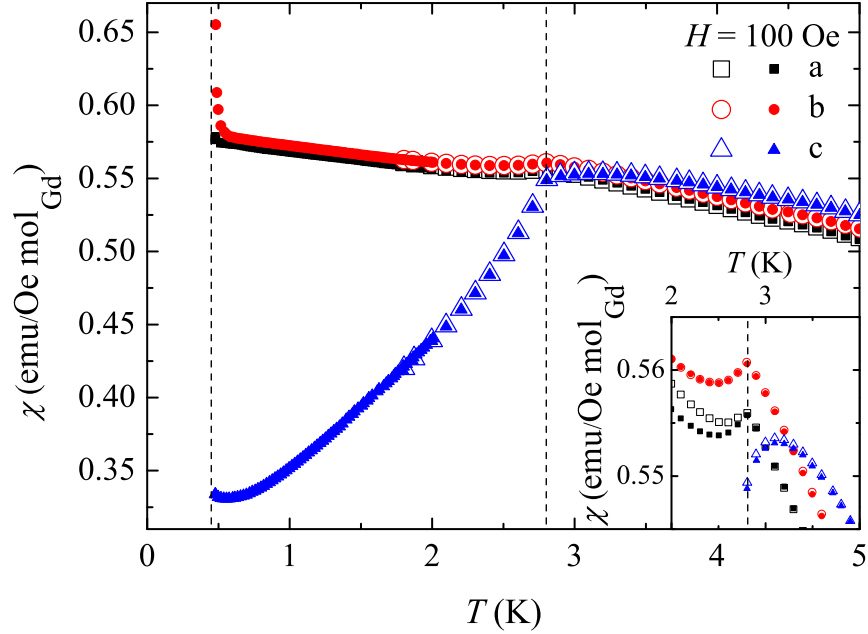
Figure 6.9: Low temperature magnetic susceptibility obtained in the temperature range of 0.5 to 5 K for a field 100 Oe applied along each of the three principal axes of $SrGd_2O_4$. Two dashed lines represent 0.47 K and 2.7 K, where λ-anomalies were observed in heat capacity data obtained for a powder sample of $SrGd_2O_4$ in zero field (see Section 6.1.4). A cusp is observed in the susceptibility at 2.7 K along both the a and b axes, and a dramatic drop occurs in $\chi(T)$ along the c axis at 2.7 K, which is highlighted in the inset. Also, around this temperature, differences between ZFC and FC measurements become apparent along all of the principal axes of $SrGd_2O_4$.

2.8 K. Demagnetisation factor corrections make no impact on the position of this phase transition. Below the transition temperature, in low applied fields such as 0.01 T, there is a slight difference between the data obtained in the FC and ZFC regimes, (see Section 4.2.1).

The lowest reachable experimental temperature when measuring magnetic susceptibility with the aid of a ^{3}He probe (see Section 4.2.1) is $\sim$0.5 K. Unfortunately this is not quite low enough to observe the second transition seen at 0.47 K in zero field for a powder sample of $SrGd_2O_4$ using heat capacity (see Section 6.1.4). However, the susceptibility data, acquired at low fields (such as 0.01 T in Fig. 6.9), along all of the principal axes of $SrGd_2O_4$ show a slight upturn in $\chi(T)$ at the lowest temperatures, and this is most visible for the susceptibility data collected with $H \parallel b$. This again hints at the presence of a second
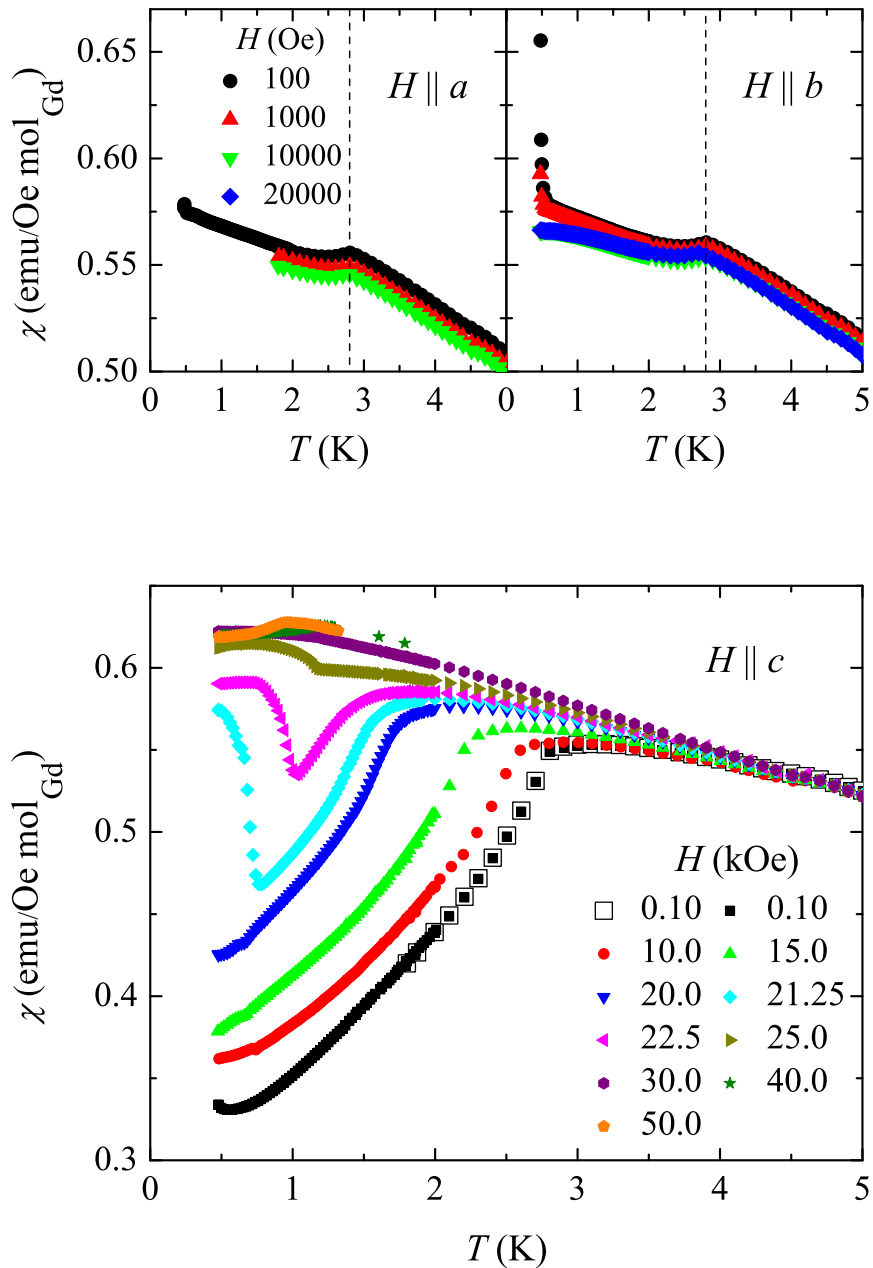
Figure 6.10: (Top) Field dependence of the magnetic susceptibility along the (left) a and (right) b axes of SrGd$_2$O$_4$. There seems to be very little difference in the behaviour at low fields and upon increasing the applied field along these axes. (Bottom) Low temperature magnetic susceptibility obtained in the temperature range of 0.5 to 5 K, and field range of 0.10 to 50 kOe, with the fields applied along the c axis of SrGd$_2$O$_4$. The transition seen at 2.7 K is suppressed by the application of higher fields, and in fields between 2 and 3 T a second feature in the magnetic susceptibility is observed. In fields above 3 T, again, only a single cusp in the low temperature susceptibility is visible.

low-temperature transition in $SrGd_2O_4$ at temperatures just below 0.5 K.

The field dependences of the low temperature magnetic susceptibilities with the fields applied along the a and b axes of $SrGd_2O_4$ are shown in the top panels of Fig. 6.10. No extra features are observed in larger fields, and this suggests that the magnetisation process along the a and b axes is quite uneventful. The field dependence of the low temperature magnetic susceptibility obtained in the temperature range of 0.5 to 5 K, and field range of 0.01 to 5 T, with the fields applied along the c axis of $SrGd_2O_4$ is shown in the bottom panel of Fig. 6.10. Upon the application of field, the transition seen at 2.7 K is suppressed to lower temperatures, which suggests that it is a transition to a long-range magnetically ordered state of $SrGd_2O_4$. In fields between 2 and 3 T a second feature in the magnetic susceptibility is observed, and in fields above 3 T, only a single cusp in the low temperature susceptibility is visible. This suggests a rich $H - T$ phase diagram for the fields applied along this axis of $SrGd_2O_4$, and this will be later discussed in Section 6.2.5.

6.2.3 Magnetisation

The field dependent magnetisation $M(H)$ and its derivative dM/dH, with H applied along the a, b, and c axes of $SrGd_2O_4$ at 0.5 K are shown in Fig. 6.12. The lower temperature single crystal data (compared to the data collected for a powder sample presented in Section 6.1.3 allow for the clearer observation of the in-field transitions present in this rare-earth oxide. These single crystal measurements reveal that for $SrGd_2O_4$ the magnetisation process for the fields applied along the a and b axes is rather uneventful.

Fig. 6.11 shows the field-dependent magnetisation and the field derivatives of the magnetisation curves obtained with the field applied along the principal axes of $SrGd_2O_4$ at 0.5 K. The data collected for $H \parallel a$ shows no features in dM/dH which remains small and nearly flat at all fields. This is similar to what is observed for $H \parallel b$, where only some saturation of the moment occurs in applied fields of above $\sim$6 T. Upon raising the temperature (data not shown), the a and b axes become harder to magnetise, but the overall process remains rather featureless.

The magnetisation process of $SrGd_2O_4$ with $H \parallel c$ is significantly more involved, with three in-field transitions seen for data collected at 0.5 K, see Fig. 6.11. The initial
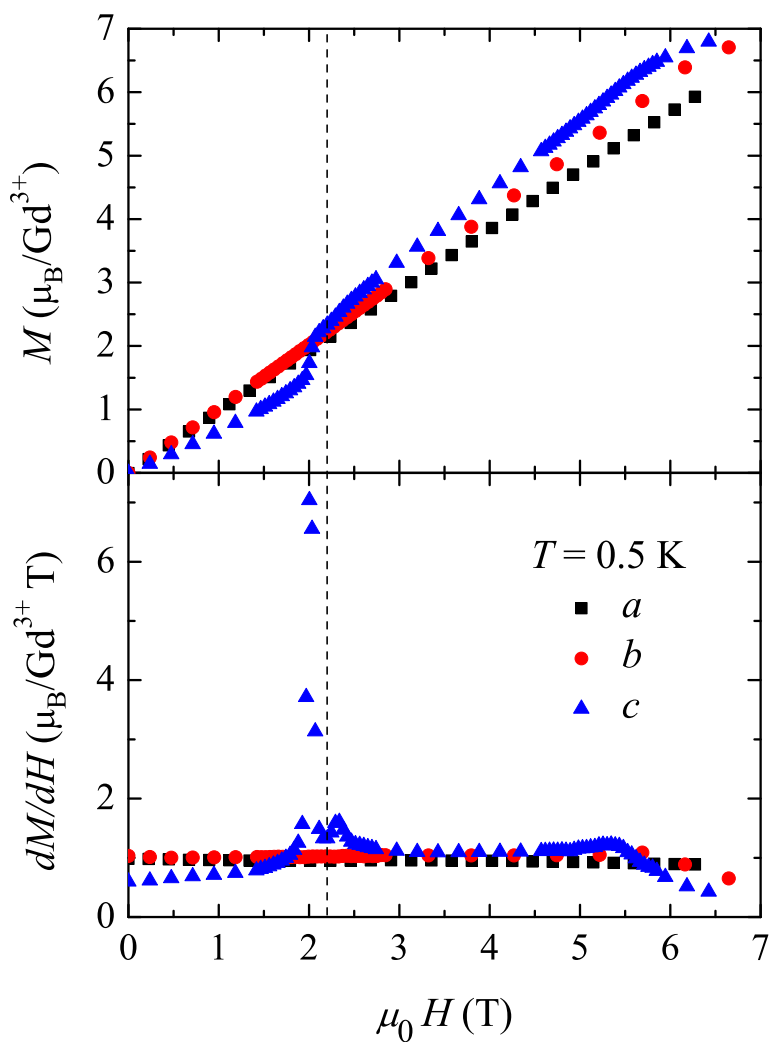
Figure 6.11: (Top) Field-dependent magnetisation curves obtained with the field applied along the principal axes of $SrGd_2O_4$ at 0.5 K in the range of 0 to 7 T. (Bottom) The field derivatives of the magnetisation. The dashed line indicates 2.2 T, the value of the field around which the plateau in dM/dH is observed at approximately one third of the value for the fully saturated moment along the c axis. This may suggest that a collinear *two-spins-up-one-spin-down* structure is being stabilised around 2.2 T when the field is applied along the c axis.
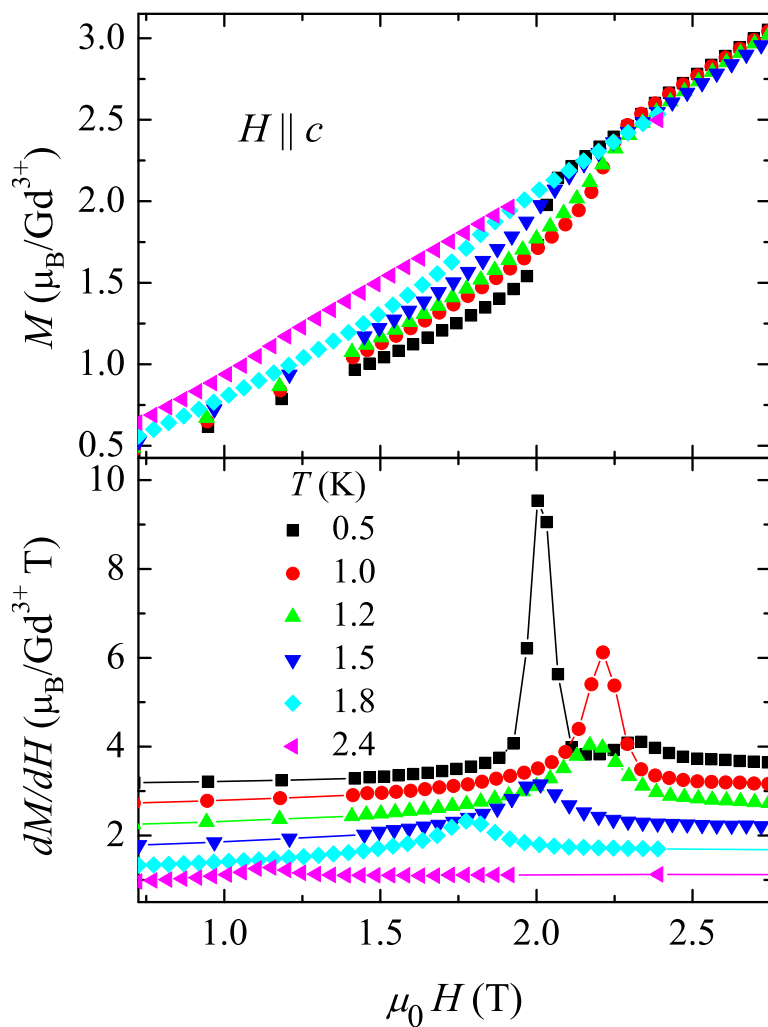
Figure 6.12: (Top) Field-dependent magnetisation curves for SrGd$_2$O$_4$ obtained at several temperatures in the field range of 0 to 7 T, for $H \parallel c$. (Bottom) The field derivatives of the magnetisation, the data have been offset for clarity. The double peak in the derivative of magnetisation seen in the data collected at 0.5 K becomes only a single peak at higher temperatures, and this single maximum in dM/dH initially is shifted up, and then down in field as the temperature is increased.

rise in the magnetisation is accompanied by a maximum in dM/dH at $H_{c1} \approx 2.0$ T, and then for a small region of the applied field the magnetisation shows much slower growth (with a minimum in dM/dH seen at 2.2 T), and then another small rise up to a second maximum in dM/dH at $H_{c2} \approx 2.33$ T. Thus for $SrGd_2O_4$ H_{c1} and H_{c2} again confine a narrow plateau with an average magnetisation value of 2.3 μ_B, which equates to roughly a third of the saturation magnetisation value observed with $H \parallel c$. The plateau is again a sign of a field induced stabilisation of a collinear *two-spins-up-one-spin-down* (uud) magnetic structure in $SrGd_2O_4$, in which on each triangle of spins, two are pointing up along the field and the third spin pointing down anti-parallel to the field direction as discussed earlier in Section 5.6 in relation to all the other Sr*Ln*$_2$O$_4$ compounds. The two peaks in dM/dH at H_{c1} and H_{c2} split from a single peak that is seen at higher temperatures (see Fig. 6.12, and the collated data for $H \parallel c$ the phase diagram shown in Fig. 6.15), and thus it seems plausible that at even lower temperatures the uud state would govern a larger region of the applied field. A third field induced transition for $H \parallel c$ is observed at $H_{c3} \approx 5.34$ T, and in even higher applied fields the magnetisation shows signs of approaching saturation. The demagnetisation corrections only have a small impact on the position of the field-induced phase transitions at H_{c1} and H_{c2} (of under 2%), but a somewhat larger effect on the position of H_{c3} (of $\sim 5\%$).

To have a better look at the region of the applied field around H_{c1} and H_{c2} with $H \parallel c$ for $SrGd_2O_4$, $M(H)$ data was collected at several temperatures, and this and the derivative of the magnetisation is shown in Fig. 6.12. The double peak in the derivative of magnetisation seen in the data collected at 0.5 K becomes only a single peak at higher temperatures, and this single maximum in dM/dH initially is shifted up, and then down in field as the temperature is increased.

Complete saturation of magnetisation is not observed at any temperature for any of the principal axes of $SrGd_2O_4$, as dM/dH remains nonzero even in the highest applied fields of 7 T, which is similar to what was concluded from the powder $M(H)$ data presented in Section 6.1.3. Also, no hysteresis with the applied field along any of the principal crystal axes of $SrGd_2O_4$ is observed, as expected from the previous measurements on the polycrystalline $SrGd_2O_4$ sample, as the magnetisation data collected upon increasing and
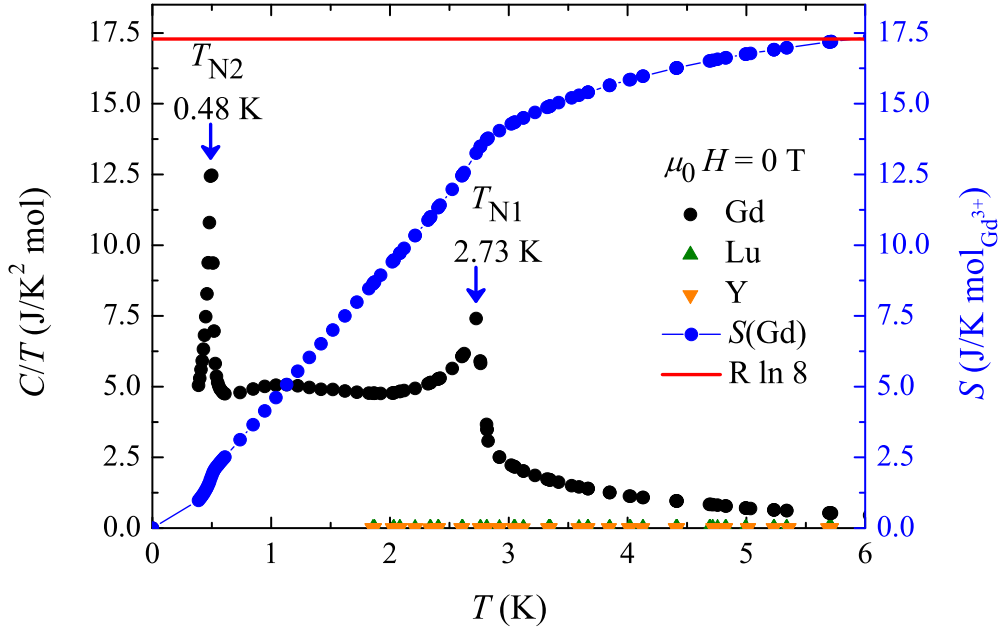
Figure 6.13: Temperature dependence of the specific heat divided by temperature of $SrGd_2O_4$ and of the nonmagnetic isostructural compounds $SrLu_2O_4$ and SrY_2O_4 measured in zero field. The non-magnetic analogues suggest that there is very little contribution to the heat capacity from the lattice below 6 K. Two λ-anomalies are observed at temperatures nearly identical to those in the powder sample. The peaks are more narrowly defined than in the powder data. The entropy is calculated by linearly extending the $C(T)/T$ curve to zero at $T = 0$ K, and integrating as described in Section 4.2.2, with the scale given on the righthand axis. By 6 K, the full magnetic entropy expected for the Gd^{3+}, $J = \frac{7}{2}$, system is recovered.

decreasing field lie on top of each other.

6.2.4 Heat capacity

The low temperature dependence of the specific heat divided by temperature of $SrGd_2O_4$ and of the nonmagnetic isostructural compounds $SrLu_2O_4$ and SrY_2O_4 was measured in zero field using a Quantum Design PPMS calorimeter (see Section 4.2.2) and is shown in Fig. 6.13. The data obtained for the single crystal sample closely resemble the data shown in Fig. 6.6 for the powder $SrGd_2O_4$, with the only slight difference being that the phase transition peaks at $T_{N1} = 2.73$ K and $T_{N2} = 0.48$ K appear to be more narrowly defined.

As before, since the lattice contribution to the specific heat of $SrGd_2O_4$ is negligible below 6 K, the magnetic entropy can be estimated by integrating the $C/T(T)$ curve which has been extended linearly down to T = 0 K. The entropy curve is also shown in Fig. 6.13, and the (blue) righthand axis should be used for the appropriate scale. In the powder data, $\sim 90\%$ of the entropy expected for the $SrGd_2O_4$ system is recovered by 6 K, but for the single crystal sample it appears that by the same temperature the full magnetic entropy expected for the Gd^{3+}, $J = \frac{7}{2}$, system is recovered.

From single crystal magnetic susceptibility and magnetisation data it has become apparent that for $SrGd_2O_4$ with $H \parallel a$ and $H \parallel b$ relatively little interesting behaviour takes place. So, the specific heat was only measured for the fields applied along the c axis, in a broad range of both fields and temperatures. The data for $C(T)$ in several applied fields are shown in the top panel of Fig. 6.14. The two phase transitions in $SrGd_2O_4$, whose temperature is defined by the λ anomalies, in seen in $H = 0$ T move closer together upon increasing the strength of the applied field. The transitions 'merge' into a single broad peak seen when $C(T)$ is measured in 2.25 T, and after subsequent increases of the field this single peak is first shifted to higher and then lower temperatures.

The specific heat measured as a function of field was also measured for $H \parallel c$, and this is shown in the bottom panel of Fig. 6.14. At the lowest measured temperature, two peaks are visible in the heat capacity data. As the temperature is increased, these two peaks also move closer together, and in a small temperature range (between 1.2 and 1.3 K) get quickly suppressed in intensity before merging together at temperatures around 1.5 K. Subsequent increases in the temperature just shift this single peak to lower fields. All of the specific heat data collected for $H \parallel c$ will also be used to form part of the $H \parallel c$ phase diagram for $SrGd_2O_4$, which is described below.

6.2.5   *H - T* phase diagram of $SrGd_2O_4$ for $H \parallel c$

By collating all of the susceptibility, magnetisation and specific heat curves for $H \parallel c$ from Sections 6.2.2, 6.2.3 and 6.2.4, a magnetic field$-$temperature phase diagram may be constructed for $SrGd_2O_4$, and this is shown in Fig. 6.15.

In order to obtain the position of the transition fields and temperatures in a consis-
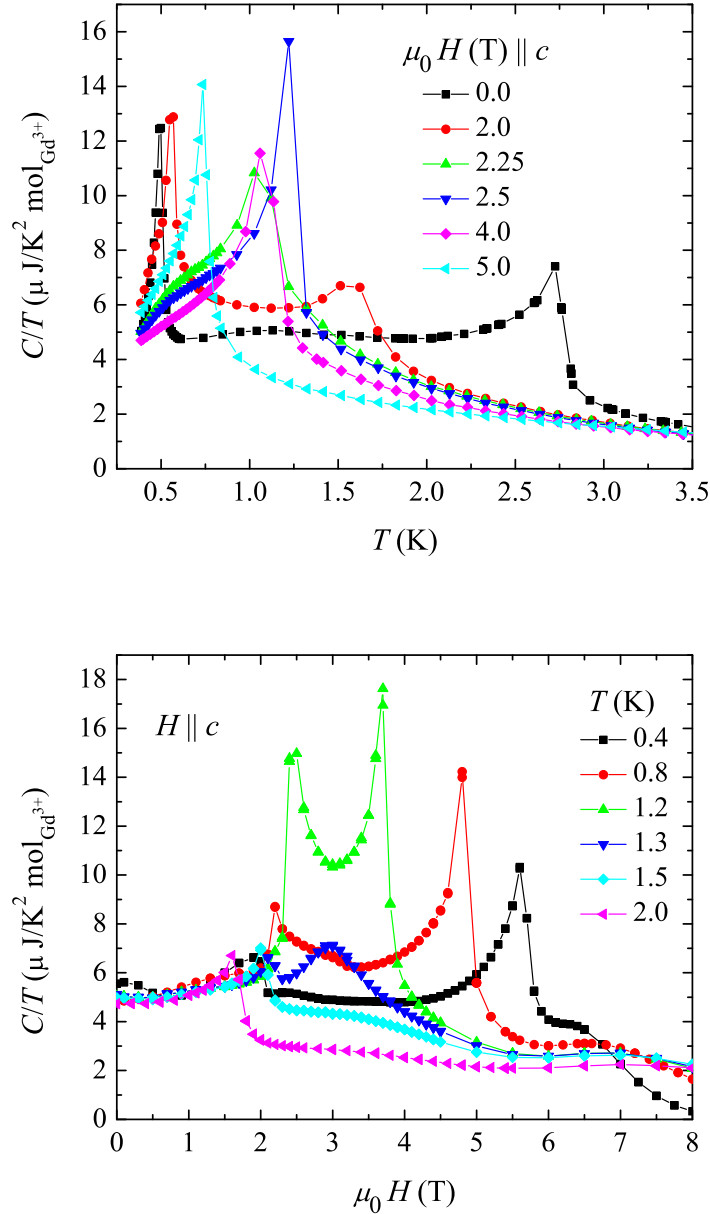
Figure 6.14: (Top) Temperature dependence of the specific heat of $SrGd_2O_4$ in several fields applied along the c axis of a single-crystal sample. The two peaks associated with the transitions get closer with higher applied fields, before merging and then this single peak is shifted to lower temperatures in the highest applied fields. (Bottom) Field dependence of the specific heat at several temperatures for a single crystal sample of $SrGd_2O_4$, when the field is applied along the c axis. The two peaks in $C(H)$ also move closer together and merge as the temperature is raised, and then get suppressed and move to lower fields for higher temperatures.
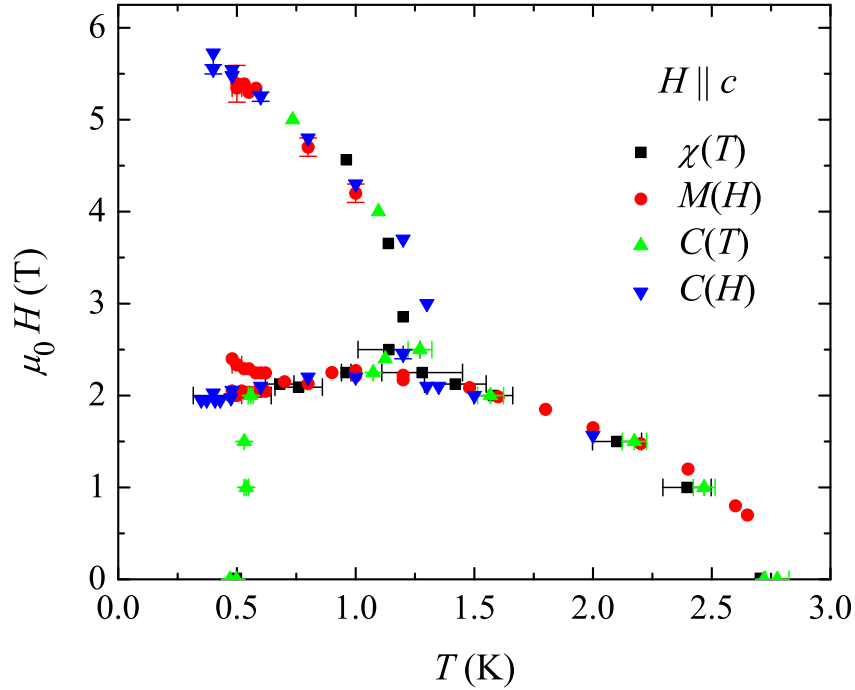
Figure 6.15: The magnetic $(H - T)$ phase diagram for $SrGd_2O_4$ with the field applied along the c axis constructed from the susceptibility, magnetisation and specific heat curves presented earlier. The methods of obtaining the phase boundaries are discussed in the text.

tent and systematic fashion, the following constraints were applied when looking for phase transitions in the $\chi(T)$, $M(H)$, $C(T)$ and $C(H)$ datasets collected with the field applied along the c axis:

1. If the transition was observed as a broad peak in susceptibility, the transition points were defined as the maxima of the peaks observed in $d(\chi T)/dT$.

2. If well defined peaks were observed in dM/dH, $C(T)$ and $C(H)$, their positions determined the critical fields and temperatures.

3. If the transition was observed as a change in the gradient of the measured bulk property (an example for the susceptibility would be the dataset collected in 3 T, and for the magnetisation measurements this was the method for determining the position of H_{c3}), linear fits to the data were made on either side of the change in the gradient,

and the transition point was defined to be where these two lines cross.

Altogether, Fig. 6.15 reveals rich and complex magnetic behaviour of $SrGd_2O_4$ when $H \parallel c$. Other than the paramagnetic regime, four extra phases may be identified by looking at the boundaries on the diagram. In zero field at least two low temperature transitions take place, with the type of magnetic order present in the intermediate phase discussed in the neutron diffraction section below. The lowest temperature magnetic structure in zero field remains unknown. With the application of field along the c axis of $SrGd_2O_4$, at the lowest temperature, three different phases appear to be present in the material. Only the intermediate phase may be guessed at from low temperature $M(H)$ measurements, as it falls in the region of magnetisation that is appropriate to support uud order, as observed in the other $SrLn_2O_4$ compounds. Finally, it seems that following thermodynamic considerations, such as those outlined in Ref. [115], the points where the transition lines meet appear to be theoretically allowed.

6.3 Neutron scattering

As described in Chapter 3, neutron scattering is a powerful tool with which to study magnetic materials, since neutrons can give information about the arrangements of the magnetic moments in a sample. However, as briefly alluded to in Section 4.3, materials containing Gadolinium are not usually studied due to the high thermal neutron absorption by naturally abundant Gd ions of 49700 barns [71]. Natural Gd consists of seven isotopes, and it is the large absorption cross sections of only two of these isotopes, ^{155}Gd and ^{157}Gd [71], that gives rise to the thermal neutron absorption problem for Gd compounds. To solve this problem, two different methods may be used. One method would be to make crystals out of isotopic ^{160}Gd, which has a small absorption cross-section of 0.77 barns and coherent scattering length of 9.15 b [71]. To obtain enough of the ^{160}Gd isotope in order to grow a single crystal of $SrGd_2O_4$, however; is prohibitively expensive, and hence the second method to overcome the high absorption of naturally abundant Gd was used instead. This method relies on the observation that the magnitude of the absorption strongly depends on the incident neutron energy, and so at high energies there occurs a minimum in the ab-
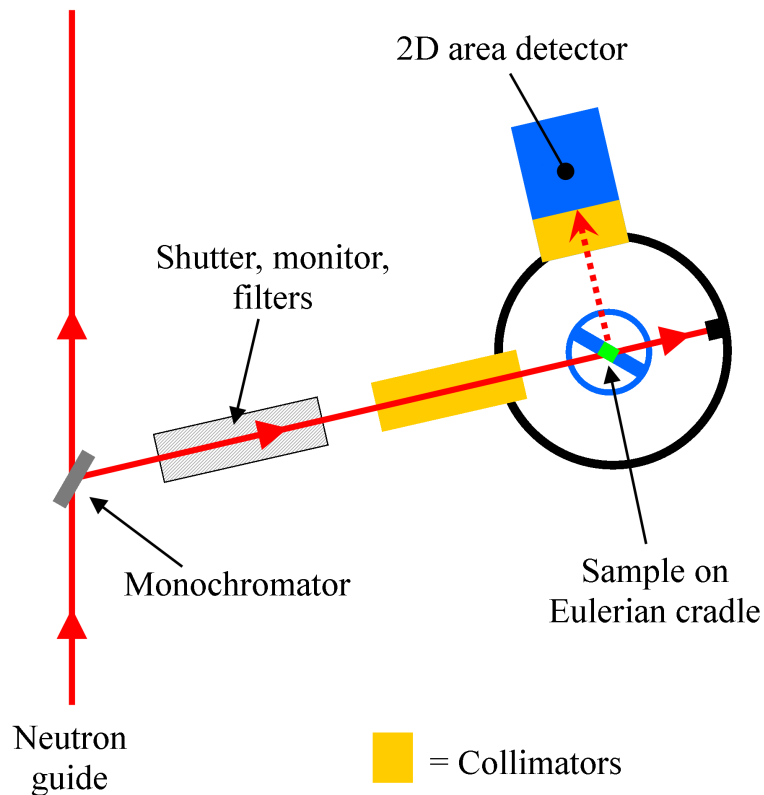
Figure 6.16: Schematic of the D9 instrument at the hot neutron guide at ILL, France. This figure made with reference to the D9 page in [89].

sorption curve for Gd [116–118]. Thus, high energy ("hot") neutrons can be used to study materials with large thermal neutron absorption cross sections. Therefore, a single crystal neutron diffraction experiment on $SrGd_2O_4$ was carried out using hot neutrons at the D9 high-resolution diffractometer at the Institut Laue Langevin in Grenoble, France.

D9 instrument, whose schematic is shown in Fig. 6.16, is built along similar principles as the D10 instrument which was described in Section 4.3.5. The instrument design allows D9 to measure scattered intensities accurately and with high resolution up to very large momentum transfers. Two different configurations of the instrument were used for the $SrGd_2O_4$ experiment: the standard four-circle mode, and the two-axis mode with the addition of a dilution refrigerator. As the D9 instrument is placed on a Tanzboden floor, a continuous choice of the incident wavelength can be made in the range of $0.35 - 0.85$ Å. A short incident neutron wavelength of 0.51 Å was obtained by using reflection from a

copper (220) monochromator throughout the $SrGd_2O_4$ experiment. The half-wavelength contamination was suppressed by a resonance filter.

For the $SrGd_2O_4$ measurements, during the 4-circle experiment, a single crystal sample (weighing 0.055 g) was fixed to a normal Al pin using a fast setting resin, and for the dilution part a second sample (weighing 0.065 g) was fixed to an oxygen free copper pin using Stycast resin. The Al sample pin was attached to the Eulerian cradle inside a cryostat that allowed scanning along all reciprocal lattice directions at low temperature. The measurements using the 4-circle geometry were made in the temperature range of 1.93 to 5 K. On D9, the scattered neutron intensity is recorded using a small (32 x 32 pixels) two-dimensional area detector.

D9 is controlled via a command lines from a computer. The data analysis software on D9 includes the usual routines for integrating the intensity of the measured Bragg reflections, fitting peak profiles and plotting the scattering profiles. For the $SrGd_2O_4$ experiment, the integrated intensity of the nuclear and magnetic reflections was extracted in the usual manner and applying the appropriate background corrections [96]. Before the data can be further analysed, absorption corrections using the geometry of the crystal and the absorption cross-sections of the relevant elements have to be carefully applied. The FullProf software can then be used to refine the crystal structure using the data collected at 5 K and magnetic structure using data collected at the lower temperatures.

Due to the Q dependence of the magnetic form factor, the scattering due to magnetic correlations can usually only be observed at low-Q values. Thus, during the 4-circle part of the D9 experiment, the lowest (hkl) reflections were attempted to be measured, with the limitations set by the use of high energy neutrons (which cannot access the lowest-Q regime, that can be probed, for example, using the D10 instrument). The 4-circle configuration of D9 allows for the investigation of reflections in the full (hkl) reciprocal space, and thus several reflections were found whose intensity increases below 2.8 K. The temperature dependence of these is shown in Fig. 6.17. Only the "raw" (non-absorption corrected) intensity of these is shown. Scans of the reciprocal space between the observed nuclear peaks from $SrGd_2O_4$ show that there is no increase in the scattering intensity at any half-integer or incommensurate positions. Also, no diffuse scattering was observed, and the width of
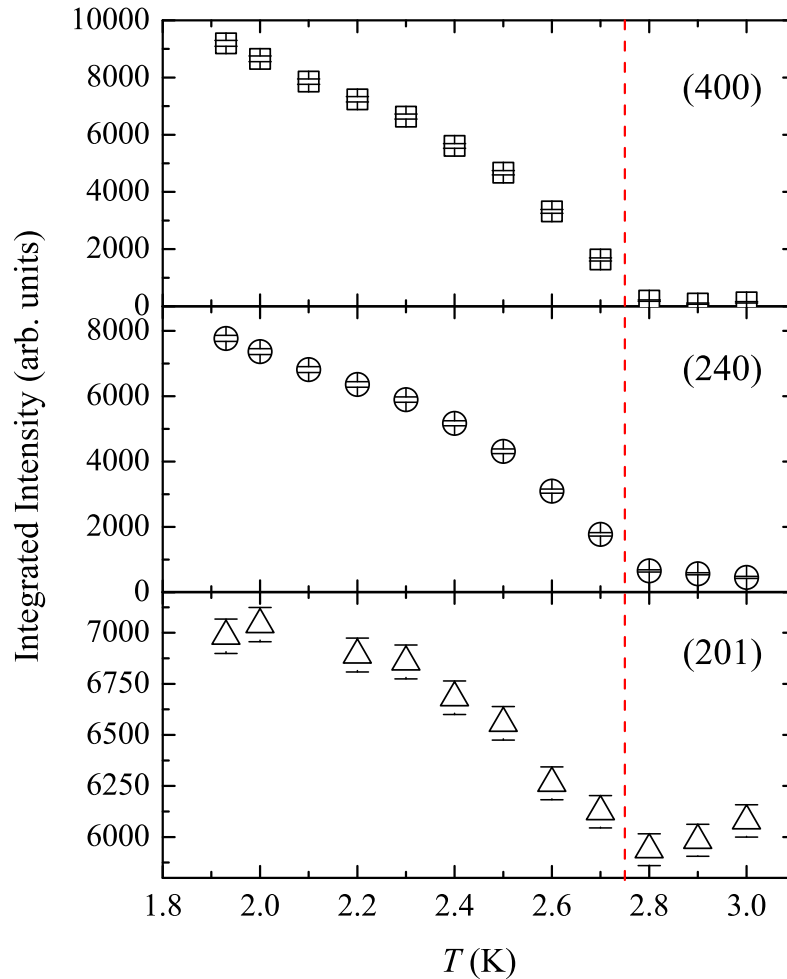
Figure 6.17: Temperature dependence of the intensity of the (400), (240) and (201) peaks from single crystal SrGd$_2$O$_4$, collated from diffraction data collected using D9, ILL. The data shown are the "raw" intensity, where no absorption corrections have been applied. It appears that (400) is a purely magnetic reflection from SrGd$_2$O$_4$, whereas (240) has a small nuclear intensity above 2.8 K. For (201) the magnetic intensity sits on top of a large nuclear peak. For all of the peaks shown, the magnetic intensity appears to go through a phase transition, and this was expected from single crystal susceptibility and specific heat measurements described in Sections 6.2.2 and 6.2.4. The dashed line indicates $T_N = 2.76$ K - the average temperature intercept obtained when plotting $I^2 \propto (T - T_N)$ for the three reflections, as shown in Fig. 6.18.
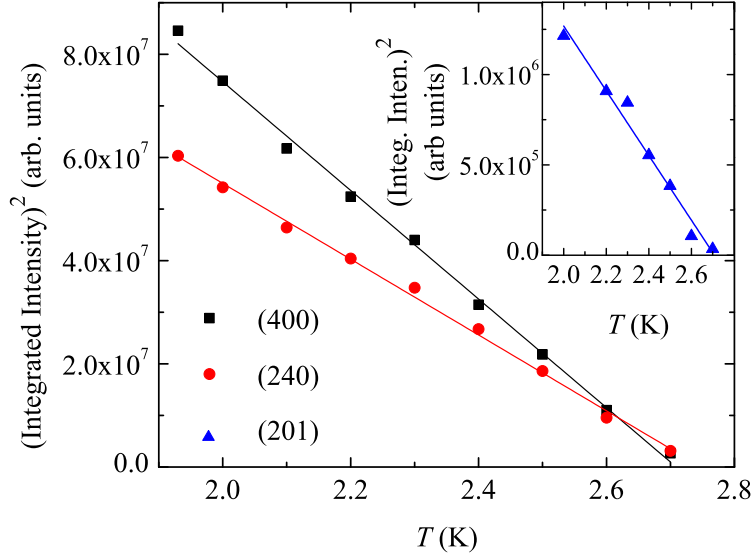
Figure 6.18: The transition temperature of T_N = 2.76 K is obtained by averaging the value of the temperature intercepts when plotting $I^2 \propto (T - T_N)$ for the (400), (240) and (201) reflections from $SrGd_2O_4$. The data for (201) is shown in the inset because it is a much weaker reflection, and the trend is not visible if it is plotted alongside (400) and (240).

measured magnetic reflections is comparable to that of the nuclear scattering. This, and the data presented in Fig. 6.17 indicates that the magnetic order that appears below 2.8 K is commensurate with the lattice, and can be indexed with the propagation vector $\mathbf{k} = 0$.

Only a limited time was allowed for the completion of the 4-circle measurements, as the larger part of the experimental time was allocated to collecting data using the dilution refrigerator set-up. However, the dilution part of the experiment was unsuccessful due to equipment failure, and no data was collected. This meant that the only full dataset gathered for $SrGd_2O_4$ was for the high-temperature part of the experiment (that can be used to solve the nuclear structure, but this has already been done using x-ray data, presented earlier), and the data collection for the intermediate $\mathbf{k} = 0$ phase was incomplete, as well as no information was obtained on the lowest temperature magnetic phase in $SrGd_2O_4$. The low temperature part of this experiment is due to be re-scheduled after the long shutdown of the ILL.

6.4 Discussion

The Gd^{3+} ion has a spin of $S = \frac{7}{2}$ and zero orbital angular momentum, which means that crystal-field splittings and anisotropy, which play a large role in the properties of the $SrHo_2O_4$, $SrEr_2O_4$ and $SrDy_2O_4$ materials are expected to be relatively unimportant in $SrGd_2O_4$. This also makes $SrGd_2O_4$ the best candidate for a realisation of a classical Heisenberg exchange antiferromagnet compared to the other $SrLn_2O_4$ compounds. For such systems, dipole-dipole interactions are expected to the leading perturbations in the Hamiltonian. The $SrGd_2O_4$ system also provides an interesting comparison and furthers the study of the influence of the crystal fields on the the physics of the $SrLn_2O_4$ and similar systems, such as $BaLn_2O_4$ [55]. The magnetic ordering schemes in these honeycomb and zigzag ladder materials can be very complex, and they can have multiple magnetic phases in their phase diagrams. It was therefore important to fully characterise the structural and magnetic properties of $SrGd_2O_4$.

In this chapter, a study of the magnetic properties of the frustrated rare earth antiferromagnet $SrGd_2O_4$ has been presented. Initially, powders of the material were produced using a standard solid state synthesis technique, and the crystal structure was studied using x-ray diffraction to check the final purity of the compounds. Previous reports for $SrGd_2O_4$ [43] indicated that no long-range order down to 1.8 K would be observed, the same as for the other members of the $SrLn_2O_4$ series. However, this has been shown to be incorrect, and in fact bulk property measurements on $SrGd_2O_4$ indicate that this compound behaves very differently to the other lanthanide compounds in the series. The bulk susceptibility for $SrGd_2O_4$ follows the Curie-Weiss law with an effective moment relatively close to the theoretical limit of 7.94 μ_B for the free ion and a Curie-Weiss temperature of $\theta_{CW} = -9.8$ K. Magnetic susceptibility and specific heat measurements on polycrystalline samples further indicate that at least two transitions take place in zero-field at low temperatures, at 2.8 and 0.47 K. Thus, changing the rare earth in $SrLn_2O_4$ systems to Gd^{3+} results in markedly different magnetic behaviour, since no other $SrLn_2O_4$ compound measured so far shows two separate transitions to different long-range orders in zero applied field.

The first high quality single crystals of $SrGd_2O_4$ have been grown using the floating zone technique, and these have been used to perform a thorough investigation into the mag-

netic properties of this compound. For $SrGd_2O_4$, the high temperature susceptibility curves are nearly identical when measured along the different principal axes, which is unlike the other $SrLn_2O_4$ compounds, where large differences may be observed [59]. This is probably the effect of low-lying crystal field levels in the other compounds, which is absent in $SrGd_2O_4$. The magnetic behaviour of $SrGd_2O_4$ as a function of applied magnetic field has also been studied. The results suggest that magnetisation processes along the a and b axes are quite unexciting, but dramatic changes are observed for applied magnetic fields along the c axis in the range of 1.5 to 2.5 T. The field induced transitions have been confirmed across multiple samples, and it may be conjectured that at least one of the phases stabilised with the applied field is an up-up-down spin order such as that seen in the other members of the $SrLn_2O_4$ family. Thus, the stabilisation of the uud spin structure which seems to be a common feature of all of the $SrLn_2O_4$ compounds. This in-field phase may be the result of all of the compounds having a similar crystallographic position for the lanthanide ions in triangular ladders that run along the c direction, on which it would be relatively easy to stabilise the uud spin structure. In even stronger applied fields there is a transition to yet another new phase. The nature of the ordered magnetic states in $SrGd_2O_4$ would be usually determined using neutron diffraction, however, for $SrGd_2O_4$ this may be difficult because of the large absorption cross-section of the Gd ions.

The results of heat capacity measurements as a function of both temperature and magnetic field give direct information about the boundaries of the phase transitions observed in $SrGd_2O_4$. Again, these measurements indicate that $SrGd_2O_4$ is very different to other $SrLn_2O_4$ compounds. Specific heat measurements, for example on $SrEr_2O_4$ [58] and $SrHo_2O_4$ (see Section 5.2.4) indicate the presence of short range correlations developing at temperatures higher than the observed transition temperatures in these materials, whereas indications of short range correlations are absent in the specific heat data collected for $SrGd_2O_4$. All of the bulk property measurements have been used to construct a magnetic phase diagram for $SrGd_2O_4$ as a function of magnetic field and temperature (for the field applied along the crystallographic c axis). There is large number of potentially unusual magnetic states observed in the $H - T$ phase diagram for $SrGd_2O_4$, but bulk property measurements on other compounds (such as the data presented on $SrHo_2O_4$ in Chapter 5)

in this series, except in the case of $SrYb_2O_4$, indicate that their phase diagrams appear to be simpler.

For all the $SrLn_2O_4$ compounds other than $SrGd_2O_4$, it seems that the magnetic moments are constrained to lie along two separate principal crystallographic directions, but in $SrGd_2O_4$ almost all of the unusual magnetic behaviour occurs for the fields applied along the c axis. This suggests that it is the crystal fields that are responsible for the origins of the highly anisotropic behaviour shown by all of the $SrLn_2O_4$ compounds other than $SrGd_2O_4$. At present, no complete description of the CEF levels exist for any of the members of the $SrLn_2O_4$ family, but this understanding should resolve the differences seen in the magnetisation processes. An interesting parallel to the behaviour of $SrGd_2O_4$ compared to other $SrLn_2O_4$ compounds may be found by looking at the pyrochlore titanates. Here, $Gd_2Ti_2O_7$ shows a transition to long range magnetic order at a higher temperature than most of the other members of the titanate family, a lot of which never show any LRO behaviour at all [119]. $Gd_2Ti_2O_7$, like $SrGd_2O_4$, represents the case where pertubations to the Hamiltonian such as the crystal fields and single ion anisotropy do not exist and yet a long range ordered state is achieved. It is thus likely that these perturbations inhibit the transitions to long-range order, for example in the $Tb_2Ti_2O_7$ and $Ho_2Ti_2O_7$ compounds, and instead compete with the Heisenberg antiferromagnetic exchange interaction [119]. Analogously, the $SrGd_2O_4$ system where crystal fields and anisotropy are absent, may be 'less' frustrated than the other $SrLn_2O_4$ compounds.

Overall, the results of the bulk property measurements would merit further experimental study using neutron diffraction. These experiments would help to investigate the different magnetic phases that are stabilised at low temperatures for different values of the applied field, but would be challenging to carry out due to the large absorption cross-section of the Gd^{3+} ions. So far, only one single crystal neutron diffraction experiment was performed on $SrGd_2O_4$, in attempt to solve the magnetic structures of this material in zero applied field. Several issues made the analysis of the data collected challenging, such as absorption corrections and the lack of complete datasets. Although a full magnetic structural solution from the neutron scattering data was not found, some conclusions may still be drawn from the experiment. As expected from heat capacity measurements, no diffuse

magnetic scattering was measured for $SrGd_2O_4$ in the temperature range studied (whereas diffuse scattering has been observed for $SrHo_2O_4$, $SrEr_2O_4$ and $SrDy_2O_4$). An antiferromagnetic structure with the ordering wavevector $\mathbf{k} = 0$ phase appears to be stabilised below the 2.8 K transition temperature. This means that the magnetic reflections in general will sit atop the nuclear peaks. This makes it difficult to find strong magnetic reflections, without first applying absorption corrections to the data. Both $SrEr_2O_4$ and $SrHo_2O_4$ also show signs of one of the magnetic *Ln* ions ordering (or partially ordering in the case of Ho) into a $\mathbf{k} = 0$ phase. Thus at least some sort of $\mathbf{k} = 0$ order seems to be common to all of the compounds in zero field. However, another zero field transition at 0.47 K for $SrGd_2O_4$ - unlike in the other $SrLn_2O_4$ compounds - means that the lowest temperature magnetic phase remains unknown and the ground state magnetic structure of $SrGd_2O_4$ cannot be conclusively deduced without further study. Currently, unlike for example $SrEr_2O_4$ and $SrHo_2O_4$, $SrGd_2O_4$ does not show a clear coexistence of two distinct antiferromagnetic components to the magnetic structure at low temperatures. However, this may change with the investigation of the lowest temperature phase using neutron scattering.

In summary, $SrGd_2O_4$ is a complex system with several competing magnetic interactions. And, although the magnetism of $SrGd_2O_4$ has been studied, there are still unanswered questions raised by the investigation into the magnetic properties of $SrGd_2O_4$ presented in this chapter. Studying the magnetism in $SrGd_2O_4$ has demonstrated the necessity of the further use of neutron diffraction for characterising this compound. Interesting new observations include the formation of multiple low-temperature magnetic phases, and the features of the magnetic behaviour of this material should be further explored in the future. In order for this further progress to be made, more neutron scattering data must be collected as a function of both temperature and the magnetic field, and this is necessary so that the different magnetic structures of $SrGd_2O_4$ can be accurately determined.

Chapter 7

Conclusions and prospects

The magnetic characterisation of the SrLn_2O$_4$ family of compounds began with the work of Karunadasa *et al.* only a few years ago [43]. Since, the properties of several of the compounds have been explored in more detail, and these studies have begun to reveal the rich variety of low-temperature, low-dimensional magnetic behaviour that is starting to attract theoretical interest. In this thesis, the results of an investigation into the magnetic properties of two geometrically frustrated compounds, SrHo$_2$O$_4$ and SrGd$_2$O$_4$, that belong to the SrLn_2O$_4$ family have been presented. The structure of the SrLn_2O$_4$ compounds consists of hexagonal layers of the magnetic Ln^{3+} ions that can be seen in the $a - b$ plane, and these honeycomb layers are connected by zigzag chains of the lanthanide ions which run along the c axis. These triangular ladders can be frustrated if the dominant exchange is antiferromagnetic, and are magnetically equivalent to one-dimensional chains with first- and second-nearest-neighbour interactions. For at least some of the compounds, including SrHo$_2$O$_4$, it appears that the intra-chain interactions in the zigzag ladders are very strong, but inter-chain couplings are weak, and thus the system shows a pronounced low-dimensional character. The crystal structure allows for two crystallographically inequivalent sites of the rare earth ions in the unit cell, and this leads to some complex interplay between these two magnetic sites, anisotropy and frustration. Most of the SrLn_2O$_4$ materials do not order at the temperatures expected from high temperature susceptibility measurements, even though they are coupled by strong exchange interactions. For some of the compounds, for example in SrHo$_2$O$_4$, long-range magnetic order is not established down to the lowest tempera-

tures, whereas for others, like $SrGd_2O_4$, the magnetic field–temperature phase diagram is dominated by many different low-temperature phases. Powder samples of the compounds were produced in order to facilitate the research undertaken, and the first single crystal of $SrGd_2O_4$ has been grown specially for this work.

The samples of $SrHo_2O_4$ have been characterised by bulk property measurements, and these have revealed the highly anisotropic nature of this compound. The low temperature phases have been probed using both powder and single crystal neutron diffraction, and these measurements have revealed the highly unusual coexistence of two different types of magnetic scattering from $SrHo_2O_4$: one has a low-dimensional character, whereas the other appears as well-defined peaks in the diffraction pattern, but only below 0.7 K. From the powder diffraction data, it is evident that the diffuse magnetic scattering that has the pronounced low-dimensional character, exists over a very large temperature range, and only appears to get more correlated with decreasing temperature. The refinement of powder neutron diffraction data revealed that the second type of order, which has the ordering wavevector $\mathbf{k} = 0$, is consistent with a structure based on a series of ferromagnetic chains running along the c axis, and these chains are coupled antiferromagnetically with each other. Within this refined structure, the magnetic moments, can only be put on one of the inequivalent Ho^{3+} ions, and are collinear with the c axis. Further single crystal neutron diffraction work revealed that the $\mathbf{k} = 0$ type scattering is *not* long-range, and that the nature of the low-dimensional scattering from $SrHo_2O_4$ is distinctly one-dimensional. The use of polarised neutron scattering has allowed for the experimental verification that the two magnetic sites have Ising-like moments that point in orthogonal directions (along the b and c axes), which is highly unusual even in the field of frustrated magnetism, and a likely explanation for this is probably bound up in the complex crystal field problem for this material. The diffraction data collected in applied fields can be directly correlated with bulk magnetisation data, and all evidence suggests that the formation of another short-range ordered phase, where an up-up-down collinear spin order is stabilised at low temperatures when the field is applied along the b axis, takes place. The modelling of the interactions consistent with these diffraction patterns is currently underway, and RMC calculations are also being attempted in order to fit the observed $SrHo_2O_4$ data.

The inelastic experiments on powder samples of $SrHo_2O_4$ have shown that the CEF in this material is far from trivial. Firstly, there are a large number of CEF levels, secondly, some of these levels change their position with temperature, and finally, some of the levels show an unusual dispersion along Q below ~ 3 K. Nonetheless, it is hoped that the study of the CEF should eventually help with understanding the origin of the magnetocrystalline anisotropy in $SrHo_2O_4$. Further single crystal inelastic neutron scattering experiments, using triple-axis spectrometers, could also help to identify in greater detail the temperature induced changes to the CEF, and clarify some of the powder data, the fitting of which is currently being attempted. It would also be beneficial to definitively separate the nuclear Schottky and the magnetic contributions to the specific heat at low temperature, so that the magnetic entropy recovered at low temperatures for $SrHo_2O_4$ could be evaluated to see if it reaches R ln(2). Such behaviour observed in other Ho compounds, for example $Ho_2Ti_2O_7$, in the presence of a strong Ising-like magnetic anisotropy, and this would provide further evidence that at low temperatures $SrHo_2O_4$ may be treated as an effective $S = \frac{1}{2}$ system.

An investigation into the properties of $SrGd_2O_4$ has also been carried out. For Gd in the ground state, $L = 0$, so crystal fields are not expected to be important (which is completely contrary to what is found in the other $SrLn_2O_4$ compounds) and the $SrGd_2O_4$ system provides a good realisation of classical Heisenberg magnetic moments. The nuclear structure of $SrGd_2O_4$ was determined from the powder x-ray diffraction data, and a complete characterisation, using specific heat, magnetisation and susceptibility measurements, on both powder and single crystal samples has revealed a variety of low-temperature transitions. The magnetic phase diagram, as a function of field and temperature, was mapped out for measurements taken with the magnetic field applied along the c axis of $SrGd_2O_4$, and a lot of low-energy phases with well-defined boundaries have been identified. The data collected for the fields applied along the a and b axes of $SrGd_2O_4$ does not show such a dramatic variety of magnetic behaviour. The bulk property measurements motivate the need to further investigate the different phases present in $SrGd_2O_4$ using neutron diffraction. Any experiments using non-isotopically enriched samples of Gd are challenging, but nonetheless they may be attempted with the use of hot neutrons. Some preliminary information on the nature of the magnetic order below the first zero field transition temperature is now

available, and it appears that a long-range $\mathbf{k} = 0$ phase is stabilised here. However, completion of the zero field experiment and subsequently refining the neutron diffraction data would be very useful for microscopically characterising the magnetic phases. A possible extension to the zero field diffraction experiments, would be to use a cryomagnet to study the phases in $SrGd_2O_4$ that are stabilised by an applied field along the c axis.

The data presented in the thesis illustrate that there is a vast difference between the magnetic behaviour of $SrHo_2O_4$ and $SrGd_2O_4$, even though the positions of the magnetic ions and the strength of the exchange interactions are comparable. This was to be expected, and it is likely that the low-temperature properties of $SrGd_2O_4$ would be quite different compared to the other $SrLn_2O_4$ compounds for which the spin-orbit coupling and crystal field anisotropies would be much more important. It was attempted to try and emphasise the similarities and differences between the different $SrLn_2O_4$ compounds throughout the thesis in light of the results obtained for $SrHo_2O_4$ and $SrGd_2O_4$. The magnetisation processes of $SrHo_2O_4$, $SrEr_2O_4$ and $SrDy_2O_4$ are thought to be particularly similar, and neutron diffraction measurements on single crystal samples reveal that $SrHo_2O_4$ and $SrEr_2O_4$ do indeed share very similar magnetic structures, and thus it would be rather interesting to investigate what happens in $SrDy_2O_4$ using single crystal neutron diffraction. Overall, the measurements on $SrHo_2O_4$ and $SrGd_2O_4$ have been imperative for conducting an investigation into the effects of frustration as a function of the rare earth element in this family of compounds.

In conclusion, the magnetism of both $SrHo_2O_4$ and $SrGd_2O_4$ has been investigated using a variety of experimental techniques. The results reveal that $SrHo_2O_4$ provides an opportunity to study an Ising spin system and $SrGd_2O_4$ is a good realisation of a classical Heisenberg system, both embedded in a low-dimensional lattice. These findings are similar to what is known about the behaviour of different rare earth ions in the pyrochlore titinate systems, where the Gd based compound is classed as a Heisenberg spin system, and the Ho system is found to have strong Ising anisotropy. However, in the $SrLn_2O_4$ compounds two inequivalent magnetic sites are available for the rare earth ions, and the weak interactions between these sites, at least for $SrHo_2O_4$ and possibly for $SrEr_2O_4$, seem to play an important role in establishing the low-temperature magnetic structure. The results presented in this thesis have stimulated collaborations with the theorists, and it will be interesting to see

what insights about the nature of the ordering mechanisms in these systems would be developed in the future. There are still matters which would merit further investigation for both $SrHo_2O_4$ and $SrGd_2O_4$, and this research could help to improve the understanding of these systems magnetic behaviour. Finally, it would be interesting to study the role of frustration as a function of the rare earth element in the $SrLn_2O_4$ family of compounds once more is known about some of the other members of the series.

Bibliography

[1] Plato, *Ion,* in *Plato: Complete Works*, edited by J. M. Cooper (Hackett Publishing Company, Indianapolis, 1997) p. 941.

[2] S. Blundell, *Magnetism: A Very Short Introduction* (OUP, Oxford, 2012).

[3] S. J. Blundell, *Magnetism in Condensed Matter* (OUP, Oxford, 2001).

[4] K. H. J. Buschow and F. R. de Boer, *Physics of Magnetism and Magnetic Materials* (Kluwer Academic, New York, 2003).

[5] J. Jensen and A. R. Mackintosh, *Rare Earth Magnetism* (Clarendon Press, Oxford, 1991).

[6] E. Merzbacher, *Quantum Mechanics,* 2nd ed. (John Wiley & Sons, Inc., New York, 1970) Chap. 12.

[7] K. W. H. Stevens, Proc. Phys. Soc. A **65**, 209 (1952).

[8] L. D. Landau, Phys. Z. Sowjun. **11**, 26 (1937).

[9] L. D. Landau, Phys. Z. Sowjun. **11**, 545 (1937).

[10] S. J. Blundell and K. M. Blundell, *Concepts in Thermal Physics,* 2nd ed. (OUP, Oxford, 2006) Chap. 24.

[11] L. Pauling, J. Am. Chem. Soc. **57**, 2680 (1935).

[12] J. Villain, Z. Phys. B **33**, 31 (1979).

[13] K. Binder and A. P. Young, Rev. Mod. Phys. **58**, 801 (1986).

[14] R. Moessner and J. T. Chalker, Phys. Rev. Lett. **80**, 2929 (1998).

[15] B. Canals and C. Lacroix, Phys. Rev. Lett. **80**, 2933 (1998).

[16] A. P. Ramirez, Annu. Rev. Mater. Sci. **24**, 453 (1994).

[17] H. T. Diep, ed., *Frustrated Spin Systems* (World Scientific, Singapore, 2005).

[18] A. P. Ramirez, *Physics of Magnetism and Magnetic Materials*, edited by K. H. L. Buschow, Vol. 13 (Elsevier, Amsterdam, 2001) Chap. 4.

[19] J. E. Greedan, J. Mater. Chem. **11**, 37 (2001).

[20] C. Lacroix, P. Mendels, and F. Mila, eds., *Introduction to Frustrated Magnetism* (Springer-Verlag, Berlin, 2011).

[21] R. Moessner and J. T. Chalker, Phys. Rev. B **58**, 12049 (1998).

[22] P. Schiffer, A. P. Ramirez, D. A. Huse, P. L. Gammel, D. J. B. U. Yaron, and A. J. Valentino, Phys. Rev. Lett. **74**, 2379 (1995).

[23] H. Fukazawa, R. G. Melko, R. Higashinaka, Y. Maeno, and M. J. P. Gingras, Phys. Rev. B **65**, 054410 (2002).

[24] S. T. Bramwell, M. J. Harris, B. C. den Hertog, M. J. P. Gingras, J. S. Gardner, D. F. McMorrow, A. R. Wildes, A. L. Cornelius, J. D. M. Champion, R. G. Melko, and T. Fennell, Phys. Rev. Lett. **87**, 047205 (2001).

[25] S. T. Bramwell and M. J. P. Gingras, Science **294**, 1495 (2001).

[26] C. Castelnovo, R. Moessner, and S. L. Sondhi, Nature **451**, 42 (2008).

[27] S. E. Palmer and J. T. Chalker, Phys. Rev. B **62**, 488 (2000).

[28] S. Sachdev, Phys. Rev. B **45**, 12377 (1992).

[29] M. F. Collins and O. A. Petrenko, Annu. Rev. Mater. Sci. **75**, 605 (1997).

[30] J. S. Gardner, M. J. P. Gingras, and J. E. Greedan, Rev. Mod. Phys. **82**, 53 (2010).

[31] A. P. Ramirez, G. P. Espinosa, and A. S. Cooper, Phys. Rev. Lett. **64**, 2070 (1990).

[32] J. T. Chalker and J. F. G. Eastmond, Phys. Rev. B **46**, 14201 (1992).

[33] R. Moessner, S. L. Sondhi, and P. Chandra, Phys. Rev. B **64**, 144416 (2001).

[34] P. Schiffer, A. P. Ramirez, D. A. Huse, and A. J. Valentino, Phys. Rev. Lett. **73**, 2500 (1994).

[35] T. Yoshioka, A. Koga, and N. Kawakami, J. Phys. Soc. Japan **73**, 1805 (2004).

[36] N. Rogado, M. K. Haas, G. Lawes, D. A. Huse, A. P. Ramirez, and R. J. Cava, J. Phys.: Condens. Matter **15**, 907 (2003).

[37] O. Tchernyshyov, Phys. Rev. Lett. **93**, 157206 (2004).

[38] S. T. Bramwell and M. J. P. Gingras, Science **294**, 1495 (2001).

[39] P. Chandra and B. Doucot, Phys. Rev. B **38**, 9335 (1988).

[40] H. J. Schulz, Phys. Rev. Lett. **77**, 2790 (1996).

[41] H. Karunadasa, Q. Huang, B. G. Ueland, P. Schiffer, and R. J. Cava, Proc. Nat. Acad. Sci. USA **100**, 8097 (2003).

[42] J.-W. G. Bos and J. P. Attfield, Phys. Rev. B **70**, 174434 (2004).

[43] H. Karunadasa, Q. Huang, B. G. Ueland, J. W. Lynn, P. Schiffer, K. A. Regan, and R. J. Cava, Phys. Rev. B **71**, 144414 (2005).

[44] L. M. Lopato and A. E. Kushchevskii, Ukrainskii Khimicheskii Zhurnal **39**, 7 (1973).

[45] B. F. Decker and J. S. Kasper, Acta Cryst. **10**, 332 (1957).

[46] A. Mattsson, P. Frojdh, and T. Einarsson, Phys. Rev. B **49**, 3997 (1994).

[47] S. Okumura, H. Kawamura, T. Okubo, and Y. Motome, J. Phys. Soc. Japan **79**, 114705 (2010).

[48] Y. Yu, L. Liang, Q. Niu, and S. Qin, Phys. Rev. B **87**, 041107 (2013).

[49] A. Möller, U. Löw, T. Taetz, M. Kriener, G. André, F. Damay, O. Heyer, M. Braden, and J. A. Mydosh, Phys. Rev. B **78**, 024420 (2008).

[50] M. Yehia, E. Vavilova, A. Möller, T. Taetz, U. Löw, R. Klingeler, V. Kataev, and B. Büchner, Phys. Rev. B **81**, 060414 (2010).

[51] O. Smirnova, M. Azuma, N. Kumada, Y. Kusano, M. Matsuda, Y. Shimakawa, T. Takei, Y. Yonesaki, and N. Kinomura, J. Am. Chem. Soc. **131**, 8313 (2009).

[52] M. Matsuda, M. Azuma, M. Tokunaga, Y. Shimakawa, and N. Kumada, Phys. Rev. Lett. **105**, 187201 (2010).

[53] F. Damay, C. Martin, V. Hardy, A. Maignan, G. André, K. Knight, S. R. Giblin, and L. C. Chapon, Phys. Rev. B **81**, 214405 (2010).

[54] F. Damay, C. Martin, V. Hardy, A. Maignan, C. Stock, and S. Petit, Phys. Rev. B **84**, 020402(R) (2011).

[55] Y. Doi, W. Nakamori, and Y. Hinatsu, J. Phys.: Condens. Matter **18**, 333 (2006).

[56] O. Ofer, J. Sugiyama, J. H. Brewer, E. J. Ansaldo, M. Månsson, K. H. Chow, K. Kamazawa, Y. Doi, and Y. Hinatsu, Phys. Rev. B **84**, 054428 (2011).

[57] G. Balakrishnan, T. J. Hayes, O. A. Petrenko, and D. M^{c}K Paul, J. Phys.: Condens. Matter **21**, 012202 (2009).

[58] O. A. Petrenko, G. Balakrishnan, N. R. Wilson, S. de Brion, E. Suard, and L. C. Chapon, Phys. Rev. B **78**, 184410 (2008).

[59] T. J. Hayes, O. Young, G. Balakrishnan, and O. A. Petrenko, J. Phys. Soc. Japan **84**, 024708 (2012).

[60] D. L. Quintero-Castro, B. Lake, M. Reehuis, A. Niazi, H. Ryll, A. T. M. N. Islam, T. Fennell, S. A. J. Kimber, B. Klemke, J. Ollivier, V. G. Sakai, P. P. Deen, and H. Mutka, Phys. Rev. B **86**, 064203 (2012).

[61] T. H. Cheffings, M. R. Lees, G. Balakrishnan, and O. A. Petrenko, J. Phys.: Condens. Matter **25**, 256001 (2013).

[62] O. A. Petrenko, L. C. Chapon, C. Ritter, and T. J. Hayes, ILL Exp. Report 5-31-1695 (2007).

[63] T. J. Hayes, G. Balakrishnan, P. P. Deen, P. Manuel, L. C. Chapon, and O. A. Petrenko, Phys. Rev. B **84**, 174435 (2011).

[64] O. A. Petrenko, T. J. Hayes, and P. Manuel, ISIS experimental report RB810337 (2009).

[65] M. T. Dove, *Structure and Dynamics* (OUP, New York, 2003).

[66] G. E. Bacon, *Neutron Diffraction* (Clarendon Press, Oxford, 1975).

[67] G. L. Squires, *Introduction to the Theory of Thermal Neutron Scattering* (Dover, New York, 1978).

[68] J. F. Nye, *Physical Properties of Crystals: Their Tepresentation by Tensors and Matrices* (OUP, Oxford, 1985).

[69] A. S. Wills, Physica B **276**, 680 (2000).

[70] G. E. Bacon and K. Lonsdale, Rep. Prog. Phys. **16**, 1 (1953).

[71] V. F. Sears, Neutron News **3**, 26 (1992).

[72] R. M. Moon, T. Riste, and W. C. Koehler, Phys. Rev. **181**, 920 (1969).

[73] O. Schärpf and H. Capellmann, Z. Phys. B **80**, 253 (1990).

[74] J. R. Stewart, P. P. Deen, K. H. Andersen, H. Schober, J. F. Barthelemy, J. M. Hillier, A. P. Murani, T. Hayes, and B. Lindenauc, J. Appl. Crystallogr. **42**, 69 (2009).

[75] A. A. Coelho, "Topas-academic, version 4.1," http://www.topas-academic.net (1992–2007).

[76] H. M. Rietveld, Acta. Cryst. **22**, 151 (1967).

[77] H. M. Rietveld, J. Appl. Cryst. **2**, 65 (1969).

[78] A. Albinati and B. T. M. Willis, *International Tables for Crystallography*, Vol. C (2006) Chap. 8.6, p. 710.

[79] J. Rodríguez-Carvajal, Physica B **192**, 55 (1993).

[80] I. Media Cybernetics, "Image-pro express version 5.0," http://www.mediacy.com (2004).

[81] J. Laugier and B. Bochu, "Orientexpress," part of the the LMGP Suite software, http://www.ccp14.ac.uk/tutorial/lmgp/index.html (2003).

[82] M. McElfresh, *Fundamentals of Magnetism and Magnetic Measurements Featuring Quantum Designs Magnetic Property Measurement System* (Quantum Design, 1994).

[83] N. Shirakawa, H. Horinouchi, and Y. Yoshida, J. Magn. Magn. Mater. **272**–**276**, e149 (2004).

[84] A. Aharoni, J. Appl. Phys. **83**, 3432 (1998).

[85] D.-X. Chen, J. A. Brug, and R. B. Goldfarb, IEEE Trans. Magn. **27**, 3601 (1991).

[86] *Physical Property Measurement System: Hardware Manual* (Quantum Design, 2000).

[87] *Physical Property Measurement System: Heat Capacity Option Users Manual* (Quantum Design, 2000).

[88] J. S. Hwang, K. Lin, and C. Tien, Rev. Sci. Instrum. **68(1)**, 94 (1997).

[89] G. Cicognani, ed., *Guide to the Neutron Research Facilities at the ILL, The Yellow Book* (2008).

[90] P. Day, J. E. Enderby, W. G. Williams, L. C. Chapon, A. C. Hannon, P. G. Radaelli, and A. K. Soper, Neutron News **15**, 19 (2004).

[91] A. C. Hannon, Nuclear Instruments and Methods in Physics Research A **551**, 88 (2005).

[92] L. C. Chapon, P. Manuel, P. G. Radaelli, C. Benson, L. Perrott, S. Ansell, N. Rhodes, D. Raspino, D. Duxbury, E. Spill, and J. Norris, Neutron News **22**, 22 (2011).

[93] J. Taylor, O. Arnold, J. Bilheaux, A. Buts, S. Campbell, M. Doucet, N. Draper, R. Fowler, M. Gigg, V. Lynch, A. Markvardsen, K. Palmen, P. Parker, P. Peterson, S. Ren, M. Reuter, A. Savici, R. Taylor, R. Tolchenov, R. Whitley, W. Zhou, and J. Zikovsky, APS March Meeting 2012, see Bulletin of the American Physical Society **57**(1), http://meetings.aps.org/Meeting/MAR12/Event/166478 (2012).

[94] O. Schärpf and H. Capellmann, Phys. Status Solidi **135**, 359 (1993).

[95] D. Richard, K. Andersen, and J. R. Stewart, "D7 lamp manual," http://www.ill.eu/instruments-support/instruments-groups/instruments/d7/more/-data-analysis/d7-lamp-manual/, (Last accessed: July 2013).

[96] C. Wilkinson, H. W. Khamis, R. F. D. Stansfield, and G. J. McIntyre, J. Appl. Crystallogr. **21**, 471 (1988).

[97] G. Cicognani, H. Mutka, and F. Sacchetti, Physica B **276**–**278**, 83 (2000).

[98] D. Richard, M. Ferrand, and G. J. Kearley, "Lamp," http://www.ill.eu/instruments-support/computing-for-science/cs-software/all-software/lamp/, (Last accessed: July 2013).

[99] H. Schober, A. J. Dianoux, J. C. Cook, and F. Mezei, Physica B **276**–**278**, 164 (2000).

[100] J. Ollivier, H. Casalta, H. Schober, J. C. Cook, P. Malbert, M. Locatelli, C. Gomez, S. Jenkins, I. J. Sutton, and M. Thomas, Appl. Phys. A **74**, S305 (2002).

[101] B. H. Toby, Powder Diffr. **21**, 67 (2006).

[102] H. Nishimori and S. Miyashita, J. Phys. Soc. Jpn. **55**, 4448 (1986).

[103] A. V. Chubukov and D. I. Golosov, J. Phys.: Condens. Matter **3**, 69 (1991).

[104] S. Ghosh, H. D. Zhou, L. Balicas, S. Hill, J. S. Gardner, Y. Qiu, and C. R. Wiebe, J. Phys.: Condens. Matter **23**, 164203 (2011).

[105] C. L. Fleck, M. R. Lees, S. Agrestini, G. J. McIntyre, and O. A. Petrenko, Europhysics Letters **90**, 67006 (2010).

[106] M. A. Hossain, I. Zegkinoglou, Y.-D. Chuang, J. Geck, B. Bohnenbuck, A. G. C. Gonzalez, H.-H. Wu, C. Schüßler-Langeheine, D. G. Hawthorn, J. D. Denlinger, R. Mathieu, Y. Tokura, S. Satow, H. Takagi, Y. Yoshida, Z. Hussain, B. Keimer, G. A. Sawatzky, and A. Damascelli, Sci. Rep. **3**, 2299 (2013).

[107] J. A. M. Paddison and A. L. Goodwin, Phys. Rev. Lett **108**, 017204 (2012).

[108] O. Young, I. Glavatskyi, and O. A. Petrenko, HZB Exp. Report PHY-01-3098 (2012).

[109] O. A. Petrenko, T. J. Hayes, P. Manuel, and L. C. Chapon, ISIS experimental report RB920448 (2012).

[110] M. Kenzelmann and B. R. Hansen, ISIS experimental report 510364 (2005).

[111] O. A. Petrenko, L. C. Chapon, T. J. Hayes, and P. Manuel, ISIS experimental report RB810337 (2009).

[112] M. Enjalran and M. J. P. Gingras, Phys. Rev. B **70**, 174426 (2004).

[113] J. A. M. Paddison, private communication, unpublished (2013).

[114] O. A. Petrenko, L. C. Chapon, C. Ritter, and T. J. Hayes, ILL Exp. Report 5-53-1920 (2009).

[115] S. K. Yip, T. Li, and P. Kumar, Phys. Rev. B **43**, 2742 (1991).

[116] "Nuclear data services," http://www-nds.iaea.org/ngatlas2/, (Last accessed: July 2013).

[117] S. J. Friesenhahn, M. P. Fricke, D. G. Costello, W. M. Lopez, and A. D. Carlson, Nuclear Physics A **146**, 337 (1970).

[118] G. Leinweber, D. P. Barry, M. J. Trbovich, J. A. Burke, N. J. Drindak, H. D. Knox, R. V. Ballad, R. C. Block, Y. Danon, and L. I. Severnyak, Nuclear Science and Engineering **154**, 261 (2006).

[119] N. P. Raju, M. Dion, M. J. P. Gingras, T. E. Mason, and J. E. Greedan, Phys. Rev B **59**, 14489 (1999).